NASA Contractor Report 3061

Investigation of Steady and Fluctuating Pressures Associated With the Transonic Buffeting and Wing Rock of a One-Seventh Scale Model of the F-5A Aircraft

Chintsun Hwang and W. S. Pi

CONTRACT NAS2-8734
NOVEMBER 1978

NASA

NASA Contractor Report 3061

Investigation of Steady and Fluctuating Pressures Associated With the Transonic Buffeting and Wing Rock of a One-Seventh Scale Model of the F-5A Aircraft

Chintsun Hwang and W. S. Pi
Northrop Corporation
Hawthorne, California

Prepared for
Ames Research Center
under Contract NAS2-8734

NASA
National Aeronautics
and Space Administration

Scientific and Technical
Information Office

1978

Section

TABLE OF CONTENTS

Page

LIST OF ILLUSTRATIONS

LIST OF ILLUSTRATIONS (Continued)

LIST OF ILLUSTRATIONS (Continued)

LIST OF ILLUSTRATIONS (Continued)

LIST OF ILLUSTRATIONS (Continued)

LIST OF ILLUSTRATIONS (Continued)

INVESTIGATION OF STEADY AND FLUCTUATING PRESSURES ASSOCIATED WITH THE TRANSONIC BUFFETING AND WING ROCK OF A ONE-SEVENTH SCALE MODEL OF THE F-5A AIRCRAFT

By Chintsun Hwang and W.S. Pi
Northrop Corporation, Aircraft Division
Hawthorne, California

SUMMARY

The report describes a wind tunnel test of a one-seventh scale F-5A model and the evaluation of pressure, force, and dynamic response measurements during buffet and wing rock. The detail instrumentation, the specially designed support system which allowed the model to oscillate in roll to simulate wing rock, are also described. The investigation was conducted under Contract NAS2-8734, sponsored by NASA Ames Research Center.

The dynamic pressure and response data were recorded on frequency-modulated (FM) tapes which were used after the test for real-time and spectral analyses. The static and rms fluctuating pressure data were reduced to non-dimensional coefficients which were applied to buffet intensity and wing rock onset studies. The dynamic pressure data obtained during the wind tunnel tests were compared and correlated with those previously recorded in a flight test program. Parametric studies were performed using the acquired test data (by varying either the model configuration or the test condition) to investigate the effects of control surface settings, Mach number, sideslip angle, etc. on buffet.

Based on the pressure (steady state and fluctuating) and response data acquired when the model was near stationary and when it was excited by flow to oscillate in roll, a limit cycle mechanism was identified which supplied energy to the aircraft model and caused the wing rock type oscillations. The major origin of the fluctuating pressures which contributed to the limit cycle was traced to the wing surface leading edge stall and the subsequent lift recovery. For typical wing rock oscillations, the energy balance between the pressure work input and the energy consumed by the model aerodynamic and mechanical damping was formulated and numerical data presented.

Section 1

INTRODUCTION

The work described in this report deals with the wind tunnel test of a one-seventh scale model of the Northrop F-5A aircraft at transonic speed to investigate the steady and fluctuating pressures associated with buffet and wing rock. The tests were performed at NASA Ames Research Center Eleven-Foot Transonic Wind Tunnel.

Under sponsorship of the Ames Research Center (ARC), Northrop previously completed Contract NAS2-6475, entitled "Investigation of Northrop F-5A Wing Buffet Intensity in Transonic Flight." That project was a flight test program to acquire and analyze F-5A aircraft wing dynamic buffet load and response data in the transonic region. Based on the flight test data evaluation, the pressure distribution on the aircraft wing during buffet was used to define the initiation of the shock front(s) and the increase in dynamic pressure intensity due to flow separation, as well as the expansion of the separation region as the angle-of-attack increased. Within the transonic region, the effects of the Mach number with a constant-q load, as well as the effects of various flap settings on the pressure distribution and aircraft responses, were delineated and correlated analytically. The flight test results are described in Reference 1. In order to compare and correlate the dynamic pressure data acquired during the wind tunnel test with those of the flight test, taking into consideration the scaling relations, the scale model tests were conducted using test conditions similar to the flight test conditions.

The F-5A scale model wind tunnel buffet investigation program was accomplished in two phases. In the first test phase, a nominally rigid sting was used. In the second test phase, a special sting was designed incorporating a torsional spring and damper which allowed the model to oscillate in roll at a natural frequency simulating the Dutch roll motion during wing-rock. Special instrumentation for the model included 28 Kulite Model LQ2-156W-4 pressure transducers, 28 static pressure taps, 3 accelerometers, and 4 wing root strain gage bridges. Tests were performed encompassing 11 model configurations defined by the external stores and control surface settings. Three

Mach numbers were selected for testing which were nominally identical to the Mach numbers used previously in the flight test program. Other test parameters were the Reynolds number and the sideslip angle. Corresponding to each test condition, various angle-of-attack settings were used up to +16 degrees, and the data were recorded for all α's in 2 to 4 degree increments.

During the wind tunnel tests, pressure, force and dynamic response measurements were recorded on frequency-modulated (FM) tapes for real-time and spectral analyses. The force, static pressure, and rms fluctuating pressure data were reduced to coefficients used for buffet intensity and wing-rock onset studies. Substantial amounts of tests, data processing, evaluation and correlation work were carried out and documented. This report consists of the following key work items.

1. Study of the stationarity of the real-time dynamic pressure data.
2. Study of the effect of Mach number, wing-tip-mounted missiles and tail deflections on buffet intensity.
3. Study of the effect of the flexible support on buffet intensity.
4. Study of the development of flow separation bubble on the scale model wing with sideslip.
5. Comparison of spectral data based on the wind tunnel test and the flight test.
6. Study of the effect of flap settings on buffet intensity.
7. Evaluation of the model response data.
8. Investigation of the wake flow effect and tail surface buffet intensity data.
9. Correlation study of dynamic pressure data under sideslip conditions.
10. Investigation of the Reynolds number effect based on the wind tunnel test data and corresponding flight test data.
11. Presentation of low-frequency-range power spectral density plots of fluctuating pressures and responses when maximum wing-rock motion occurred.

12. Determination of the system aerodynamic damping by applying the Randomdec program corresponding to the model wing-rock.

13. Investigation of the aerodynamic hysteresis effect on F-5A wing-rock behavior based on a limit cycle concept.

14. Nondimensional data presentation and comparison with similar data obtained in other separated flow tests.

15. Analytical formulation of scale model modal data generation and stability prediction allowing for aeroelastic effect.

The program was conducted under the sponsorship of Ames Research Center, National Aeronautics and Space Administration. The NASA program monitor is Mr. Charles F. Coe. Messrs. Donald Buell and Dennis Riddle of Ames Research Center participated and contributed substantially in the conduction of the wind tunnel tests. At Northrop, other than the authors of this report, the key contributors included Dr. Wilford Wong and Mr. Brent Bennett. The flexible support device of the test model was designed by Messrs. Mel C. Sanders and John E. Black.

1.1 Symbols and Units

b,c	Mean aerodynamic chord or wing span, meters
$c/c_{cr} = \zeta = g_R/2$	Damping ratio
$C_{(\ )}$	Nondimensional aerodynamic derivatives
C_p	Static pressure coefficient
$C_{\bar{p}}$	RMS pressure coefficient
f	Frequency, Hz
$F_{(\ )}$	Generalized force matrices, kilonewtons, etc.
h	Flight altitude or wing translatory movement, meters
$k = \omega b/V$	Reduced Frequency
L	Characteristic length
M	Mach number
M_s, M_R, $I_{(\ )}$	Total mass or total mass moment-of-inertia, kilograms, etc.
$n = fL/V$	Non-dimensional frequency
p,P	Fluctuating pressure, kilonewtons/(meter)^2; p also the roll rate, radians/second
$<p>$	RMS value of the fluctuating pressure, kilonewtons/(meter)^2
P_o	Static pressure, kilonewtons/(meter)^2
P_T	Total pressure, kilonewtons/(meter)^2
q,Q	Free stream dynamic pressure, kilonewtons/(meter)^2
r	Yaw rate, radians/second
R_N	Reynolds number, (meter)$^{-1}$ or non-dimensional
S	Wing surface area, (meter)^2
U,V	Freestream speed, meters/second
y	Spanwise distance from the roll axis, meters
α,α_o	Angle-of-attack, degrees
α^*	Critical angle-of-attack, degrees
β	Sideslip angle, degrees

δ_a	Aileron deflection, degrees
δ_f	Trailing edge flap angle, degrees
δ_h	Horizontal tail deflection, degrees
δ_n	Leading edge flap angle, degrees
$\lambda = i\omega(1+i\zeta)$	Eigenvalue
ρ_o	Maximum correlation coefficient
τ'	Time delay, seconds
φ	Roll oscillation angle, degrees
ϕ	Power spectral density of pressure (kilonewtons/meter^2)^2/Hz
ω	Circular frequency, radians/second
$\omega_F, \omega_s, \omega_R$	Natural circular frequencies, radians/second

Matrices

$[A], [A_{(\ )}]$	Generalized AIC matrix, newtons/meter
$[C_{(\ )}]$	Damping coefficient matrices, newton - second/meter
$\{f_{(\ )}\}$	Fourier transforms of force matrices, newtons
$\{F(\ )\}$	Generalized force matrices, newtons
$[g_F]$	Modal damping coefficient matrix
$\{h_{(\ )}\}$	Fourier transforms of deflection matrices, meters
$[K_{(\ )}]$	Structural stiffness matrices, newtons/meter
$[K_F]$	Modal stiffness matrix, newtons/meter
$[K_s]$	Stiffness matrix for the flexible support, newtons/meter, etc.
$[T]$	Rigid body transformation matrix
$\{x\}, [X]$	Modal deflection matrices
$[Z]$	Modal impedance matrix, newtons/meter
$\{\alpha\}$	Modal amplitude matrix, meters

Section 2

WIND TUNNEL TEST PROGRAM

The buffet wind tunnel test program was carried out on a one-seventh scale model of the F-5A airplane at Ames Research Center Eleven-Foot Transonic Wind Tunnel. The objective of the test program is to obtain wind tunnel pressure, force, and dynamic response measurements with which to develop methods for predicting buffet intensity and wing-rock instability at transonic speed. The program was accomplished in two entries. During Phase I, the first entry, a standard sting was used. The second tunnel entry (Phase II) was carried out with a flexible support system that allowed for model oscillations, especially those degrees of freedom corresponding to the Dutch roll motion during wing-rock.

Previous to the model tests, a buffet flight test program was conducted using a fully instrumented F-5A aircraft. The test results of the flight test are described in Reference 1. The scale model tests were conducted using test conditions similar to the flight test conditions so that the dynamic pressure data acquired during the flight test and the scale model tests may be compared and evaluated, taking into consideration the scaling relations.

The F-5A is a single-seat fighter capable of carrying stores at wing and fuselage pylon stations. The flight test was conducted with two wing-tip stores (AIM-9B Missiles) with guide rails; otherwise the wing was clean. The scale model tests were conducted with and without the wing-tip missiles. A combination of deflected leading edge and trailing edge flaps as well as the case of completely retracted flaps were used in the test program. A three-view drawing of the F-5A is shown as Figure 1.

The basic wing airfoil of the F-5A is a NACA 65A004.8 section modified as follows. From the 40% chord to the 66.6% chord, the thickness distribution corresponds to a NACA 004.8-64 airfoil. Aft of the 82% chord, the airfoil is composed of straight lines forming a 7° trailing edge angle. Between the 66.6% chord and the 82% chord, the section has been curve-

Airfoil Section	NACA 65A004.8 (Modified)
Area (Reference)	15.79 m^2 (170.00 ft^2)
Span (clean tips)	7.696 m (25.25 ft)
Aspect Ratio	3.75
Taper Ratio	.20
Sweepback (25% Chord)	24°
Mean Aerodynamic Chord	2.356 m (7.73 ft)
Dihedral Angle	0
Incidence Angle	0

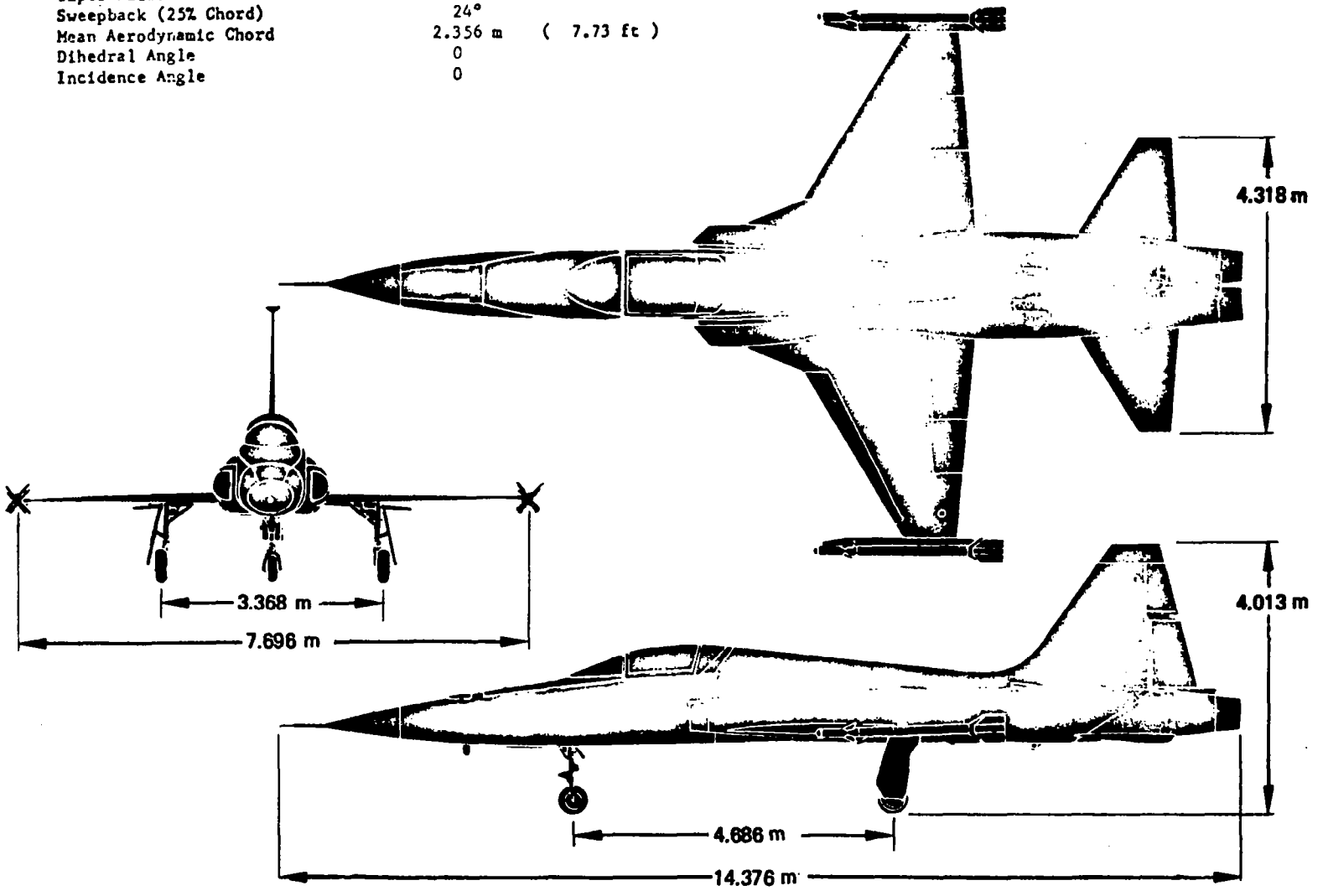

Figure 1. Basic Dimensions of F-5A

fitted so that the ordinates, slopes, and curvature at the end points are continuous. The airfoil is cambered to a NACA (.65) 50 five-digit series mean line. The mean line is rotated so that the straight aft portion lies in the wing chord plane and the camber appears as a 1% leading edge droop. The airfoil is constant over the entire span.

The horizontal tail of the F-5A is all-movable and has an unmodified NACA 65A004 section with the following physical dimensions and configurations:

Area, Total	5.48 m^2	(59 ft^2)
Area, Exposed	3.07 m^2	(33.03 ft^2)
Aspect Ratio, Exposed	2.88	
Sweepback (25% Chord)	25°	
Mean Aerodynamic Chord, Exposed	1.222 m	(3.68 ft)

The vertical tail airfoil is a modified NACA 65A004 section. The airfoil is composed of straight lines aft of the 72% chord. The basic dimensions of the vertical tail are:

Area, Exposed	3.83 m^2	(41.2 ft^2)
Aspect Ratio, Exposed	1.22	
Taper Ratio, Exposed	.25	
Sweepback (25% Chord)	25°	
Mean Aerodynamic Chord, Exposed	1.990 m	(6.53 ft)

2.1 Model Configuration and Instrumentation

The one-seventh scale F-5A model was modified as necessary to correspond to the F-5A airplane on which dynamic pressure measurements have been made in flight. Specifically, removable wing-tip stores were mounted. Since local irregularities are detrimental to pressure measurements, the model surface was smoothed where necessary. Discontinuities greater than 0.02 mm (0.0008 inch) were eliminated, and surface waviness was minimized such that waviness height to waviness length did not exceed 0.002. A typical measurement of the wing top surface profile along Wing Station 8.00 (inches) is shown in Figure 2.

A new leading edge flap at one deflection angle was provided on the right wing with instrumentation. This flap provided a smooth transition

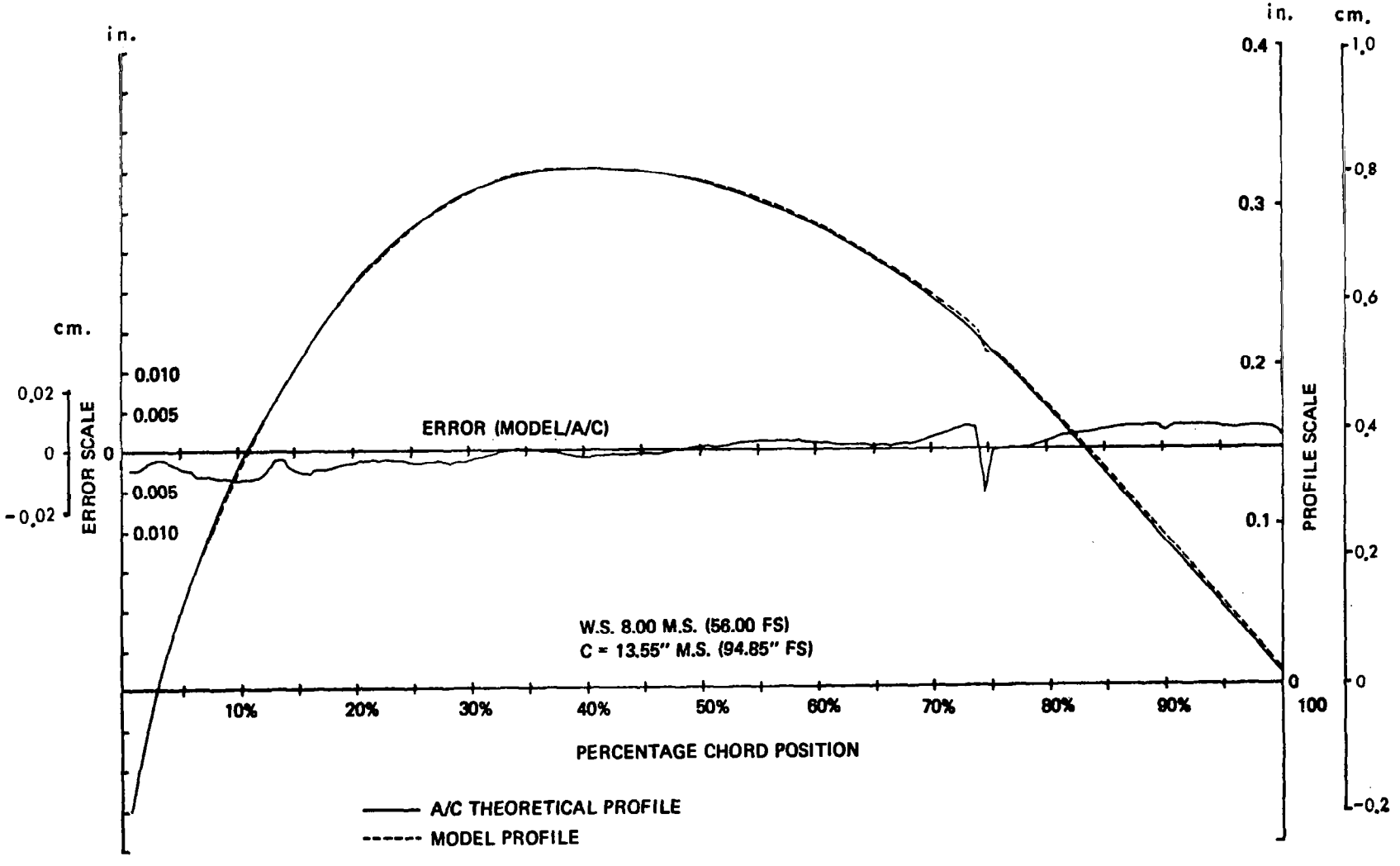

Figure 2. F-5A 1/7-Scale Wing Top Surface Profile Data

into the wing contour and did not simulate the full-scale aircraft in having rearward and forward steps at this transition. (The same leading edge flap deflection was available for the left wing through use of an existing part.) The new leading edge flap (5° deflection at root section) was attached to the wing by means of existing attach areas.

The aileron can be deflected to various angles using existing brackets. The trailing edge flap is capable of being deflected in 5-degree increments down to 40° through use of a serrated disc. The left and right horizontal tails can be deflected from -20° to +10° in 5-degree increments through use of a serrated disc. Typical boundary layer transition strips were installed on the test model during the buffet test program.

The F-5A scale model was equipped with 28 static pressure taps and an equal number of dynamic pressure transducers located closely to each other. Because of certain cutouts on the scale model, some transducers were located in slightly varied chordwise positions as compared to the airplane installations. The static pressure taps consists of 0.76 mm inside diameter tubes terminating flush and square with the surfaces, and were connected to a six module scanivalve located at the front portion of the fuselage internal cavity. The dynamic transducers were Kulite Model LQ2-156W-4 with closed reference chambers. Specifically, 21 pressure taps and Kulite transducers were installed on the right wing, of which 18 taps and dynamic pressure transducers were located on the wing top surface with the remaining three sets located on the bottom surface. Three taps and dynamic transducers were located on the top surface of the left wing. Four taps and dynamic transducers were installed on the right horizontal tail with two sets each on the top and bottom surfaces. The transducers were mounted in such a way as to minimize model strain effects on the dynamic pressure measurements. For this purpose, the cutouts and wiring paths were designed to maintain the structural integrity of the model. Electrical leads from the transducers were connected to shielded-pair wires (with shields insulated from the model) as close to the transducers as practical while retaining good accuracy in the force measurements. The dynamic instrumentation was bonded flush with the wing surface with epoxy. Pressure taps were soft-soldered in the leading edge flap. No pressure taps were installed on the right wing leading edge flap with 0° deflection.

In addition, a pair of semi-conductor type bridge gages (Kulite ULP-120-160) were installed on both wing root sections to measure the bending and torsion moments of the wing under dynamic loads. These were designated as 1b, 1t, for the right wing and 2b, 2t, for the left wing. Three accelerometers (Endevco 2264-150) were installed in the model CG location and both wing-tips inside the sidewinder missiles. The accelerometers were designated as 1a, 2a, 3a, with 1a located at the right wing-tip, 2a at the left wing-tip, and 3a at the CG. Transition strips were installed on the wing and tail surfaces of the scale model at approximately 10% chordwise positions. The detail instrumentation locations on the wing are illustrated in Figure 3. In the figure, a number inside the parentheses indicates that the corresponding transducers are on the lower lifting surface, while a number with no parentheses indicates that the transducers are on the top surface. Table 1 gives the instrumentation information in a tabulated form.

2.2 Model Support Systems Corresponding Vibration Modes

Fixed Support System - Phase I

As described previously, during Test Phase I, a standard sting was used to support the model. A six-component balance was installed inside the model fuselage in front of the sting mounting system. The outputs from the balance were designated as 1n, 2n, for the side forces, r for the roll moment and 0_a for the axial force. After the F-5A scale model was installed in the Eleven-Foot Transonic Tunnel, the model and the support system were subjected to sinusoidal excitations to determine the modal characteristics of the assembly. The modal data obtained during the test were recorded graphically in Figure 4. In addition to the natural modes of Figure 4, a support system bending mode was observed at 6.6 Hz. A support system torsion mode was observed at 105 Hz. In both cases, the model behaved as a rigid inertia mass. A mode corresponding to balance roll was observed at 13.6 Hz.

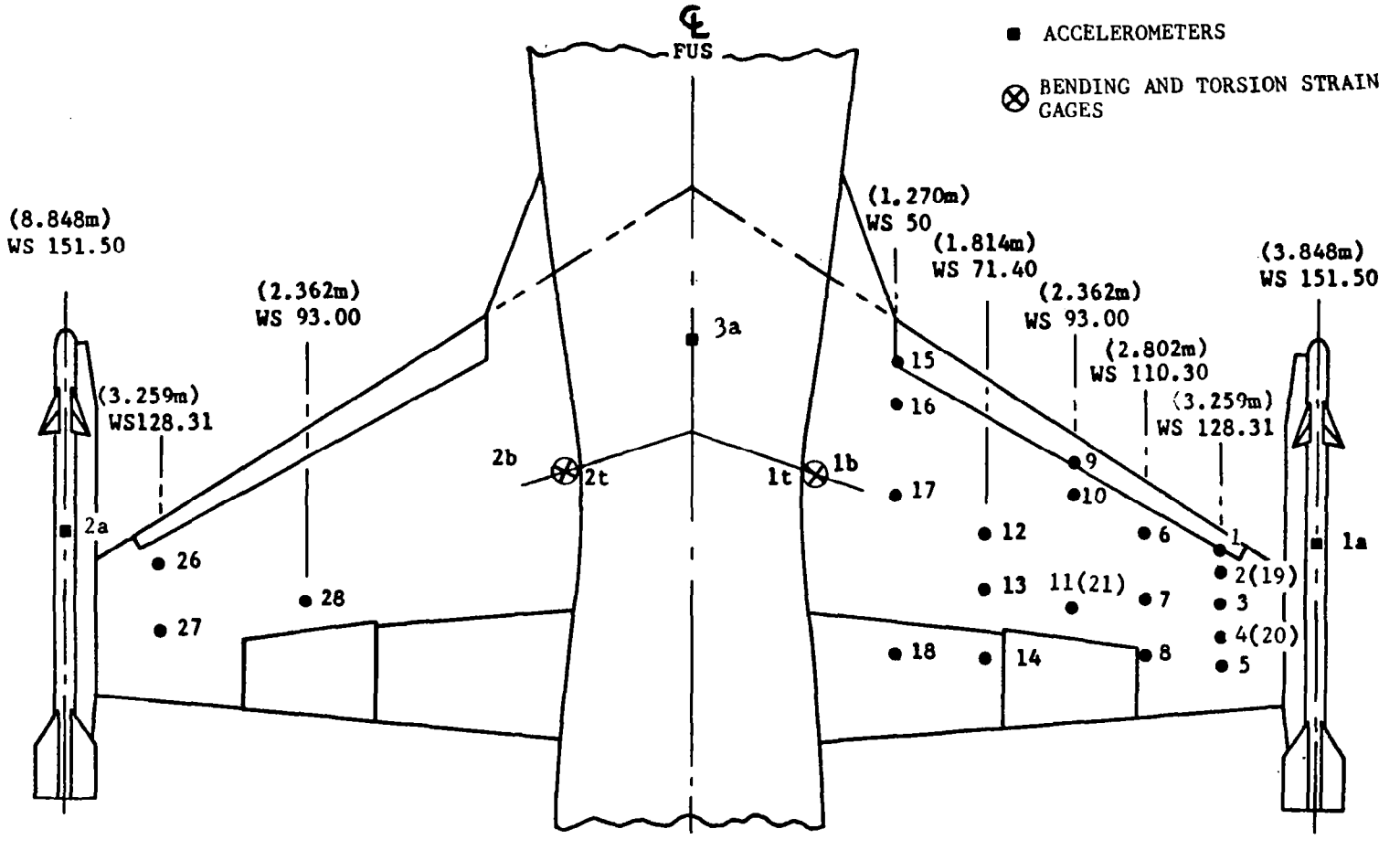

Figure 3. Locations of Dynamic Instrumentation on F-5A Scale Model

TABLE 1 F-5A SCALE MODEL INSTRUMENTATION

RH WING INSTRUMENTATION

SYMBOL		$WS^{\dagger}$		$Y^{\dagger}$		%
STATIC PRESS. TAP	PRESS. TRANSDUCER			DIST. FROM LE		CHORD
1S	1	3.259	(128.31)	.1102	(4.34)	10
2S	2	"	"	.2646	(10.416)	24
3S	3	"	"	.4413	(17.374)	40
4S	4	"	"	.6618	(26.054)	60
5S	5	"	"	.8273	(32.571)	75
6S	6	2.802	(110.30)	.3142	(12.369)	22
7S	7	"	"	.7140	(28.112)	50
8S	8	"	"	1.071	(42.168)	75
9S	9	2.362	(93.00)	.1741	(6.853)	10
10S	10	"	"	.3656	(14.392)	21
11S	11	"	"	1.044	(41.111)	60
12S	12	1.814	(71.40)	.9375	(36.911)	44
13S	13	"	"	1.278	(50.323)	60
14S	14	"	"	1.704	(67.102)	80
15S	15	1.270	(50.00)	.2518	(9.912)	10
16S	16	"	"	.5035	(19.824)	20
17S	17	"	"	1.057	(41.622)	42
18S	18	"	"	2.014	(79.289)	82
(19S) *	(19) *	3.259	(128.31)	.2646	(10.416)	24
(20S) *	(20) *	"	"	.6618	(26.054)	60
(21S) *	(21) *	2.362	(93.00)	1.044	(41.111)	60
BENDING STRAIN GAGE	TORSION STRAIN GAGE					
1b	1t	0.773	(30.45)	1.234	(48.59)	43
ACCELEROMETER						
1a		3.848	(151.50)	-.2934	(-11.55)	--

TABLE 1 F-5A SCALE MODEL INSTRUMENTATION (CONTINUED)

LH WING INSTRUMENTATION

SYMBOL		WS†	Y†	%
STATIC PRESS. TAP	PRESS. TRANSDUCER		DIST. FROM LE	CHORD
26S	26	3.259 (128.31)	.2646 (10.416)	24
27S	27	" "	.6618 (26.054)	60
28S	28	2.362 (93.00)	1.044 (41.111)	60
BENDING STRAIN GAGE	TORSION STRAIN GAGE			
2b	2t	0.773 (30.45)	1.234 (48.59)	43
ACCELEROMETER				
2a		3.848 (151.50)	-.2934(-11.55)	--

RH HORIZONTAL TAIL INSTRUMENTATION

SYMBOL		WS†	Y†	%
STATIC PRESS. TAP	PRESS. TRANSDUCER		DIST. FROM LE	CHORD
22S	22	1.814 (71.40)	.2757 (10.85)	40
23S	23	1.270 (50.00)	.4368 (17.20)	40
(24S) *	(24) *	1.814 (71.40)	.2757 (10.85)	40
(25S) *	(25) *	1.270 (50.00)	.4368 (17.20)	40

* () Indicates the transducer mounted on the lower surface.

† All dimensions are meters for the full scale aircraft.
The corresponding values in the parentheses are inches.

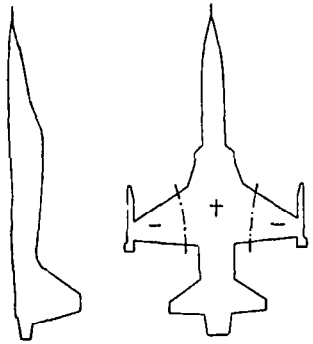

First Wing Bending
53.5 Hz

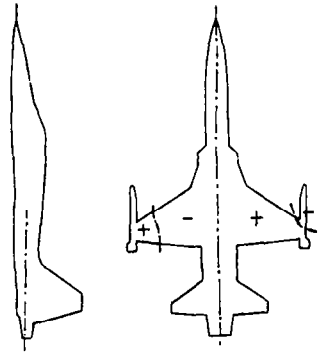

Rigid Body Roll and Wing
Antisymmetrical Bending
71.0 Hz

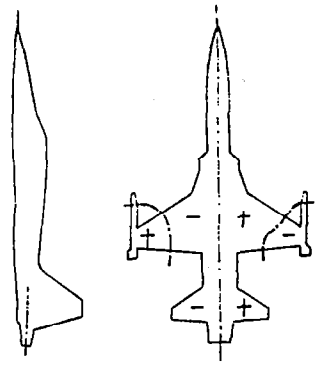

Wing Antisymmetrical
Bending, 82.7 Hz

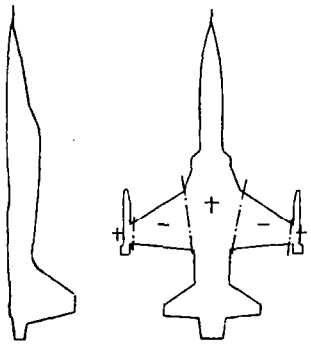

Wing Second Symmetrical
Bending, 171.0 Hz

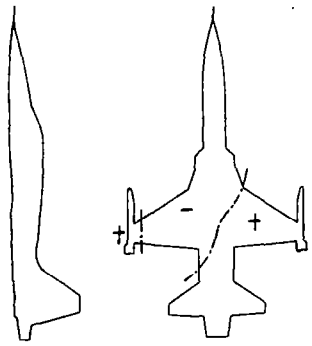

Fuselage and Wing
Asymmetrical Bending
172.5 Hz

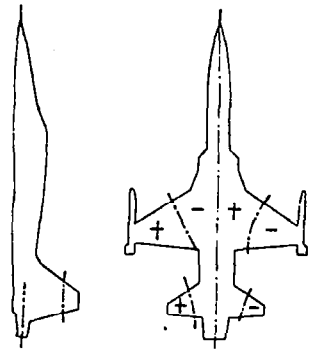

Wing and Tail
Antisymmetrical Bending,
210 Hz

Figure 4. Vibration Modes of F-5A Scale Model Mounted on a Sting in Ames Eleven-Foot Transonic Wind Tunnel – Test Phase I

Flexible Support System - Phase II

The full-scale F-5A displays a wing-rock natural frequency of about 0.5 to 1.0 Hz. This corresponds to a model frequency of 3.5 to 7.0 Hz. Since it is infeasible to allow the model to rotate freely about the roll axis in a wind tunnel test, a support system with a flexible roll constraint was designed for Phase II of the test program. This roll constraint was designed to have a natural frequency approximately equal to the natural wing-rock frequency so that impedance to the desired roll mode is minimized. The system allowed the model to oscillate $\pm 30°$ in roll. An adjustable damping device and a roll angle measuring potentiometer also formed part of the assembly. Except for the elimination of the balance unit, the pressure and response data instrumentations of the model remained unchanged from the first test phase. Dynamic data such as the roll angle, the model pitch and yaw oscillation angles, and the damping coefficient of the damper were recorded.

The flexible support unit (Figure 5) was assembled with a specially designed hollow sting whose external dimensions were comparable to the standard sting used in the Eleven-Foot Transonic Tunnel. The overall length of the sting was 2.553 m (100.5 in.). At approximately one-third the length of the sting measured from the front end, a steel insert was fitted inside the sting which was used to anchor the rear end of a torsion bar. The torsion bar, designed to oscillate with the scale model along the roll axis with natural frequency of 3.5 Hz, had splines cut at both ends. With the rear end anchored to the sting insert as described above, the front end of the torsion bar extended approximately 0.1842m (7.25 in.) from the front end of the hollow sting.

The front portion (0.324 m or 12.75 in.) of the sting was machined to accept two needle bearings and two lightweight thrust bearings which were fit into the inside of a sleeve shaped spacer. After the bearings were assembled, the spacer was fixed to the model fuselage body through a 1.27 cm (0.5 in.) pin.

Beyond the bearing subassembly, the front tip of the sting was fitted with internal splines. The splines were used to accept the rear end of the damper subassembly shaft. The damper subassembly, measured approximately 0.1651 m (6.5 in.), consisted essentially of the internal shaft, and the external housing and their attachments. The internal shaft was tied through the external splines to the sting front end. It was thus stationary along the roll axis. The external housing was fixed to the scale model through locating pins. The damper shaft was assembled with a 240° partial cylinder to form a 120° fan shaped cavity on top of the shaft. Correspondingly, the damper housing was attached with a fan shaped piston which covered an arc of 60°. When properly assembled with a number of seals and spacers, etc., and hydraulic liquid added to the cavity, the damper housing may rotate $\pm 30°$ about the shaft subassembly, while the hydraulic liquid was forced to move from one side of the piston to the other through three metering holes cut in the piston. The sizes of the metering holes which allowed the liquid to move were controlled by a spool shaft. By adjusting the lengthwise position of the spool shaft, the size of the metering holes were varied and thus the amount of damping supplied by the damper unit could be controlled. The damper unit was locked out and the model prevented from roll oscillation when the metering holes were completely blocked by the spool shaft. The linear movement of the spool shaft was controlled by a Globe motor through a screw jack device. The fast acting lock-out mechanism of the spool shaft was activated by two solenoids through a rocker arm.

In front of the damper unit, and behind the two solenoids assembled inside the model fuselage, an angular potentiometer was used to measure the roll angle of the scale model relative to the sting.

In addition to the angle-of-attack measuring device at the base of the sting, a danglometer was installed on top of the sting at a lengthwise location about one-third from the front end of the sting. Strain gages were installed on the sting which were calibrated to determine the sting deflections in both the pitch and yaw planes.

The calibration curves of the hydraulic damper with the scale model installed on the sting assembly obtained before and during the tests are shown in Figure 6. The modal data of the assembly (the model and the support) during the test were recorded graphically in Figure 7. In addition, the first sting bending mode was observed at 6.7 Hz and the nominal natural frequency of roll oscillation was 3.5 Hz.

2.3 Test Points

This program included the major test conditions conducted in the flight test program. These flight test conditions were M = 0.75, 0.85, and 0.925 for the wing leading and trailing edge flaps at 0° each and at 4° and 12°, respectively. The wind tunnel program substituted a wing leading edge flap deflection of 5° for the deflection of 4° flight tested. The wind tunnel model did not provide a 4° leading edge flap deflection. It was expected that the difference of 1° in the deflection angle will not affect the test data significantly.

The wind tunnel program also included a buildup of flap deflections. This was conducted to investigate the individual effects of each control surface and to provide the basis to measure the interaction effect between the two control surfaces. For Phase I testing, 52 test runs altogether (i.e., test points) were performed encompassing 11 model configurations defined by the control surface deflections, etc. (leading edge flap δ_n, trailing edge flap δ_f, aileron δ_a, horizontal tail surface δ_h, wing-tip missiles on or off, wing transition strips on or off). Three Mach numbers were selected for testing (0.75, 0.85, 0.925) which were nominally identical to the numbers used previously in a flight test program. The nominal Reynolds numbers used in the first phase were 13.94×10^6, 12.30×10^6, 11.48×10^6 and 7.38×10^6 per m. Based on the model mean aerodynamic chord of 0.3366 m, the corresponding Reynolds numbers were 4.68×10^6, 4.14×10^6, 3.86×10^6, and 2.48×10^6. Another test run parameter was the sideslip angle, which was set to either

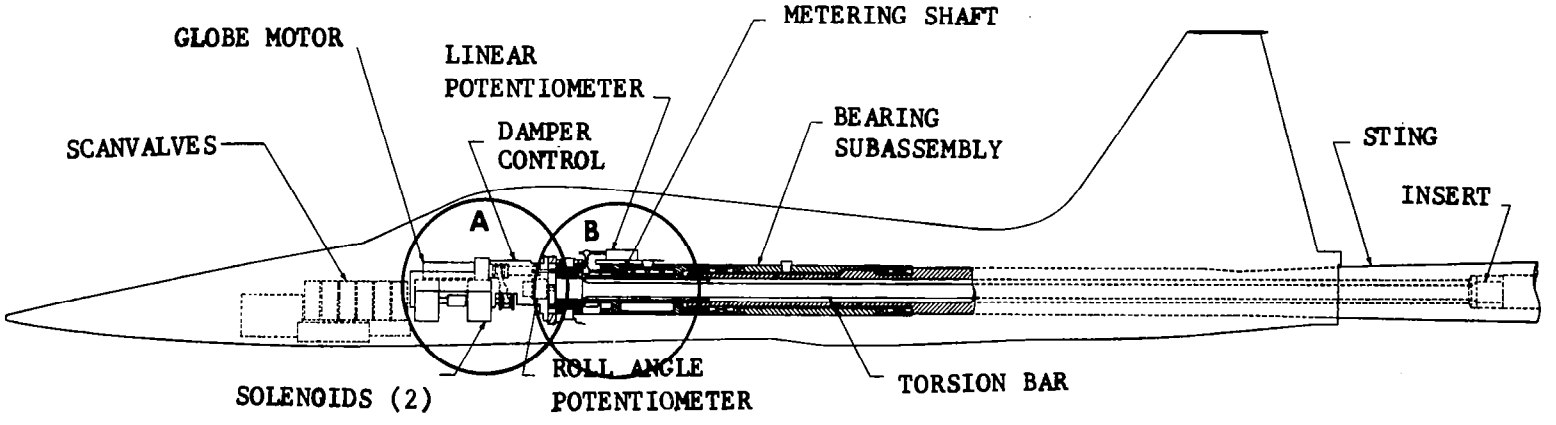

Figure 5. Section View of the F-5A
Scale Model and the Flexible Roll Device Mounted on the Sting (Continued)

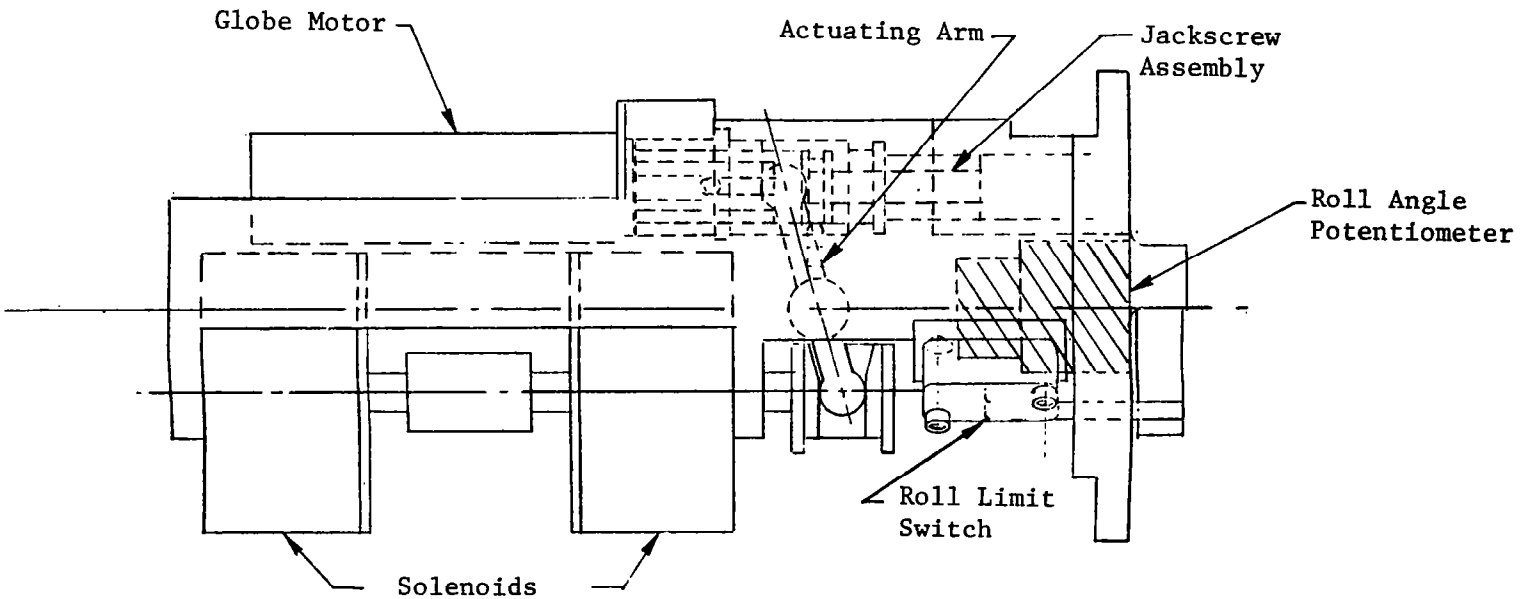

View A - Damper Actuator Assembly

Figure 5. Section View of the F-5A Scale Model and the Flexible Roll Device Mounted on the Sting (Continued)

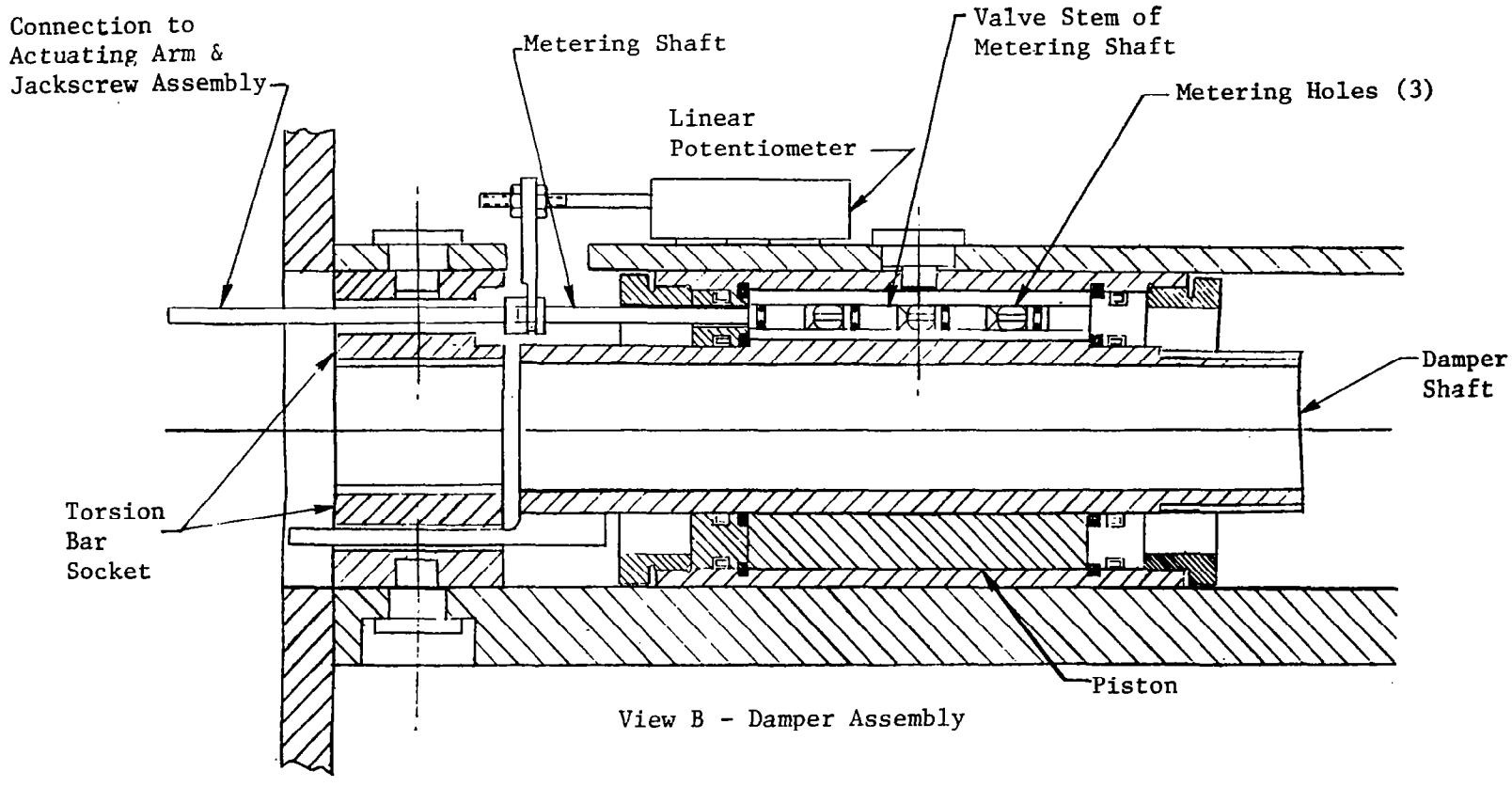

Figure 5. Section View of the F-5A Scale Model and the Flexible Roll Device Mounted on the Sting (Concluded)

CURVE I RUNS 1-16
CURVE II RUNS 17,18
CURVE III RUNS 19,20
CURVE IV RUNS 21-29 (RUN 24 CALIBRATION DATA UNCERTAIN)

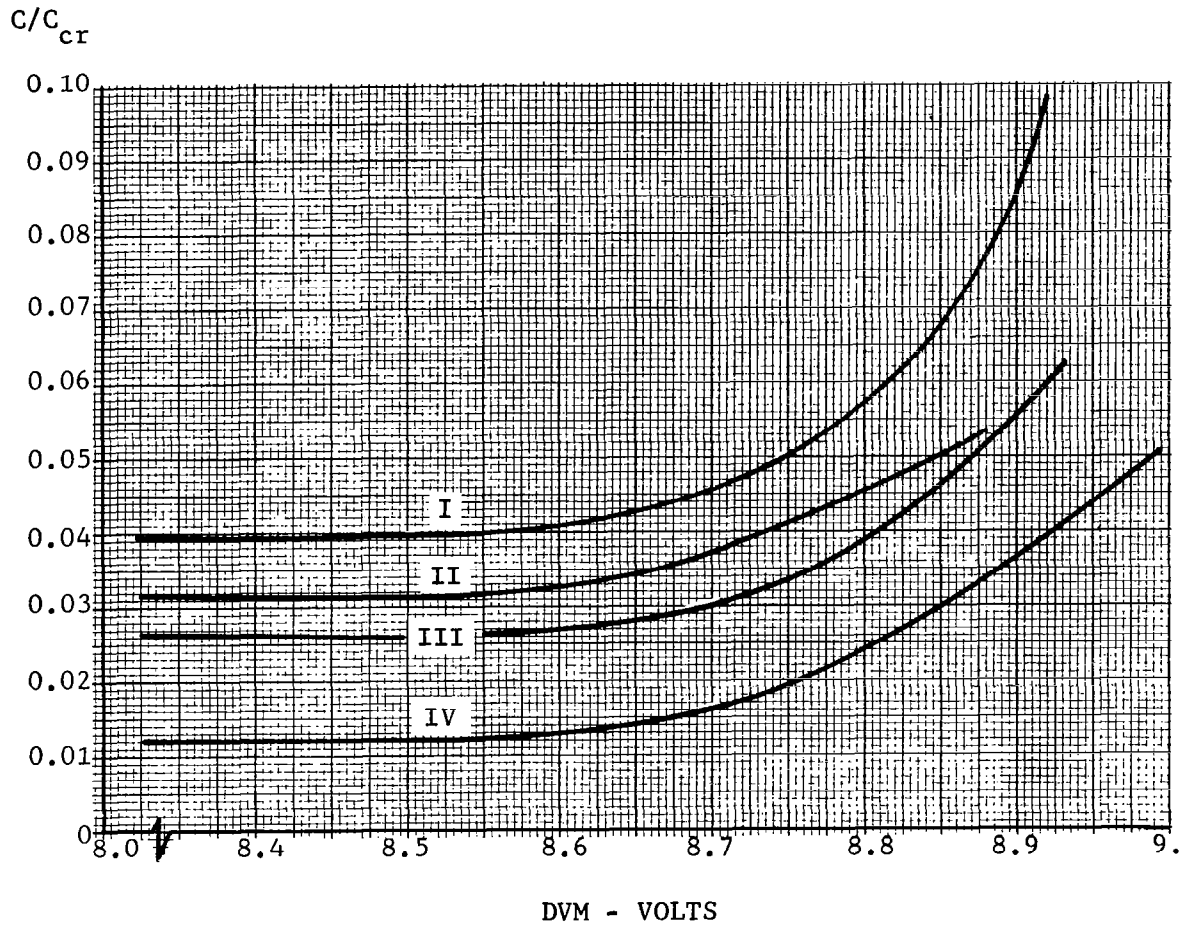

Figure 6. Calibration curves of the Hydraulic Damper with the F-5A Scale Model Installed

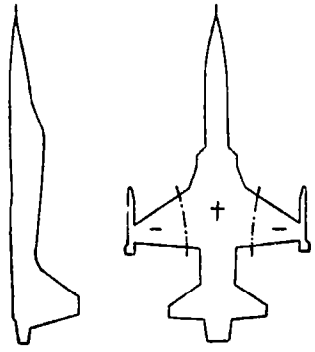

First Wing Bending
51.6 Hz

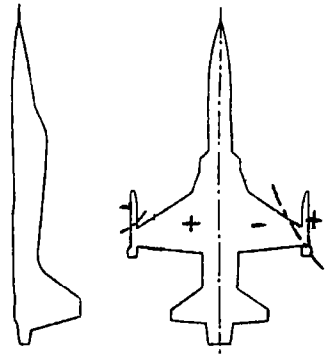

Rigid Body Roll and Wing
Antisymmetrical Bending
66.3 Hz

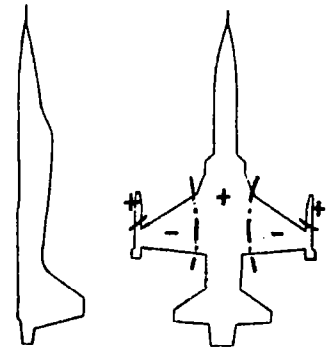

Missile and Wing
Symmetrical Bending
72.4 Hz

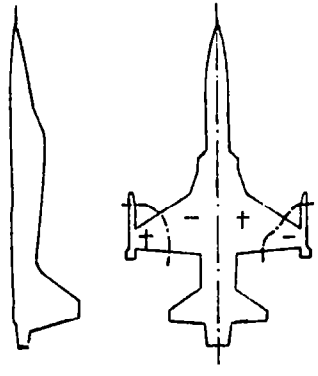

Wing Antisymmetrical
Bending, 81.8 Hz

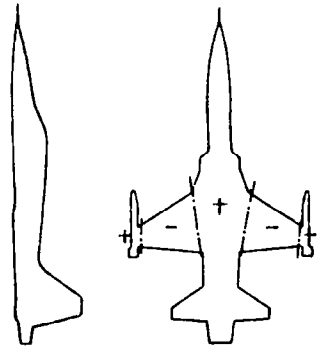

Wing Second Symmetrical
Bending, 170.2 Hz

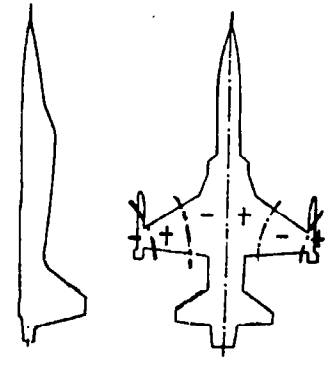

Wing
Antisymmetrical Bending,
206 Hz

Figure 7. Vibration Modes of F-5A Scale Model Mounted on a Flexible Support in Ames Eleven-Foot Transonic Wind Tunnel - Test Phase II

0° or ±8° for each individual run. All tests were conducted as pitch polars, i.e., the angle-of-attack was varied while the sideslip is held constant. Corresponding to each test point, the angle-of-attack was stepped up from 0° through 4°, 6°, 8°, 10°, 12°, 14°, 16°, and the data were recorded for all α's. A description of the Phase I test points is given in Figure 8.

As described previously, the second tunnel entry (Phase II) was carried out with a flexible support system that allowed for model oscillations, especially those degrees of freedom corresponding to the Dutch roll motion. A total of 29 runs were made, identified as test points 1-29. Except for the support flexibility, the Phase II run conditions were essentially duplicates of those of Phase I. A constant Reynolds number of 7.38×10^6/m was used throughout Phase II. The Phase II test points and their corresponding test point numbers of Phase I are given in Figure 9. Furthermore, Table 2 describes the test points or pairs of test points used to investigate certain effects during parametric studies along with the corresponding subsection numbers as they appeared in this report.

CONFIGURATION	β	δ_n/δ_f	δ_h	δ_a	M = 0.75	M = 0.85	M = 0.925	R_N (/M) AND OTHER REMARKS
LE FLAP = 5 – MISSILES ON – δ_h = 0								
$x_1 n_4 w_{10}$ (1)	-8 0 8 0	5/0 ↓	0 ↓	0/0 ↓			5 3 6 7	$R_N = 11.48 \times 10^6$ ↓ $R_N = 7.38 \times 10^6$
BASIC CONFIGURATION – δ_n/δ_f = 5/12 – MISSILES ON – δ_h = 0								
$x_1 n_4 f_2 w_{10}$ (2)	-8 0/VAR 8	5/12 ↓	0 ↓	0/0 ↓	13/18 17	12/16 15	9 8/11 10/14	$R_N = 7.38 \times 10^6$ ↓ PRES SUM AMP
δ_n/δ_f = 5/12 – MISSILES ON – δ_h = -10								
$x_1 n_4 f_2 w_{10}$ (3)	-8 0 8	5/12 ↓	-10 ↓	0/0 ↓	22		20 19 21	$R_N = 7.38 \times 10^6$ ↓
δ_n/δ_f = 5/0 – MISSILES ON – h = 0 – δ_a = 15/-20 OR -20/15								
$x_1 n_4 w_{10} a_1$ (4) (5)	0 0	5/0 5/0	0 ↓	15/-20 -20/15	24 26		23 25	$R_N = 7.38 \times 10^6$ ↓
δ_n/δ_f = 5/12 – MISSILES OFF – δ_h = 0								
$x_1 n_4 f_2$ (6) (7)	-8 0 8 0	5/12 ↓	0 ↓	0/0 ↓	32 33 35	30 31	29 27 28 34	$R_N = 7.38 \times 10^6$ ↓ ALL WING TRANSITION STRIPS OFF IN CONFIGURATION (7)
δ_n/δ_f = 0/0 – MISSILES OFF – δ_h = 0								
x_1 (8)	-8 0 8	0/0 ↓	0 ↓	0/0 ↓			37 36 38	$R_N = 11.48 \times 10^6$ ↓
δ_n/δ_f = 0/0 – MISSILES ON – δ_h = 0								
$x_1 w_{10}$ (9)	-8 0 8 0	0/0 ↓	0 ↓	0/0 ↓	43 44	42	40 39 41 45	$R_N = 11.48 \times 10^6$ R_N = 13.94, 12.30, & 11.48×10^6 $R_N = 11.48 \times 10^6$ $R_N = 7.38 \times 10^6$
δ_n/δ_f = 0/12 – MISSILES ON – δ_h = 0								
$x_1 f_2 w_{10}$ (10)	-8 0 8	0/12 ↓	0 ↓	0/0 ↓			47 46 48	$R_N = 11.48 \times 10^6$ ↓
δ_n/δ_f = 0/0 – MISSILES ON – δ_h = -10								
$x_1 w_{10}$ (11)	-8 0 8	0/0 ↓	-10 ↓	0/0 ↓	52		50 49 51	$R_N = 7.38 \times 10^6$ ↓

*TEST POINTS ARE IDENTIFIED BY NUMBERS 1-52 WITH THE EXCEPTIONS OF NUMBERS 1, 2, 4 WHICH WERE UNRECORDED. BLANK SPACE INDICATES POINT NOT TESTED. A SPACE DIVIDED BY A SLASH LINE INDICATES THAT AN ADDITIONAL TEST POINT WAS RUN WITH EITHER VARIABLE β'S OR PRESSURE SUM AMPLIFIERS.

*β, δ_n, δ_f, δ_h, δ_a, ARE IN DEGREES WHICH ARE NOT SHOWN IN THE TABLE

Figure 8. Table of Phase I Test Points

CONFIG	TORQUE TUBE Hz	DAMPING	α	β	MODEL δ_n/δ_f	MODEL δ_h	MODEL δ_a	MACH NUMBER .75	MACH NUMBER .85	MACH NUMBER .925	ReN 10^6/M	PHASE I RUN NOS.	REMARKS
$x_1n_4f_2w_{10}$ (2)	3.5	+	A	0	5/12	0	0/0	(2)	(9)	3 (5)	7.38	13 12 8	BASIC FLIGHT TEST CONDITIONS
				8	5/12	0	0/0			4 (6) (7)		10	
				-8	5/12	0	0/0			(8)		9	
$x_1n_4f_2w_{10}$ (3)				0	5/12	-10	0/0	(13)		(10) (14)		22 19	DEFLECTED HORIZONTAL TAIL
				8	5/12	-10	0/0			(11)		21	
				-8	5/12	-10	0/0			(12)		20	
$x_1n_4w_{10}$ (1)				0	5/0	0	0/0			(15) (16)		7	
$x_1n_4w_{10}a_1$ (4)				0	5/0	0	15/-20	(18)		(17)		24 23	AILERON EFFECTS
$x_1n_4w_{10}a_1$ (5)				0	5/0	0	-20/15			(19)		25	
$x_1n_4f_2w_{10}$ (2)				8	5/12	0	0/0	(20)				17	
x_1w_{10} (9)				0	0/0	0	0/0	(24)		(21)		44 39	
				8	0/0	0	0/0			(22)		41*	
				-8	0/0	0	0/0			(23)		40*	
x_1w_{10} (11)				0	0/0	-10	0/0			(25)		49	
				8	0/0	-10	0/0			(26)		51	
				-8	0/0	-10	0/0			(27)		50	
$x_1f_2w_{10}$ (10)				0	0/12	0	0/0			(28)		46*	
x_1 (8)	3.5	+	A	0	0/0	0	0/0			(29)	7.38	36*	MISSILES OFF

† VARIABLE

A: α = 0, 4, 6, 8, 10, 12, 14, 16 (NUMBER OF POINTS CAN BE REDUCED BASED ON SURVEY AT EACH CONDITION)

* PHASE I DATA COUNTERPART AT $R_N = 11.48 \times 10^6$/M

Figure 9. Table of Phase II Test Points

TABLE 2 DESCRIPTION OF TEST POINTS USED TO INVESTIGATE CERTAIN EFFECTS DURING PARAMETRIC STUDIES

TYPE OF EFFECT	PHASE NO.-RUN NO.	SUBSECTION NO.
Mach Number	I-19 vs I-22	3.3
Tip-Mounted Missiles	I-8 vs I-27	3.3
Flap Settings	I-8 vs I-39	4.2
Reynolds Number	I-39 vs Flight Test 825 Run 5	4.4
	I-43 vs Flight Test 825 Run 7	4.4
Tail Deflection & Wake Flow	I-39 vs I-49	3.3, 4.7
	I-19, I-8 vs I-19, I-13 vs I-22, I-43 vs I-52	4.7
Sideslip	I-8 vs I-10, I-8 vs I-9	3.3
	I-10, I-28, I-38, II-6	3.5
	II-11 vs II-12	4.8
Flexible Support System (Phase I vs Phase II)	I-8 vs II-5	3.4, 4.3, 4.6
	I-9 vs II-8, I-10 vs II-6, I-17 vs II-20	3.4
	I-19 vs II-14, I-36 vs II-29, I-39 vs II-21	3.4
	I-40 vs II-23, I-41 vs II-22	3.4
	I-51 vs II-26	4.6

Section 3

PRESENTATION OF TEST DATA

All the testing specified in Figures 8, 9, were performed at Ames Research Center Eleven-Foot Transonic Wind Tunnel. After a scan of test results, the recorded force and static pressure data were reduced to coefficients and the dynamic pressure and response data were stored on the frequency-modulated magnetic tapes for subsequent real-time and spectral processing. In this section, the processing and evaluation of the real-time test data as well as the static and dynamic pressure distributions are presented, followed in a subsequent section by the spectral analysis of the test data.

3.1 Static Pressure and Dynamic Pressure Distributions

The static pressure and dynamic pressure data were examined first for correlation with buffet intensity and with onset of wing-rock. The tunnel data acquired during Run 8, Phase I, are presented below. Run 8 data will be used as the base line data to evaluate the various effects to transonic buffet due to configuration and flight condition changes.

Run 8 of Phase I test was conducted in test model configuration 2 (Figure 8). This configuration included the tip-mounted Sidewinder missiles. The leading edge and trailing edge flap angles were 5°/12°. The horizontal tail surface and aileron settings were 0°. The nominal sideslip angle was 0°. The run was conducted at M = .926 with a Reynolds number of 7.402×10^6/m (2.256×10^6/ft). The dynamic pressure was 18.232 KN/m^2 (380.8 psf). The Reynolds number of the model, based on the mean aerodynamic chord, was 2.49×10^6.

Run 8 covered the angle-of-attack settings from 0° to 16° in seven steps. Typical static and rms dynamic pressure coefficient distributions

on the right wing upper surface acquired during the run are presented in Figure 10 --- in this figure, the termination points C_p and $C_{\bar{p}}$ at L.E. and T.E. were arbitrary and should not be taken literally. Referring to Figure 10, the development of the supersonic flow and the accompanying shock-induced separation can be seen in the variation of static pressure coefficient C_p along the chordwise direction with increasing angle-of-attack. The two conditions (supersonic flow and shock-induced separation) corresponded to the high negative C_p levels and subsequent flow recompression. The shock-induced separation moved upstream with increasing angle-of-attack. The increase in rms pressure coefficient $C_{\bar{p}}$ in the shock/boundary layer interaction and downstream separated region can be clearly seen.

It was noted that as the separation region developed over the upper wing surface with increasing angle-of-attack, the condition which corresponded to the separated flow developing over a "substantial" part of the outer wing occurred over a relatively narrow angle-of-attack range ($\Delta\alpha \sim 2°$). For tests conducted at a fixed angle-of-attack within this range, the dynamic pressures were found to be highly non-stationary, particularly, in the shock boundary layer interaction region. This behavior may be observed in the real time dynamic pressure traces as illustrated in the next subsection.

3.2 Real Time Data for Dynamic Pressures and Model Responses

The real time dynamic pressure traces of Run 8, Phase I, are presented in Figures (11-13) for transducers 2, 3, and 4 which are located at W.S. 128.31 corresponding to the 24, 40, and 60% chordwise stations, respectively. Figure 11 is for $\alpha = 8°$ in which the shock interaction and the separated flow condition occurred in the wing trailing edge region as described previously (compare with Figure 10). The incipient shock interaction point was very close to transducer No. 4 as indicated by the random positive peaks in Figure 11. It was clear that this condition, a degree of non-stationarity existed in the location of the shock interaction region.

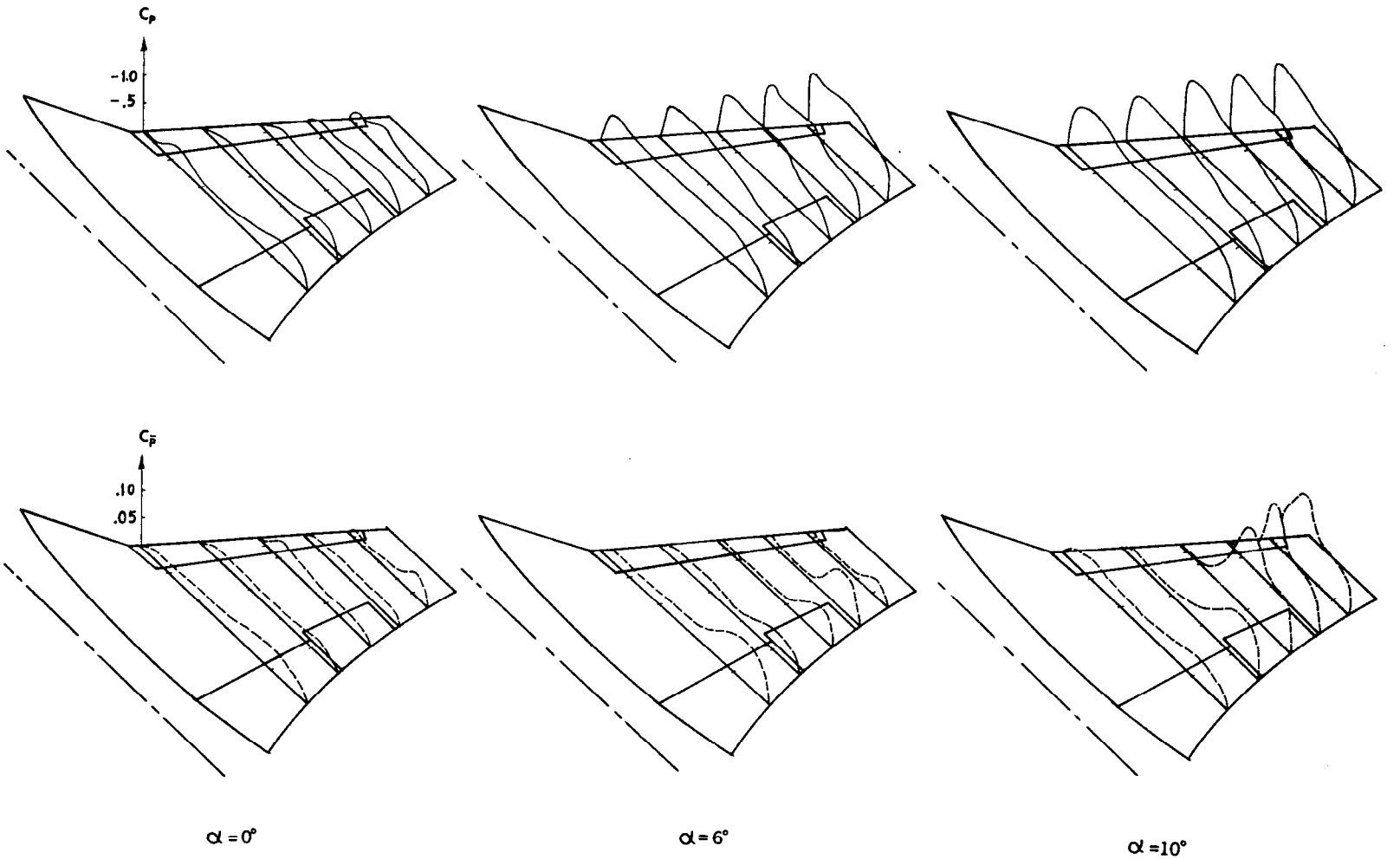

Figure 10. Static Pressure (C_p) and RMS Pressure ($C_{\bar{p}}$) Coefficient Distributions on the Right Wing Upper Surface, Run 8, Phase I - Configuration 2, $\beta = 0°$, $M \doteq .926$, $\delta_n/\delta_f = 5°/12°$, $\delta_h = 0°$ (Continued)

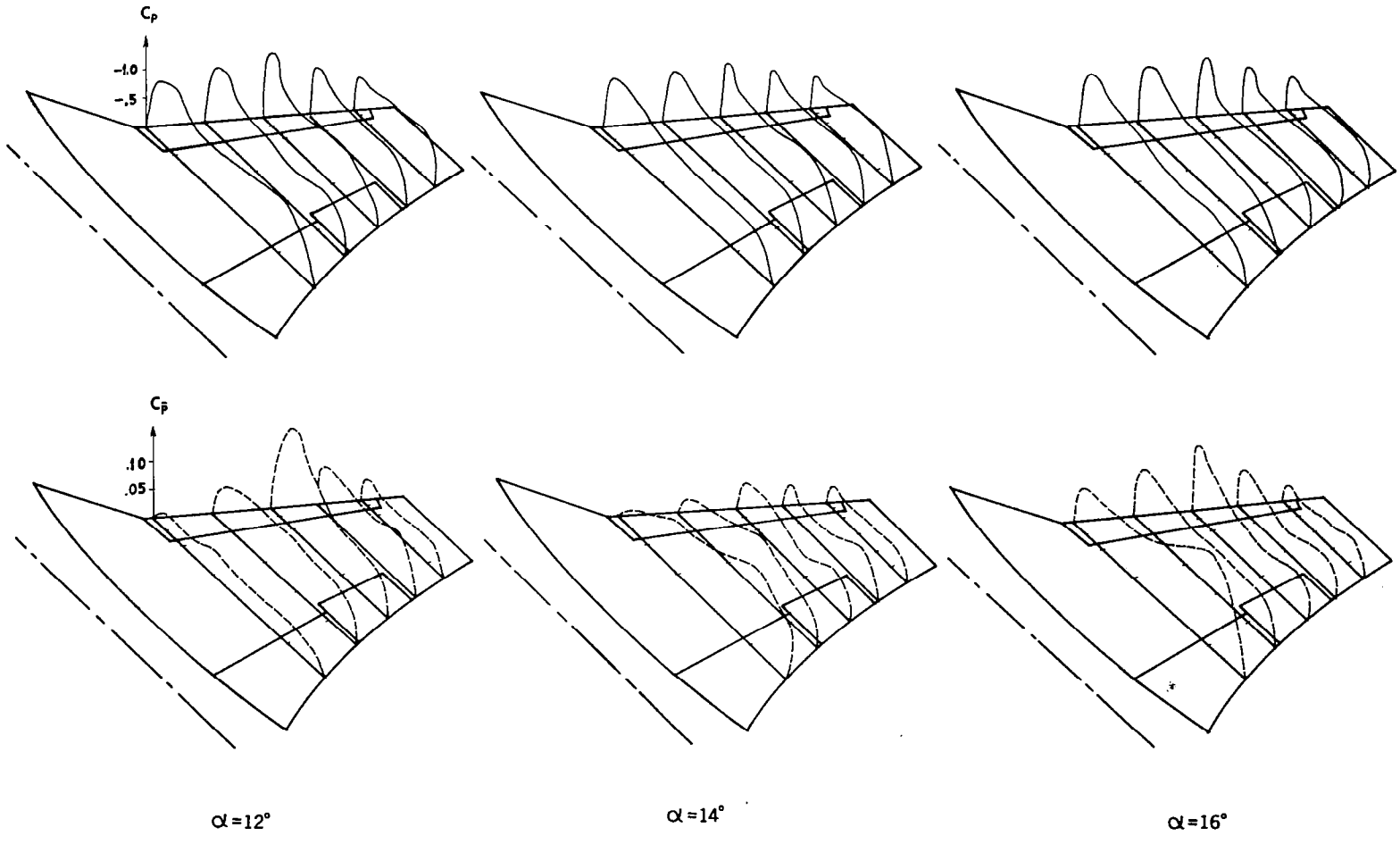

Figure 10. Static Pressure (C_p) and RMS Pressure ($C_{\bar{p}}$) Coefficient Distributions on the Right Wing Upper Surface, Run 8, Phase I - Configuration 2, $\beta = 0°$, M = .926, $\delta_n/\delta_f = 5°/12°$, $\delta_h = 0°$ (Concluded)

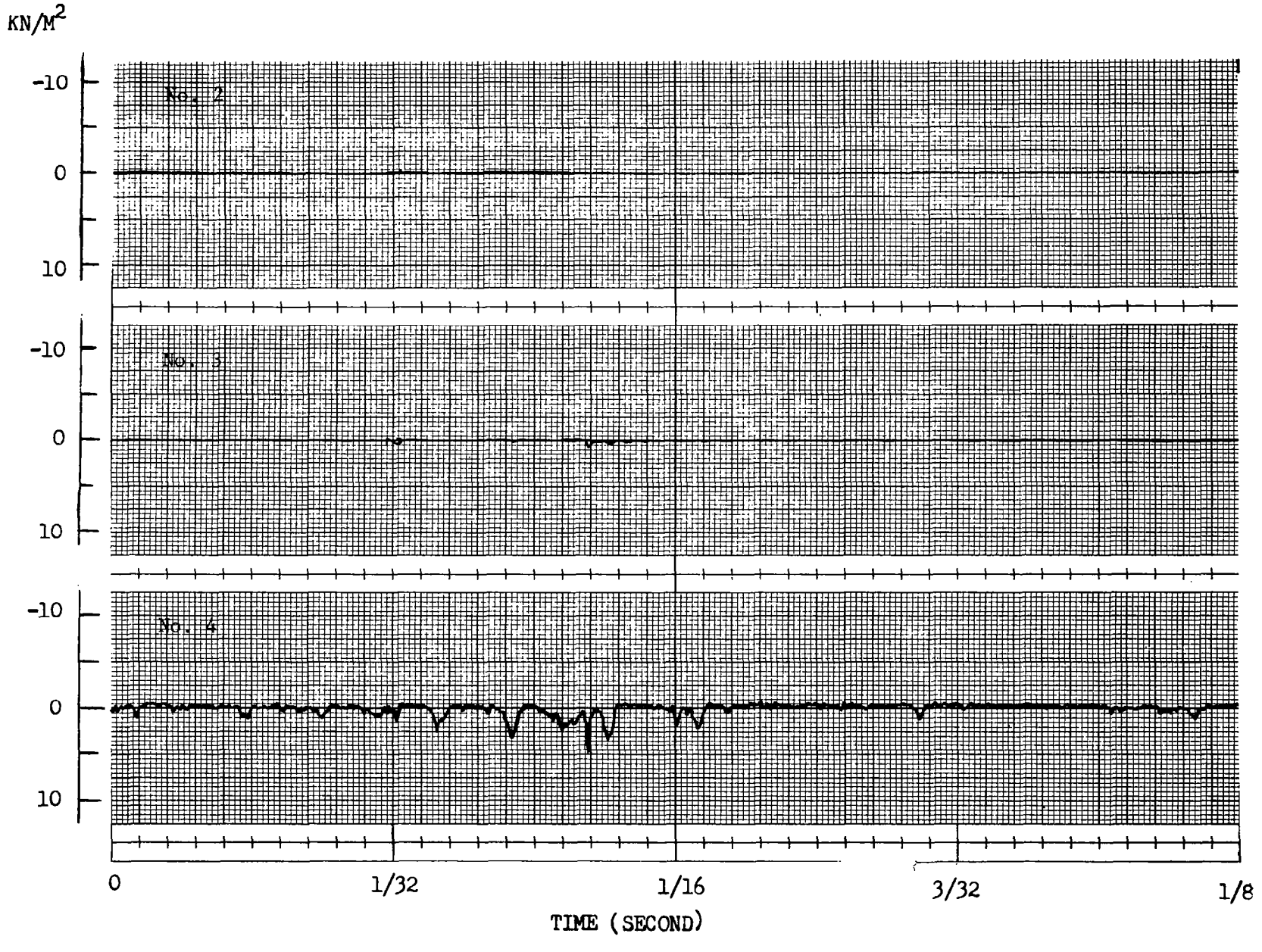

Figure 11. Dynamic Pressures of Transducer Nos. 2, 3, 4 of the F5-A Model, Run 8, Phase I - Configuration 2, $\alpha = 8°$, $\beta = 0°$, M = .926, $\delta_n/\delta_f = 5°/12°$, $\delta_h = 0°$

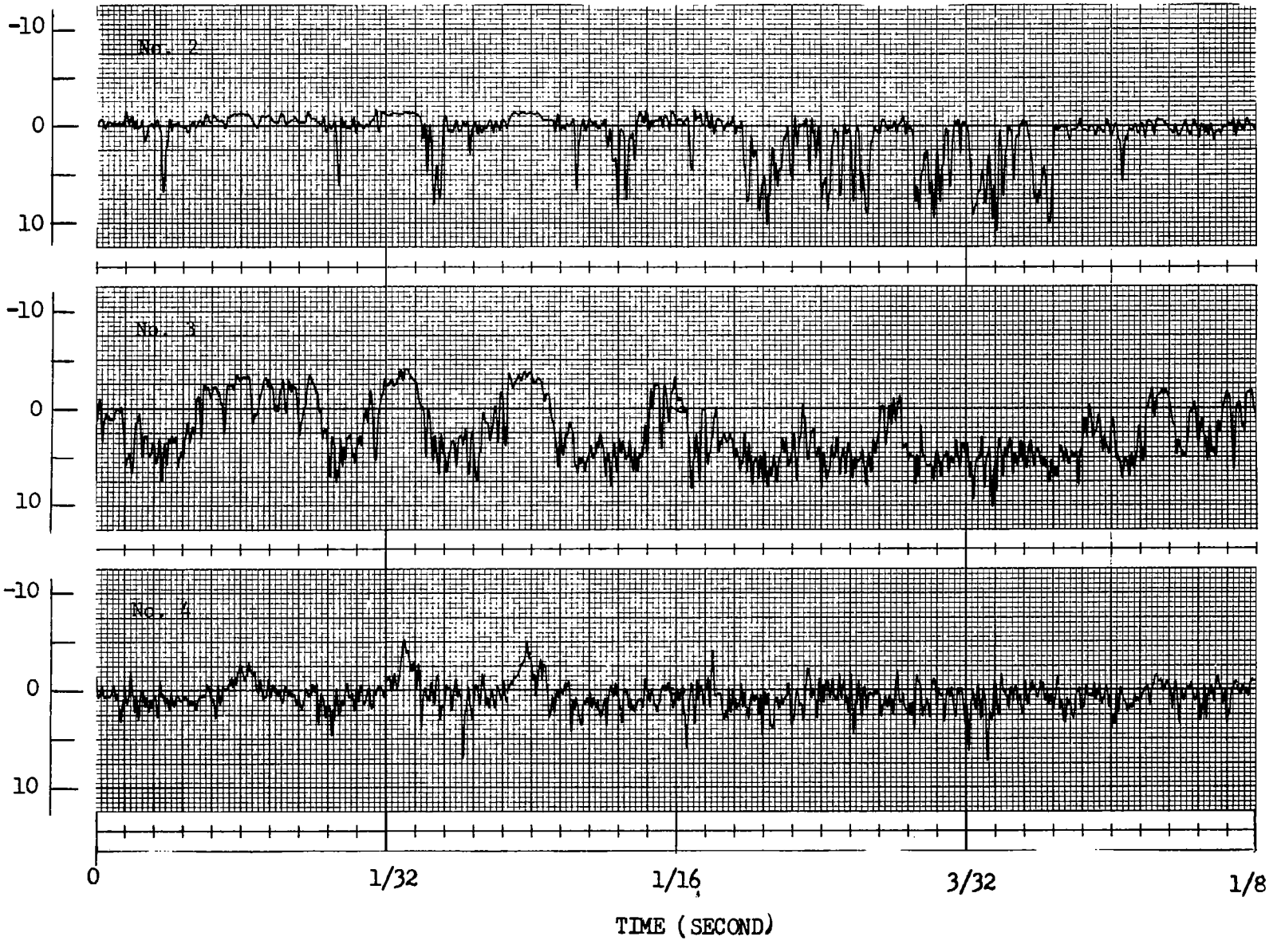

Figure 12. Dynamic Pressures of Transducer Nos. 2, 3, 4 of the F-5A Scale Model Run 8, Phase I - Configuration 2, $\alpha = 10°$, $p = 0°$, $M = .926$, $\delta_n/\delta_f = 5°/12°$, $\delta_h = 0°$

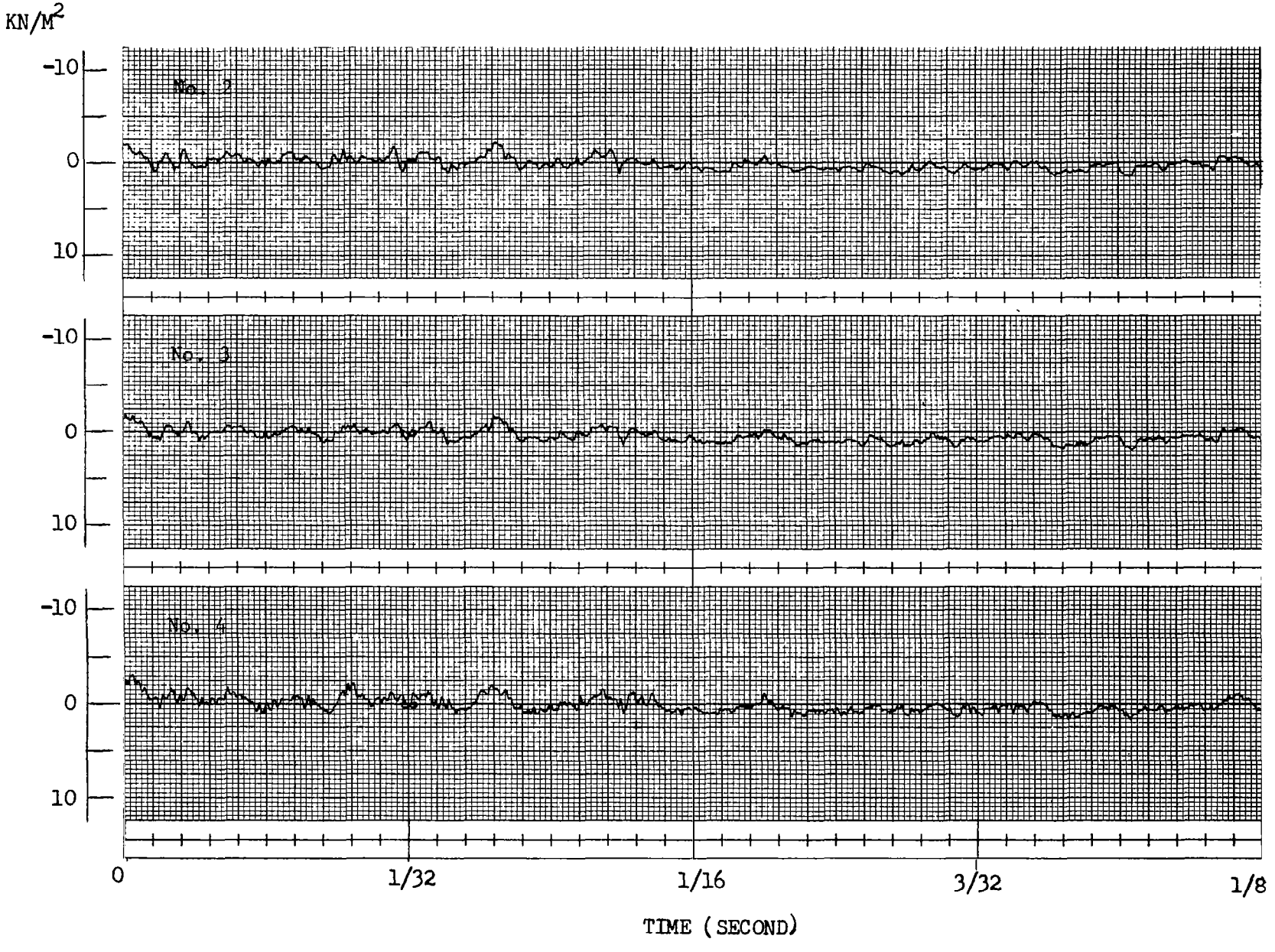

Figure 13. Dynamic Pressures of Transducer Nos. 2, 3, 4 of the F-5A Scale Model. Run 8, Phase I - Configuration 2, $\alpha = 16°$, $\beta = 0°$, M = .926, $\delta_n/\delta_f = 5°/12°$, $\delta_h = 0°$

By increasing the angle-of-attack by 2° to α = 10°, Figure 12 shows the shock interaction point had advanced to the 20% chord point (transducer No. 2). However, the flow was highly random with the shock interaction region oscillating between the 20 and 40% chord points. Figure 13 shows the same data at an angle-of-attack (α = 16°) in which the outboard wing was fully stalled (compare with Figure 10). The turbulence can be seen to possess a more stationary character at this condition. In a larger time scale, the non-stationary fluctuation of the rms dynamic pressures for transducers 2, 3, 4, corresponding to α = 10° is shown in Figure 14. The rms values of this figure were obtained by the integration of data within a traveling window 40 ms in width. As will be described later, the power spectral processing of the real time pressure data was applied to a finite and variable time span according to the frequency range of processing. In the high frequency range (up to 10 KHz), data from a relatively small time span was used for each ensemble. Averaging of the data from a number of ensembles yielded the power spectral density. A progressively longer time span was used for PSD processing in the lower frequency ranges. As a result, the non-stationarity of the data may cause substantial deviation and uncertainty in the spectral density functions for conditions such as the case of α = 10° depending on the frequency range and the specific ensemble time span selected for processing.

In the second test phase, a special sting was designed incorporating a torsional spring and damper which allowed the model to oscillate in roll at a natural frequency simulating the Dutch roll motion during wing-rock. The maximum roll angle was 30° single amplitude. In order to demonstrate the effect of rolling motion, typical response data of Run 5, Phase II, at α = 10° as recorded on an oscillograph are shown in Figures 15 and 16. The test conditions are described below.

Configuration 2, δ_n/δ_f = 5°/12°

δ_a = 0°/0°, δ_h = 0°

M = .925

R_N = 7.382 x 10^6/m (2.25 x 10^6/ft)

P_o = 29.80 KN/m^2 (622.47 psf)

Q = 18.20 KN/m^2 (377.70 psf)

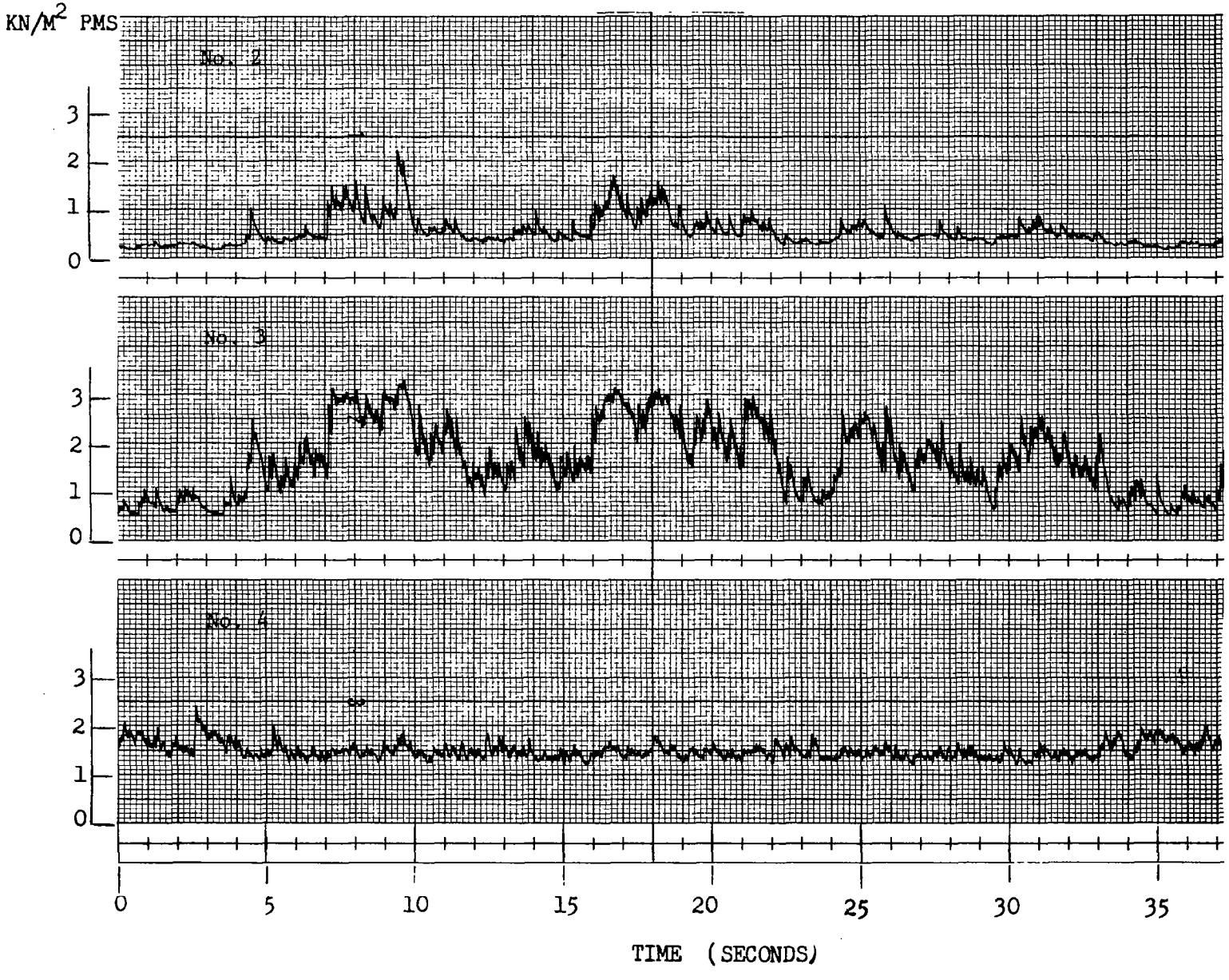

Figure 14. RMS Pressure Histories of Transducer Nos. 2, 3, 4 of the F-5A Scale Model. Run 8, Phase I - Configuration 2, $\alpha = 10°$, $\beta = 0°$, M = .926, $\delta_n/\delta_f = 5°/12°$, $\delta_h = 0°$

The nominal natural frequency of roll oscillation was 3.5 Hz. The damping ratio (c/c_{cr}) of the roll device was approximately 0.05. With increasing α, the model started to oscillate with substantial amplitude at $\alpha = 10°$. Typical response data obtained at $\alpha = 10°$ as recorded on an oscillograph are shown in Figures 15 and 16. In Figure 15, the roll angle and the pitch angle oscillations due to sting bending are presented. Evidently the oscillations started in a random manner, reached a peak of approximately 20° single amplitude, and then died out. The major frequency of oscillations was 4.0 Hz. The pitch angle oscillations had the same major frequency and were in phase with the roll oscillations. The random appearance of the roll oscillations and the subsequent reduction in oscillation amplitude were typical of the model motion at and above the critical angle-of-attack throughout the test phase. The response in this case was of the random type, as distinguished from the cyclic or periodic type (see, for example, Figure 39, page 77 of this report). For the case of random responses, the buffet pressures excited the model in a random fashion. When the narrow band pressure spectral density reached a certain level, the model was driven to oscillation of ever-increasing amplitude. After the oscillation reached a certain amplitude, either the buffet pressure intensity dropped, or the aerodynamic damping of the model reached such a level as to drastically reduce the oscillation amplitude as shown in Figure 15. The time of appearance and the length of the sustained oscillations were both random. On rare occasions, the model oscillated continuously without letdown until the test condition changed. Also, the highest amplitude of oscillations occurred at or near the critical angle-of-attack α^*. The oscillation amplitude usually dropped with increasing angle-of-attack beyond α^*. This behavior was observed even when the dynamic pressure PSD level continued to increase with increasing α. Covering the identical time span of Figure 15, Figure 16 shows the right wing root bending moment, the right wing-tip rms acceleration and the CG acceleration time histories. An application of the Randomdec program to determine the system aerodynamic damping corresponding to high-amplitude roll motion will be presented later in this section.

3.3 Comparison of Pressure Distributions Under Various Model Configurations and Test Conditions for the Fixed Model

Evaluation of test data has shown that significant flow pattern development on the aircraft lifting surfaces and the resulting changes in the

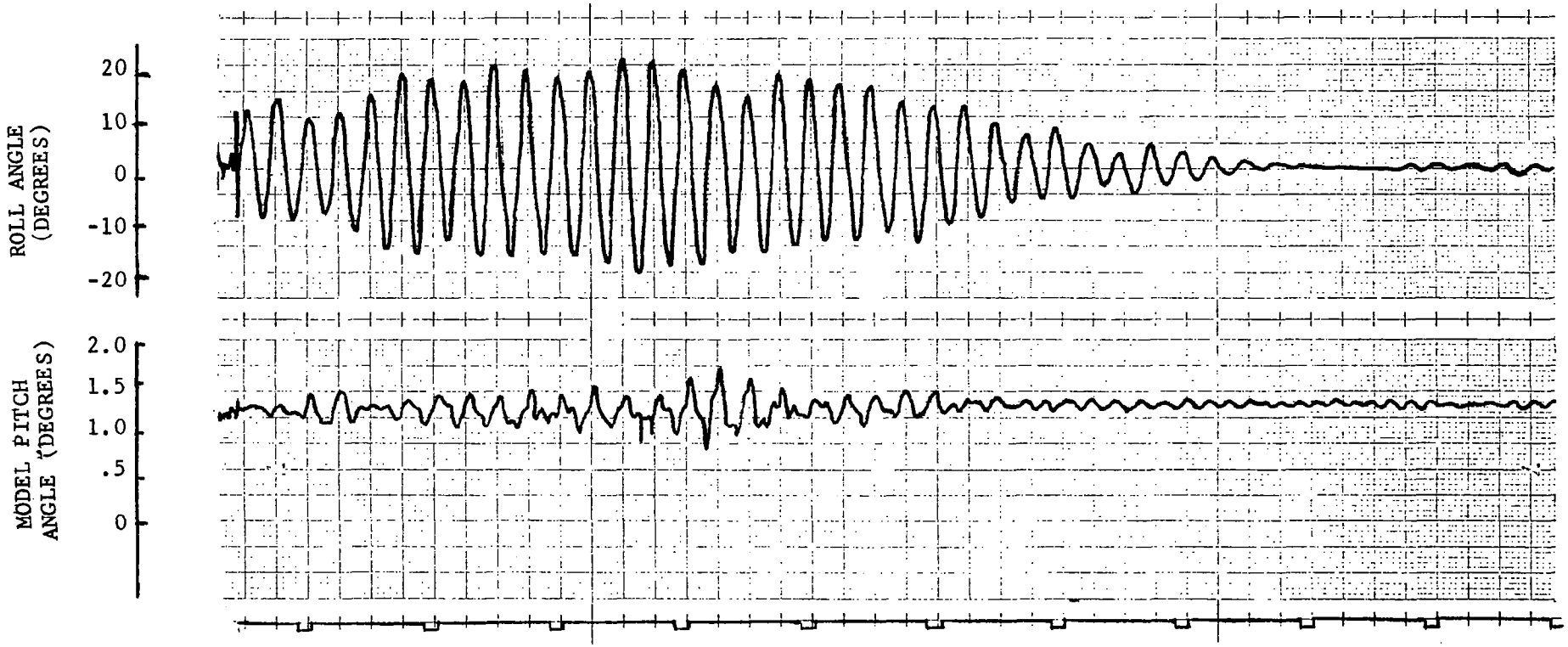

Figure 15. Oscillographs of F-5A Model Roll Angle and Pitch Angle Recorded During Run 5, Phase II, $\alpha = 10°$, $\beta = 0°$, $M = 0.925$, $\delta_a/\delta_f = 5°/12°$, $\delta_h = 0°$ (Timing marks appeared on bottom trace at one second intervals.)

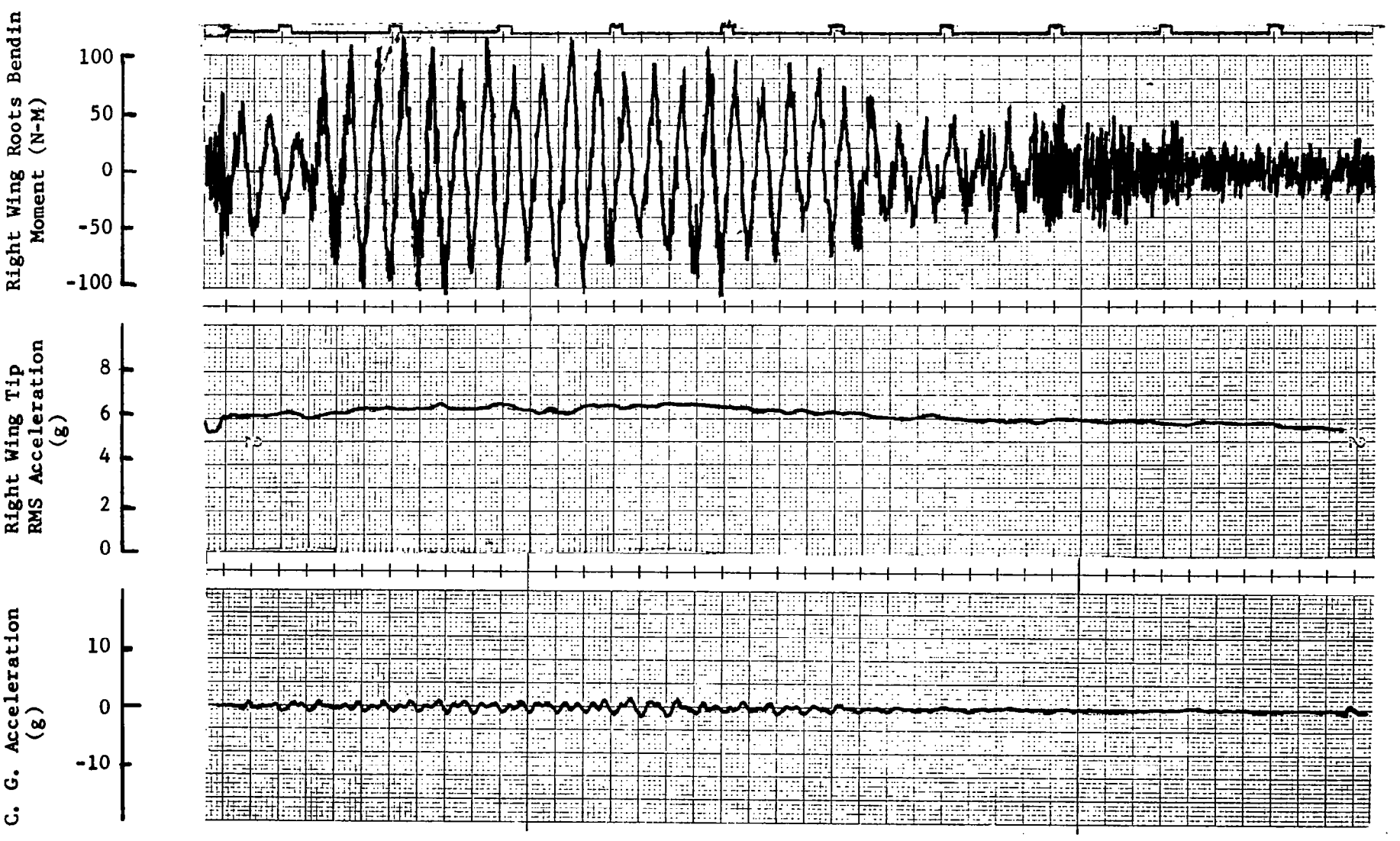

Figure 16. Oscillographs of F-5A Model Right Wing Bending Moment, Right Wing-Tip RMS Acceleration and CG Acceleration Recorded During Run 5, Phase II, $\alpha = 10°$, $\beta = 0°$, $M = 0.925$, $\delta_n/\delta_f = 5°/12°$, $\delta_h = 0°$. (Timing marks appeared on top trace at one second intervals.)

static and dynamic pressure distributions occurred in the angle-of-attack range 6 degrees to 12 degrees. A detail study on the pressure distribution provided insight to the aircraft buffet mechanism. In the subject test program, 52 separate runs were made during the first test phase. Parametric changes in either the model configuration or test condition were carried out systematically. By comparing the pressure patterns corresponding to two test runs where the difference was limited to a single test parameter, the net effect of the changing parameter to aircraft buffet may be identified. In the following, comparisons were performed on a number of test run pairs based on the static and the dynamic pressure coefficient distributions. Effect of flap settings will be presented in the next section together with the power spectral density plots.

Mach Number Effect

In Figure 17, the dynamic pressure coefficient distributions for Runs 19 and 22, Phase I, are presented. Runs 19 and 22 were conducted under model configuration 3, i.e., $\delta_n/\delta_f = 5°/12°$, $\delta_a = 0°$, $\beta = 0°$, $\delta_h = -10°$. Tip-mounted missiles were present in both runs. Run 19 was conducted at $M = 0.925$ and Run 22 at $M = 0.75$. The comparison of the two runs demonstrated the classical Mach number effect on aircraft wing flow separation. At $M = 0.925$ (Run 19), the shock boundary may be traced through the peak dynamic pressure locus. It was initiated near the trailing edge of the wing-tip region and gradually expanded toward the inboard and upstream region with increasing α. The wing top surface was completely separated at $\alpha = 12°$. For $M = 0.75$ (Run 22), the leading edge induced flow separation appeared up to approximately 61 percent semi-span at $\alpha = 6°$. With increasing α, the flow of the wing top surface was completely separated. Throughout the process, no prominent dynamic pressure peaks were in evidence that identified the local shock.

Sideslip Effect

Figure 18 shows the dynamic pressure distributions for Run Nos. 8 and 10. Both runs were conducted using model configuration 2, i.e., $\delta_n/\delta_f = 5°/12°$, $\delta_a = 0°/0°$, $\delta_h = 0°$. The wing was attached with wing-tip-

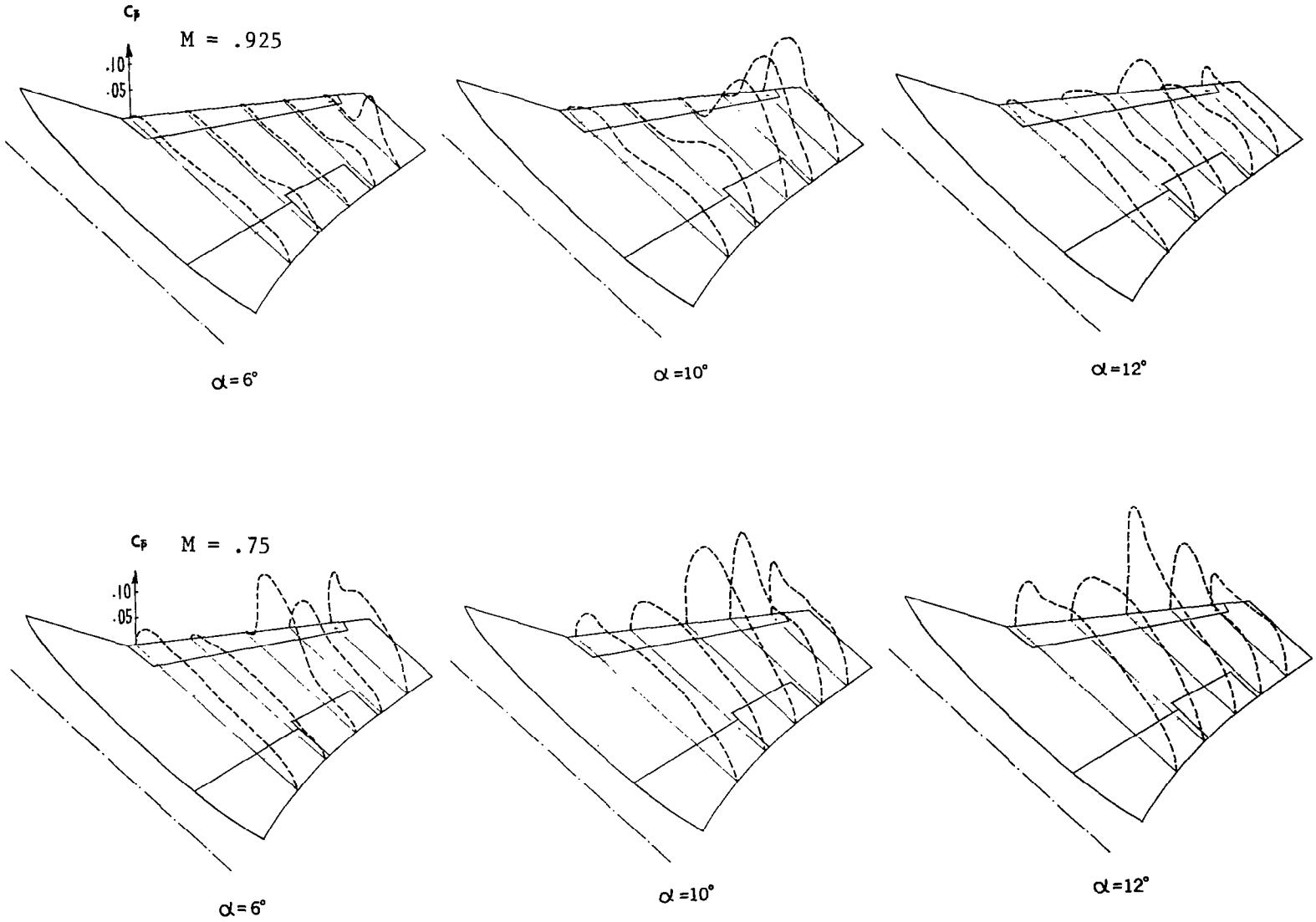

Figure 17. Dynamic Pressure Comparison Due to Mach Number Effect — Run 19 (top) Versus Run 22, Phase I, $\beta = 0°$, $\delta_n/\delta_f = 5°/12°$, $\delta_h = -10°$

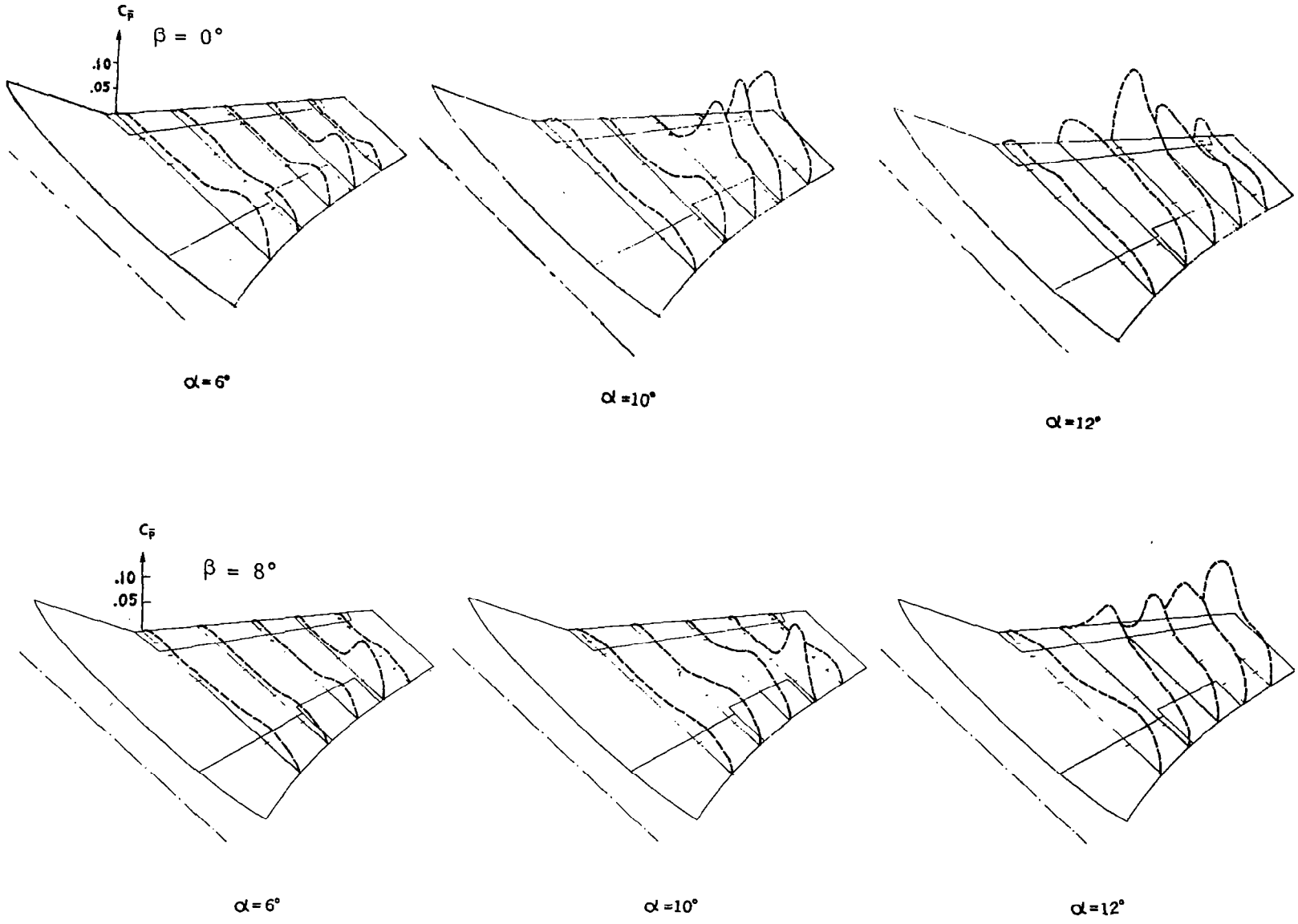

Figure 18. Dynamic Pressure Comparison Due to Sideslip Angle Effect - Run 8 (top) Versus Run 10, Phase I, M = 0.925, $\delta_n/\delta_f = 5°/12°$, $\delta_h = 0°$

mounted Sidewinder missiles. Both runs had a Mach number of 0.925 with a Reynolds number of 7.38×10^6/m (2.25×10^6/ft). The sideslip angle β of Run 8 was zero, while in Run 10, $\beta = 8°$, the flow direction was somewhat closer to a line normal to the right wing leading edge. Furthermore, the vortex effect created by the front fuselage to the right wing was alleviated with a positive β. The two factors described above directed to a turbulence-free and more favorable pressure gradient along the chordwise direction, which tended to move the shock and shock-induced flow separation downstream. Throughout the α range presented in the figure, the shock and the shock-induced flow separation were retarded and pushed downstream corresponding to a positive β (Run 10). It was further noticed that beyond $\alpha = 12°$, the flow on the top wing was completely separated. As a result, the dynamic pressure distributions for the two cases became less and less distinguishable.

Figure 19 is a set of similar pressure plots for Run Nos. 8 and 9. Run 9 was conducted with a sideslip angle $\beta = -8°$, which was expected to exhibit a reverse trend of Run 10 ($\beta = 8°$), i.e., forward movement of the shock front for the same α. Indeed, this was the case, especially for $\alpha = 10°$. For $\alpha = 6°$, the almost complete flow separation along the wing chord at 85 percent semi-span was conspicuous for $\beta = -8°$. The exact reason for this behavior remained to be resolved. Additional discussion on the development of flow separation bubble on the scale model with sideslip will be presented later in this section.

Effect of the Tip-Mounted Missiles

Figure 20 presents the dynamic pressure distributions of Run Nos. 8 and 27. Run 27 was identical to Run 8 except that the tip-mounted missiles were absent in the former case. An examination of the figure indicated that at $\alpha = 10°$, the missileless wing-tip caused the flow separation to be effectively suppressed. As soon as the suppressing effect was no longer dominating, the dynamic pressure patterns of the two runs then became almost indistinguishable (see $\alpha = 12°$). In other words, the tip-mounted missiles

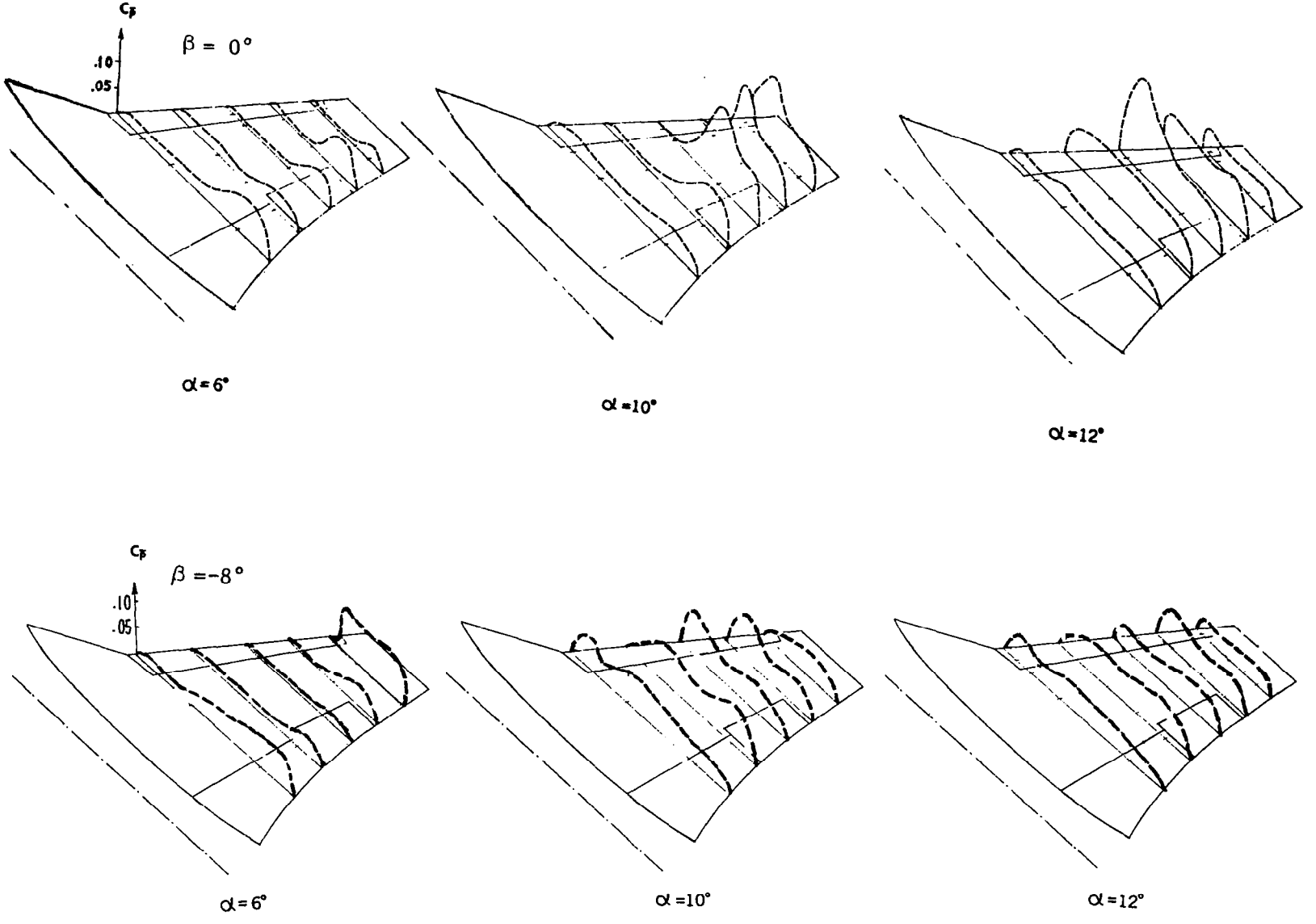

Figure 19. Dynamic Pressure Comparison Due to Sideslip Angle Effect — Run 8 (top) Versus Run 9, Phase I, M = 0.925, $\delta_n/\delta_f = 5°/12°$, $\delta_h = 0°$

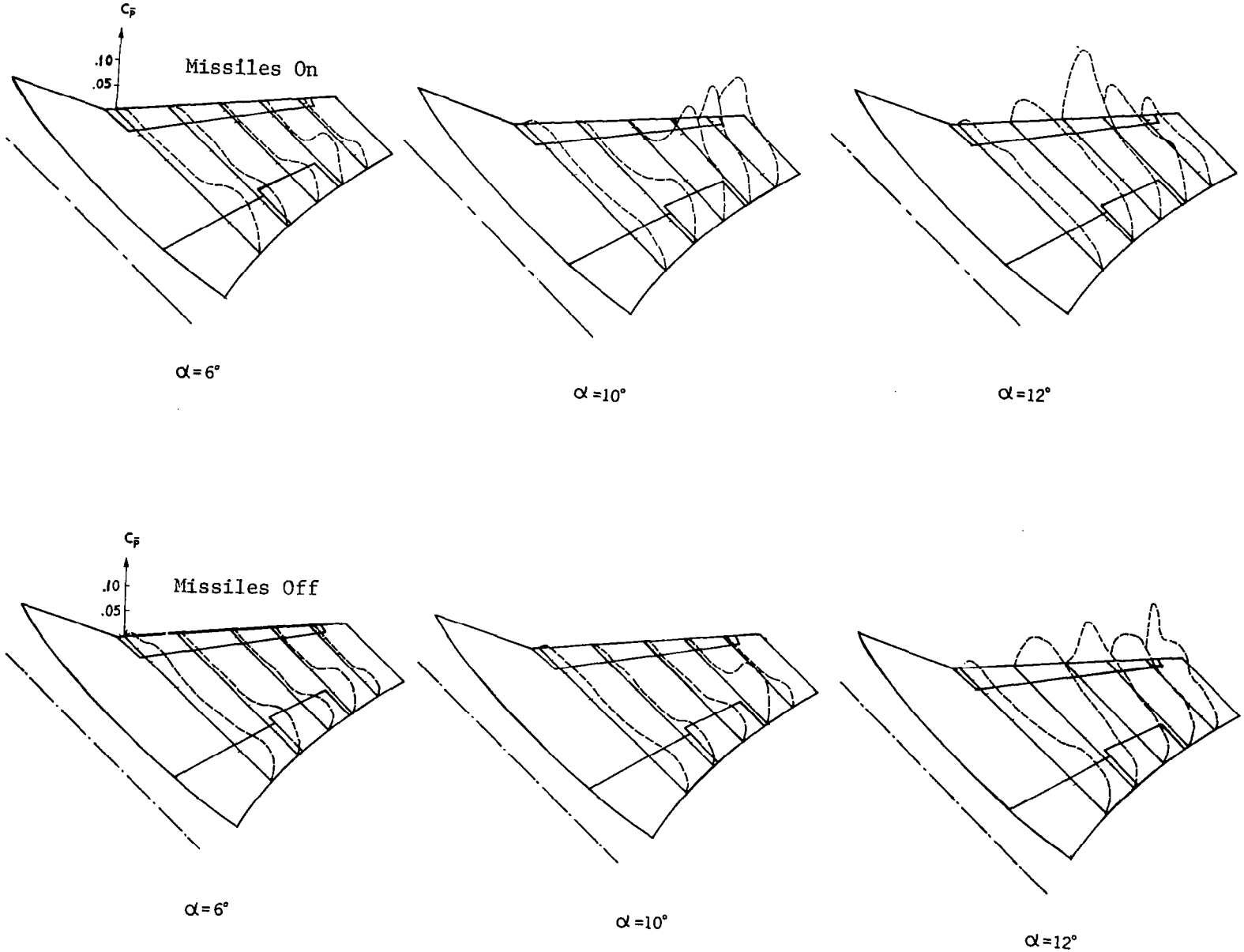

Figure 20. Dynamic Pressure Comparison Due to Wing-Tip-Mounted Sidewinder Missiles — Run 8 (top) Versus Run 27, Phase I, $\beta = 0°$, $M = 0.925$, $\delta_n/\delta_f = 5°/12°$, $\delta_h = 0°$

had an adverse effect in promoting the flow separation at a certain critical α angle. This effect was greatly diminished after the critical angle-of-attack was surpassed.

Tail Deflection Effect

Both Run Nos. 39 and 49 were conducted with retracted leading edge and trailing edge flaps. The ailerons were also retracted. Both runs were made at M = 0.925, while Run 39 had a somewhat higher Reynolds number (11.50×10^6/m versus 7.38×10^6/m for Run 49). The major difference between the two runs was that Run 39 featured a horizontal tail surface setting of 0 degree, while that of Run 49 was -10 degrees.

In Figure 21, the dynamic pressures of the two runs are presented. In examining this figure, it was noted that the deflected horizontal tail tended to delay or alternate its shock-induced flow separation in that part of the wing directly upstream of the tail. Correspondingly, for a given angle-of-attack, the shock strength and the level of dynamic pressure behind the shock tended to be stronger in the outer half span of the wing. This effect was most prominent at α range 8°-10°. Beyond this, the effect of the tail surface setting became less prominent.

3.4 Comparison of Dynamic Pressure Coefficient Distributions For the Fixed and Flexibly-Supported Models

In Phase I tests, the Northrop F-5A model was supported on a regular sting with a balance unit located inside the fuselage. In the Phase II tests, the same model was supported on a flexible system which allowed the model to oscillate along the roll axis under unsteady aerodynamic forces. A hydraulic damping device was installed to regulate the angle of oscillation. The details of the flexible system are described in the previous section.

In Figures 22 through 25, the dynamic pressure coefficient distributions on the right wing upper surface acquired during the two test phases under identical test conditions are presented. The plots cover the angle-of-attack range α = 6°, 10°, 12°. The results of Phase I are plotted on the top of the figures with the corresponding data of Phase II plotted below. The test configuration and the run conditions are described in the following paragraph.

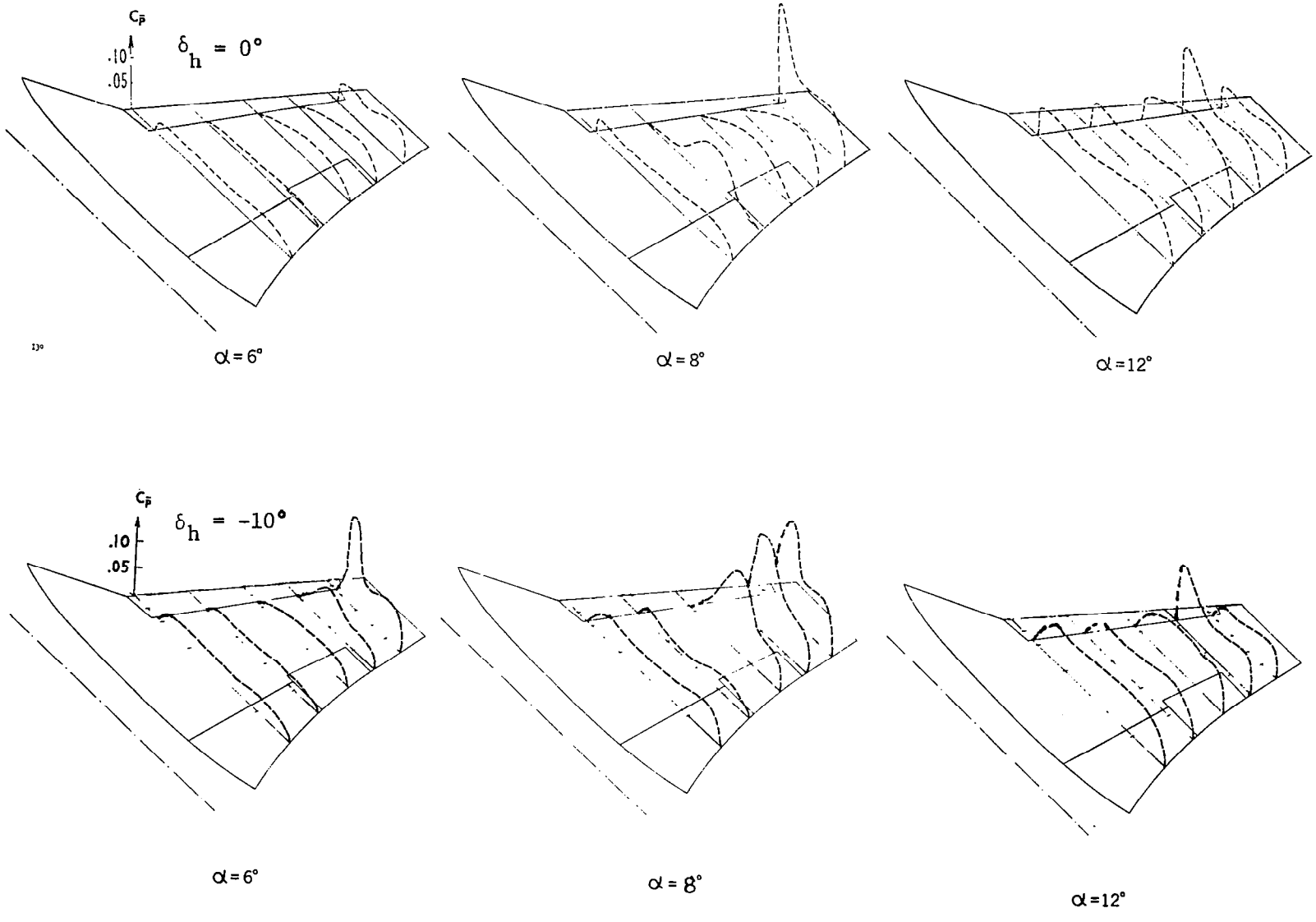

Figure 21. Dynamic Pressure Comparison Due to Horizontal Tail Surface Setting — Run 39 (top) Versus Run 49, Phase I, $\beta = 0°$, $M = 0.925$, $\delta_n/\delta_f = 0°/0°$

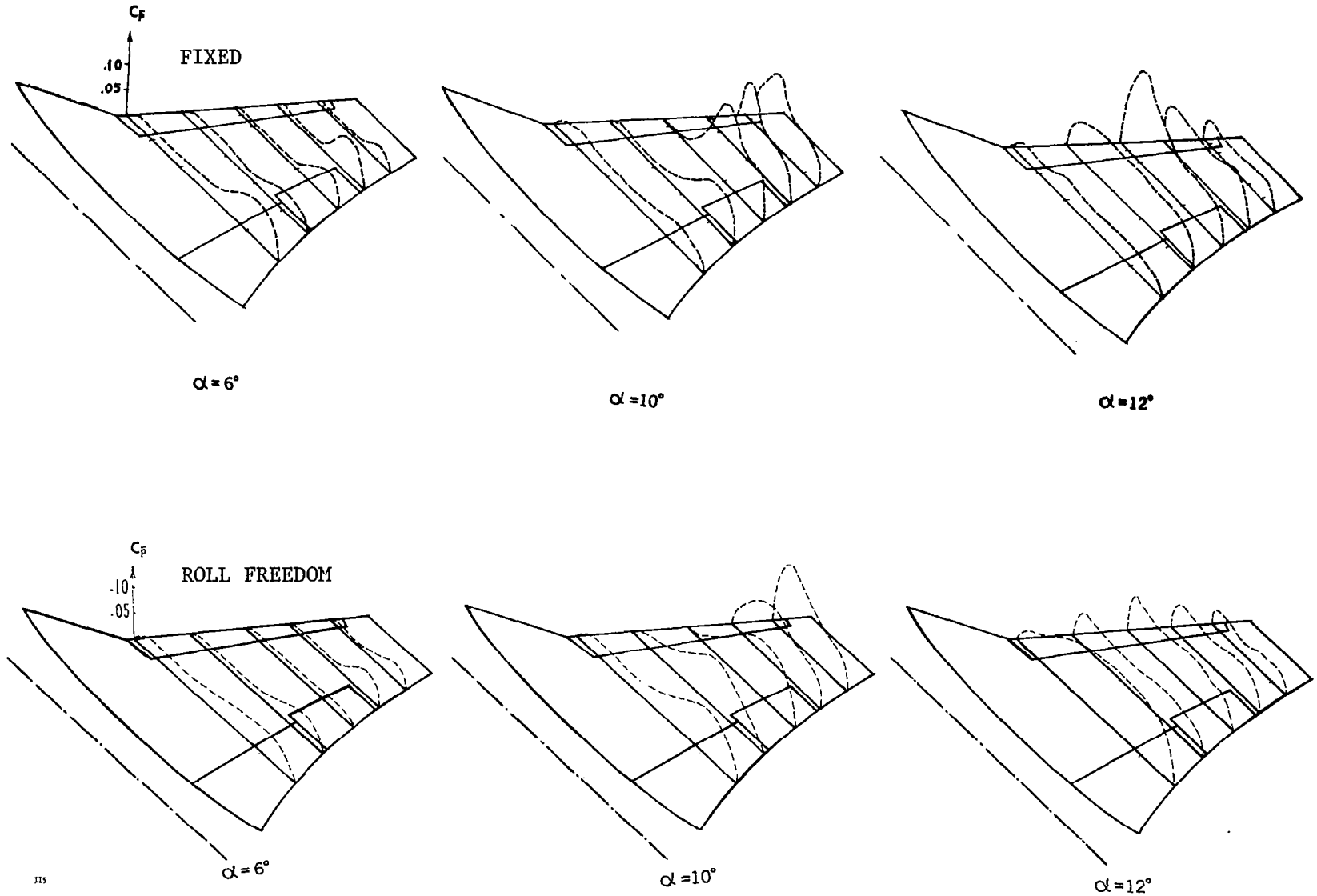

Figure 22. Comparison of Dynamic Pressure Coefficient Distributions for the Fixed Model (top) and the Oscillating Model - Configuration 2, $\beta = 0°$, $M = .925$, $\delta_n/\delta_f = 5°/12°$, $\delta_h = 0°$, $\alpha^* = 10°$

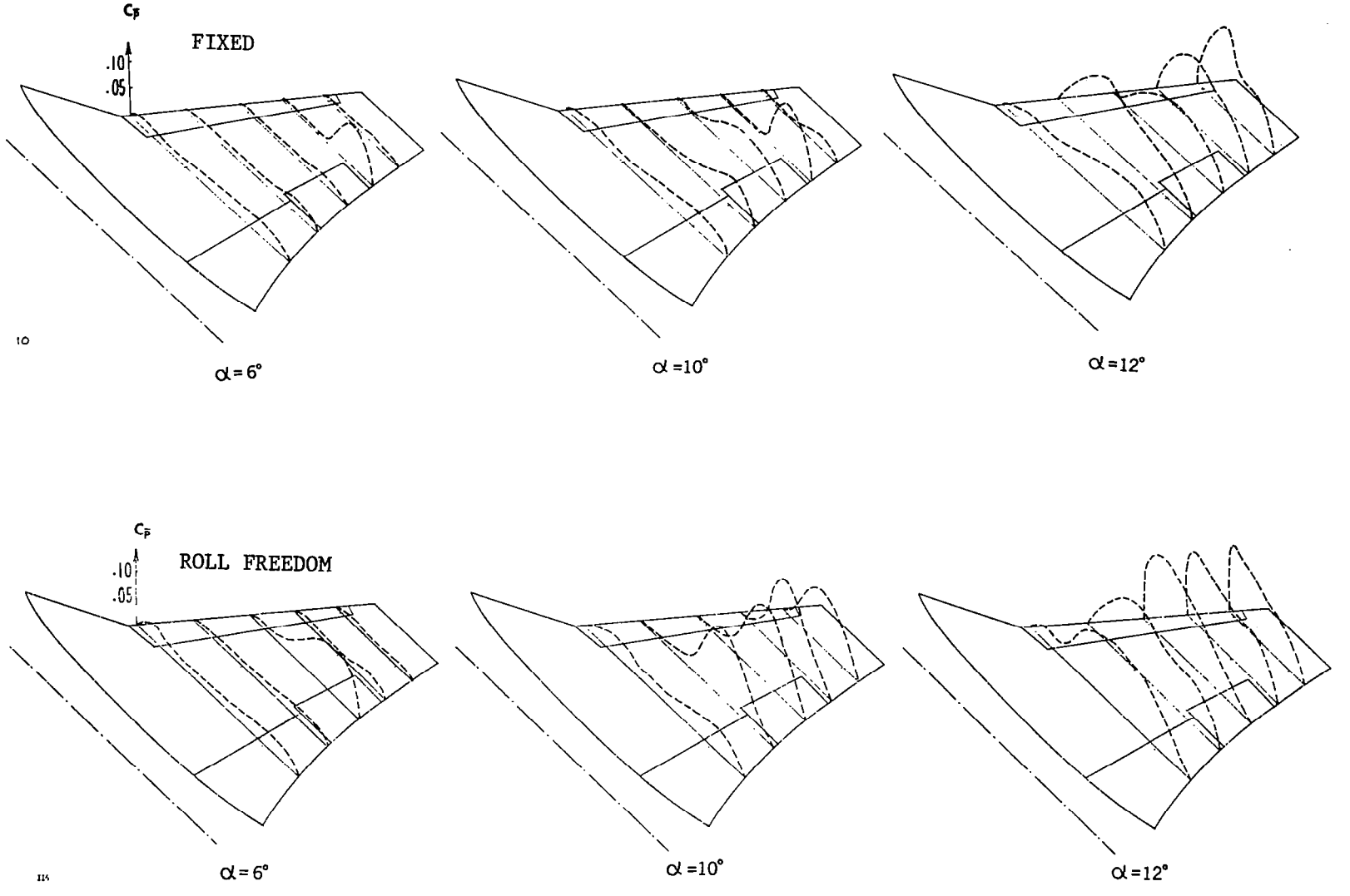

Figure 23. Comparison of Dynamic Pressure Coefficient Distributions for the Fixed Model (top) and the Oscillating Model - Configuration 2, $\beta = 8°$, $M = .925$, $\delta_n/\delta_f = 5°/12°$, $\delta_h = 0°$, $\alpha^* = 12°$

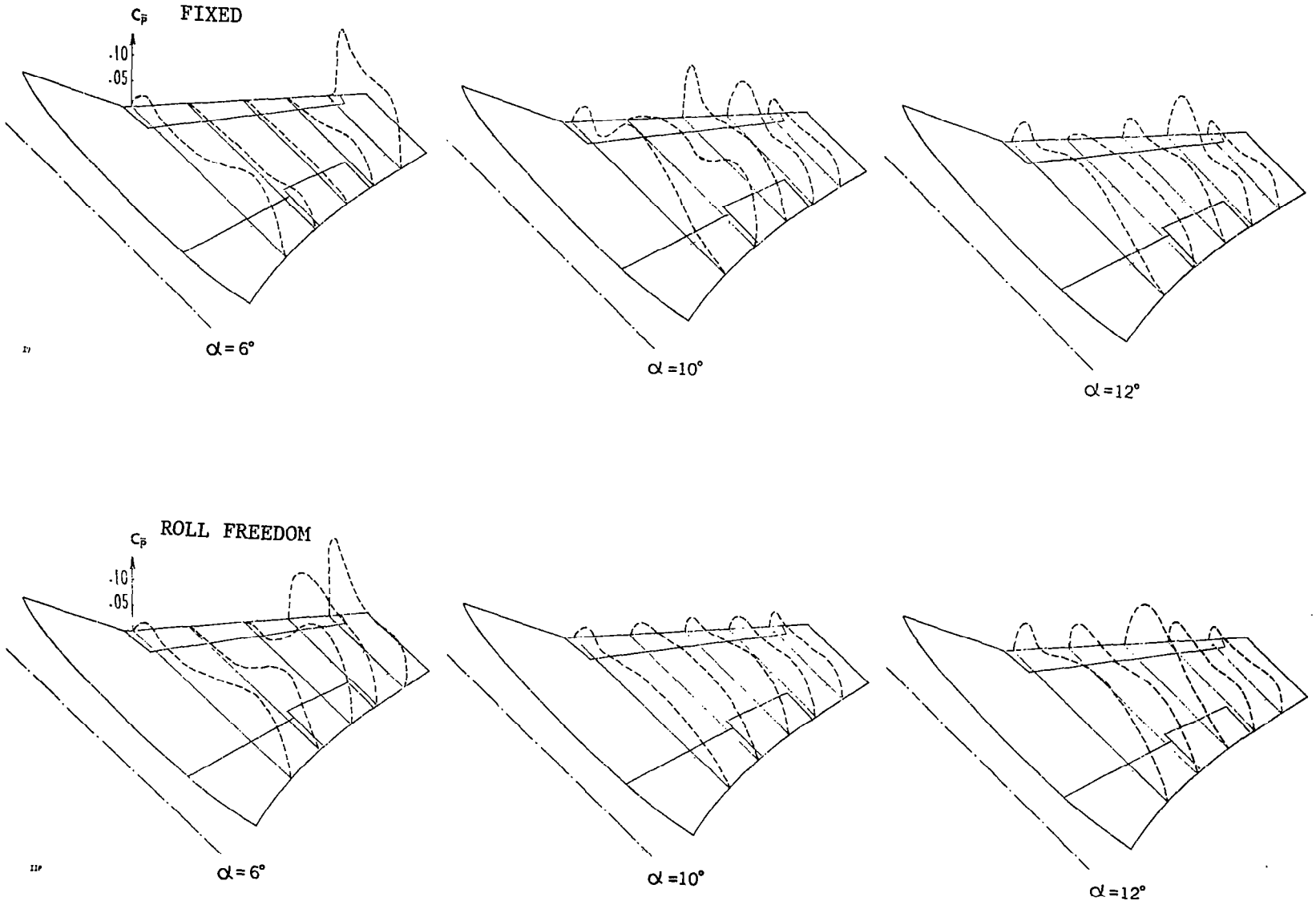

Figure 24. Comparison of Dynamic Pressure Coefficient Distributions for the Fixed Model (top) and the Oscillating Model - Configuration 2, $\beta = -8°$, M = .925, $\delta_n/\delta_f = 5°/12°$, $\delta_h = 0°$, $\alpha* = 11°$

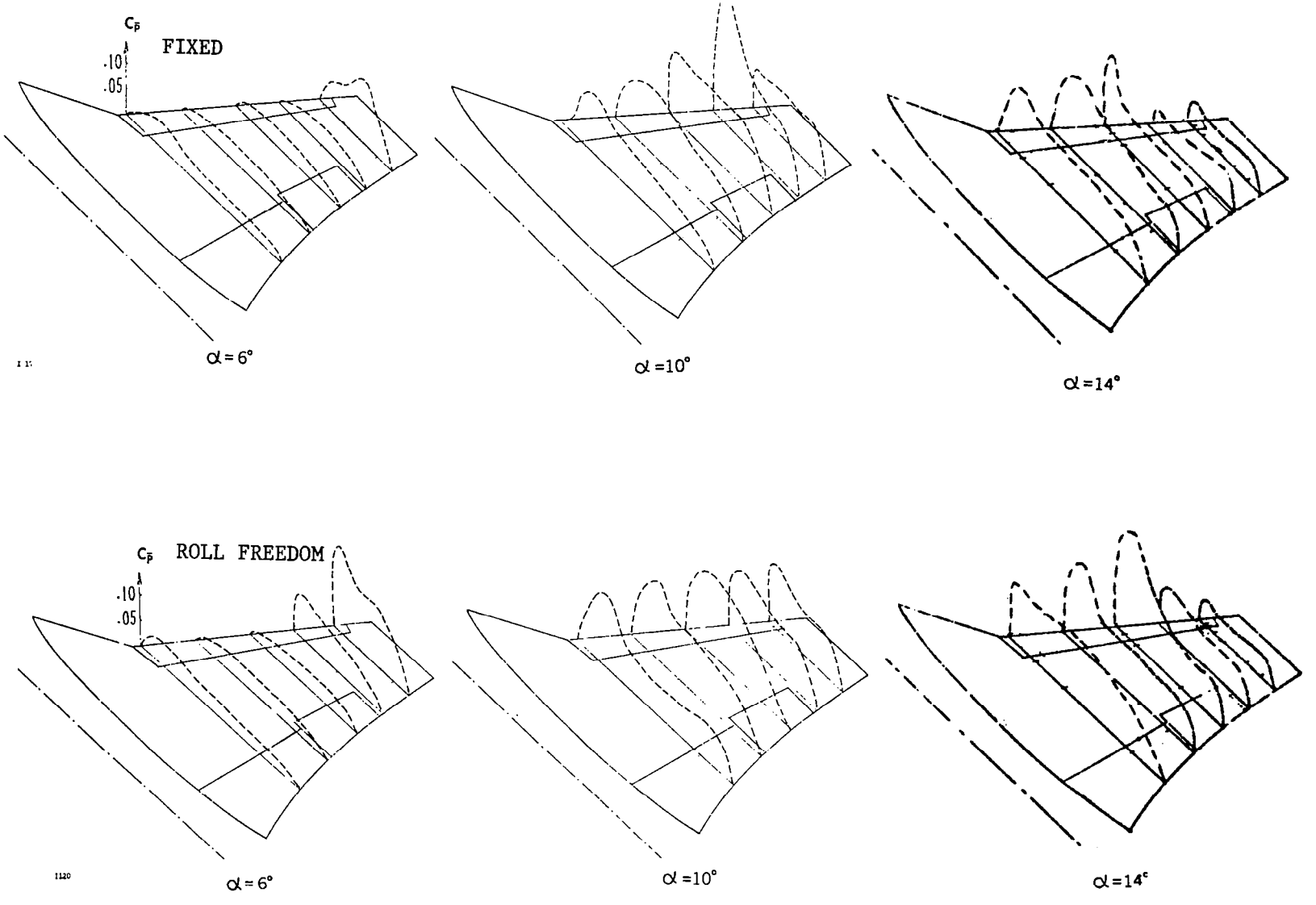

Figure 25. Comparison of Dynamic Pressure Coefficient Distributions for the Fixed Model (top) and the Oscillating Model - Configuration 2, $\beta = 8°$, $M = .75$, $\delta_n/\delta_f = 5°/12°$, $\delta_h = 0°$, $\alpha^* = 14°$

Figures 22, 23, 24: Configuration 2, $\delta_n/\delta_f = 5°/12°$, $\delta_h = 0°$, $\delta_a = 0°/0°$, Sidewinder missiles at wing-tips, M = 0.925, $R_N = 2.485 \times 10^6$. Figure 25: Same conditions as above except that M = .75.

Additional dynamic pressure coefficient comparisons for the fixed and flexibly-supported model were made in Figures 26 to 30 for the following cases:

Figure 26: Configuration 3, $\delta_n/\delta_f = 5°/12°$, $\delta_h = -10°$, $\delta_a = 0°/0°$, Sidewinder missiles at wing-tips, M = 0.925, $R_N = 2.485 \times 10^6$.

Figure 27: Configuration 8, $\delta_n/\delta_f = 0°/0°$, $\delta_h = 0°$, $\delta_a = 0°/0°$, no Sidewinder missiles, M = 0.925, $R_N = 2.485 \times 10^6$.

Figures 28-30: Configuration 9, same as Configuration 8 except that Sidewinder missiles were installed at wing-tips, M = 0.925, $R_N = 2.485 \times 10^6$.

The specific test phase and run numbers presented in Figures 22-30 are tabulated below:

	Test Phase-Run No.	Test Phase-Run No.	Sideslip Angle	α^*
Figure 22	I-8	II-5	$\beta = 0°$	10°
Figure 23	I-10	II-6	$\beta = 8°$	12°
Figure 24	I-9	II-8	$\beta = -8°$	11°
Figure 25	I-17	II-20	$\beta = 8°$	14°
Figure 26	I-19	II-14	$\beta = 0°$	10°
Figure 27	I-36	II-29	$\beta = 0°$	8° - 10° intermitteni
Figure 28	I-39	II-21	$\beta = 0°$	8°
Figure 29	I-41	II-22	$\beta = 8°$	10°
Figure 30	I-40	II-23	$\beta = -8°$	10°

α^* = the angle-of-attack at which the flexibly-supported model started to oscillate along the roll axis.

In examining the pressure distributions for the fixed model and the flexibly-supported model, the following conclusions may be drawn:

1. For angles-of-attack under the critical angle α^*, it was expected that the dynamic pressure coefficient distributions would be identical in phases I and II under otherwise identical test conditions. The plotted data showed that corresponding to the two phases, the trends of the dynamic pressure coefficient distributions were the same which reflected the shock development (for M = 0.925) and the expansion of the flow separation region, etc. However, substantial deviation in local pressure did exist. For instance, in Figure 24, at α = 6 degrees, the rms pressure levels along 61 percent and 72.8 percent semi-spans were substantially higher for Phase II. Contrarily, in Figure 25, α = 10 degrees, the very high rms pressure peak at 20 percent chord and 72.8 percent semi-span location shown in Phase I was not observed in Phase II. These variations of the dynamic pressure data indicated a certain degree of randomness of the buffet phenomenon, with a predictable trend development for any given test condition.

2. In general, at the critical angle-of-attack α^* when the model started to oscillate along the roll axis, the model motion tended to make the pressure distribution more even, spacewise. This condition was observed in a number of cases, but with prominent exceptions. One exception was Figure 23, $\alpha = 12°$, where the high dynamic pressure for the model with roll freedom may be contributed to the coincident location of the shock region and the pressure transducer(s).

3. For $\alpha > \alpha^*$, the differences in the dynamic pressures of the fixed and oscillating models tended to diminish as the angle-of-attack was further increased.

Referring to Figure 26, the extremely high $\bar{C}_p$ value (0.2788) of transducer No. 1 at α = 10 degrees indicated that the data was recorded prior to the large amplitude model oscillations, which also started at α^* = 10 degrees. It can be visualized that an intense shock was originated at a location near transducer No. 1, which served as an anchoring point of the shock line on the wing surface. Toward the inboard stations, the lesser rms peaks indicated either

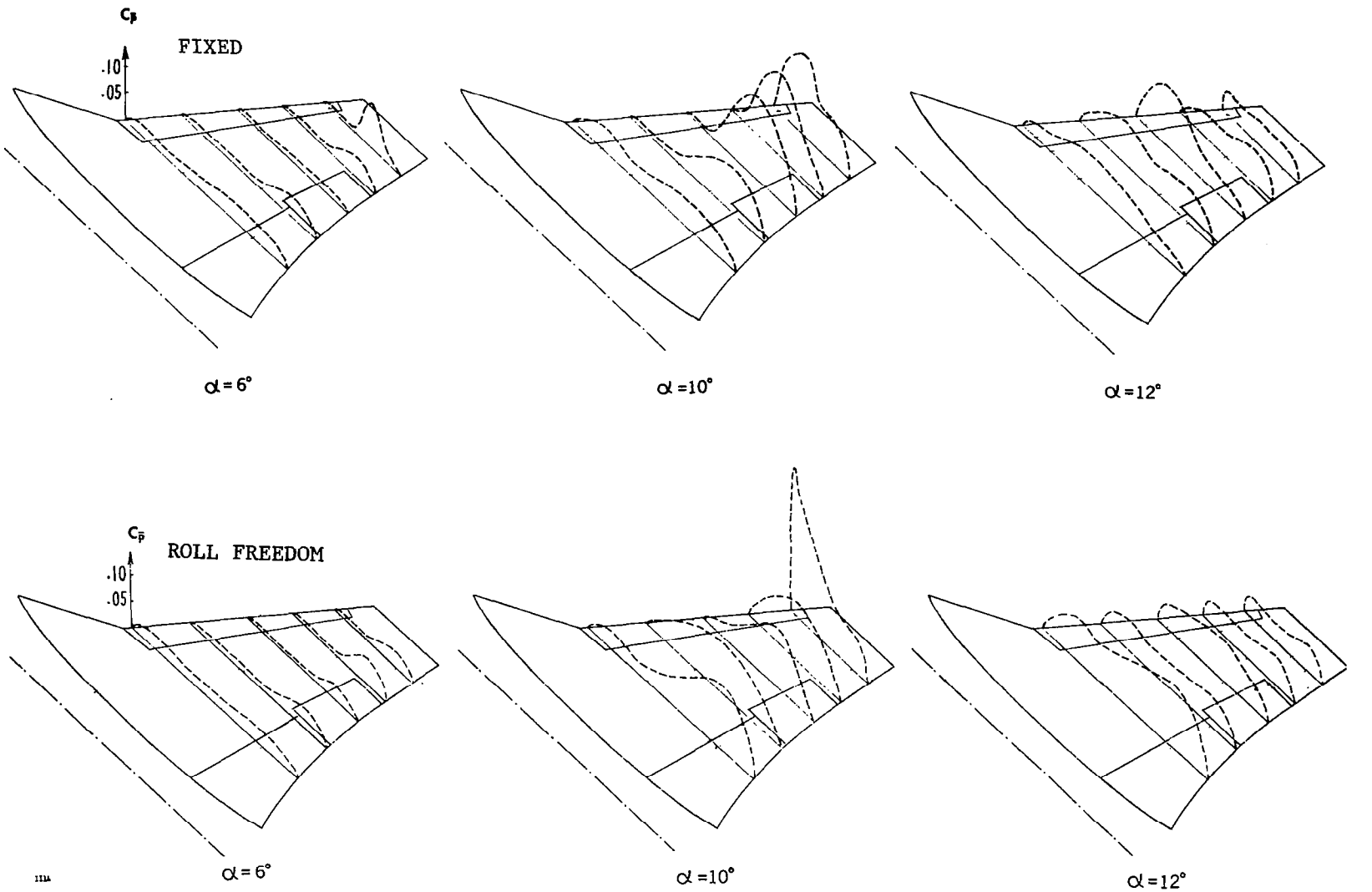

Figure 26. Comparison of Dynamic Pressure Coefficient Distributions for the Fixed Model (top) and the Oscillating Model - Configuration 3, $\beta = 0°$, M = .925, $\delta_n/\delta_f = 5°/12°$, $\delta_h = -10°$, $\alpha^* = 10°$

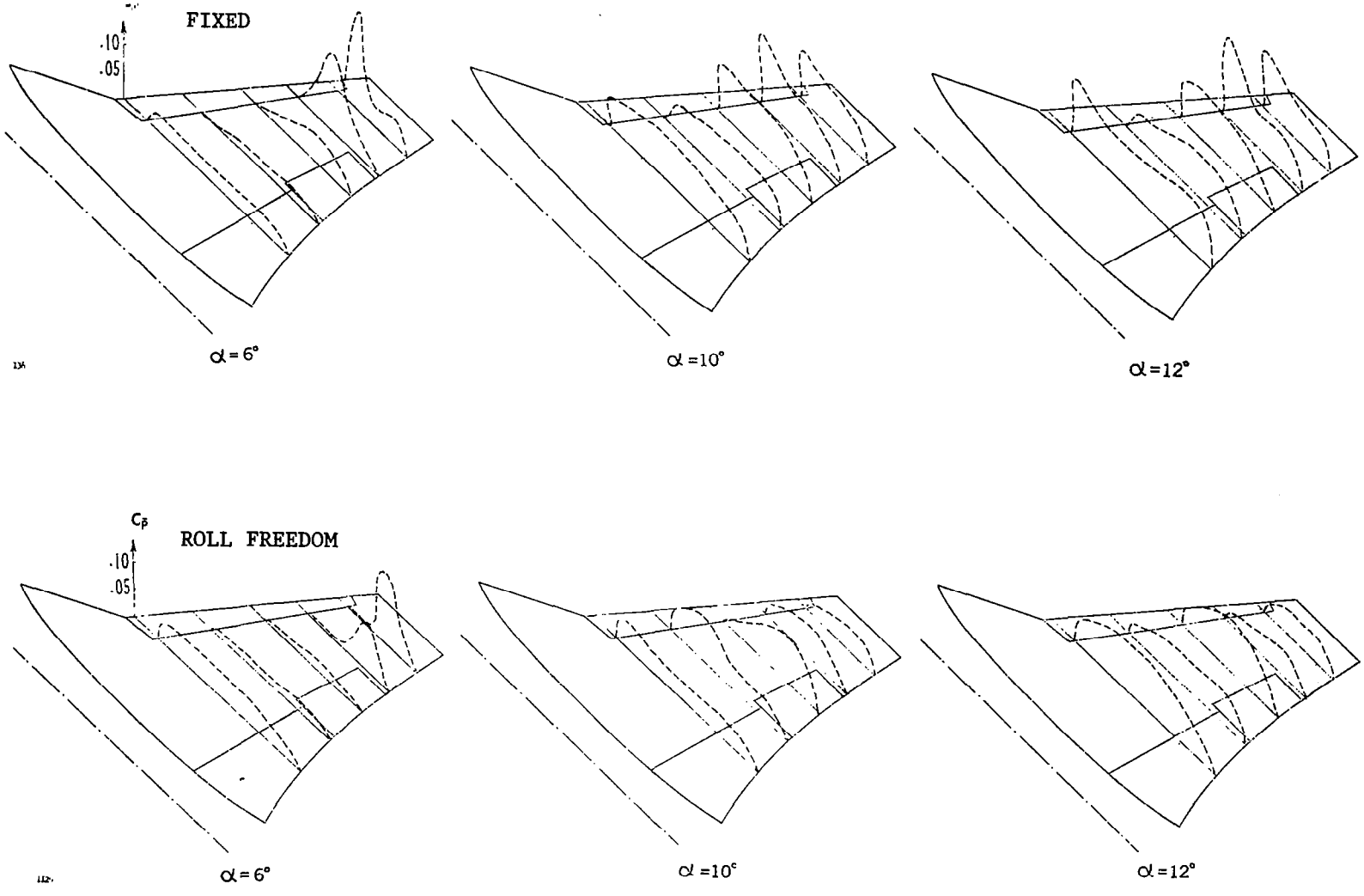

Figure 27. Comparison of Dynamic Pressure Coefficient Distributions for the Fixed Model (top) and the Oscillating Model - Configuration 8, $\beta = 0°$, M = .925, $\delta_n/\delta_f = 0°/0°$, $\delta_h = 0°$, Missiles Off, $\alpha^* = 8° - 10°$ (Intermittent)

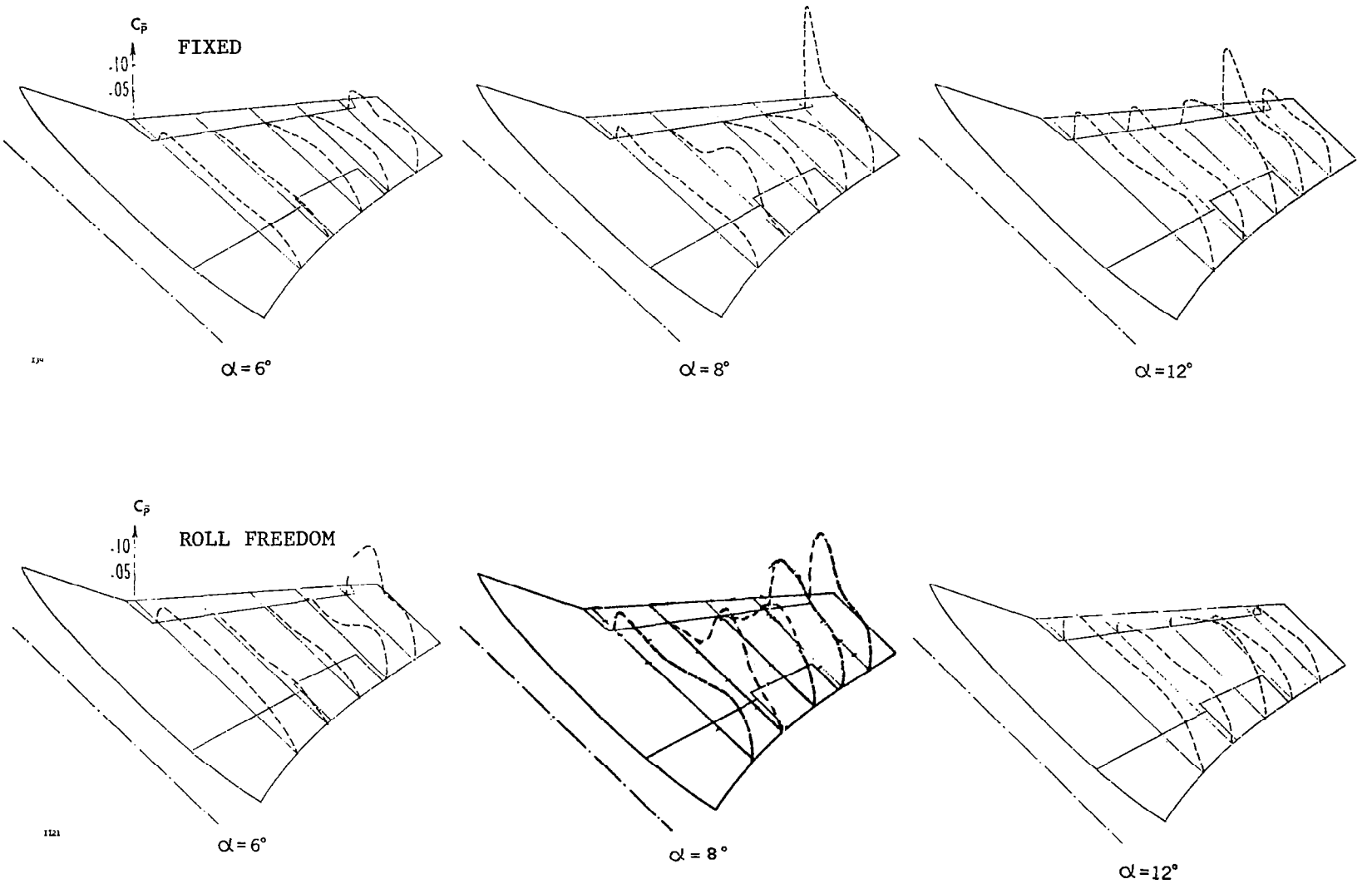

Figure 28. Comparison of Dynamic Pressure Coefficient Distributions for the Fixed Model (top) and the Oscillating Model - Configuration 9, $\beta = 0°$, M = .925, $\delta_n/\delta_f = 0°/0°$, $\delta_h = 0°$, $\alpha^* = 8°$

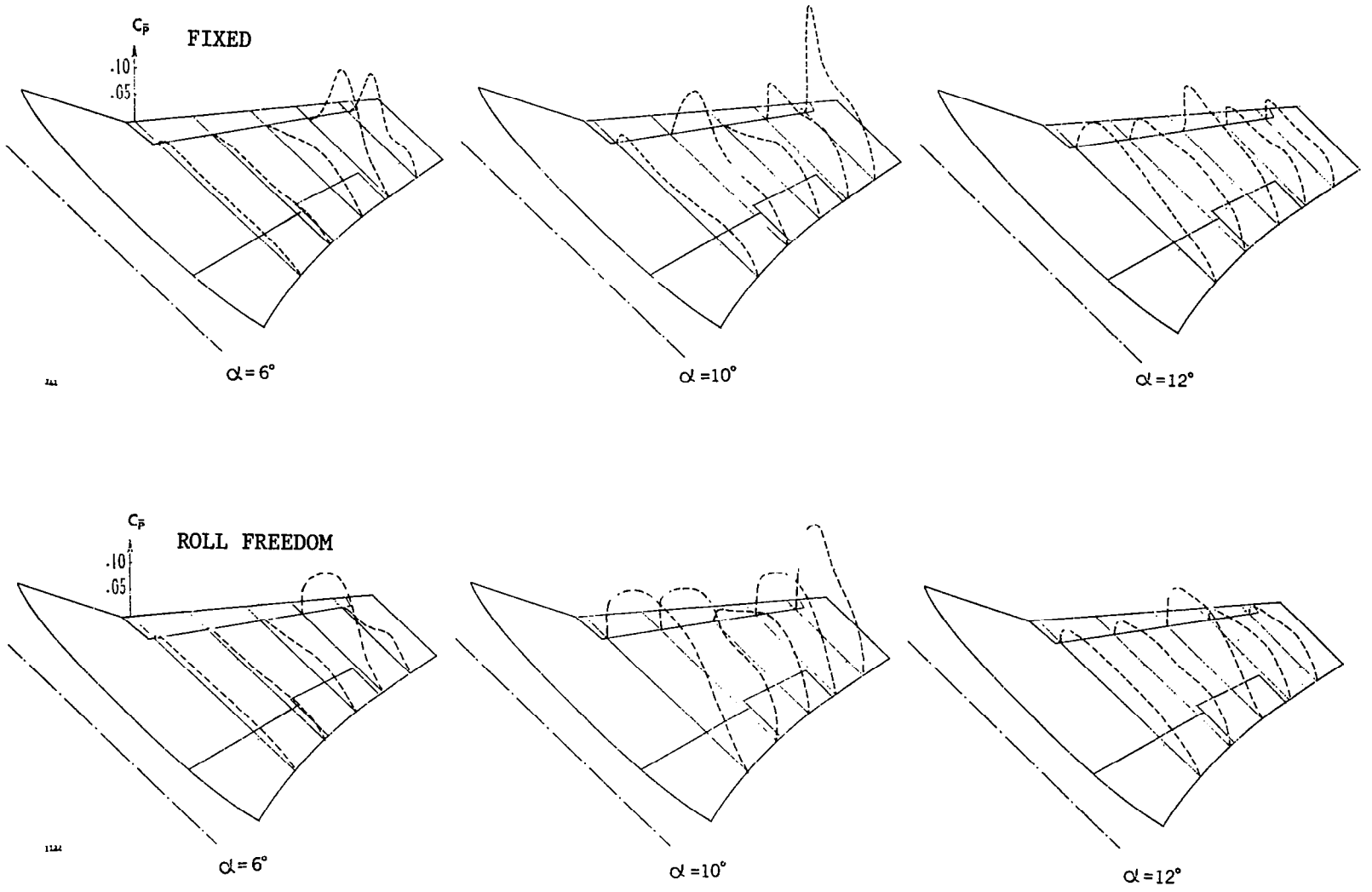

Figure 29. Comparison of Dynamic Pressure Coefficient Distributions for the Fixed Model (top) and the Oscillating Model - Configuration 9, $\beta = 8°$, M = .925, $\delta_n/\delta_f = 0°/0°$, $\delta_h = 0°$, $\alpha^* = 10°$

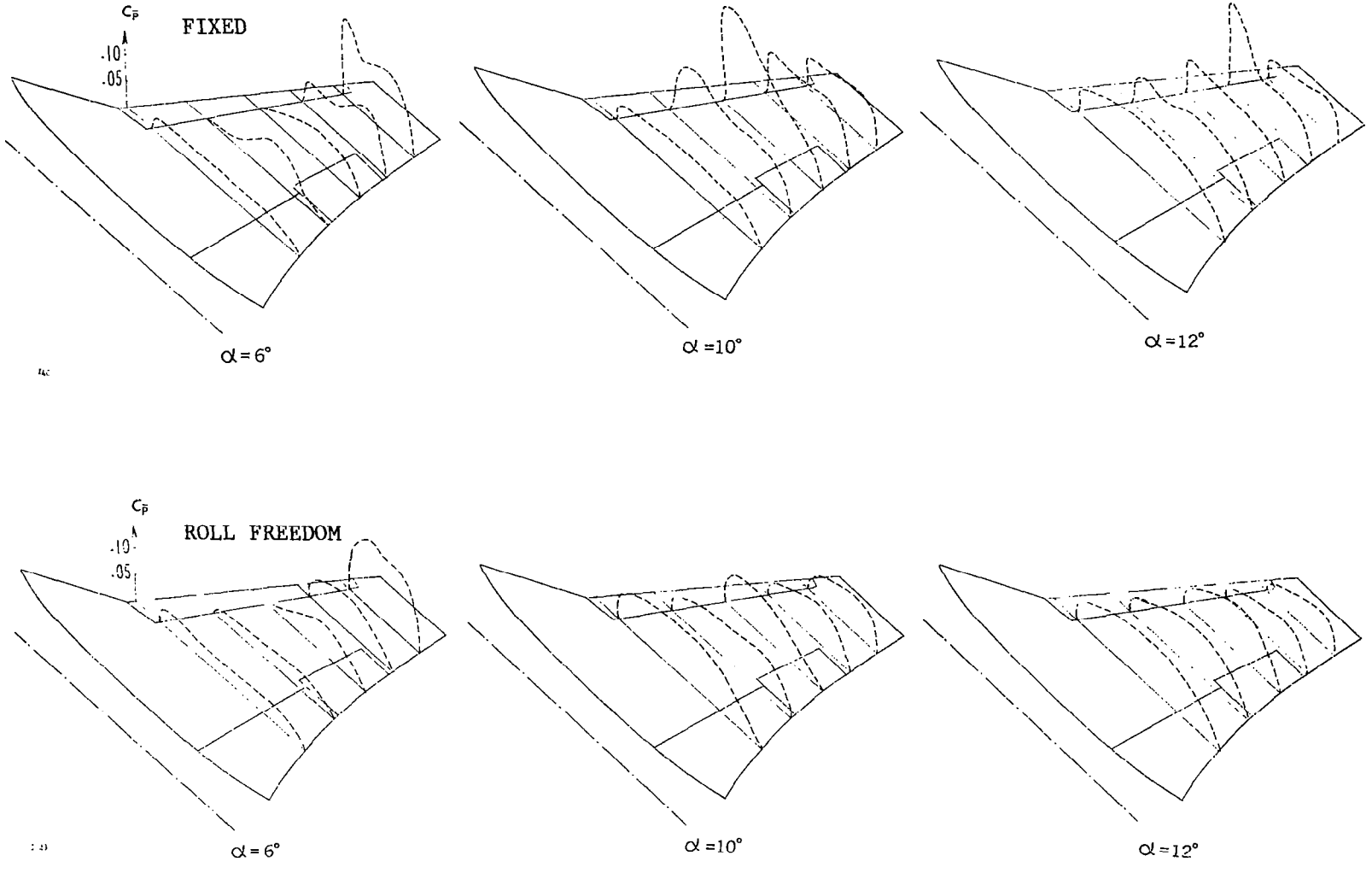

Figure 30. Comparison of Dynamic Pressure Coefficient Distributions for the Fixed Model (top) and the Oscillating Model - Configuration 9, β = -8°, M = .925, δ_n/δ_f = 0°/0°, δ_h = 0°, α^* = 10°

reduced shock strength, or unstable shock location, or most possibly that the shock was not located precisely over the pressure transducer. Similar phenomenon may be observed in Phase I, Run 39 data at α = 8 degrees (Figure 28) and Phase I, Run 41 data at α = 10 degrees (Figure 29).

Referring to Figure 27, corresponding to the model tested without tip-mounted missiles, the substantial differences in the shock line location between Phases I and II at α = 6 degrees indicated the sensitivity of shock location to minor variations in test conditions. The lack of the tip-mounted missiles, and their trailing vortex flow, seemed to aggravate the situation and make the shock location and the resulting flow pattern less stable, as compared to the cases with tip-mounted missiles.

Comparison of power spectral density data for fixed and flexibly-supported models (Run 8, Phase I vs Run 5, Phase II) will be presented in next section.

3.5 The Development of Flow Separation Bubble on the Scale Model with Sideslip

For the purpose of detecting a special trend in separation bubble development on the wing surface, a number of rms pressure coefficient distribution ($C_{\bar{p}}$) data were examined. Attention was directed toward the pressure data on the right wing upper surface when the model had a positive sideslip (β = 8 degrees). For those runs, the right wing was on the windward side. The runs under study and the test conditions are tabulated below:

Run No.	Run 10 Phase I	Run 28 Phase I	Run 38 Phase I	Run 6 Phase II
Configuration	2	6	8	2
δ_n / δ_f	5°/12°	5°/12°	0°/0°	5°/ 0°
δ_a	0°/0°	0°/0°	0°/0°	0°/0°
δ_h	0°	0°	0°	0°
β	8°	8°	8°	8°
M	.929	.927	.927	.926
R_N, /m	7.441×10^6	7.379×10^6	11.51×10^6	7.382×10^6
P_o, KN/m^2	30.35	30.21	47.83	29.90
P_T, KN/m^2	52.96	52.62	83.37	52.05
Q, KN/m^2	18.32	18.17	28.80	17.96

In the four runs listed above, Run 10, Phase I and Run 6, Phase II were conducted with the wing-tip missiles installed. The tip missiles were off for the remaining two runs. The rms pressure coefficient distributions ($C_{\bar{p}}$) for the four runs with variable α are plotted in Figures 31 to 34. It may be pointed out that $C_{\bar{p}}$ is identical to $\langle p \rangle/q$ as defined by Mabey in Reference 4. In dealing with the general cases of the separated flow, Mabey noted that close to the reattachment point of a separation bubble, a maximum value of $\langle p \rangle/q$ or $C_{\bar{p}}$ between 0.04 and 0.10 was usually recorded. For the F-5A data being processed, $C_{\bar{p}}$ was in the order of 0.01 or less in the unseparated flow region. When the local flow became separated, a substantial increase of $C_{\bar{p}}$ value was always observed. The $C_{\bar{p}}$ value in the separated flow region of the wing may vary within the range of 0.04 to 0.16. In isolated cases, the local $C_{\bar{p}}$ value was as high as 0.28 which identified a strong local shock, see, for instance, Figure 26, $\alpha = 10°$. On the horizontal tail, the maximum $C_{\bar{p}}$ value was substantially higher than 0.16. It was found convenient to use the above-mentioned $C_{\bar{p}}$ values recorded on the wing surface to trace the development of a separation bubble and the region of the separated flow. The validity of this approach was confirmed by comparison of the flow separation data developed in a F-5A flight test program using tufts on the wing surface.

In Figure 31, five plots of the $C_{\bar{p}}$ coefficients for Run 10, Phase II are presented corresponding to $\alpha = 4$ degrees, 6 degrees, 8 degrees, 10 degrees, 12 degrees. At $\alpha = 4$ degrees, the single high value of $C_{\bar{p}}$ at 72.8 percent semi-span and 75 percent chordwise position (transducer No. 8, see Figure 3) indicated the appearance of a shock-induced separation bubble at that location. Judging from the proximity of the location to the trailing edge, and considering the subsequent flow developments, the separation bubble seemed to extend toward the trailing edge and no reattachment took place on the wing surface. The separation bubble remained at the same general location at $\alpha = 6$ degrees but the $C_{\bar{p}}$ value was further increased to 0.079. At $\alpha = 8$ degrees, the separated flow region was extended inboard toward the aileron and the trailing edge flap, with additional chordwise expansion toward the leading edge at $\alpha = 10$ degrees. Up to $\alpha = 10$ degrees, the flow at 85 percent semi-span seemed to remain completely unseparated. When α reached 12 degrees, a major expansion of the separation bubble took place. Except for a limited

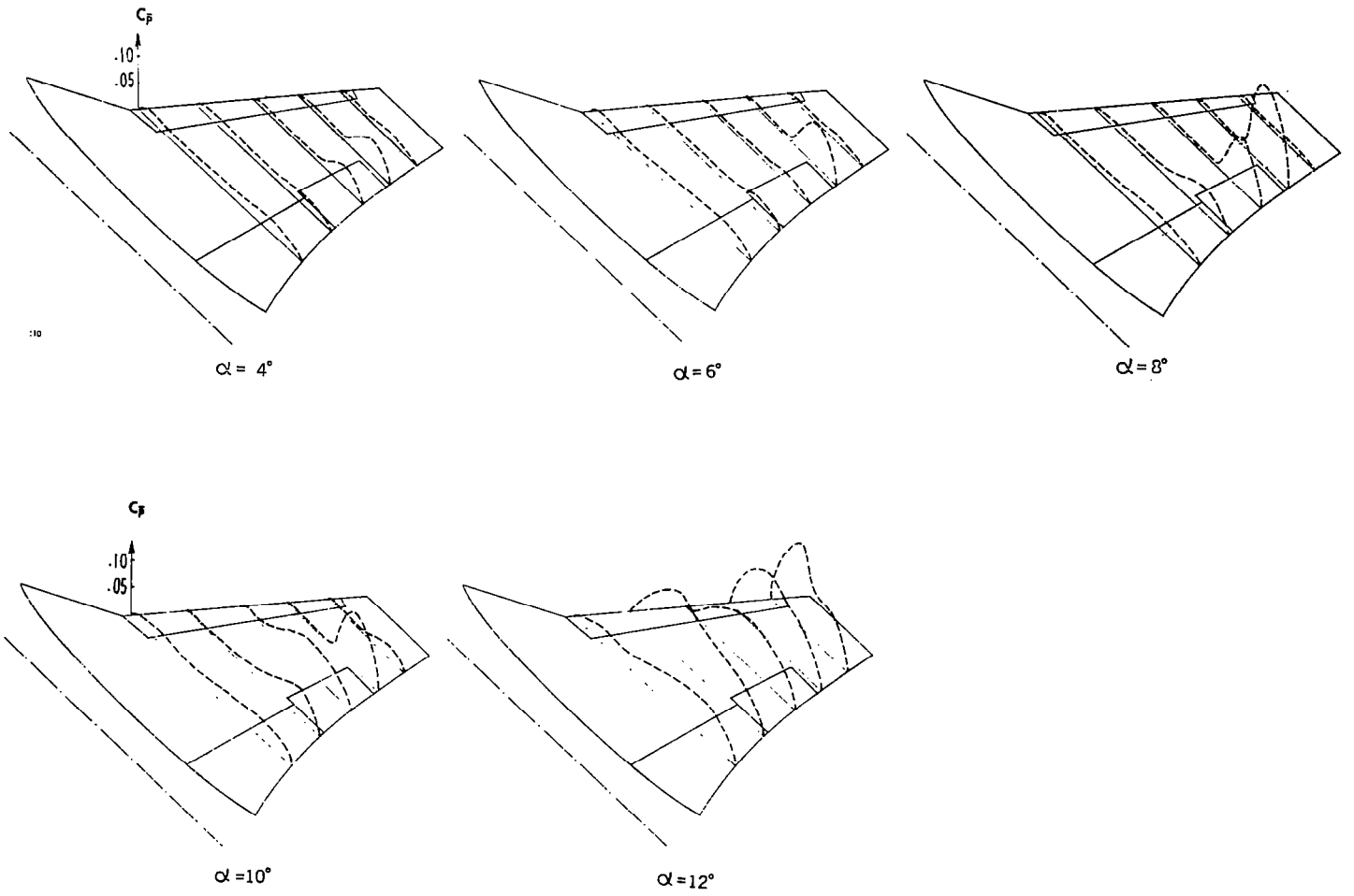

Figure 31. Dynamic Pressure Coefficient Distributions of the F-5A Scale Model, Run 10, Phase I - Configuration 2, β = 8°, M = .929, δ_n/δ_f = 5°/12°, δ_h = 0°

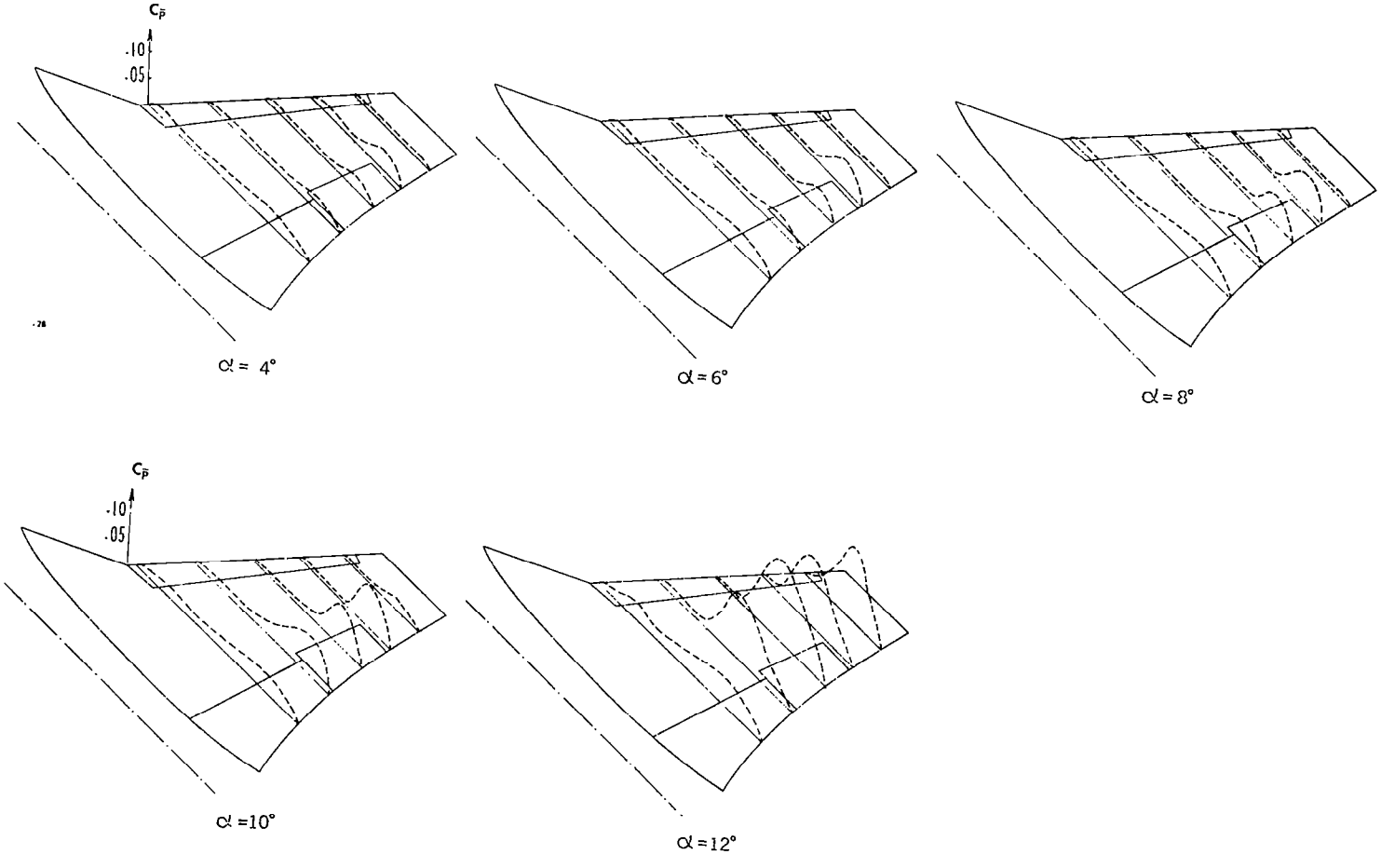

Figure 32. Dynamic Pressure Coefficient Distributions of the F-5A Scale Model, Run 28, Phase I - Configuration 6, β = 8°, M = .927, δ_n/δ_f = 5°/12°, δ_h = 0°, Missiles Off

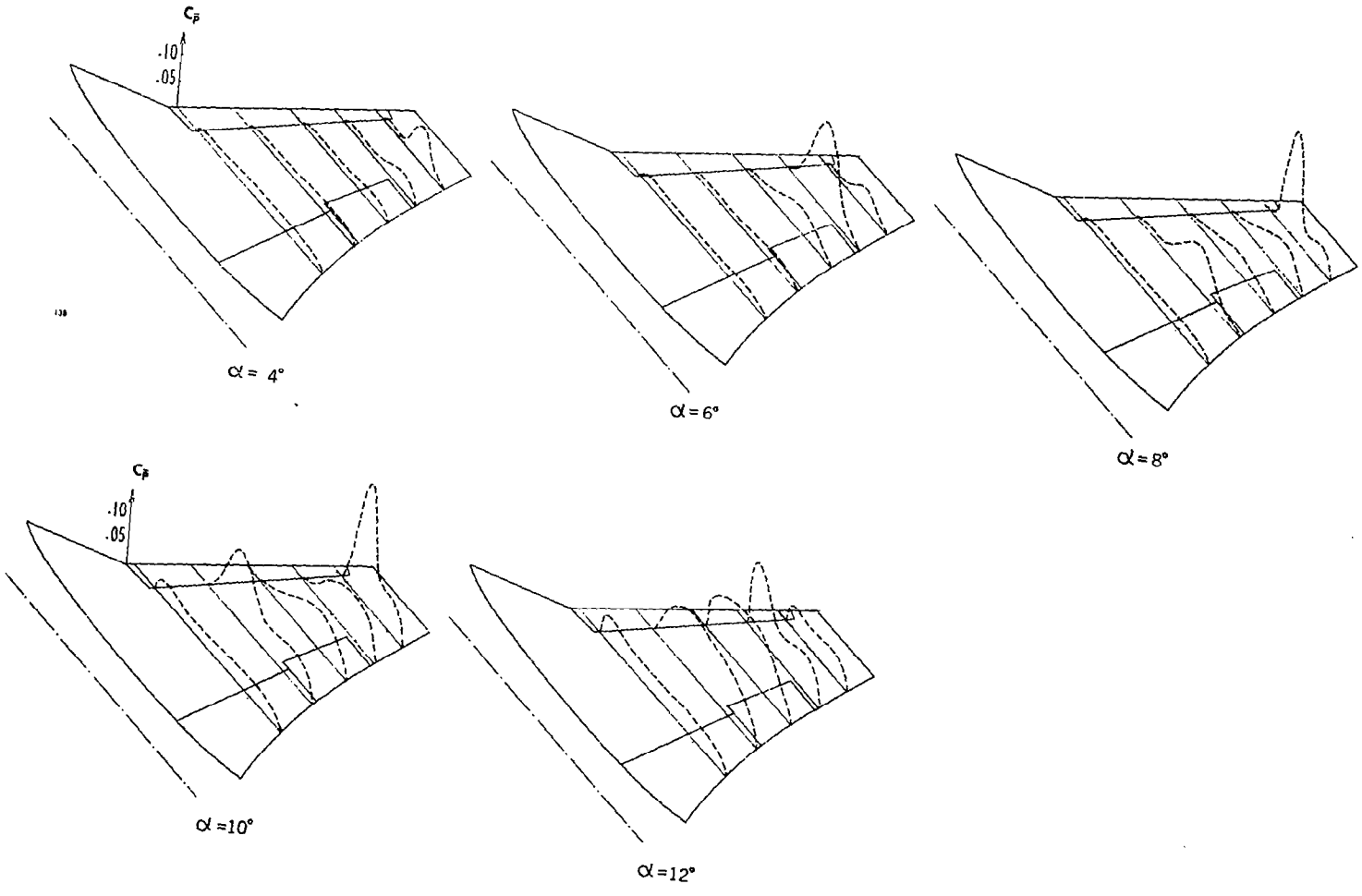

Figure 33. Dynamic Pressure Coefficient Distributions of the F-5A Scale Model, Run 38, Phase I– Configuration 8, $\beta = 8°$, M = .927, $\delta_n/\delta_f = 0°/0°$, $\delta_h = 0°$, Missiles Off

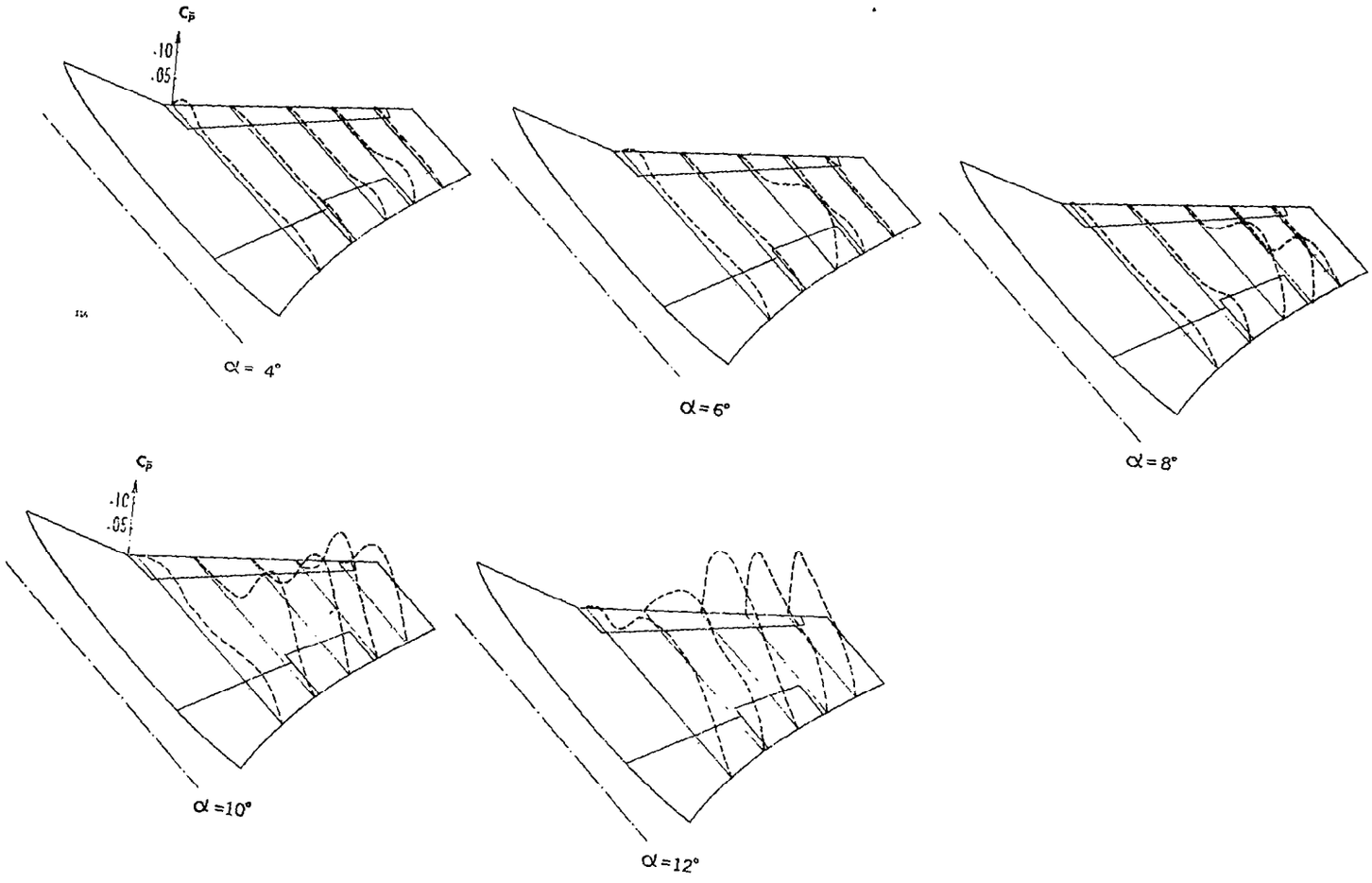

Figure 34. Dynamic Pressure Coefficient Distributions of the F-5A Scale Model, Run 6, Phase II - Configuration 2, $\beta = 8°$, $M = .926$, $\delta_n/\delta_f = 5°/0°$, $\delta_h = 0°$

area on the extended leading edge flap, the flow on the top surface of the right wing became completely separated. In visualizing the development of the separated flow on the windward side of the semi-span in a sideslip condition, it may be noted that the slanted air stream flow direction (positive β for the right wing) seemed to create a favorable flow condition in its wing-tip region to retard the local flow separation. Similar behavior may be noted, with individual variations, in the other three runs where the sideslip angle was also 8 degrees (Figures 32 to 34). For Phase I, Run 28 (Figure 32), the separated flow development was very similar to Phase I, Run 10 described above. For Phase I, Run 38 (Figure 33), both leading edge and trailing edge flaps were retracted, the location of the initial flow separation seemed to be closer to the wing-tip as reflected in the $C_{\bar{p}}$ distribution at α=4 degrees. The location of the maximum $C_{\bar{p}}$ coefficient moved spanwise alternatively inboard and outboard as the angle-of-attack was increased. In comparing with Figure 32, where the leading and trailing edge flaps were extended (δ_n/δ_f=5°/12°), it seemed that the extended trailing edge flaps tended to keep the shock induced flow separation region toward the inboard portion of the semi-span at a moderate angle-of-attack (α = 8°). This can be attributed to the increased camber in the inboard portion for the extended flap cases. The initial development of flow separation for Phase II, Run 6 (Figure 34) was very similar to those of Phase I, Run 10 (Figure 31). This was as it should be since both runs featured the same model configuration except for the support flexibility.

The dynamic pressure data for the leeward side of the wing semispan for the model with a sideslip were examined. In all cases, flow separation seemed to originate at the wing-tip region. This was in contrast to the windward side, where flow separation was developed initially at a location other than the wing-tip region. Correlation study of pressure data under sideslip conditions will be presented in the next section.

3.6 Determination of the System Aerodynamic Damping Using the Randomdec Program

In the tests carried out during Phase II, as described previously in subsection 3.2, the major model motion was due to support flexibility which allowed substantial Dutch Roll type oscillations known to be important in aircraft buffet. As the angle-of-attack setting approached the critical angle-of-attack α^*, the model started to oscillate with substantial amplitudes along the roll axis, with correspondingly lesser amplitudes in yaw and sideslip. The major frequency of the oscillation was approximately 4.0 Hz. On rare occasions, the model oscillated steadily and continuously throughout the recording period, such as Run 26 at $\alpha = \alpha^* = 10°$. The real time data of pitch, yaw, and roll oscillations are given in Figure 35. Under most test conditions, the motion was random. The oscillations started in a random manner, reached a maximum amplitude and then died out. Typical real time data of roll and yaw oscillations, obtained in Run 5, Phase II, at $\alpha = \alpha^* = 10°$ are shown in Figure 36a. In Figure 36b, the data in a shorter time segment (between the two arrowheads shown in Figure 35a) are repeated with an enlarged time scale. Based on the real time data, it was clear that the yaw angle oscillations had the same major frequency with a slight phase shift from the roll oscillations. The yaw oscillation amplitude was comparatively low. It was believed that the aerodynamic damping of the model changed abruptly at the critical angle-of-attack α^* which affected the oscillation amplitudes. The Randomdec program was chosen to determine the system aerodynamic damping based on the measured roll oscillations.

The Randomdec program has been used extensively in determining the damping of a major response mode under random excitation such as that expected in transonic wind tunnel testing. For multiple-mode responses, proper filter techniques are used to enhance the processing of the primary mode data. To obtain a Randomdec signature, a number of data segments are collected, each having the same initial amplitude (or other characteristics, such as the normalized initial peak, etc.). Ensemble averaging is performed on the accumulated data. If the system is linear and the excitation random and stationary, the ensemble average then converges to the transient response of the system, due to the selected set of initial conditions.

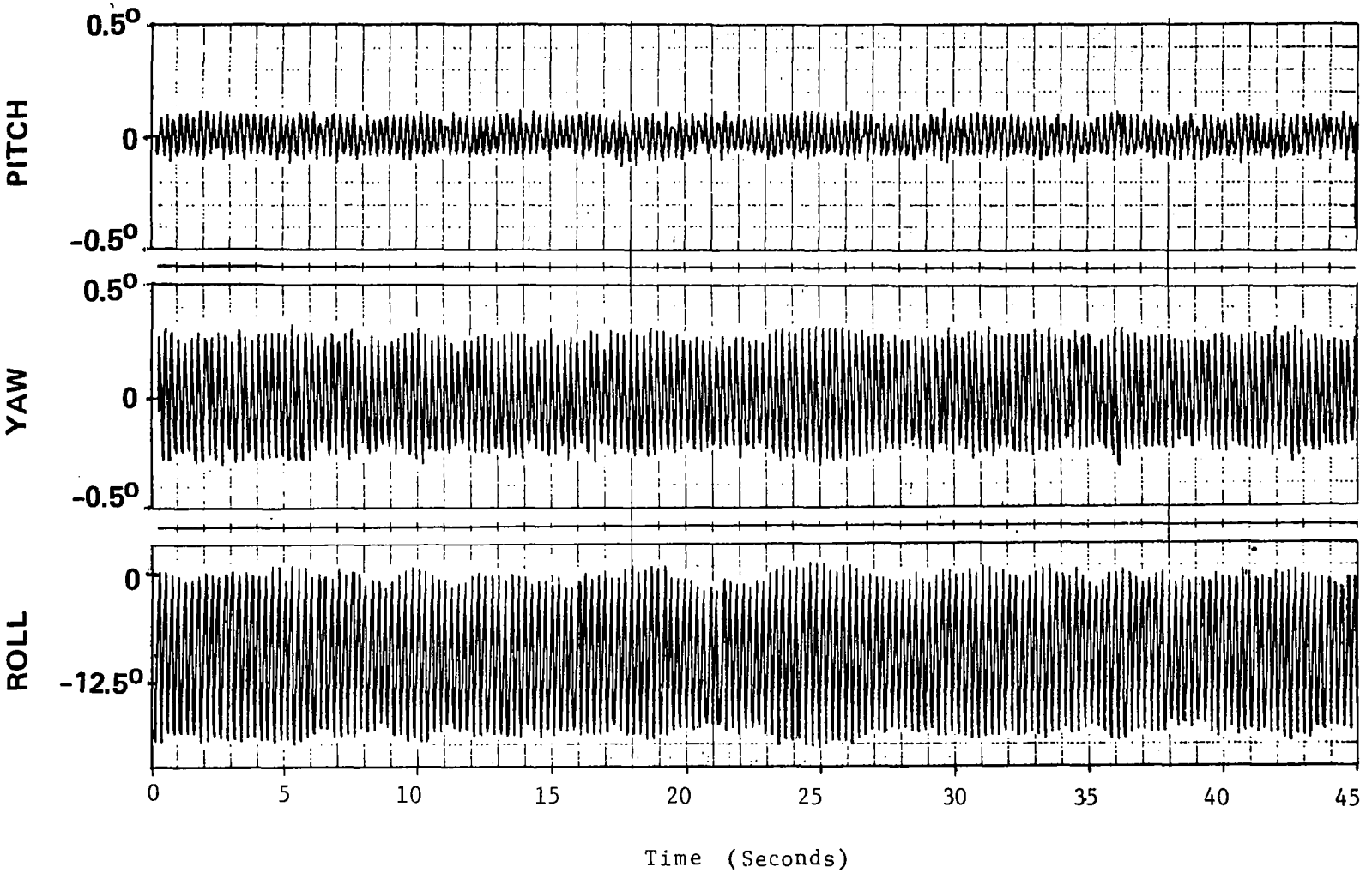

Figure 35. Time Histories of F-5A Model Pitch Angle, Yaw Angle and Roll Angle Recorded During Run 26, Phase II, $\alpha = 10°$, $\beta = 8°$, $M = 0.925$, $\delta_n/\delta_f = 0°/0°$, $\delta_h = -10°$.

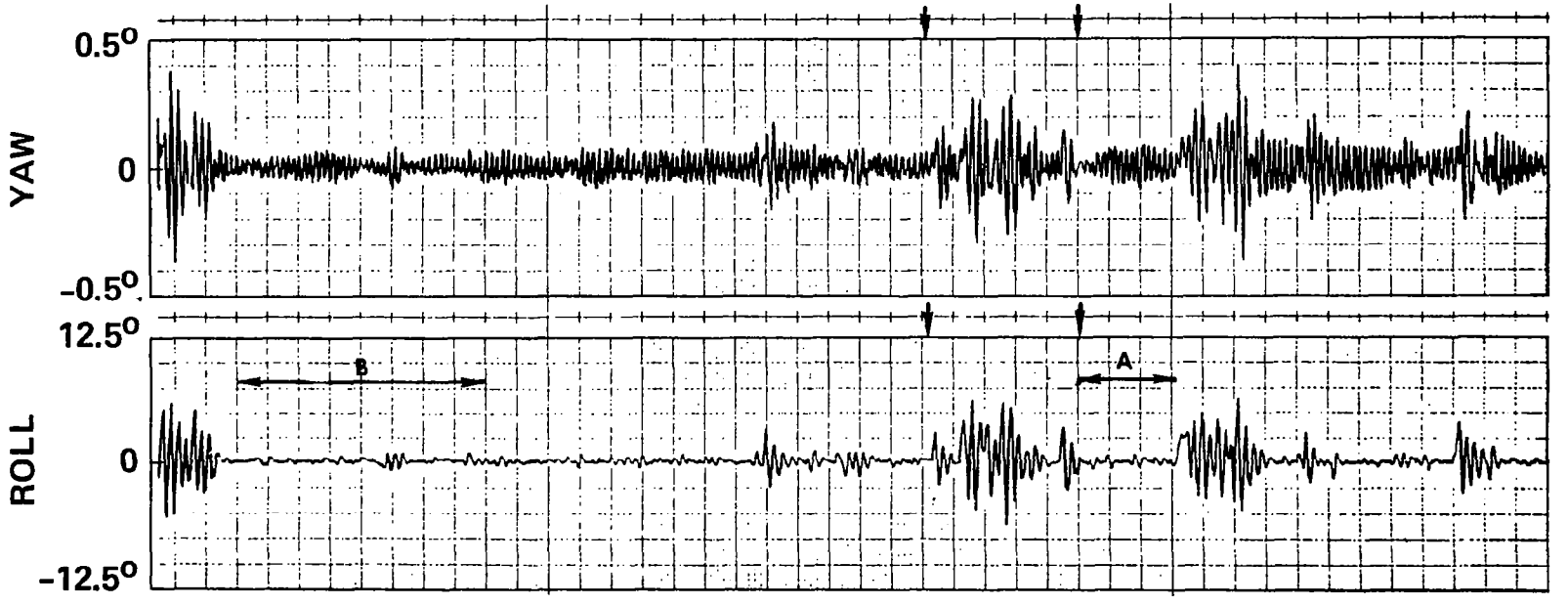

Figure 36a. Time Histories of F-5A Model Yaw Angle and Roll Angle Recorded During Run 5, Phase II, $\alpha = 10°$, $\beta = 0°$, $M = 0.925$, $\delta_n/\delta_f = 5°/12°$, $\delta_h = 0°$. (Timing marks appeared on top trace at one second intervals)

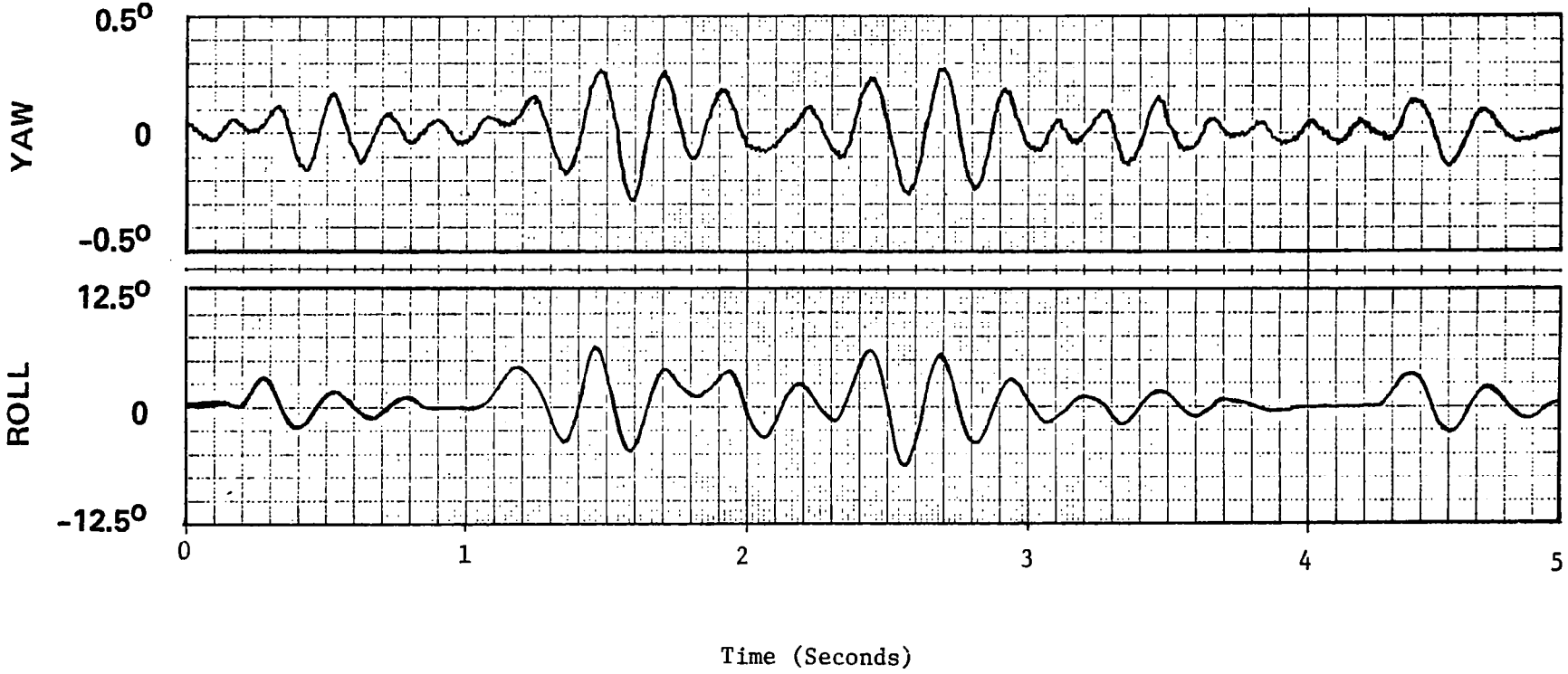

36b. Time Histories of F-5A Model Yaw Angle and Roll Angle Recorded During Run 5, Phase II, $\alpha = 10°$, $\beta = 0°$, $M = 0.925$, $\delta_n/\delta_f = 5°/12°$, $\delta_h = 0°$

Two sets of measured roll data were digitized to provide the input to the Randomdec program. For Run 26, $\alpha = \alpha^* = 10°$, the model oscillated steadily and continuously throughout the recording period. For Run 5, $\alpha = \alpha^* = 10°$, the motion was highly random. The measured roll data were digitized covering the complete recording period with a sampling rate of 521 samples/sec. A low pass analog filter with a cutoff frequency of 220 Hz was used during the digitizing process.

Run 26 of Phase II test was conducted in test model configuration 11, $\delta_n/\delta_f = 0°/0°$, $\delta_h = -10°$, $\delta_a = 0°/0°$, $\beta = 8°$, Sidewinder missiles at wing-tips, M = 0.925, and $\alpha^* = 10°$. Since the steady roll motion of Run 26 had only one major frequency of oscillations at approximately 4.0 Hz, no special filter technique was required to obtain the Randomdec signature. Figure 37 shows the Randomdec signature obtained using a data span of 34 seconds (or 17,775 samples) with 140 ensemble averages. The damping ratio (structural damping plus aerodynamic damping) was 0.000816. The natural frequency was 3.976 Hz. Based on the calibration curves of the hydraulic damper with the F-5A scale model installed (Figure 6), the damping ratio of the model with air off is 0.012. As a result, the aerodynamic damping ratio for Run 26 at $\alpha = 10°$ was estimated to be -.0112.

For Run 5 at $\alpha = \alpha^* = 10°$, the lengths of the selected time segments for various phases (the initial, high-amplitude, termination phases) were rather short and the statistical errors are expected to be very high. For most time segments, difficulties were encountered in obtaining a meaningful Randomdec signature which might represent a free vibration decay curve even though the roll signal was bandpass filtered before determining the Randomdec signature. It was believed to be caused by the short time span used. However, a meaningful signature was acquired for one specific segment (as indicated by letter A in Figure 36a) with low roll amplitudes. The result is given in Figure 38. For segment A, a total number of 1626 samples (3.1 seconds) were used and 11 ensemble averages were made. The natural frequency obtained was 3.48 Hz and the damping ratio was 0.0176. The corresponding structural damping ratio was 0.0575 for Run 5 and the aerodynamic damping ratio was thus -.0399. A

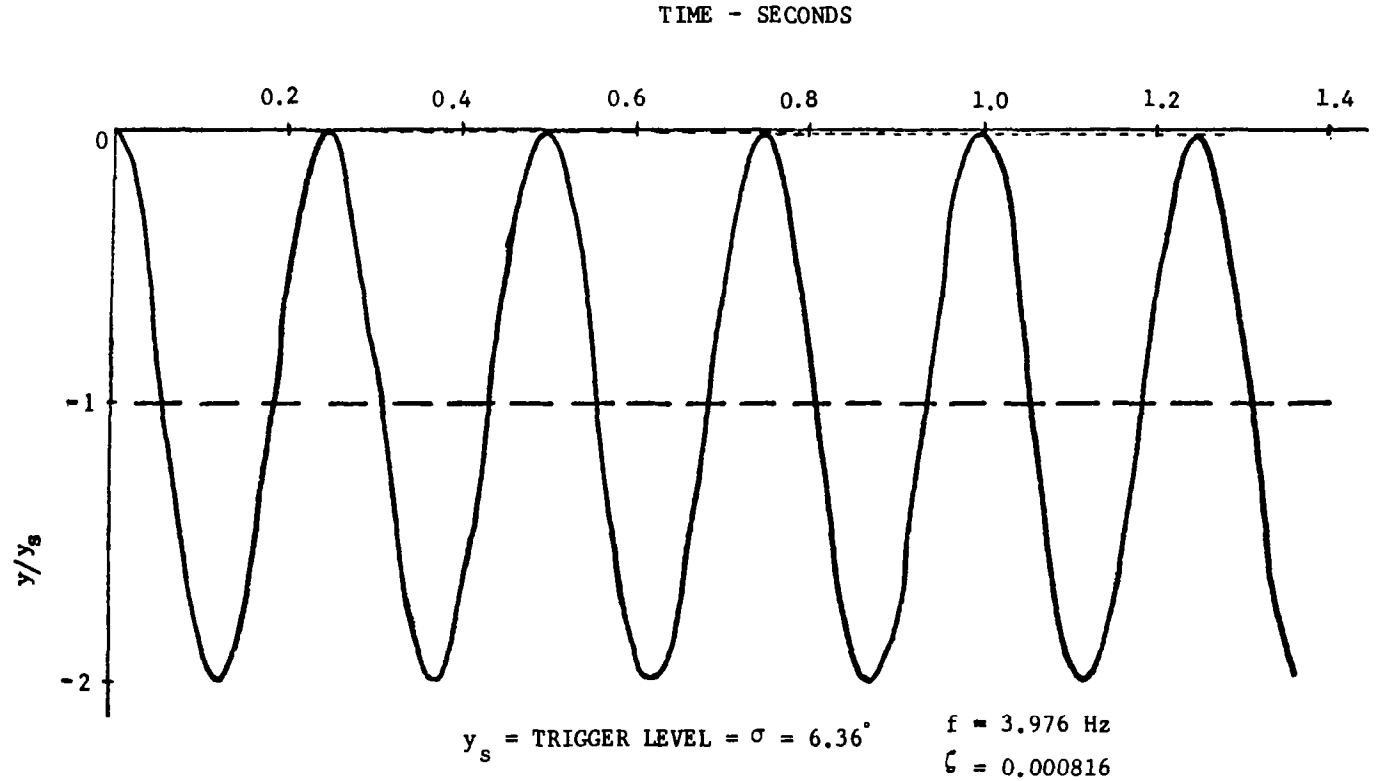

Figure 37. Randomdec Signature of Roll Oscillations of the F-5A Scale Model, Run 26, Phase II, $\alpha = 10°$, $\beta = 8°$, $M = 0.925$, $\delta_n/\delta_f = 0°/0°$, $\delta_h = -10°$.

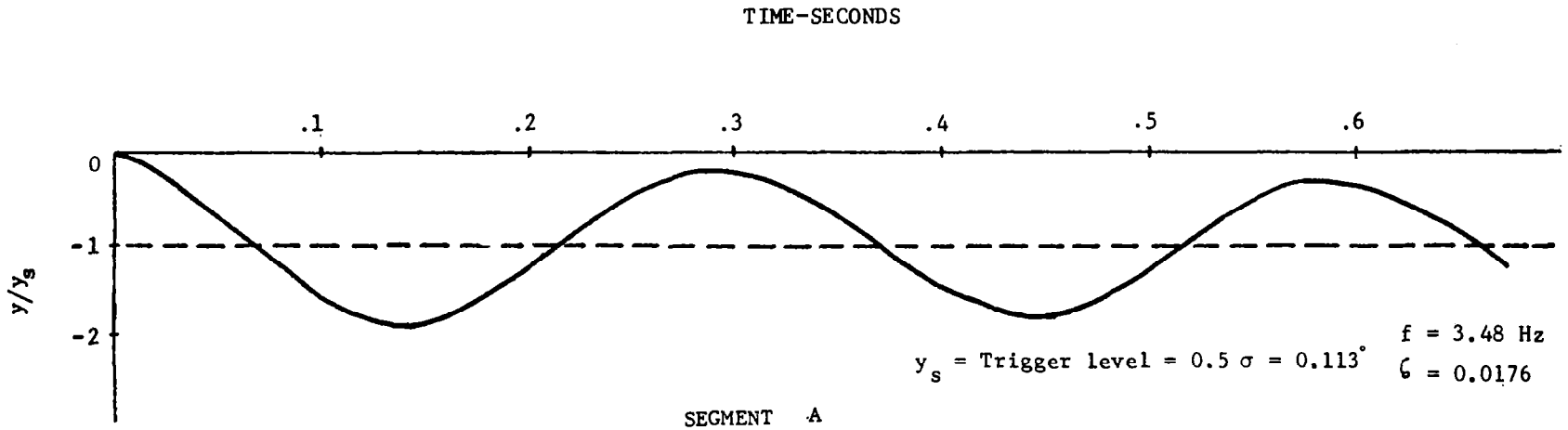

Figure 38. Randomdec Signature of Roll Oscillations of the F-5A Scale Model, Run 5, Phase II, $\alpha = 10°$, $\beta = 0°$, M = 0.925, $\delta_n/\delta_f = 5°/12°$, $\delta_h = 0°$.

bandpass digital filter was applied to the roll signal before determining the Randomdec signature. The cutoff frequencies of the bandpass filter were 2.5 Hz and 3.8 Hz and the difference between a cutoff frequency and the frequency where the filter has attenuated approximately 6 dB was 0.8 Hz. The above work experience indicated that the Randomdec technique for damping evaluation is applicable to test cases with a stable primary mode of excitation. For the case of purely random excitation of the scale model under buffet, the success of the technique is dependent on the relative amplitude of the primary mode of excitation, the frequency of occurrences of the major excitation mode, the data time span, and maybe other contributing factors.

3.7 Aerodynamic Hysteresis and the Limit Cycle Concept

In Phase II, two types of model oscillations along the roll axis were observed. In one type, the oscillation was approximately a constant-amplitude sinusoidal motion. The corresponding local pressure data also featured a periodic pattern, even though highly nonlinear with respect to the model motion. In a second type, the oscillation was essentially sinusoidal, but the amplitude of the oscillation changed from cycle to cycle. The roll motion existed in a pattern of irregular bursts, and interspersed by periods of near zero oscillation. The first type of oscillation was named the cyclic type; a typical case was Run 26, Phase II (illustrated in Fig-

(Figure 35), with the following test conditions:

$\delta_n/\delta_f = 0°/0°$, $\delta_h = -10°$

$\delta_a = 0°/0°$

$M = 0.925$, $Q = 17.95$ KN/m^2 (375.0 psf)

$R_N = 7.382 \times 10^6$/m (2.25×10^6/ft), or 2.48×10^6 based on the mean aerodynamic chord of the model

$\alpha = \alpha^* = 10°$, $\beta = 8°$, $c/c_{cr} = 0.012$

The corresponding run in Phase I is Run 51, which had identical model configuration as Run 26, Phase II shown above. It is noted that the Phase I runs were made with a standard sting with minimum roll flexibility, as against the case of Phase II where a special sting with substantial roll flexibility was used. The Reynolds number of Run 51, Phase I was 7.38×10^6.

The second type of oscillation was named the random response type. A typical case was Run 5, Phase II, (illustrated in Figure 36), with the test conditions as shown below:

$\delta_n/\delta_f = 5°/12°$, $\delta_h = 0°$

$\delta_a = 0°/0°$

$M = 0.925$, $Q = 18.20$ KN/m^2 (377.7 psf)

$R_N = 7.382 \times 10^6$/m (2.25×10^6/ft), or 2.48×10^6 based on the mean aerodynamic chord of the model

$\alpha = \alpha^* = 10°$, $\beta = 0°$, $c/c_{cr} = 0.057$

The corresponding Phase I is Run 8, of which the Reynolds number was 7.38×10^6.

The real time roll oscillation and the corresponding fluctuating pressure data are further illustrated in Figure 39 for Run 26, Phase II. In Figure 39, P_3, P_4, P_5 represent the local fluctuating pressures at 85% semi-span of the right wing top surface, with transducers located at 40%, 60% and 75% chordwise positions. On top of the oscillograph plots, the local

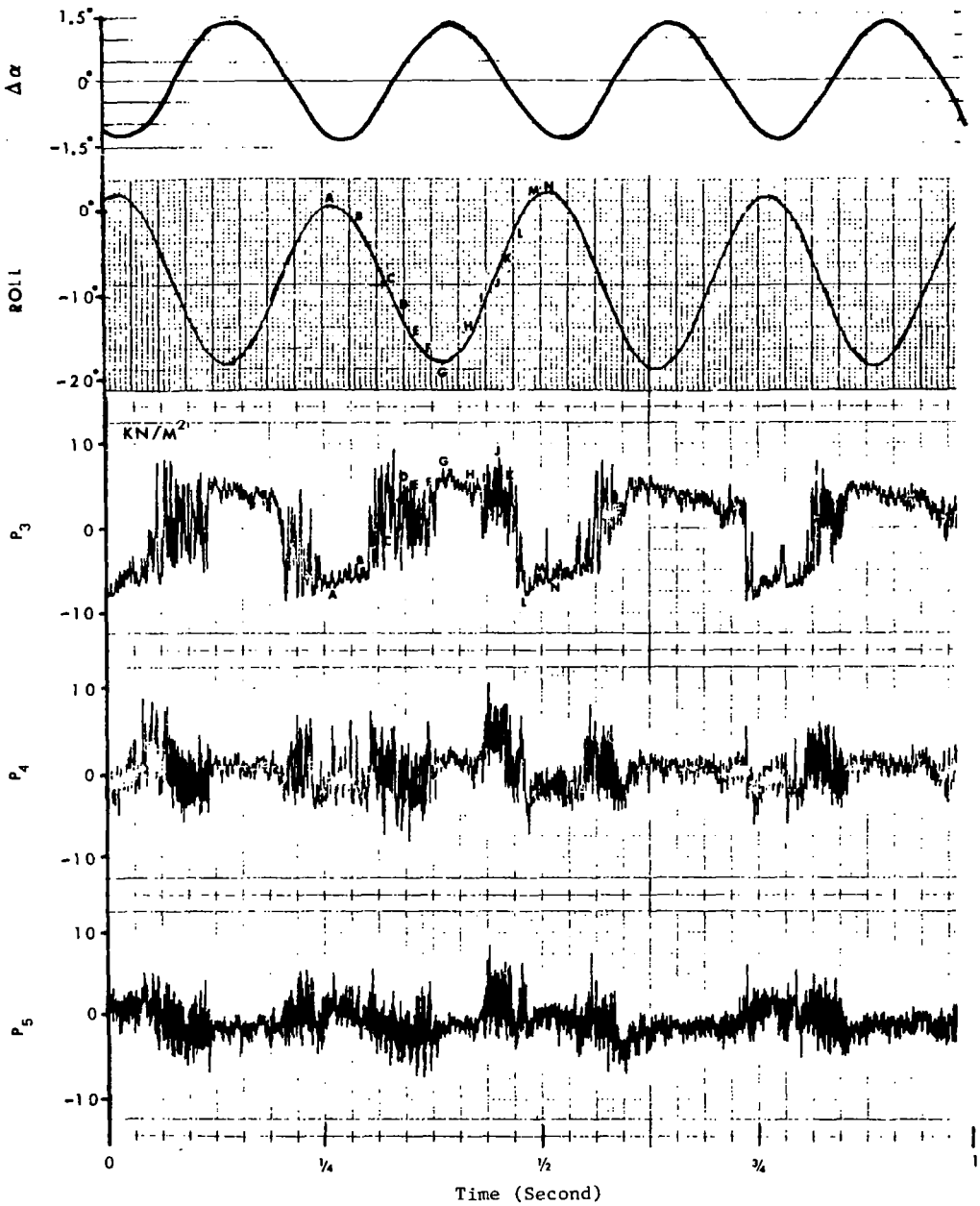

Figure 39. Real Time Data of the Roll Oscillations and the Corresponding Local Pressures of Transducer Numbers 3, 4, 5 of the F-5A Scale Model, Run 26, Phase II, $\alpha = 10°$, $\beta = 8°$, $M = 0.925$, $\delta_n/\delta_f = 0°/0°$, $\delta_h = -10°$, $Q = 17.95$ KN/m², $c/c_{cr} = 0.012$.

$\Delta\alpha$ oscillation was presented based on the following:

$$\Delta\alpha = -\varphi \cos \alpha_o \sin \beta + (\varphi y/U) \cos \beta \qquad (1)$$

where φ is the roll oscillation angle, y is the spanwise distance from the roll axis, and U is the tunnel air speed. In examining the fluctuating pressure data vs. the local $\Delta\alpha$ changes, it was apparent that the sudden pressure changes, representing the loss of lift or lift recovery, and the high amplitude oscillations, representing the unstable shock movement during transition from local unseparated flow to flow separation (or vice versa), followed a cyclic pattern which was synchronized with the local $\Delta\alpha$ changes. Specifically, when the local $\Delta\alpha$ was changed from negative to positive, the shock oscillations and the subsequent flow separation tended to lead the $\Delta\alpha$ change. When the $\Delta\alpha$ was changed from positive to negative, the local pressure change (a lift recovery) was usually more clear cut reflecting the momentum of the local flow moving the shock front rearward toward the trailing edge. The detail behavior of the fluctuating pressures and their impact on aircraft wing rock can be best studied together with the static pressure development on the wing surface.

In Figures 40, 41, the chordwise static pressure distribution for Run 51, Phase I and Run 26, Phase II are plotted side by side to illustrate the effect of roll oscillations to local static pressure distributions. Both figures are for 85% semi-span of the right wing. Figure 40 shows the upper surface pressure data corresponding to the nominal angle-of-attack range from 0° to 12°. Figure 41 shows the lower static surface pressure data for selected α's when substantial changes in upper surface pressures took place.

Referring to Figure 40, for Phase I corresponding to a standard rigid sting, the high pressure gradient near the midchord for α = 6°, 8° indicated a shock induced flow separation in the rear semi-chord region. At α = 10°, the shock moved forward and became less distinct. As a result, the pressure

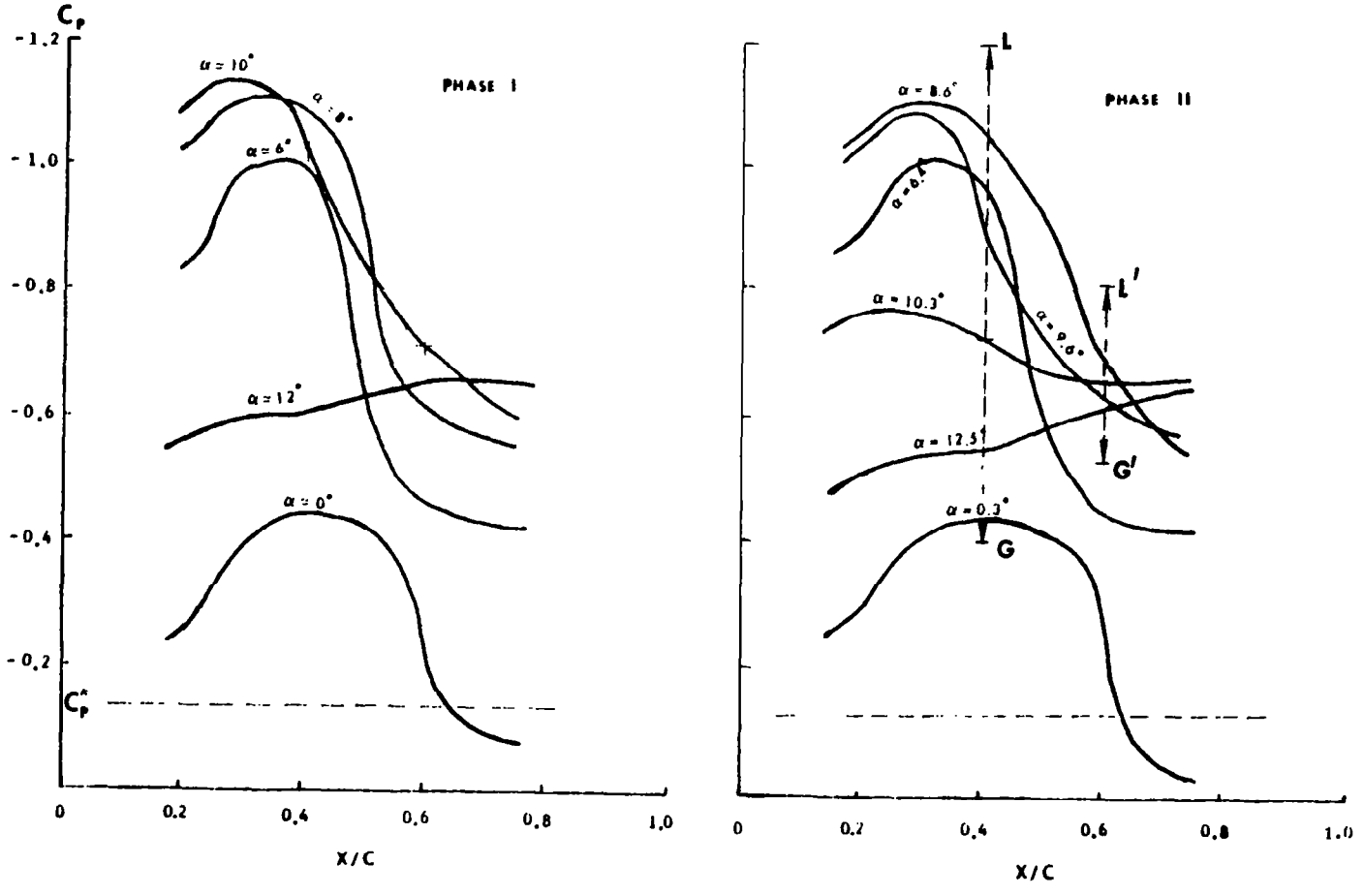

Figure 40. Chordwise Static Pressure Distribution at the Top Surface of 85 Percent Semispan, F-5A Right Wing. The Left Plot is Based on Run 51, Phase I, Data. The Right Plot is Based on Run 26, Phase II, Mean Value Data. GG', LL' Indicated Range of Dynamic Pressure Changes for α Nominal = 10.3°.

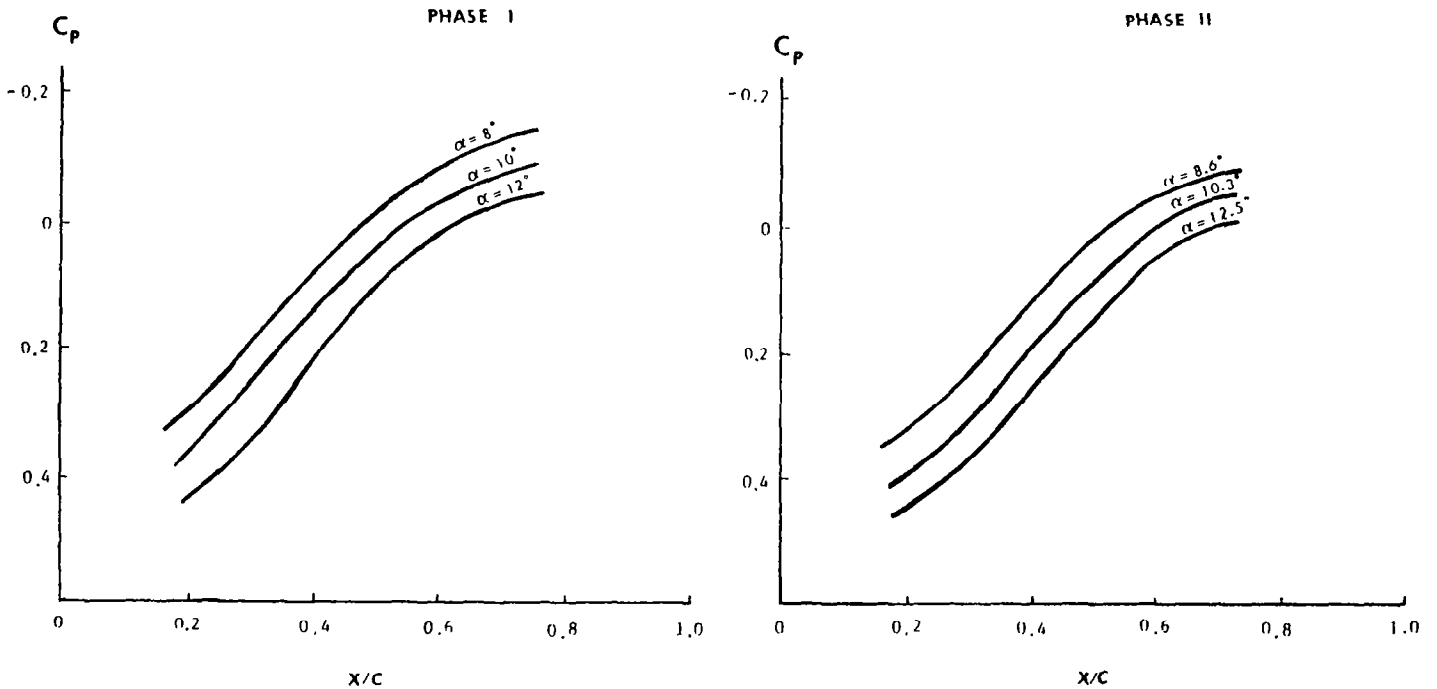

Figure 41. Chordwise Static Pressure Distribution at the Bottom Surface of 85 Percent Semispan, F-5A Right Wing. The Left Plot is Based on Run 51, Phase I, Data. The Right Plot is Based on Run 26, Phase II, Mean Value Data.

gradient was more evenly distributed along the chordwise location. With increasing angle-of-attack, $\alpha = 12°$ reflected a major breakdown of the unseparated flow. At this α, the leading edge induced flow separation caused a substantial loss in lift in the outer semi-span of the wing. (The actual flow breakdown happened at an α slightly greater than 10°.)

The Phase II data of Figure 40 show the corresponding static pressure distribution at 85% semi-span when the model was free to oscillate along the roll axis. The test results indicated the model was near stationary up to $\alpha = 9.6°$. As to be expected, the static pressure data up to this α closely resembled the Phase I data. At $\alpha = \alpha^* = 10.3°$, sustained roll oscillation took place with a roll frequency of approximately 4 Hz. Selected real time response and fluctuating pressure data at this α were shown previously in Figure 39. The ranges GL, G'L' on Figure 40 indicate the extent of the fluctuating pressure changes based on Figure 39 data. Beyond $\alpha = 10.3°$, the roll oscillations had either reduced amplitude, or in some cases, completely disappeared. Correspondingly, the static pressure distribution at 85% semi-span followed a similar pattern to that acquired in Phase I.

Corresponding to the critical α range when drastic pressure redistribution took place on the upper surface of the right wing, the lower surface static pressure data are plotted in Figure 41 for both phases. In examining these data, and the real time fluctuating pressure data of the lower surface, it can be concluded that the lower surface flow was not affected to any appreciable degree by the model oscillation. In other words, no or little interaction between the lower surface pressure distribution and the aircraft oscillatory movements was observed.

In order to investigate the static and dynamic pressure behavior on the left wing (the leeward side for $\beta = 8°$) corresponding to the same test condition (Run 26, Phase II) when sustained roll oscillations took place, the data of Run 27, Phase II for the right wing were examined (Figure 42). Run 27 was performed with identical model and tunnel conditions of Run 26 with the exception that $\beta = -8°$. The use of the leeward side (right) wing pressure data of $\beta = -8°$ to replace the leeward side (left) wing pressure data of $\beta = 8°$ was necessary because of the scant number of pressure transducers installed on the left wing. The above substitution implied the assumption of perfect symmetry of the test model and the wind tunnel along their central sections.

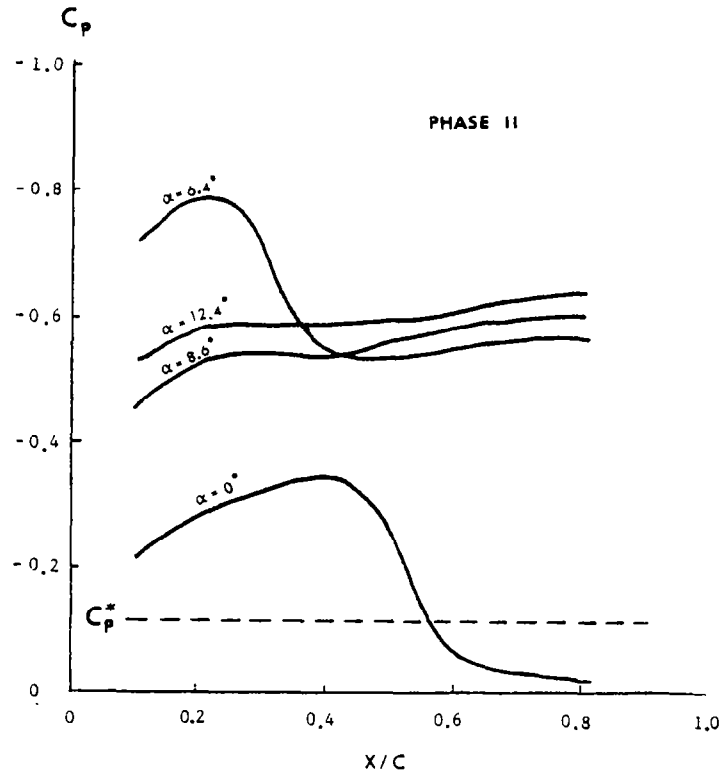

Figure 42. Chordwise Static Pressure Distribution at Top Surface of 85 Percent Semispan, F-5A Right Wing Based on Run 27, Phase II, Mean Value Data, Q = 17.95 KN/m^2.

Referring to Figure 42, and comparing the data with the windward side data of Figure 40, it was seen that prior to complete flow separation, the lift distribution on the leeward side was lower than that on the windward side. This behavior partially contributed to the positive sideslip angle of Run 26 which acted with the wing sweepback to reduce the mean effective angle-of-attack on the leeward (left) side. At higher α, the vortex shedding and wake turbulence effect of the fuselage, and possibly other factors, contributed to the asymmetrical pressure distribution of the wing. In general, complete flow separation appeared earlier on the leeward wing in the upper surface near the wing tip. It was also noted that the static pressure on the leeward wing surface varied in a moderate manner during the roll oscillations at the critical angle-of-attack, $\alpha^* = 10.3°$. The above information indicated that the major contributing factor to wing rock of F-5A with sideslip was due to the pressure fluctuation on the top surface of the windward semi-span.

Combining the mean static pressure data of Figure 40 corresponding to $\alpha = 10.3°$ for Run 26, Phase II, and the extreme fluctuating pressure data taken from points such as G, L as identified in Figure 39, a plot of the range of the chordwise pressure distribution during a roll oscillation cycle is shown in Figure 43.

An examination of Figure 43 indicated dynamic overshoot of the static pressures for both positive and negative $\Delta\alpha$. For negative $\Delta\alpha$, the maximum lift was generated along the chord section higher than those recorded in steady state tests. The maximum lift occurred prior to the time when the minimum $\Delta\alpha$ value was reached, indicating a phase lead of 30° to 45°. Using the convention of Reference 8 for α overshoot, the following may be stated for the wing strip in the neighborhood of 85% semi-span.

$$\Delta\alpha_s = K_a \left[-\varphi \cos \alpha_o \sin \beta + (\dot{\varphi} y/U) \cos \beta\right] \qquad (2)$$

$$K_a \cong 2$$

where K_a is the dynamic overshoot coefficient. The above equation and the pressure data as illustrated in Figures 39 to 43 indicated that the oscillating dynamic loads, if any, were dependent on the amplitude and phase of the

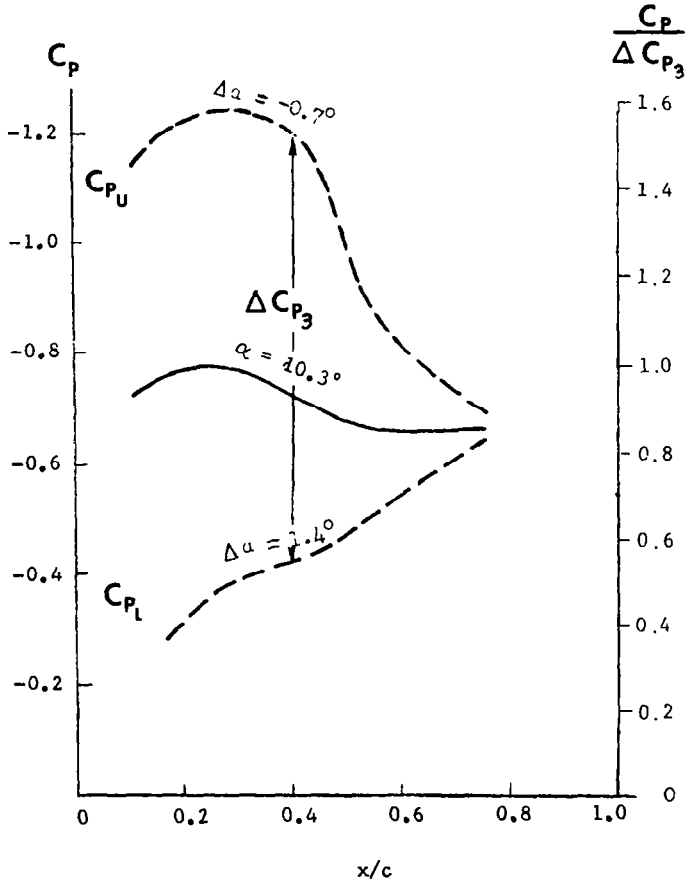

Figure 43. Range of Spanwise Static Pressure Distribution at Top Surface of 85 Percent Semispan, F-5A Right Wing During Simulated Wing Rock Oscillations, Run 26, Phase II, k = .028, Q = 17.95 KN/m^2.

roll oscillations during wing rock. The dynamic loads and the motion thus formed an interacting pair. The existence of limit cycle type oscillations was determined by the energy balance of (1) the input to the aircraft in the form of fluctuating loads caused by motion-induced flow separation, (2) the energy consumed by aerodynamic damping when the aircraft oscillated in roll, possibly with other coupled motions. The energy input to the aircraft, essentially due to the fluctuating pressure loads on the top surface of the right wing for $\beta = 8°$, may be computed based on the C_p data vs the local translatory motion due to the roll oscillation. In Figure 44, the local C_p data for a typical station P_3 are plotted vs the translatory motion h and the local angle of attack $\alpha + \Delta\alpha$. To estimate the work done by the fluctuating forces in one oscillation cycle, the following assumptions are made:

(1) The work was essentially in the form of the fluctuating pressure applied to the top surface of the windward semi-span, and may be represented by the loads on a wing strip with width Δb and located at 85% semi-span. The corresponding local oscillatory motion is $he^{i\omega t} = \varphi y e^{i\omega t}$.

(2) The C_p contour along the chordwise direction was defined by the upper and lower limit values of Figure 43. The fluctuating pressures varied in coordination with each other so that the limit cycle loop as described in Figure 44 for C_{p_3} was followed by all pressures along the chordwise direction. Admittedly, this is a simplified assumption which served only to describe the fluctuating pressure trend.

Applying the above assumptions, the work input per oscillation cycle simulating wing rock is:

$$Wk = \oint C_{p_3} \Delta b \; A \; Q \; dh \tag{3}$$

$$A = \int_o^c \frac{C_{p_\ell} - C_{p_u}}{\Delta C_{p_3}} dx \tag{4}$$

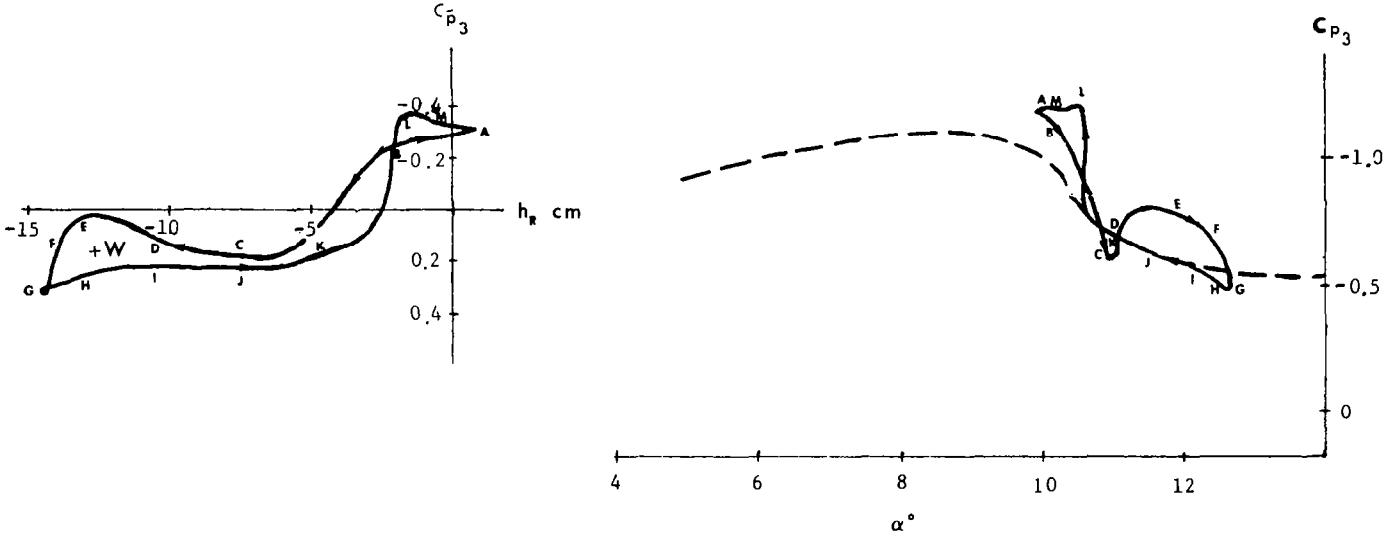

Figure 44. Dynamic and static Pressure Coefficients $C_{\bar{p}}$, C_p vs. Local Translatory Motion h_R and Local Angle-of-Attack α as observed from the Oscillating Model of F-5A, Pressure Transducer No. 3, Run 26, Phase II, $\beta = 8°$, M = 0.925, $\delta_n / \delta_f = 0°/0°$, $Q = 17.95$ KN/m^2, $c/c_{cr} = 0.012$.

where Q is the dynamic pressure, C_{p_ℓ}, C_{p_u} are the lower and upper C_p values as defined in Figure 43. A is the area covered by C_{p_ℓ} and C_{p_u} and integrated from the leading edge to the trailing edge, using the scale on the right hand of the plot. The integral $\oint$ covers the complete oscillation cycle. Based on the scale relations between the model and the aircraft, if the angle of oscillation is the same for the aircraft and the model, the work input per oscillation cycle as shown in equation (3) may be converted to aircraft scale as follows:

$$Wk_{aircraft} = L^3 \times (Q_{aircraft}/Q_{model}) \times Wk_{model}$$

where L = 7 is the model linear scale factor. In the following, all the data are referred to the scale model results.

The energy consumed by aerodynamic damping, and in the case of the test model, the additional mechanical damping built into the support system, are:

$$E = \oint (g_R M_R \omega_R - L_p) \dot{\varphi} \, d\varphi \qquad (5)$$

$$L_p = C_{\ell_p} Q S b^2/2U$$

where M_R is the modal mass in roll, g_R is the mechanical damping coefficient, ω_R is the circular frequency, φ is the roll oscillation amplitude, C_{ℓ_p} is the roll damping coefficient, S is the wing surface area, b is the aircraft wing span and U is the free-stream velocity. The energy balance condition for constant amplitude wing rock oscillation is then:

$$\oint C_{p_3} \Delta b \, AQ \, dh = \oint (g_R M_R \omega_R - L_p) \dot{\varphi} \, d\varphi \qquad (6)$$

In the above equation, the value Δb, or the effective width of the wing tip area with significant fluctuating pressures to supply work to the limit cycle, is treated as a parameter. This parameter is determined by the energy balance condition. The numerical values of the parameters used to calculate the energy balance condition for Run 26, Phase II, $\alpha = \alpha^* = 10°$ are shown below.

$M_R = 0.00437 \ m^2\text{-kg}$, $g_R = 2 \ c/c_{cr} = 0.024$

ω_R = 25.13 rad/sec , Q = 17.95 KN/m^2

S = 0.3244 m^2 , b = 1.1 m

U = 299 m/sec , c_{ℓ_p} = -0.135

A = 0.1076 m , $\oint C_{p_3}\, dh$ = 0.0163 m

φ_{max} = 9° , $\oint \dot{\varphi}\, d\varphi = \pi \varphi_{max}^2\, \omega_R$ = 2.17 sec^{-1}

Based on the above data, the following estimate of energy balance is reached:

E = 6.159 m-N/cycle

(of which 43.5% is due to mechanical damping, 56.5% is due to aerodynamic damping

Wk = 0.3445 Δb m-N/cycle

$\Delta b = 0.35 \times (\frac{b}{2})$ = 0.1923 m

The real time roll oscillation and the fluctuating pressure data of Run 5, Phase II are illustrated in Figure 45. The approximate $\Delta\alpha$ data due to the local downwash and upwash strokes are generated and plotted on the top of the figure. P_1, P_3, P_4, P_5 were located at 85% semispan of the right wing top surface, and at 10%, 40%, 60%, and 75% chordwise positions respectively. Run 5 was conducted with zero β. The roll oscillation amplitude was substantially lower than the corresponding value of Run 26, Phase II (see Figure 39), partially because of the higher mechanical damping set for the support system. The oscillations were irregular and intermittent. In examining Figure 45 data, it was noted that the flow at P_1 was unseparated for the majority of the time, with intermittent lift losses which were synchronized with $\Delta\alpha$ changes. The continuous pressure fluctuations at P_3, P_4, P_5 indicated a separated flow mostly induced by a shock located somewhere between P_1 and P_3. The lift losses at P_1, i.e., sudden pressure increases, appeared when $\Delta\alpha \cong 0$ and $\dot{\alpha}$ = +, a condition inducing leading edge stall and local flow separation. The lift losses at $\Delta\alpha \cong 0$ indicated a phase lead of the flow separation caused by the dynamic

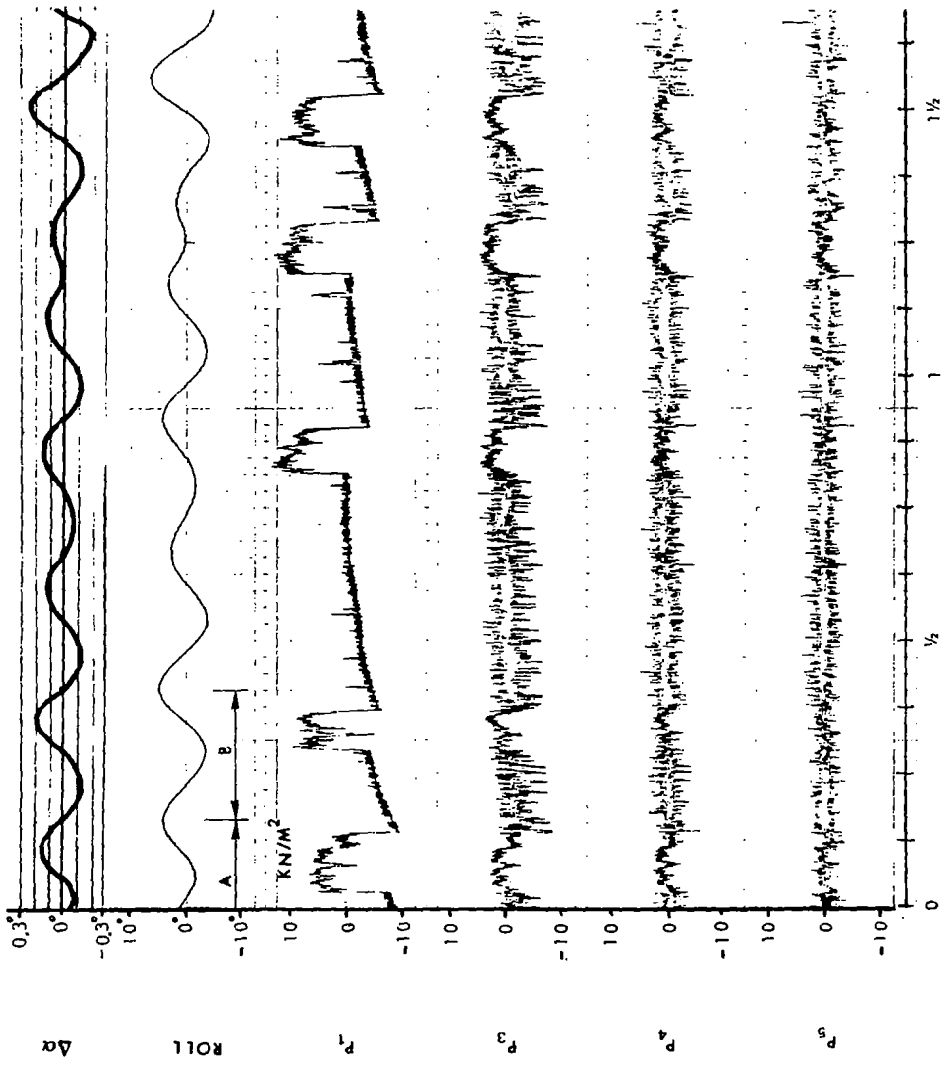

Figure 45. Real Time Data of the Roll Oscillations and the Corresponding Local Pressures of Transducer Numbers 1, 3, 4, 5 of the F-5A Scale Model, Run 5, Phase II, $\alpha = 10°$, $\beta = 0°$, $M = 0.925$, $\delta_n/\delta_f = 5°/12°$, $\delta_h = 0°$, $Q = 18.2$ KN/m^2, $c/c_{cr} = 0.057$.

effect. The lift recovery at P_1 appeared at $\dot{\alpha} = -$, even though $\Delta\alpha$ may still be positive at the time. The overall picture was a state of moderate instability, with the shock line located close to the leading edge. An intermittent movement of the shock line toward the leading edge caused the complete stall of the local section. The local stall was partially recovered within one half oscillation cycle or less. Typical limit cycle data for P_1 are presented in Figure 46. In the figure, the local C_{p_1} vs. α data are also plotted. The very limited $\Delta\alpha$ changes restricted the C_p variation away from the ramp representing the steady state loss of lift. The narrow $\Delta\alpha$ range for the test case was considered restrictive, not being a typical free flight condition. In a free flight, any roll oscillations would introduce coupled yaw and sideslip oscillations, which in turn would cause substantial increase in $\Delta\alpha$ range when the nominal angle-of-attack α_o was high.
It was also noted that if the random turbulences were ignored, the cyclic pressure fluctuations (being the source of the limit cycle energy input), appeared only near the outer span leading edge area. This was in contrast to Run 26, Phase II case where the pressure fluctuations appeared in substantial amplitude throughout the majority of the chord length (see Figure 39). As a result, the wing rock type oscillations of Run 5, Phase II, representative of cases of zero β for the test phase, were intermittent and limited in oscillation amplitude

The energy balanced condition for a cycle of nonstationary wing rock oscillation such as cycle A and B of Figure 45 may be written as:

$$Wk = \frac{1}{2} M_R \omega_R^2 (\varphi_2^2 - \varphi_1^2) + \oint (g_R M_R \omega_R - L_p) \dot{\varphi} \, d\varphi \qquad (7)$$

where Wk is the work input per oscillation cycle, φ_1, φ_2 are the initial roll oscillation amplitudes (at $\dot{\varphi} = 0$) of the oscillation cycle. The first term in the right hand side of the above equation denotes the potential energy change of the flexible roll device. Similar assumptions may be made for the work input as in the stationary ($\beta \neq 0$) case (see Equation 3), with the exception that, for $\beta = 0$, top surface strips Δb on both sides of the wing contribute to the limit cycle. The following numerical data are presented for a typical oscillation cycle (cycle B in Figures 45 and 46):

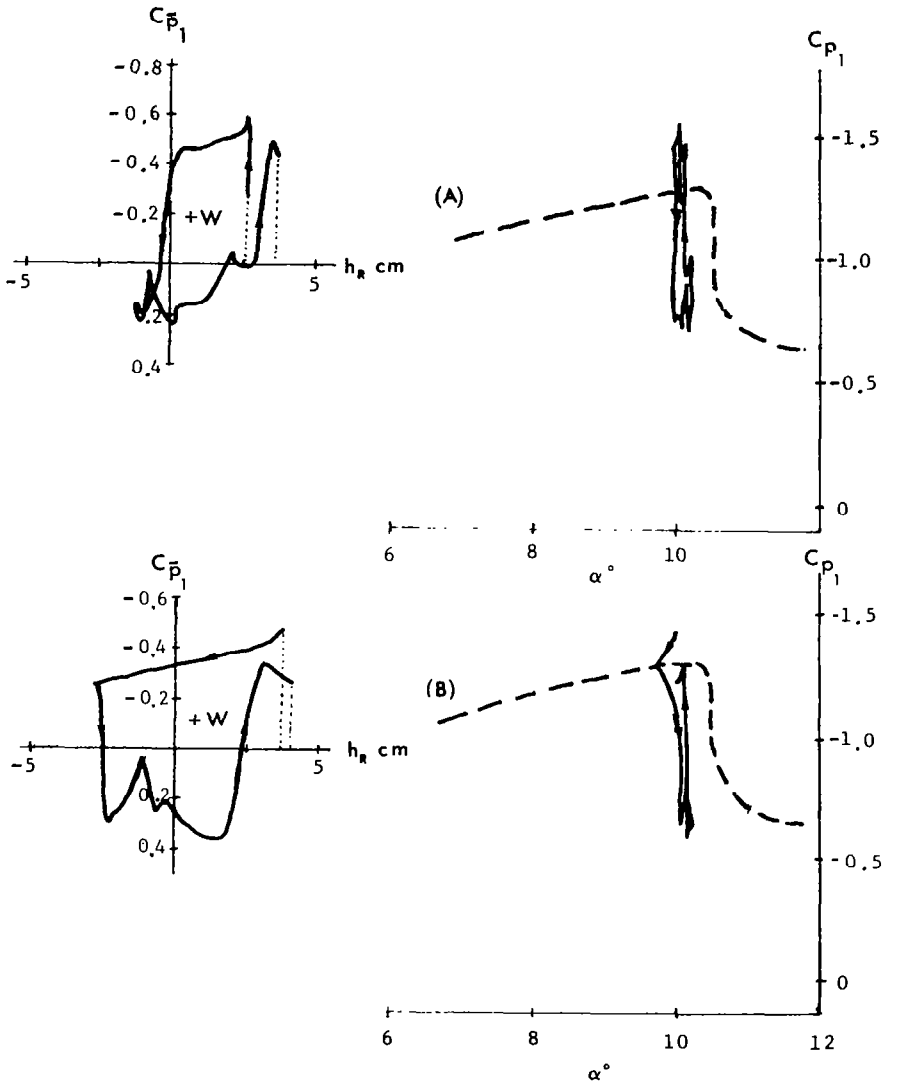

Figure 46. Dynamic and Static Pressure Coefficients $C_{\bar{p}}$, C_p vs. Local Translatory Motion h_R and local Angle-of-Attack α as observed from the Oscillating Model of F-5A, Pressure Transducer No. 1, Run 5, Phase II, β = 0°, M = 0.925, δ_n/δ_f = 5°/12°, δ_h = 0°, Q = 18.2 KN/m^2 , c/c_{cr} = 0.057.

$g_R = 0.114$, $Q = 18.2\ KN/m^2$

$U = 301.1\ m/sec$, $A = 0.0524\ m$

$\oint C_{p_1} dh = 0.00308\ m$, $\varphi_1 = 4°$

$\varphi_2 = 5°$, $\oint \dot{\varphi}\, d\varphi = 0.3767\ sec^{-1}$

$E = 2.82$ m-N/cycle

(of which 76.6% is due to mechanical damping, 21.4% is due to aerodynamic damping)

$Wk = 2\oint c_{p_1} \Delta b\ AQ\ dh = 5.88\ \Delta b$ m-N/cycle

$PE = \frac{1}{2} M_R \omega_R^2 (\varphi_2^2 - \varphi_1^2) = 1.776$ m-N/cycle

$\Delta b = 0.1425 \times (\frac{b}{2}) = 0.077\ m$

In evaluating the above data representing the cyclic and the random response cases simulating wing rock, the following conclusions may be drawn:

1. Wing rock was generated by a limit cycle mechanism due to the fluctuating pressure changes on the wing top surface, especially near the wing tip region. In the cases observed, the major reason for the pressure changes was the motion induced $\Delta\alpha$ which alternately caused leading edge stall and recovery. The amount of energy input to the limit cycle, to be consumed by aerodynamic and/or mechanical damping, may be evaluated quantitatively.

2. Based on kinematics, the roll oscillations acted together with α_o, β to cause substantial $\Delta\alpha$ changes which contributed to the limit cycle. Wing rock amplitude was thus dependent on the steady state sideslip angle β.

3. With a sideslip angle β, the upper wing surface on the windward side contributed the majority of the fluctuating pressures which caused wing rock.

4. With $\Delta\alpha$, the local fluctuating pressure coefficient followed the ramp curve during leading edge stall and the consequent loss of lift. Dynamic overshoot was observed in both the lift loss and recovery phases.

5. Based on the observations of the wind tunnel test data, a preliminary mathematical model of aircraft wing rock was developed which illustrated the motion-coupled limit cycle mechanism. Since the limit cycle defining the energy input to the aircraft was dependent on a number of flight condition parameters, no uniqueness condition can be established at this time to define and predict wing rock. Nevertheless, it is known that wing rock was directly related to the lift loss (ramp) of the C_p vs. α curve covering the fluctuating-pressure-active region of the wing. Additional acquisition and processing of controlled test data as those described above may further refine and quantify the preliminary mathematical model of aircraft wing rock described in this report.

Section 4

SPECTRAL AND STATISTICAL PROCESSINGS OF TEST DATA

In the previous section, the real-time pressure and response data as well as the static and dynamic pressure distributions were presented. Assuming that the random pressure and response date were stationary within a limited time span, standard spectral processing techniques may be applied. The spectral processing consisted of the determination of the power spectral densities of the pressure and response data, as well as the spatial correlation functions of any two sets of data. A brief outline of the processing techniques may be found in Reference 1.

4.1 Typical Pressure Power Spectra - Phase I

The dynamic pressure data acquired during Run 8, Phase I were processed to generate the power spectral density functions. The corresponding pressure distributions on the right wing upper surface were given in Figure 10.

In Figures 47 and 48, four sets of data were used to generate the power spectral density functions of pressure transducer Nos. 1 and 2, respectively. These correspond to α = 0 degree, α = 8 degrees, α = 12 degrees, α = 16 degrees. The data time span used in the processing were as follows:

Freq. Range (Hz)	Record Processed (Sec.)	No. of Records Used	Total Processed Data Time (Sec.)
0 - 200	2	16	32
200 - 2,000	.200	16	3.2
2,000 - 10,000	.040	16	0.64

Referring to Figure 47, the PSD scale on the right side, and the frequency scale on the top of the plots were based on actual tunnel test conditions. The corresponding scales on the left and bottom sides of the plots were transposed scales of the PSD data if the tests were performed under

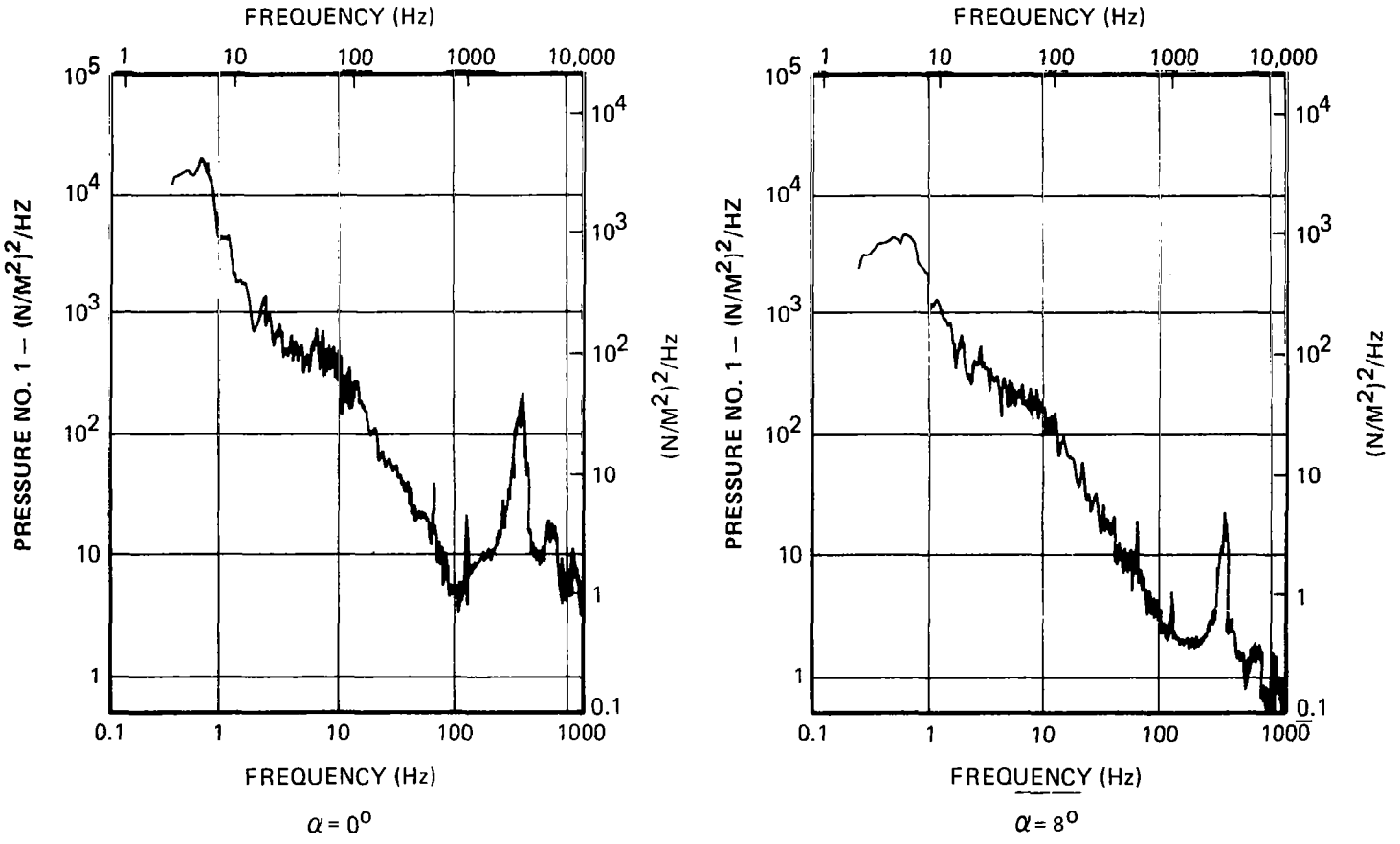

Figure 47. Pressure PSD Plots of Transducer No. 1 for F-5A Scale Model, Run 8, Phase I, $\beta = 0°$, M = .926, $\delta_n/\delta_f = 5°/12°$, $\delta_h = 0°$ (Continued)

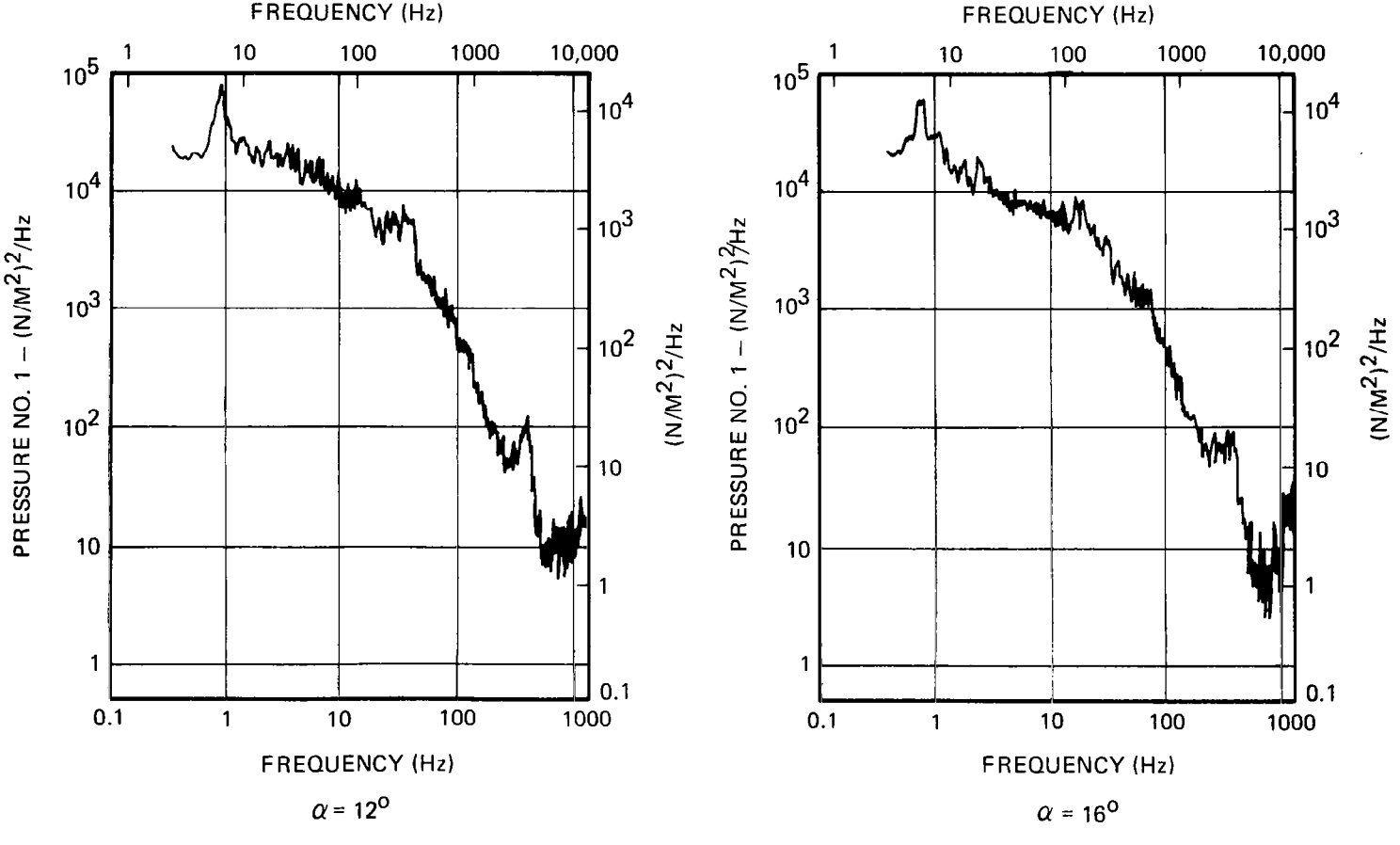

Figure 47. Pressure PSD Plots of Transducer No. 1 for F-5A Scale Model, Run 8, Phase I, $\beta = 0°$, M = .926, $\delta_n/\delta_f = 5°/12°$, $\delta_h = 0°$ (Concluded)

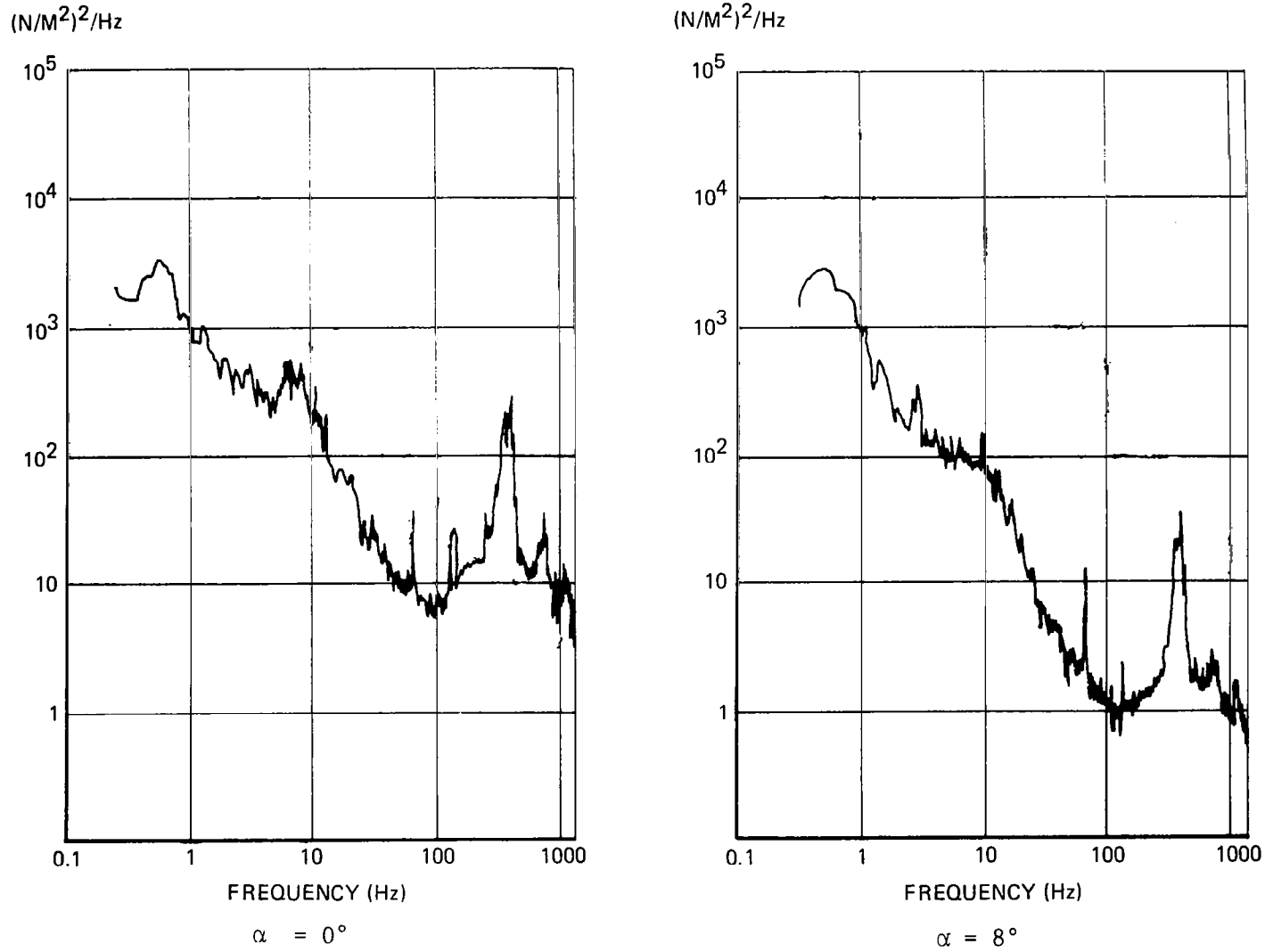

Figure 48. Pressure PSD Plots of Transducer No. 2 for F-5A Scale Model, Run 8, Phase I, $\beta = 0°$, $M = 0.926$, $\delta_n/\delta_f = 5°/12°$, $\delta_h = 0°$.

The Scales are Based on Flight Test 871 Conditions. (Continued)

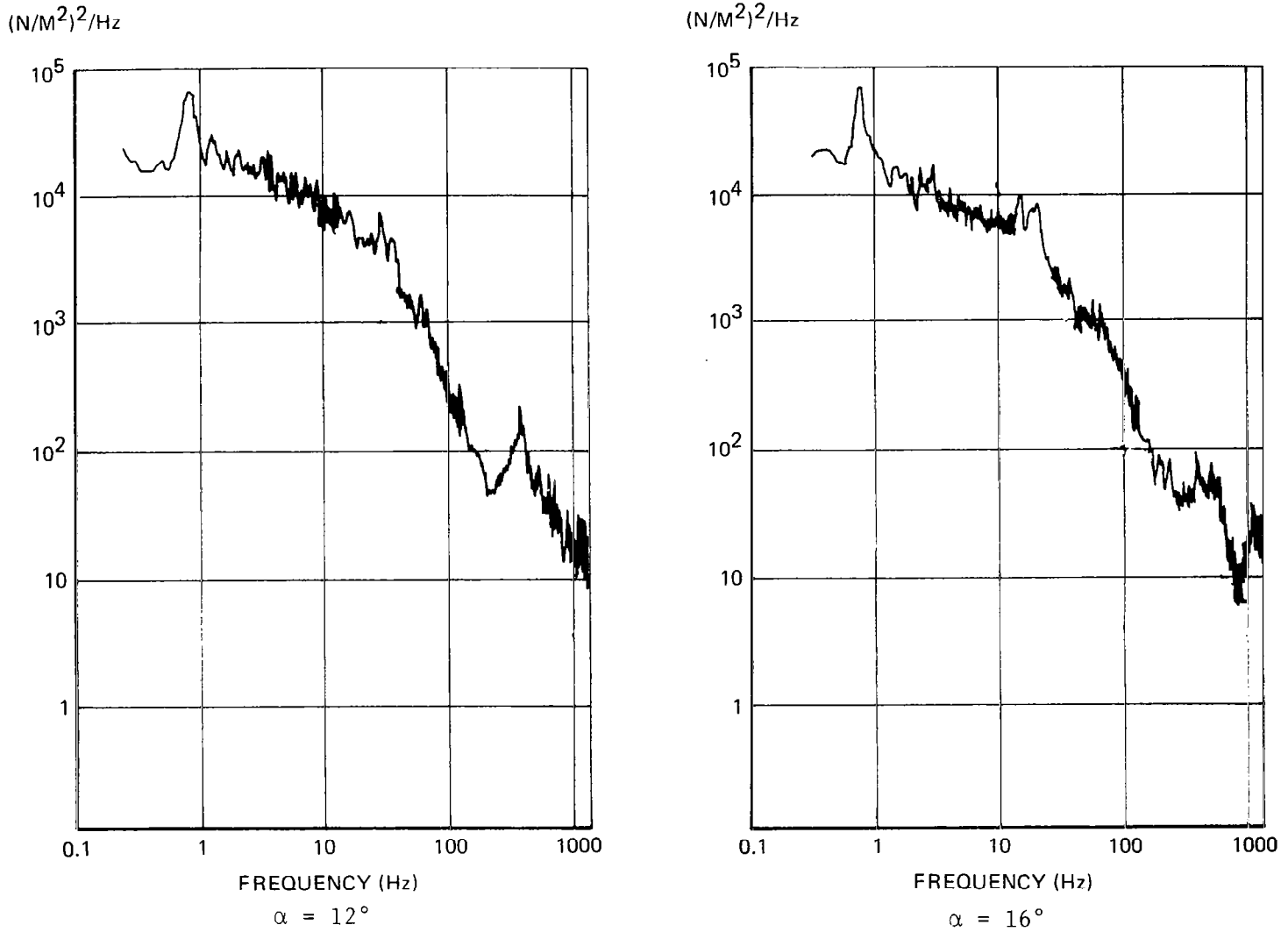

Figure 48. Pressure PSD Plots of Transducer No. 2 for F-5A Scale Model, Run 8, Phase I, $\beta = 0°$, $M = 0.926$, $\delta_n/\delta_f = 5°/12°$, $\delta_h = 0°$.

The Scales are Based on Flight Test 871 Conditions. (Concluded)

an equivalent flight test condition of F-5A. The scaling conversion was based on the Q, V, and c data of F-5A test aircraft N6009, Flight No. 871 (see Reference 1, pp. 43-55):

$M = .925$	$h = 10{,}668$ m
$Q = 14.36$ KN/m^2	$V = 274.3$ m/sec.
$c = 2.356$ m	$\delta_n/\delta_f = 4°/12°$
$R_N = 17.24 \times 10^6$	

In Figures 47 and 48, for α = 0 degree and 8 degrees, the peaks at approximately 3000 Hz and above (tunnel test frequency scale) were identified as tunnel noises. (See Reference 5). These peaks became less significant as the angle-of-attack and PSD level increased (α = 12°, 16°). The substantial increase in the PSD level at α = 12 degrees signaled the local flow separation.

For α = 10 degrees, the pressure PSD data were processed for transducer Nos. 2, 3, 4 using the same processed data time as shown in the table relating to transducer No. 1 pressure data. The results are presented in Figure 49. At α = 10 degrees, transducer Nos. 3 and 4 were under the separated flow, while No. 2 was still in the unseparated flow region. The PSD level difference between the unseparated and separated flows was 10 dB or more except at the high frequency region. Because of the close proximity of the transducers, the similarity of the PSD patterns suggested a high degree of spatial correlation of the dynamic pressures. This point will be investigated further.

In order to observe the influence of the wake flow to the horizontal tail during aircraft buffet, the pressure PSD data were processed for transducer Nos. 12, 22, 24 corresponding to α = 0 degree, 8 degrees, 12 degrees, 16 degrees. The results are presented in Figure 50. Transducer No. 12 was located at W.S. 71.4 or 47 percent semi-span and 40 percent chordwise location of the upper wing surface (see Figure 3). Transducer Nos. 22, 24 were located on the horizontal tail at the same semi-span location downstream of No. 12 and 40 percent of the local chord. No. 22 was on the upper surface and No. 24 on the lower surface. In examining the figure, it was noted that unseparated flow appeared at transducer No. 12 when α = 0 degree, 8 degrees, and also at transducer No. 22 when α = 0 degree.

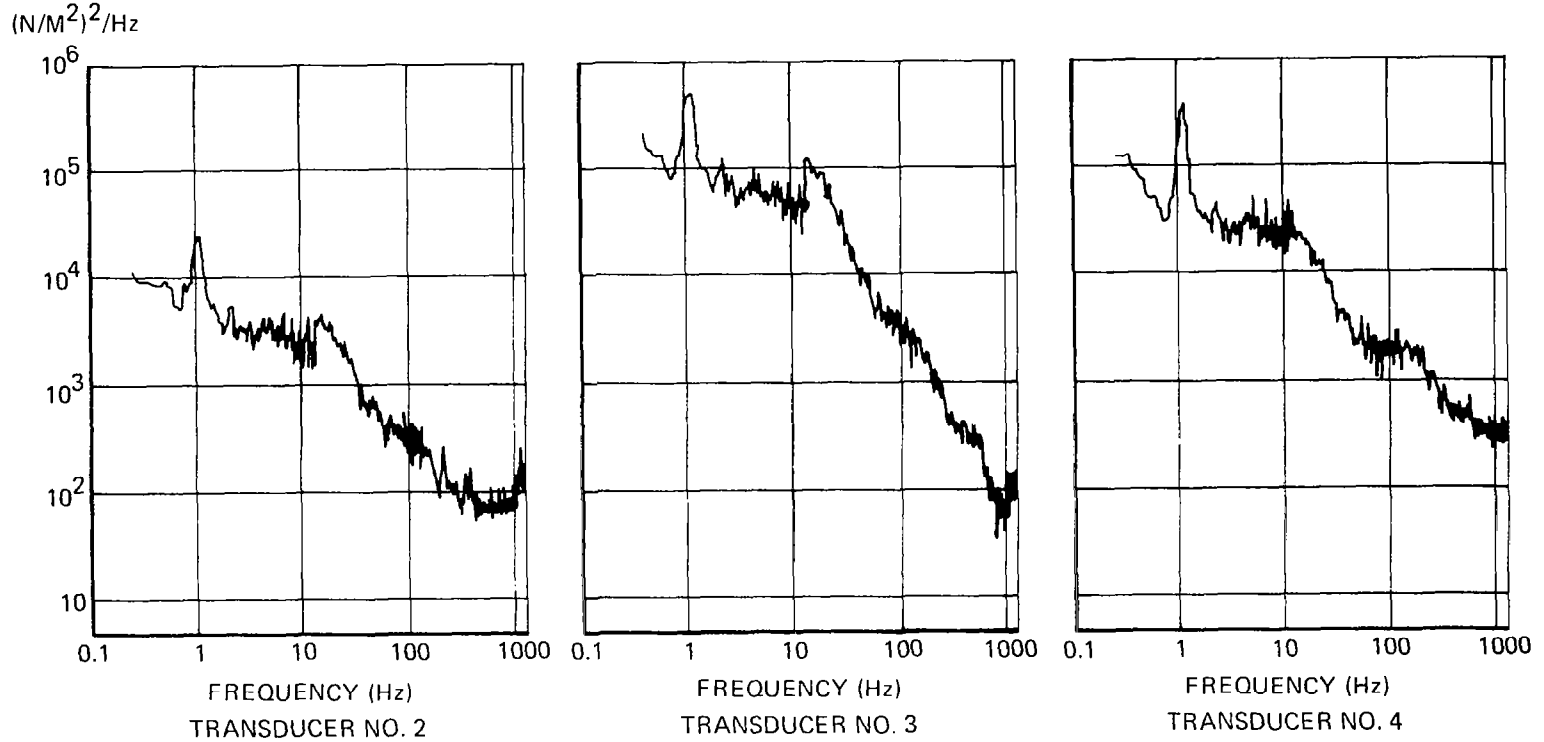

Figure 49. Pressure PSD Plots of Transducer Nos. 2, 3, 4 for F-5A Scale Model, Run 8, Phase I, $\alpha = 10°$, $\beta = 0°$, $M = .926$, $\delta_n/\delta_f = 5°/12°$, $\delta_h = 0°$. The Scales have been Modified to Conform to Flight Test 871 Conditions.

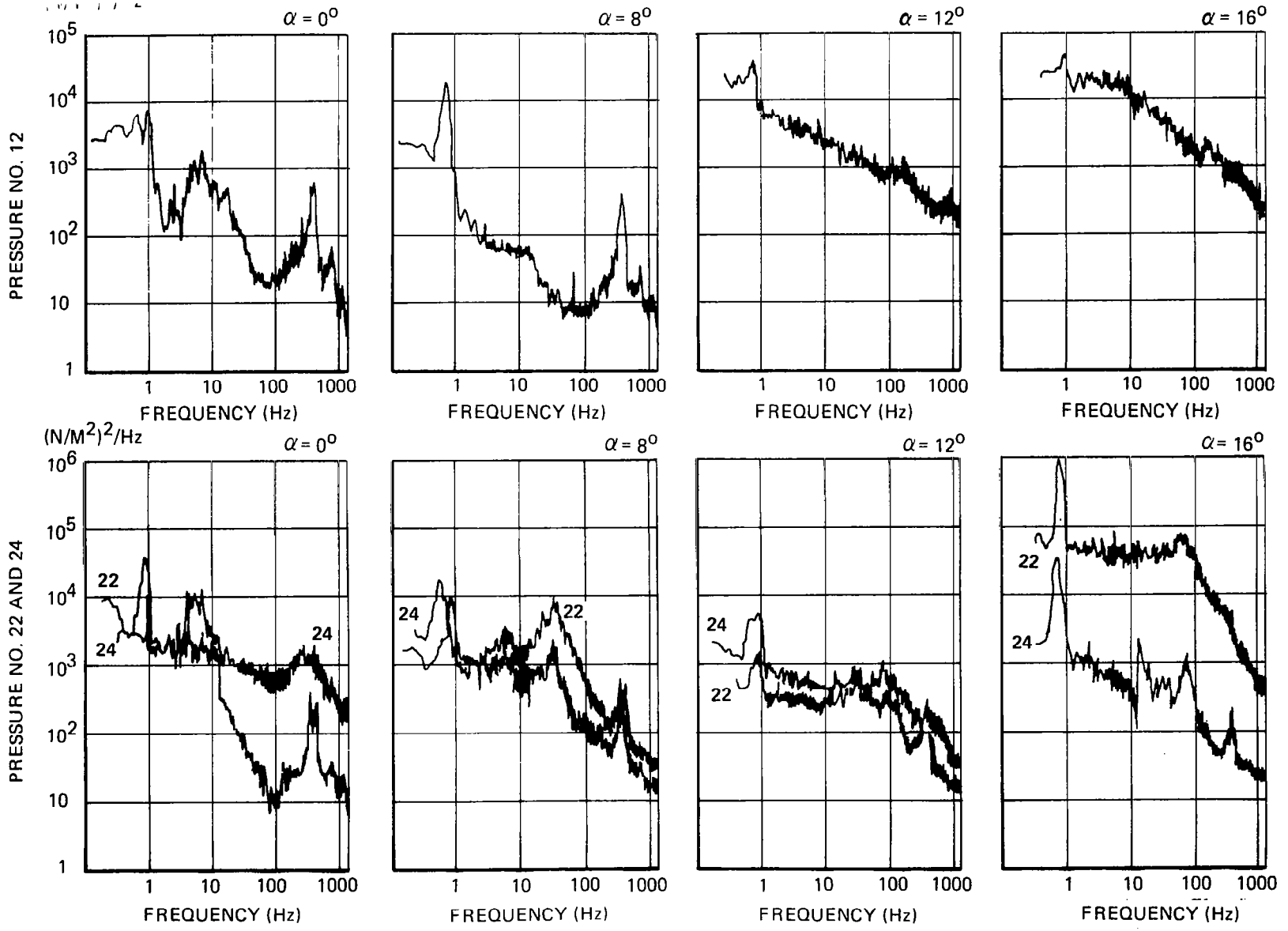

Figure 50. Pressure PSD Plots of Transducer Nos. 12, 22, 24 for F-5A Scale Model, Run 8, Phase I, $\beta = 0°$, M = .926, $\delta_n/\delta_f = 5°/12°$, $\delta_h = 0°$. The Scales have been Modified to Conform to Flight Test 871 Conditions.

Otherwise, the local flow was separated. The similarity of PSD curves of transducer No. 12 and No. 22 at α = 0 degree suggested a certain degree of spatial correlation, most possibly due to the dominance of characteristic wind tunnel noise. At α = 8 degrees, 12 degrees, transducer No. 22 and No. 24 featured almost identical PSD curves, reflecting a strong wake flow condition. At α = 16 degrees, the very high PSD level of transducer No. 22 indicated the high turbulence due to both wake flow and horizontal tail top surface flow separation. This PSD curve was one of the highest broad-band spectral level recorded in the test program. The high dynamic pressure intensity on the tail surface for large α's was expected to affect the control characteristics of the aircraft, as compared to the direct buffet pressure excitation through the aircraft wing. In the following subsection, the effect of flap settings will be described.

4.2 Effect of the Flap Settings

Effect of the flap settings was examined using test data of Run 8 and Run 39, Phase I. Run 39 was conducted in test model configuration 9. The configuration featured wing-tip-mounted Sidewinder missiles. The leading and trailing edge flaps were in the retracted positions (δ_n/δ_f = 0°/0°). The aileron and horizontal tail surface settings were 0 degree. The nominal sideslip angle was 0 degree. The run was conducted at M = 0.925 with a dynamic pressure of 28.30-28.68 KN/m^2 (591-599 psf). The nominal Reynolds number was 11.483 x 10^6/m (3.50 x 10^6/ft).

A comparison of dynamic pressure distributions of Runs 8 and 39 at critical α's is shown in Figure 51. The major difference between Run 8 and Run 39 was the extended flaps of the former (δ_n/δ_f = 5°/12°) and the completely retracted flaps of the latter (the camber effect). Furthermore, there existed a difference in Reynolds number, 7.402 x 10^6/m for Run 8 vs. 11.483 x 10^6/m for Run 39. Since the two Reynolds numbers were of the same order of magnitude, the major difference in the pressure distribution may be attributed to the camber effect. (This point was borne out by detail comparison of the dynamic pressure data presented later.)

In Run 39, as the angle-of-attack increased from 0 degree to 8 degrees, the separation-inducing shock moved speedily toward the leading edge in the wing-tip region. At α = 8 degrees, high rms dynamic pressure was observed at 85 percent semi-span close to the leading edge. With further α increase, the peak dynamic pressure location moved rapidly along the leading edge toward the fuselage. This behavior was different from the case of Run 8 where the shock-induced flow separation region appeared first throughout the semi-span in the trailing edge region at approximately α = 8 degrees.

With additional increase in α, the shock front and the separated flow boundary moved upstream toward the leading edge. At α = 14 degrees, 16 degrees, the complete upper wing surface was subjected to the separated flow. The rms dynamic pressures were highest in the region from the fuselage up to 72.8 percent semi-span, with the wing-tip region showing lower dynamic pressures.

In general, at moderate angle-of-attack, the deflected leading edge flap of Run 8 tended to push the flow separation boundary further downstream as compared to the case of the retracted leading edge flap. The extended trailing edge flap tended to keep the shock-induced flow separated in region further inboard. This can be attributed to the increased camber in the inboard portion of the semi-span for the extended flap case. As far as the shock and the shock-induced flow separation region are concerned, the flow behavior at various wing sections was more uniform along the span-wise direction with the deflected flaps. The above-mentioned differences were most prominent at α = 6 degrees, 8 degrees. With further increase in α, the differences in the flow behavior became less distinct as the upper surface was completely under separated flow.

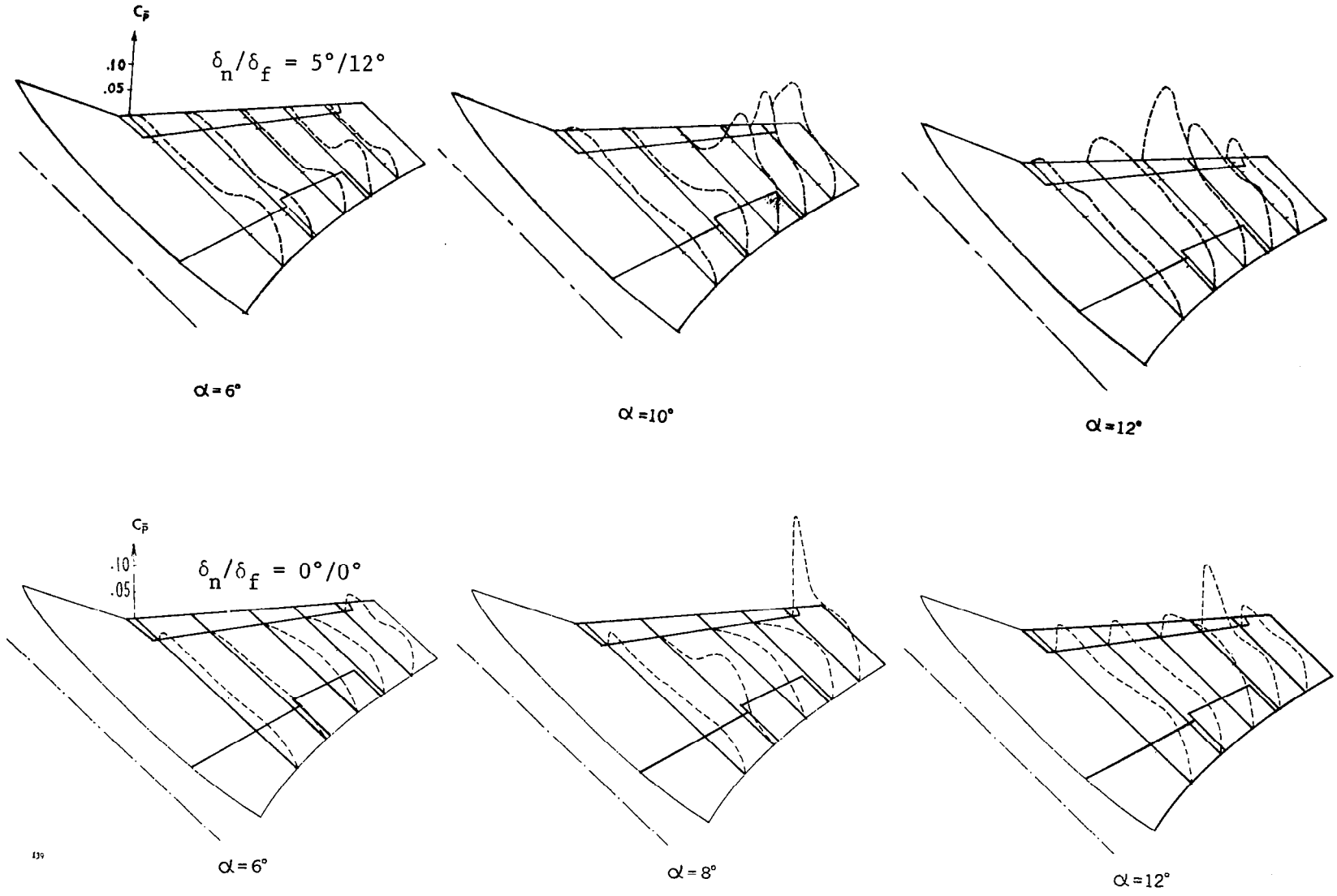

Figure 51. Dynamic Pressure Comparison Due to Leading and Tailing Edge Flap Settings - Run 8 (top) vs. Run 39 Phase I. $\beta = 0°$ $M = 0.925$ $\delta_s = 0°$

The pressure power spectral density plots of Run 39 are presented in Figures 52 to 54 for Transducers Nos. 2, 12, 18 respectively. Each set of PSD plots has four curves corresponding to α = 0 degree, 8 degrees, 12 degrees, 16 degrees. The scales have been modified to conform to Flight 825, Run 5 condition of a F-5A test aircraft (see Reference 1). The modification of scales was consistent with the PSD data of Run 8 presented previously (Figures 47 to 50).

In comparing the PSD plots of transducer No. 2, Run 39 (Figure 52) with those of Run 8 (Figure 48), it was noted that the major difference in the PSD trend appeared at α = 8 degrees. At this angle, the PSD level of Run 39 at transducer No. 2 was substantially higher than the corresponding PSD of Run 8. This same peak may also be observed in the pressure rms plot in Figure 51 for α = 10 degrees. For the other α angles (0°, 12°, 16°), the PSD plots of transducer No. 2 for the two runs were almost identical to minute details. In general, under otherwise identical test conditions, the difference in the flap angle settings seemed to affect the movement of the shock boundary, the peak dynamic pressure level where the shock appeared, and the resulting development of the separated flow. At a given station away from the flaps, the dynamic pressures were pretty much defined by whether the local flow was unseparated or separated and the instantaneous angle-of-attack, irrespective of the flap angle settings.

In examining the PSD plots of transducer No. 12 which represented a typical mid-span location on the top surface of the wing (Figures 50, 53), it was noted that for the same α, the differences of PSD trends between Run 8 and Run 39 were not substantial. At any frequency band, the difference in PSD levels for the two runs remained mostly at 5 dB or less.

Figure 54 shows PSD plots of transducer No. 18 of Run 39 which was located on the top surface of the undeflected trailing edge flap. No comparable data were processed for Run 8. In general, the PSD's of transducer No. 18 were similar to those of transducer No. 12 for the same α's. The exception was the PSD of transducer No. 18 at α = 16 degrees which resembled a white noise distribution throughout the frequency band of interest.

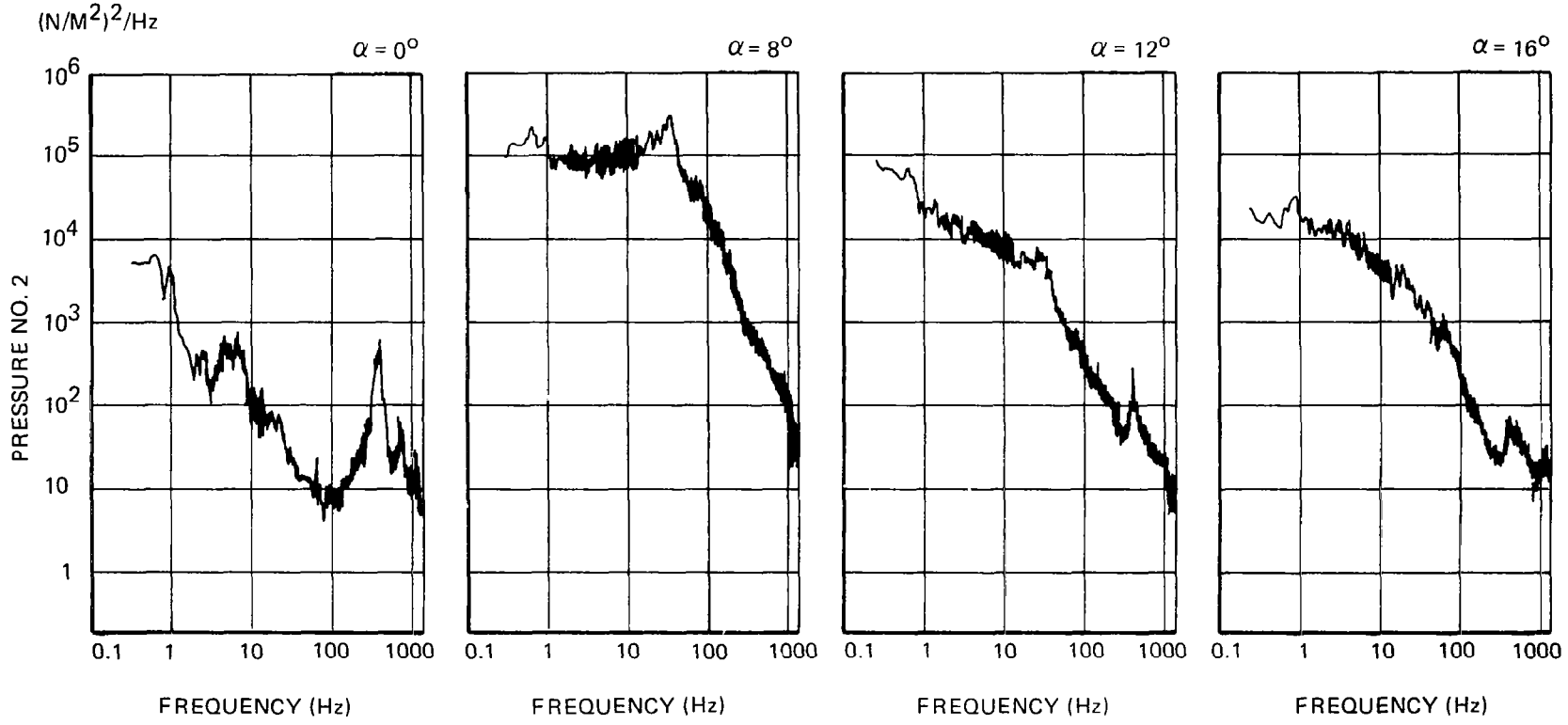

Figure 52. Pressure PSD Plots of Transducer No. 2 for Scale Model in Run 39, Phase I, $\beta = 0°$, M = .925, $\delta_n/\delta_f = 0°/0°$, $\delta_h = 0°$. The Scales have been Modified to Conform to F-5A Aircraft Flight Test 825, Run 5 Conditions.

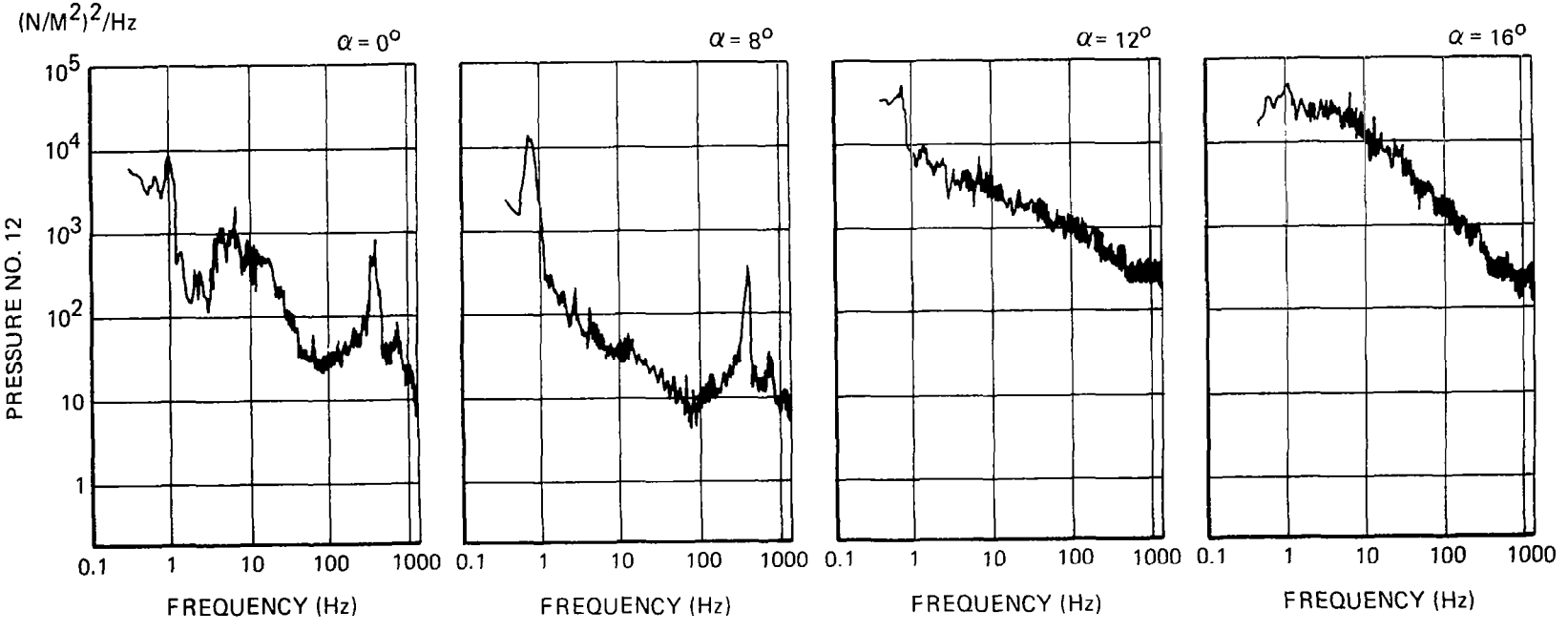

Figure 53. Pressure PSD Plots of Transducer No. 12 for Scale Model in Run 39, Phase I, $\beta = 0°$, $M = .925$, $\delta_n/\delta_f = 0°/0°$, $\delta_h = 0°$. The Scales have been Modified to Conform to F-5A Aircraft Flight Test 825, Run 5 Conditions.

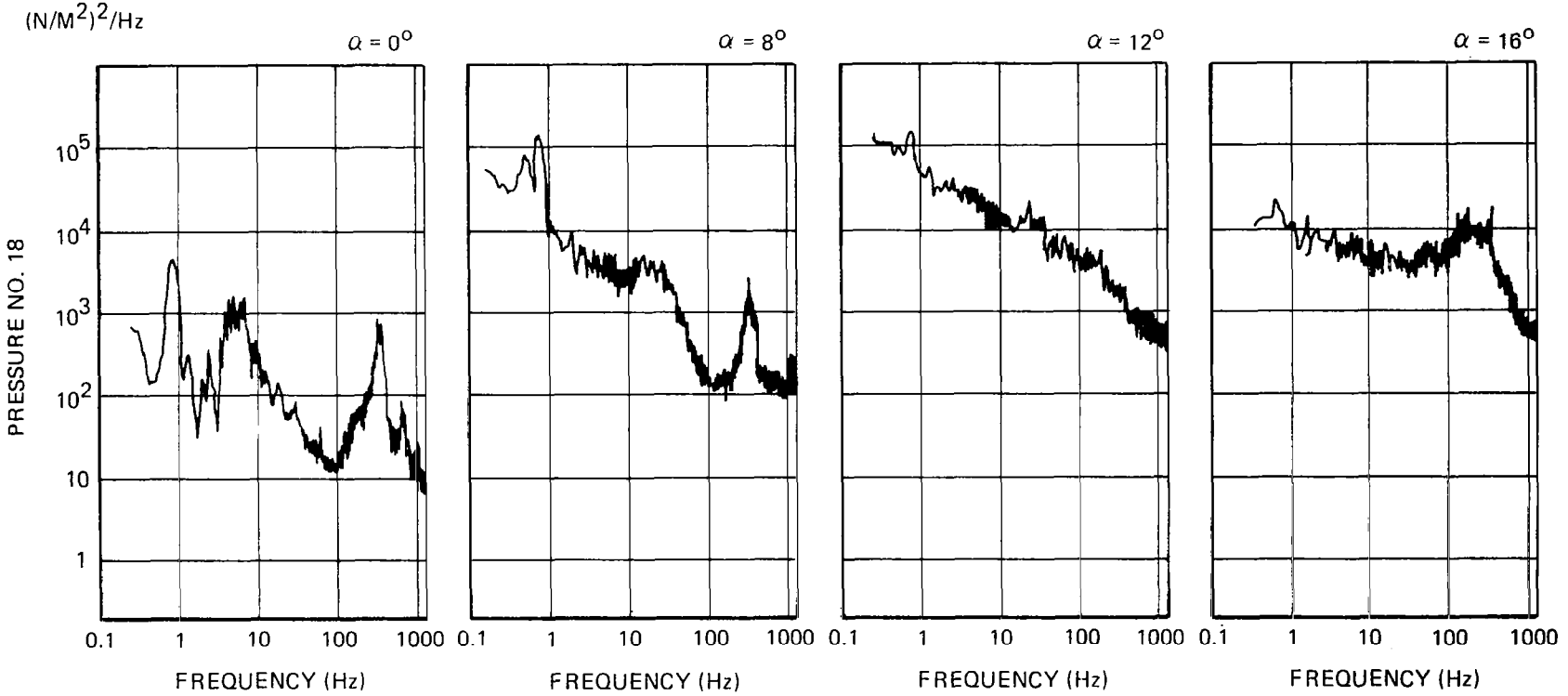

Figure 54. Pressure PSD Plots of Transducer No. 18 for Scale Model in Run 39, Phase I, $\beta = 0°$, $M = .925$, $\delta_n/\delta_f = 0°/0°$, $\delta_h = 0°$. The Scales have been Modified to Conform to F-5A Aircraft Flight Test 825, Run 5 Conditions.

4.3 Comparison of Pressure PSD Data for the Fixed and Flexibly-Supported Models

Run 5, Phase II was conducted with the same model configuration (No.2) as Run 8, Phase I, except that in the second test phase, the model was supported on a flexible system. The tip-mounted Sidewinder missiles were included in the configuration. The leading edge and trailing edge flap settings were 5°/12°. The horizontal tail surface and aileron settings were 0 degree. The nominal sideslip angle was 0 degree. The run was conducted at M = 0.925. The dynamic pressure was 18.2 KN/m^2 (377.7 psf). The Reynolds number was 7.38 x 10^6/m (2.25 x 10^6/ft). The critical angle-of-attack was 10 degrees at which the model oscillated along the flexible roll axis. Typical dynamic pressure coefficient distributions on the right wing upper surface for Run 8, Phase I and Run 5, Phase II were given in Figure 22. The plots cover the angle-of-attack range α = 6 degrees, 10 degrees, 12 degrees.

In Figure 22, at α = 6 degrees, the rms pressure coefficient distributions for Run 8, Phase I and Run 5, Phase II are qualitatively similar. Both reflected the development of the shock-induced flow separation covering approximately 30 percent of the chord toward the wing trailing edge. At α = 10 degrees, when roll oscillation took place for the flexibly-supported model, the Phase II results indicated a somewhat less distinct shock front location, possible due to the oscillatory change in the effective angle-of-attack caused by the wing roll motion. For α = 12 degrees, the complete wing upper surface was under separated flow. The oscillating model featured more evenly distributed rms pressure coefficients as compared to the Phase I data.

Examination of the static pressure distributions for Run 8, Phase I and Run 5, Phase II (not shown in this report) showed that the C_p coefficient developments on the wing upper surface with α - changes remained essentially the same for the two runs. In either case, the highest C_p amplitude (negative pressure) developed at approximately α = 10 degrees, when the flexibly-supported model started to oscillate in roll. The C_p

amplitudes showed moderate reduction as the angle-of-attack was further increased. The upper surface of the horizontal tail exhibited moderate negative C_p (in order of -0.10) up to α = 12 degrees. Beyond which, the C_p amplitude increased substantially with α. At α = 16 degrees, the C_p at transducer No. 22 reached -0.7142 in Run 8, Phase I and -0.7062 in Run 5, Phase II.

In Figures 55,56, the power spectral density functions of pressure transducer Nos. 1, 12, 22, 24 for Run 5, Phase II are plotted with those corresponding to Run 8, Phase I shown previously in Figures 47,50 for comparison purpose. The angle-of-attack range covers α = 0 degree, 8 degrees, 12 degrees, 16 degrees. The scales used were modified to conform to the equivalent flight test condition of the F-5A, as was the case in Figure 47. In both figures (55,56), two arrowheads were attached to the PSD plot at the upper left corner. They identified the pressure PSD peaks corresponding to (1) the sting bending for the supporting systems, with a natural frequency of approximately 6.6 Hz, or 0.865 Hz after the frequency scale was modified to conform to Flight Test 871 conditions, (2) the first wing symmetrical bending, with a natural frequency of approximately 53.5 Hz, or 7.01 Hz based on the modified frequency scale.

Referring to Figure 55, the PSD data for transducer No. 1 and No. 12 were almost identical for the two runs with the exception of the very low frequency region corresponding to the roll oscillation natural frequency of the flexible support. The slightly higher PSD level of the flexibly-supported model gave a good indication on the effect of the induced dynamic pressures due to model oscillation. The peak at approximately 340.6 Hz (based on the modified frequency scale) or 2600 Hz in actual test condition was characteristic PSD peak of the tunnel noise. The tunnel noise peak was prominent at low angle-of-attack when the overall dynamic pressure levels on the wing surface were low.

The corresponding tail surface pressure PSD comparison for the two runs is shown in Figure 56 for transducer No. 22 and No. 24. In this case, more prominent deviations of the PSD levels were observed, especially at α = 8 degrees. It is reasonable to assume that the differences at α = 8 degrees,

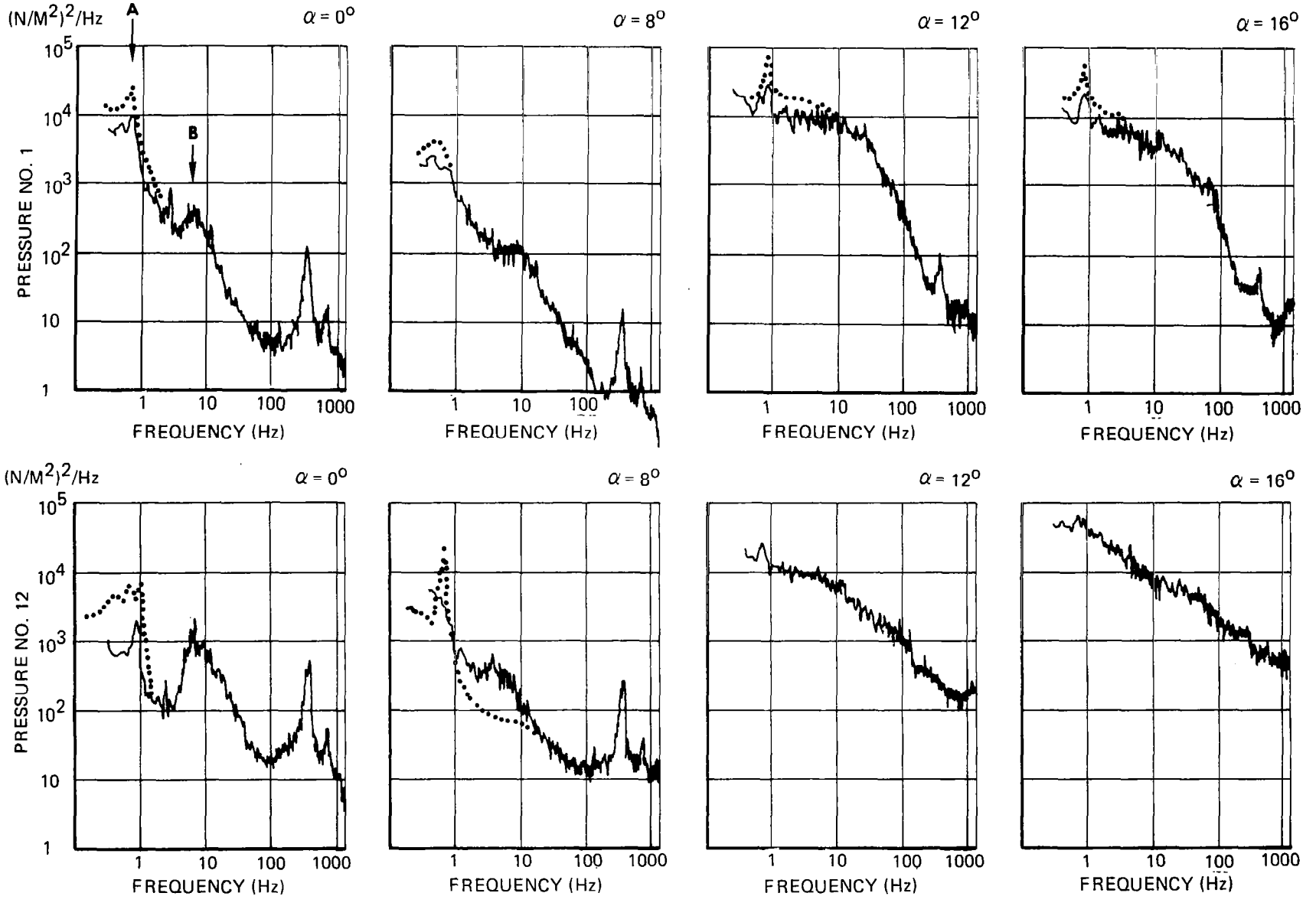

Figure 55. Comparison of Wing Pressure PSD Data for Configuration 2 for the Regularly-Supported Model (Run 8, Phase I, Indicated in Dotted Lines) and the Flexibly-Supported Model (Run 5, Phase II, Indicated in Solid Lines), $\beta = 0°$, $M = 0.925$, $\delta_n/\delta_f = 5°/12°$, $\delta_h = 0°$. The Scales are Modified to Conform to Flight Test No. 871 Conditions. The arrowheads identify (A) the Sting Bending Mode and (B) the First Wing Symmetrical Bending Mode.

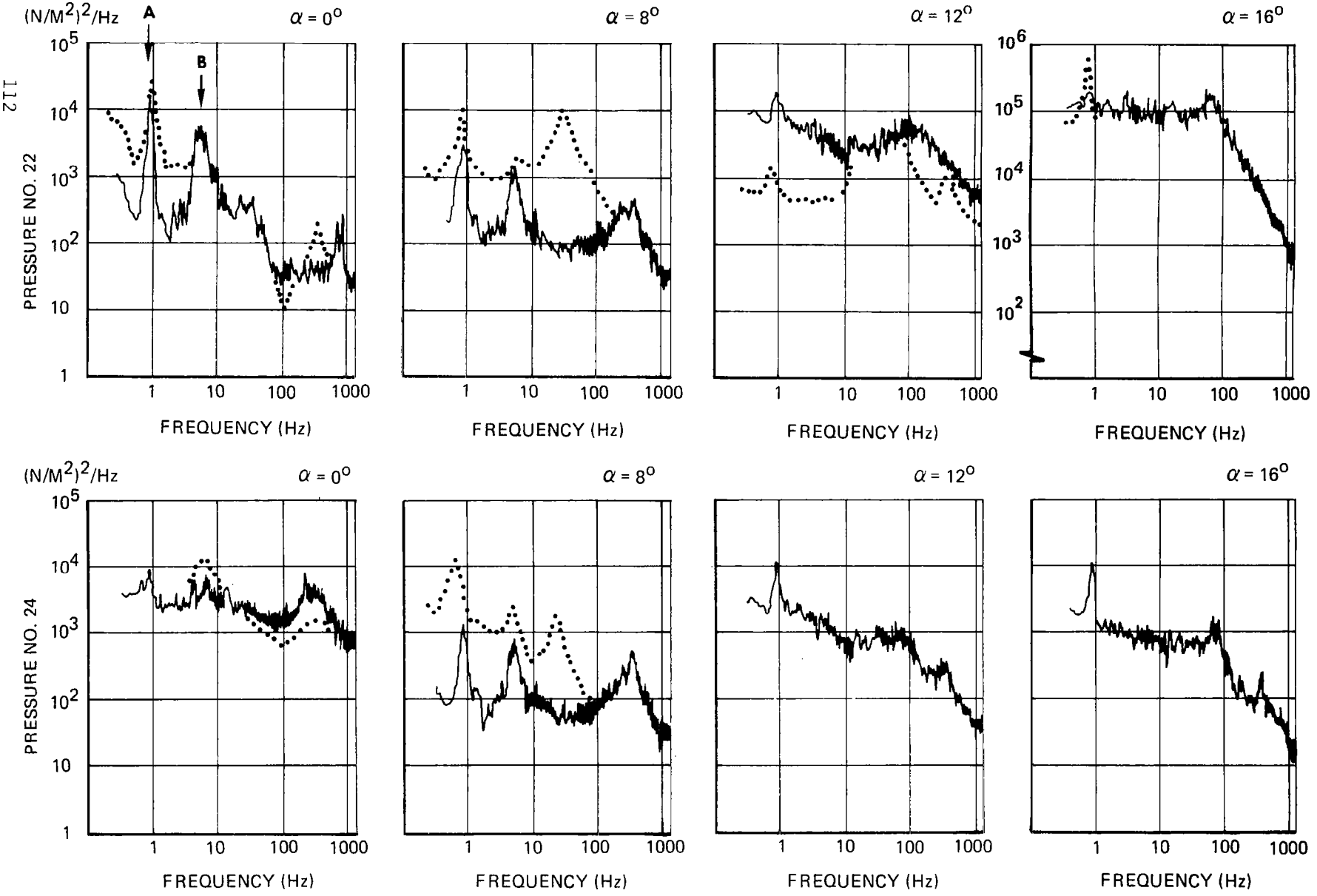

Figure 56. Comparison of Horizontal Tail Surface Pressure Data for Configuration 2 for the Regularly-Supported Model (Run 8, Phase I, Indicated in Dotted Lines) and the Flexibly-Supported Model (Run 5, Phase II, Indicated in Solid Lines), $\beta = 0°$, $M = 0.925$, $\delta_n/\delta_f = 5°/12°$, $\delta_h = 0°$. The Scales are Modified to Conform to Flight Test No. 871 Conditions. The Arrowheads Identify (A) the Sting Bending Mode and (B) the First Wing Symmetrical Bending Mode.

prior to large amplitude model oscillation ($\alpha^* = 10°$), were due to minute test condition changes which affected the dynamic pressures in the wake flow region. At α = 16 degrees, the PSD curves for the two runs were almost identical, as were the case of the wing surface transducers (Figure 56).

4.4 Comparison of Measured Power Spectral Data with Flight Test Spectral Data - Reynolds Number Effect

Comparison of measured power spectral data with equivalent flight test spectral data for M = 0.925 case was made using the data recorded during Run 39, Phase I test. The features as well as the development of flow pattern of Run 39 were described in subsection 4.2. The right wing top surface static and dynamic pressure coefficient distributions are plotted in Figure 57. Figure 58 are the pressure PSD plots for transducer No. 2 of the scale model during Run 39, Phase I test. In these plots, only converted PSD and frequency scales (to Flight 825 conditions) were presented. The three plots consisted of PSD data as described below:

$\alpha = 8°$	marked (a)
$\alpha = 12°$	marked (b)
$\alpha = 16°$	marked (c)

All scale model PSD data were plotted in solid lines. For comparison purposes, the corresponding PSD data of a transducer at the identical geometrical position on the F-5A test aircraft acquired in Flight 825 Run 5 ($M_o = 0.925$, h = 10,668m, $\delta_n/\delta_f = 0°/0°$, $R_N = 17.24 \times 10^6$) were overplotted on the figure in broken curves. Specifically, the PSD data were based on approximately 0.5 second pressure records of a transonic maneuver performed by the test aircraft. These PSD data were identified as:

$\alpha = 7.2° - 8.6°$	marked (A)
$\alpha = 11.4° - 13.2°$	marked (B)
$\alpha = 13.9°$	marked (C)

No comparison was made at the beginning of the maneuver.

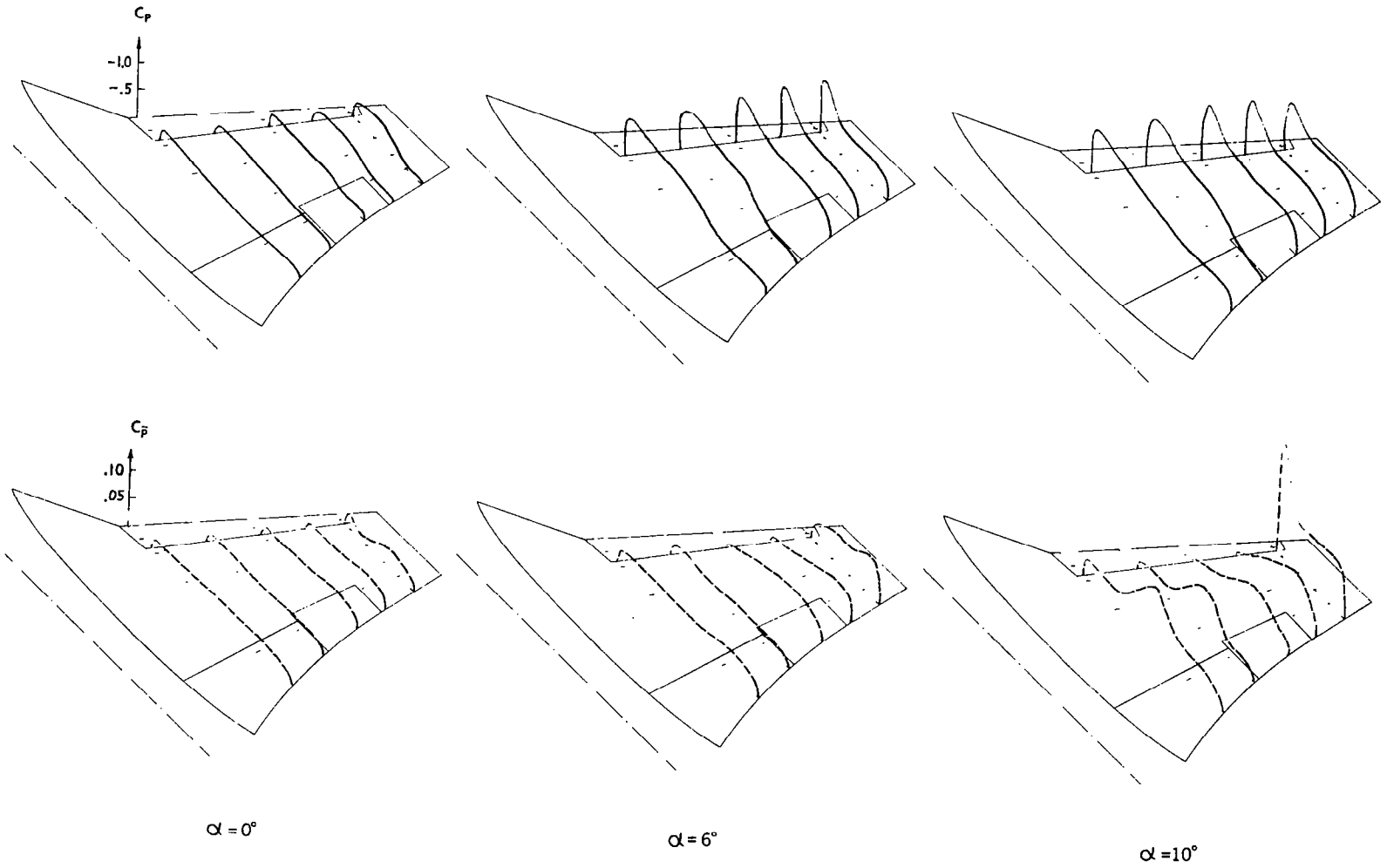

Figure 57. Static Pressure (C_p) and RMS Pressure ($C_{\bar{p}}$) Coefficient Distribution on the Right Wing Upper Surface, Run 39, Phase I, $\beta = 0°$, M = 0.925, $\delta_n/\delta_f = 0°/0°$, $\delta_h = 0°$ (Continued)

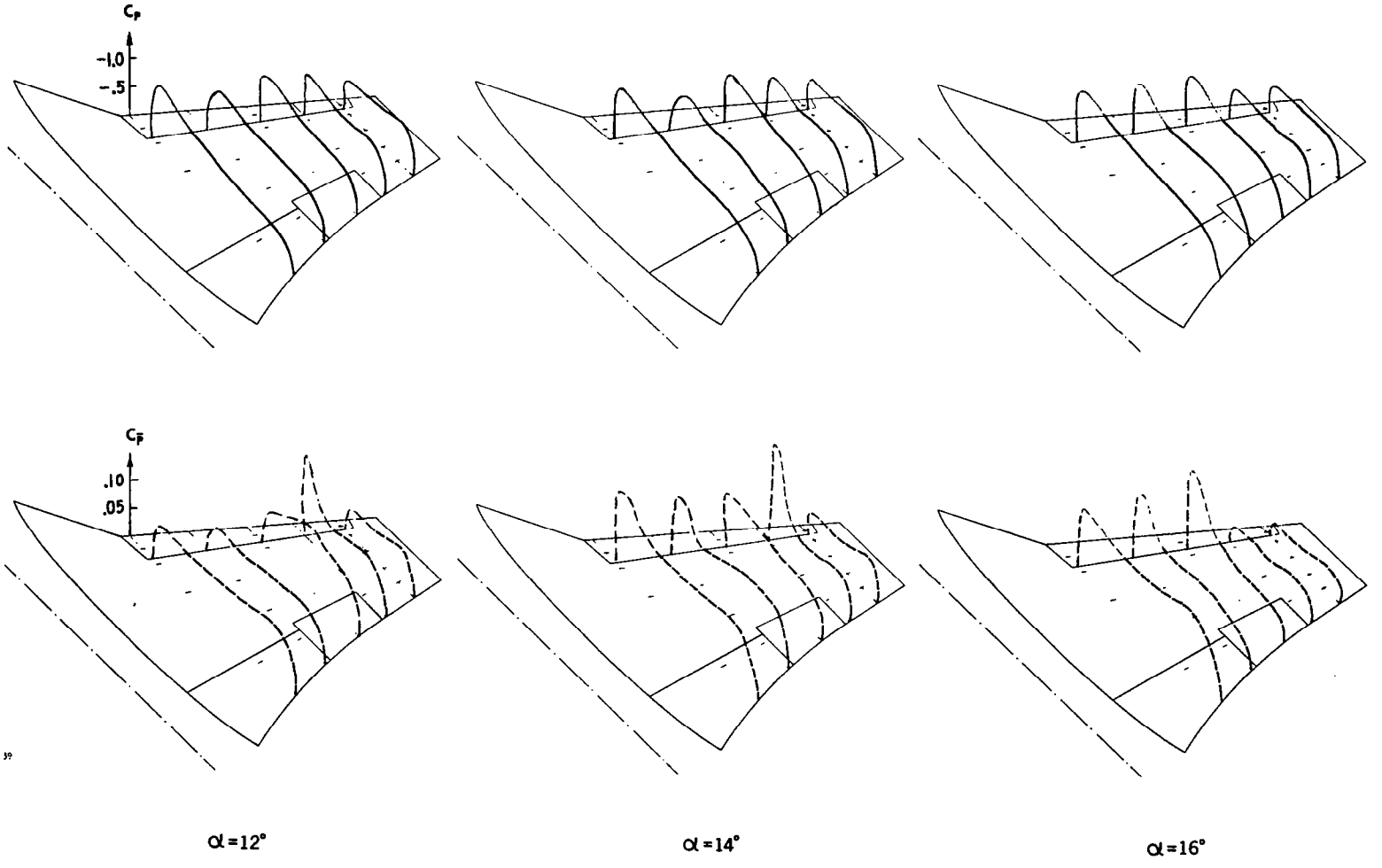

Figure 57. Static Pressure (C_p) and RMS Pressure ($C_{\overline{p}}$) Coefficient Distribution on the Right Wing Upper Surface, Run 39, Phase I, $\beta = 0°$, $M = 0.925$, $\delta_n/\delta_f = 0°/0°$, $\delta_h = 0°$ (Concluded)

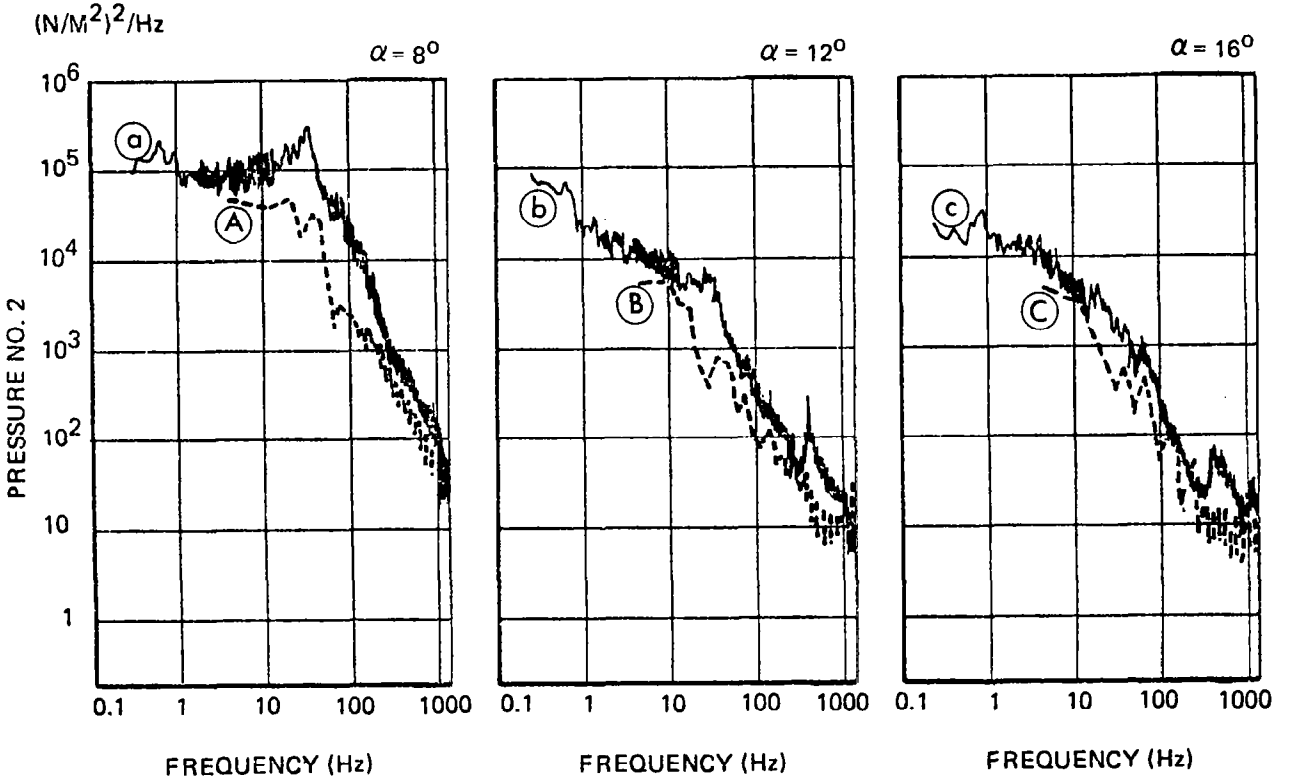

(a) α = 8°
(A) α = 7.2-8.6°

(b) α = 12°
(B) α = 11.4-13.2°

(c) α = 16°
(C) α = 13.9°

Figure 58. Pressure PSD Plots of Transducer No. 2 for Scale Model in Run 39, Phase I and F-5A Aircraft in Flight Test 825, Run 5, M = 0.925, δ_n/δ_f = 0°/0°, δ_h = 0°. The Scales are Based on Flight Test 825 Conditions.

In comparing the scale model and the aircraft pressure PSD data at transducer location No. 2, it was noted that the PSD levels and the frequency distributions of the tunnel test and flight test data were quite comparable.

For a typical inboard transducer, No. 12 of Figure 3, the pressure PSD data are presented in Figure 59. The identification letters for the scale model and the F-5A aircraft flight test data conventions were the same as in Figure 58. In comparing the scale model and the aircraft pressure data, it was found that except at $\alpha \simeq 8°$, the PSD levels and the frequency distributions of the tunnel test and flight test data were again quite comparable. At $\alpha = 8°$, a difference of PSD level as much as 15 dB was observed. The peak of the tunnel test data at approximately 230 Hz and above were caused by tunnel noises. For the scale model, the PSD levels also showed an average of 20 dB increase when α was changed from 8° to 12°, indicating a drastic expansion of the separated flow region on the wing surface in the inboard area. This phenomenon was also observed in Figure 53. In comparing the two cases for station 12, it seemed that in the transition stage (from separated flow to shock-induced flow separation), the actual aircraft local transition appeared at a lesser angle-of-attack. After the transition, the local pressure rms level corresponding to a separated flow condition were about the same for the actual aircraft and for the scale model.

Similar comparison was made for the flight and model test results for M = .75 case. The test data of Run 43, Phase I were used. Run 43 was conducted with model configuration 9, i.e., all flaps and control surfaces at retracted positions. Two sidewinders were mounted on the wing-tips. Run 43 was executed at M = 0.75. The dynamic pressure was 30.23 KN/m^2 (631.3 psf). The Reynolds number was 13.99 x 10^6/m (4.264 x 10^6/ft.). The model Reynolds number was 4.71 x 10^6. At M = 0.75, the flow separation was leading edge induced. The phenomenon may be traced through the static and dynamic pressure coefficient plots with increasing α (Figure 60). At α = 6 degrees, separation existed in 85 percent semi-span location up to the tip. At α = 10 degrees, the separation region moved inboard toward 33 percent semi-span location.

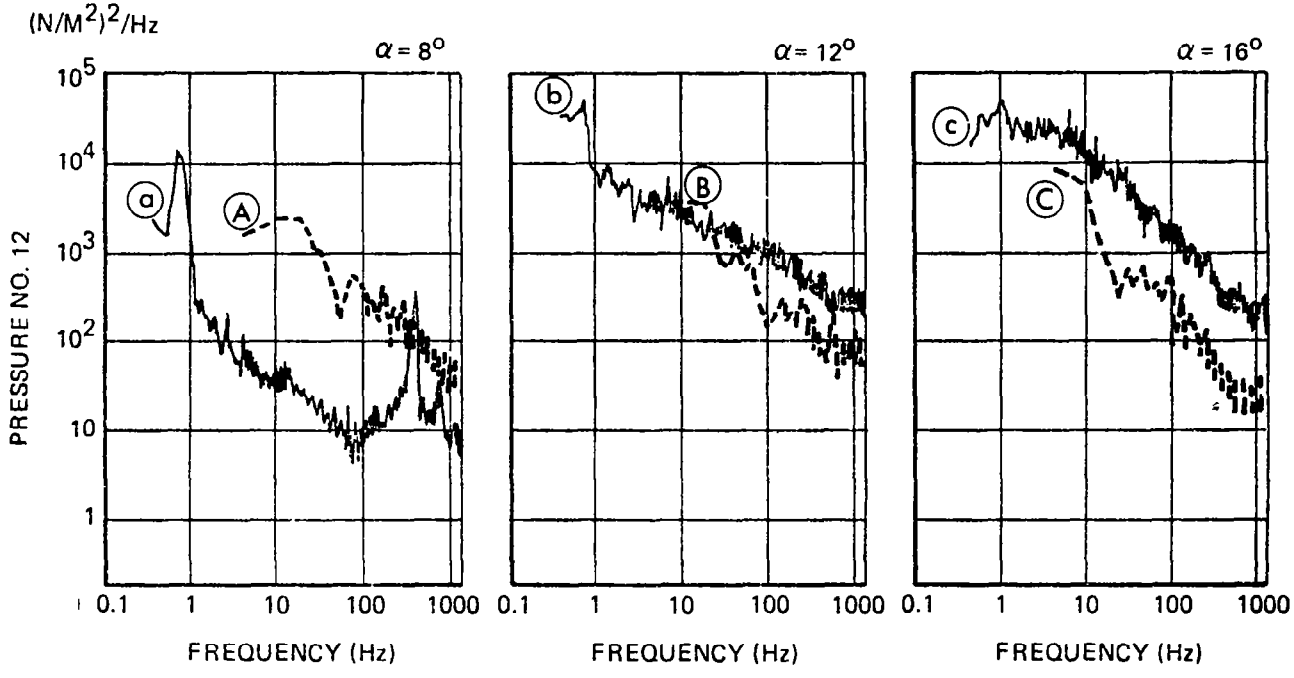

(a) α = 8°
(A) α = 7.2-8.6°

(b) α = 12°
(B) α = 11.4-13.2°

(c) α = 16°
(C) α = 13.9°

Figure 59. Pressure PSD Plots of Transducer No. 12 for Scale Model in Run 39, Phase I and F-5A Aircraft in Flight Test 825, Run 5, M = 0.925, δ_n/δ_f = 0°/0°, δ_h = 0°. The Scales are Based on Fight Test 825 Conditions.

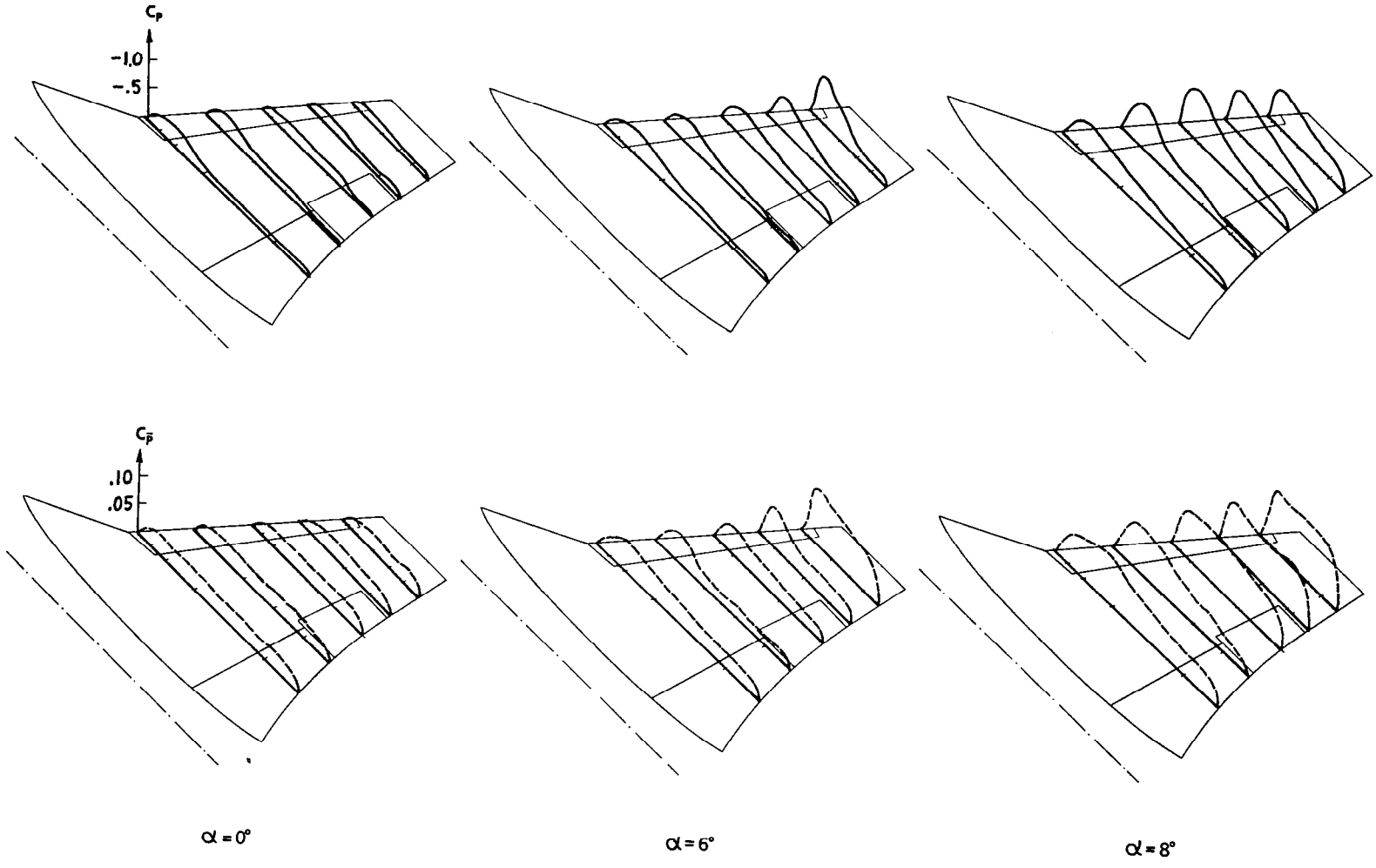

Figure 60. Static Pressure (C_p) and RMS Pressure ($C_{\bar{p}}$) Coefficient Distributions on the Right Wing Upper Surface, Run 43, Phase I - Configuration 9, $\beta = 0°$, $M = .75$, $\delta_n/\delta_f = 0°/0°$, $\delta_h = 0°$ (Continued)

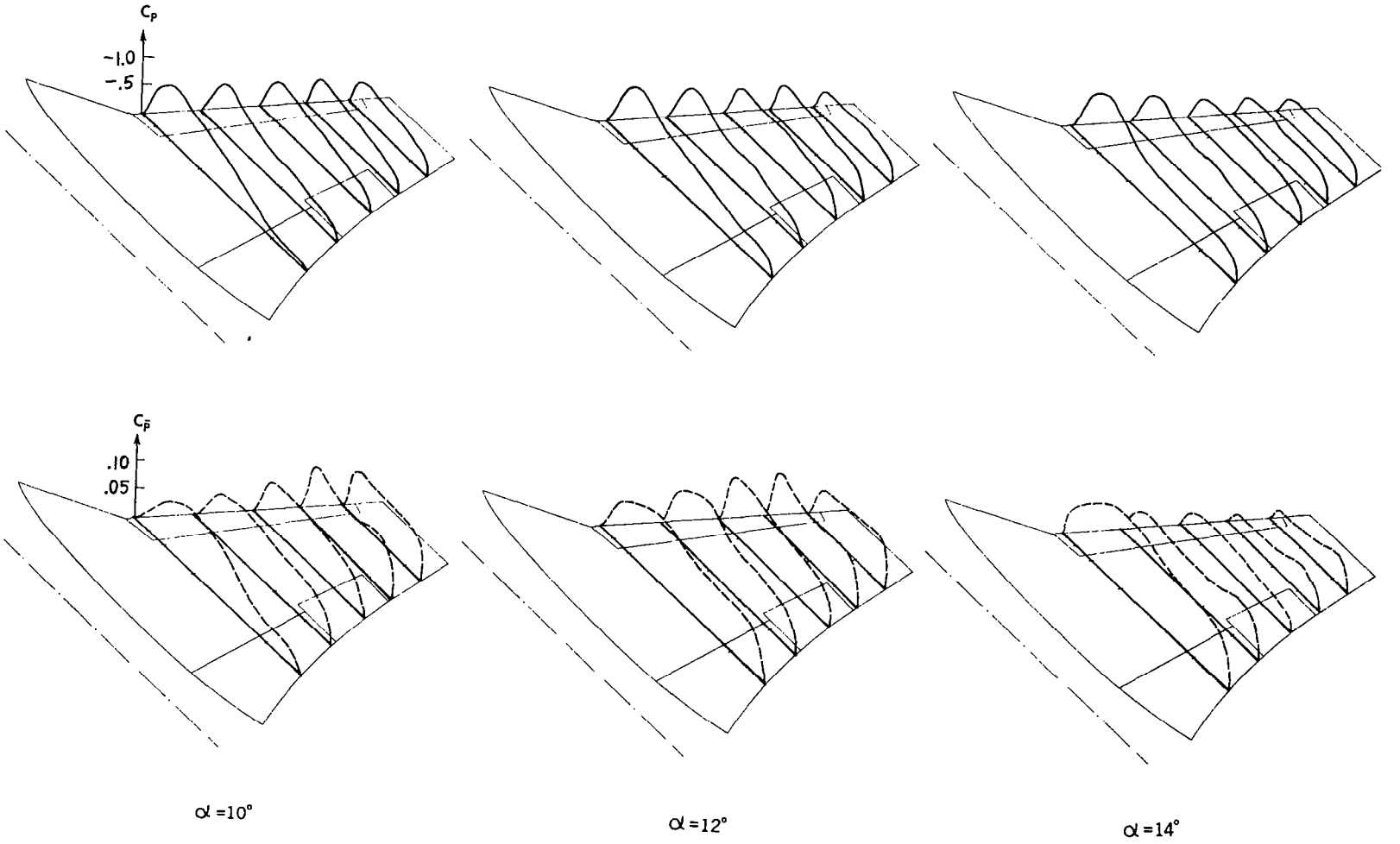

Figure 60. Static Pressure (C_p) and RMS Pressure ($C_{\bar{p}}$) Coefficient Distributions on the Right Wing Upper Surface, Run 43, Phase I - Configuration 9, $\beta = 0°$, $M = .75$, $\delta_n/\delta_f = 0°/0°$, $\delta_h = 0°$ (Concluded)

At α = 12 degrees, the complete upper wing surface was subjected to separated flow. This separation behavior was similar to the F-5A aircraft test data that also showed gradual development of flow separation with increasing α at M = 0.75 (Figure 34, Reference 1).

The PSD plots of pressure transducer Nos. 2, 5 and 11 based on Run 43 and α = 8 degrees, 12 degrees and 14 degrees are presented in Figures 61 to 63, respectively. The Run 43 data are identified by lower case letters a, b, and c. The PSD and frequency scales of the scale model data are on the righthand side and the bottommost portion of each plot. Also plotted on these figures are the corresponding PSD data obtained in Flight Test 825, Run 7 under the following flight conditions:

$$M = 0.75$$
$$h = 7{,}772 \text{ m } (25{,}000 \text{ ft.})$$
$$\delta_n/\delta_f = 0°/0°$$
$$R_N = 18.90 \times 10^6$$

Store: Wing-tip-mounted Sidewinders

Run 7, Flight 825 aircraft configuration and the Mach number were identical to the corresponding scale model test conditions of Run 43. Run 43 had a zero sideslip angle, while the sideslip angle of Run 7, Flight 825 was variable throughout the maneuver. The flight test PSD data are identified by capital letters A, B, and C, with the appropriate angle-of-attack range marked under each plot. The flight test and scale model data are plotted over each other taking into consideration the model scaling relation. The flight test PSD and frequency scales are on the left side and at the bottom directly under each plot. The arrowheads on the pressure PSD plots (Figures 61 to 63) for α = 8 degrees identify the peak frequencies corresponding to the rigid body and flexible mode motions of the scale model as defined in subsection 2.2 (page 13) and Figure 4 (page 17).

An examination of Figures 61 to 63 indicates that with allowance made for the difference in the flight test and model test conditions including the sideslip angle, the continuous changing angle-of-attack during flight, the difference in the structural modes of the aircraft and model, etc., the developments of the dynamic pressures for the two cases could be correlated.

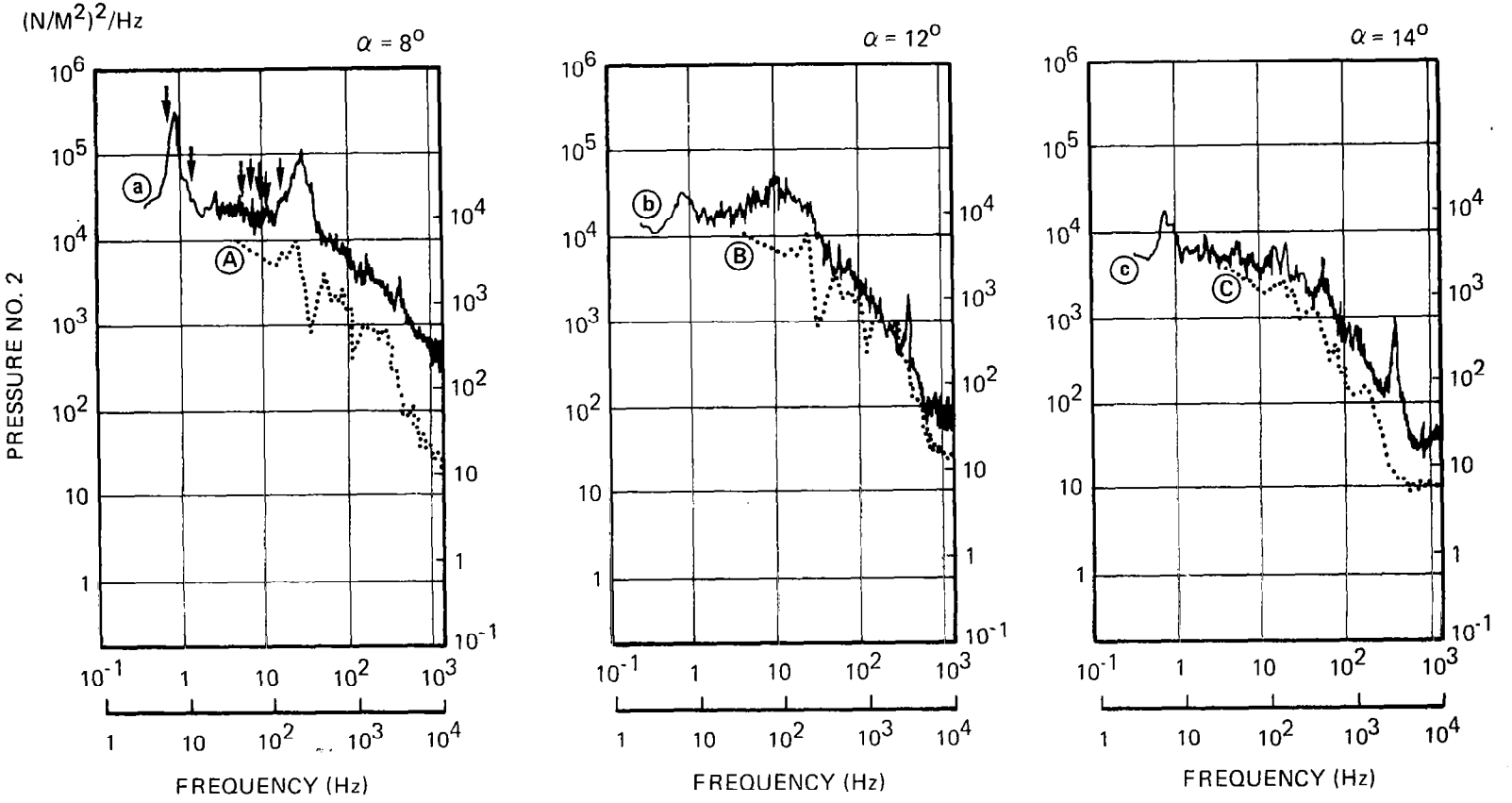

Figure 61. Pressure Plots of Transducer No. 2 for Scale Model in Run 43, Phase I and F-5A Aircraft in Flight Test 825, Run 7, M = .75, $\delta_n/\delta_f = 0°/0°$, $\delta_h = 0°$. The Left-Hand Scale and the Upper Frequency Scale are Based on the Flight Test Data.

The Right-Hand Scale and the Lower Frequency Scale are Based on the Scale Model Data.

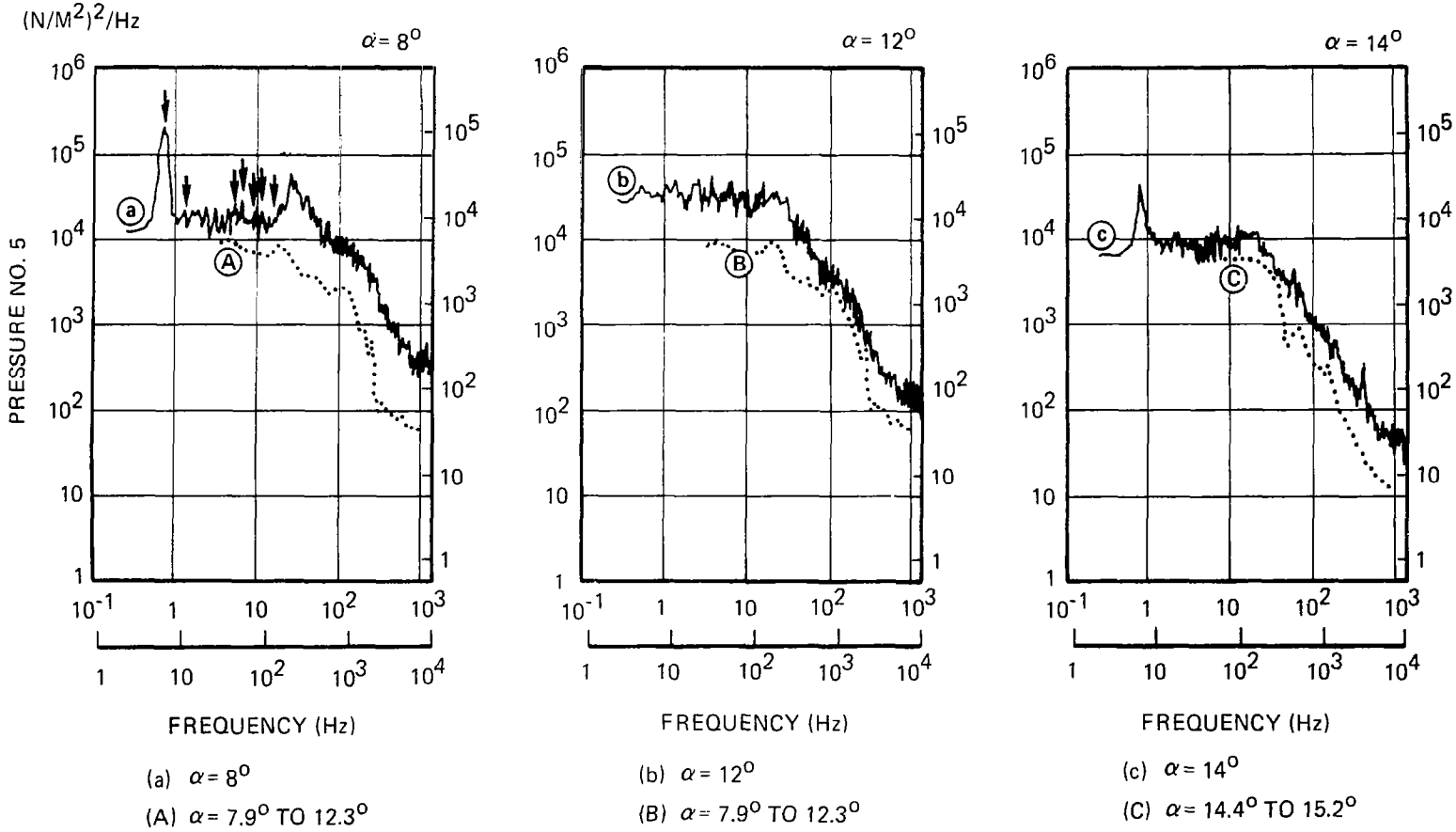

Figure 62. Pressure PSD Plots of Transducer No. 5 for Scale Model in Run 43, Phase I and F-5A Aircraft in Flight Test 825, Run 7, M = .75, δ_n/δ_f = 0°/0°, δ_h = 0°. The Left-Hand Scale and the Upper Frequency Scale are Based on the Flight Test Data. The Right-Hand Scale and the Lower Frequency Scale are Based on the Scale Model Data.

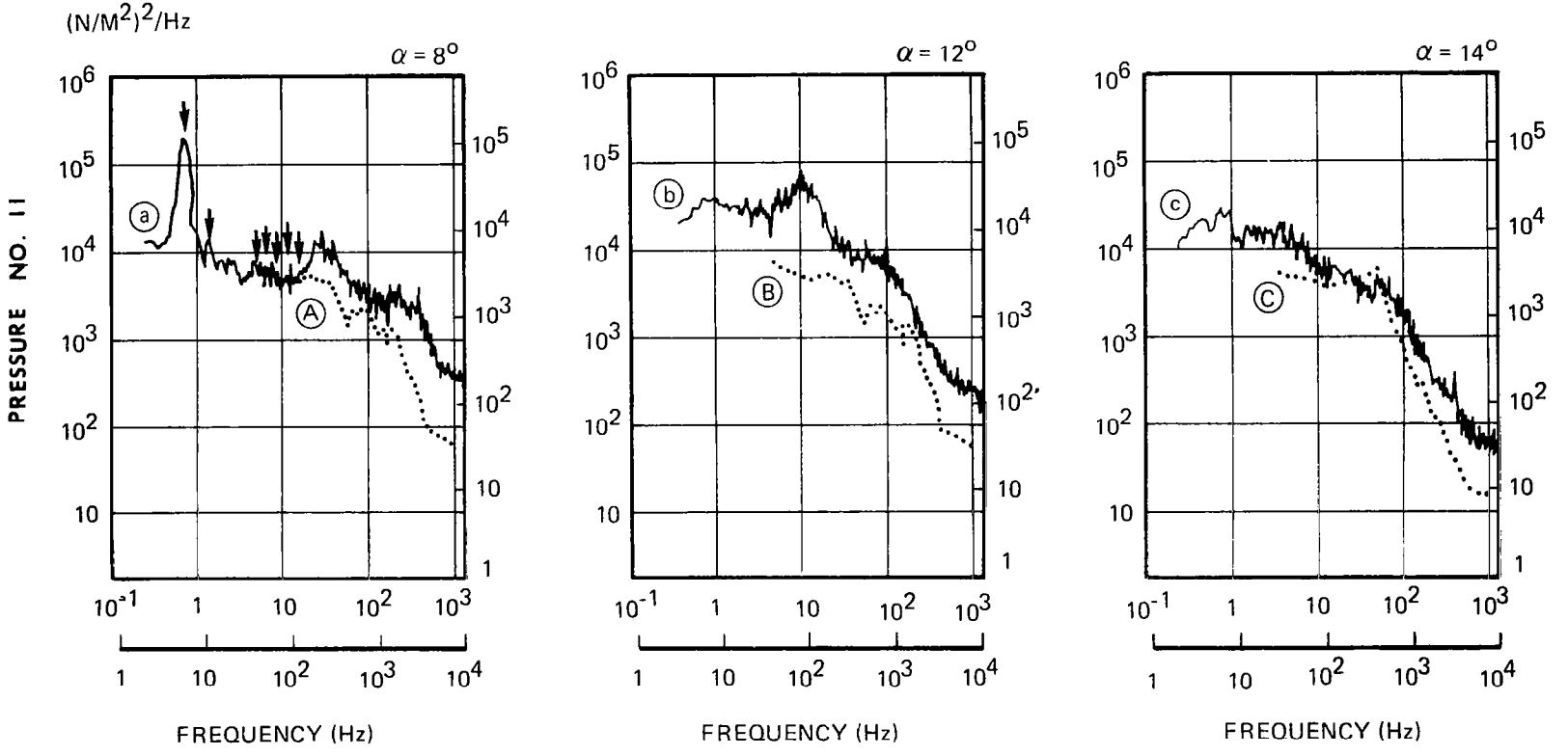

Figure 63. Pressure PSD Plots of Transducer No. 11 for Scale Model in Run 43, Phase I and F-5A Aircraft in Flight Test 825, Run 7, M = .75, δ_n/δ_f = 0°/0°, δ_h = 0°. The Left-Hand Scale and the Upper Frequency Scale are Based on the Flight Test Data. The Right-Hand Scale and the Lower Frequency Scale are Based on the Scale Model Data.

In general, the flight test pressure PSD levels were somewhat lower (in the order of 5 dB) than the corresponding model test data. The consistent deviation in the spectral level might be contributed, at least partially, to the Reynolds number effect corresponding to the flight and tunnel test conditions (R_N = 18.90 x 10^6 vs. 4.71 x 10^6).

In the transonic range with flow separation, it is known that the Reynolds number effect is significant for wings with thick airfoil, such as those with a thickness/chord ratio of 8 to 10 percent. In actual flight conditions where the Reynolds number is high, the shock-induced transition point is further downstream as compared to the low Reynolds number case if other conditions are identical. In model tests for the same flow condition, except with a lower Reynolds number, the flow transition strip tends to trigger the flow separation prematurely. The result is less favorable lift distribution and drag. Furthermore, the location of the transition strip is known to affect the flow separation significantly for thick airfoils.

For thinner airfoils - e.g., the F-5A with NACA 65A004.8 wing airfoil sections - it is expected that the Reynolds number effect is less significant. For M = 0.75 and 0.925, the range of Reynolds numbers of the available data is as follows:

TYPE OF TEST	M = 0.75	M = 0.925
Flight Tests	18.90 x 10^6	17.24 x 10^6
Tunnel Tests	2.48 x 10^6 to 4.71 x 10^6	2.48 x 10^6 to 4.71 x 10^6

The flight test and model test data for the F-5A were examined to evaluate the Reynolds number effect. Since only dynamic pressure transducers were used in the flight tests, which did not yield valid static pressure data, a comparison of the dynamic pressure coefficients and spectral makeups in the separated flow region as well as the transition line as a function of α were used to determine the Reynolds number effect.

Figures 64 and 65 present the dynamic pressure coefficient distributions of Run Nos. 39 and 43, Phase I test and corresponding flight test 825 data

...ure Coefficient Distributions for Scale Model in Run 39,
...925. Run 5 Conditions, M = 0.925,

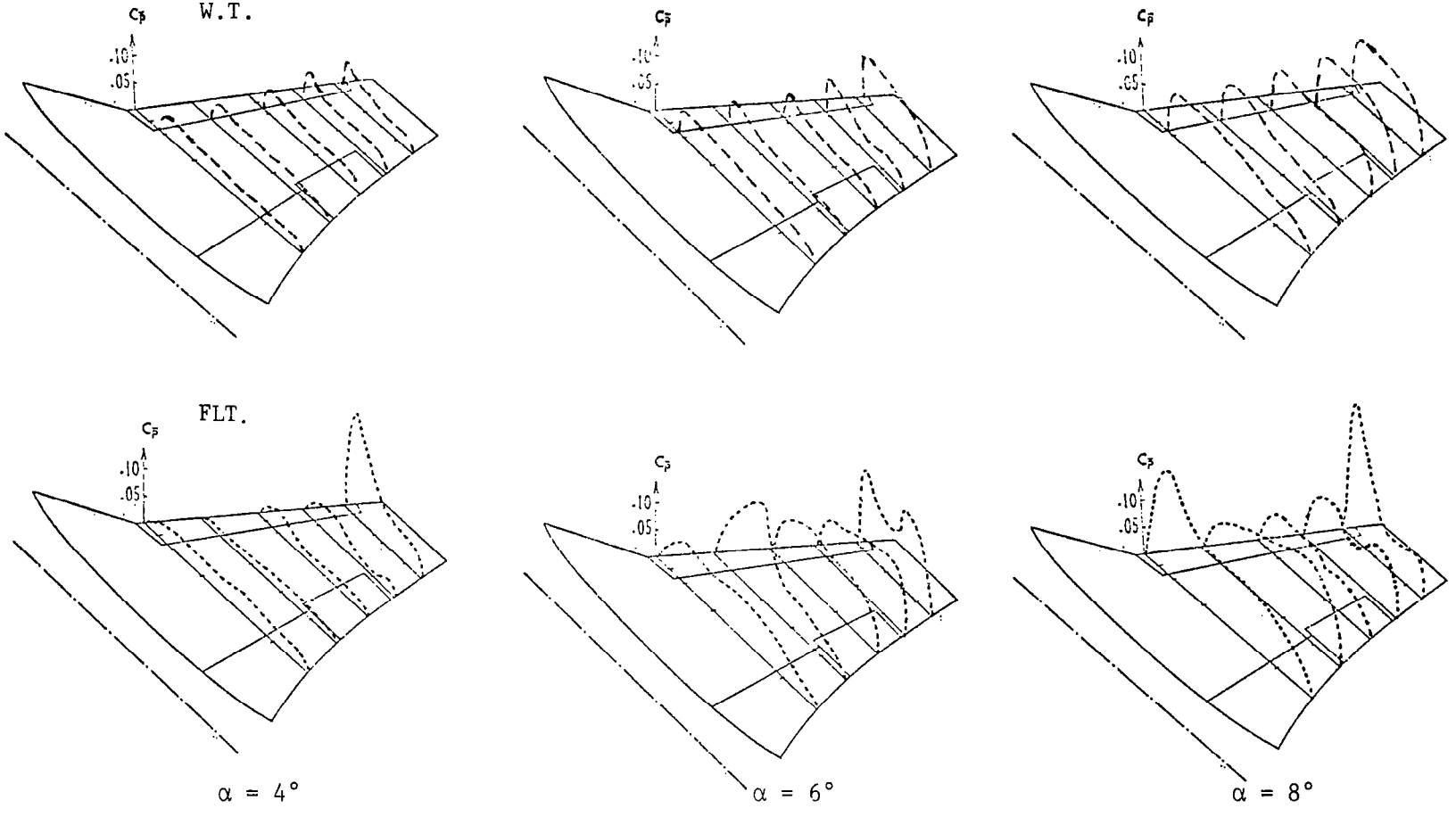

Figure 65. Comparison of Dynamic Pressure Coefficient Distributions for Scale Model in Run 43, Phase I and F-5A Aircraft in Flight Test 825 Run 7 Conditions, M = 0.75, δ_n/δ_f = 0°/0°.

for α = 4°, 6°, and 8°. The model Reynolds numbers for Run Nos. 39 and 43 were 3.87 x 10^6 and 4.71 x 10^6, respectively.

Based on the data shown in Figures 64 and 65, it was found that the trend of development and expansion of the flow separation region were similar for the wind tunnel model test and the corresponding flight test. In general, measured in angle-of-attack, it took the scale model approximately an addition 2°-4° to develop a similar separation flow pattern on the top wing surfaces. For M = 0.925 case (Figure 64), at a given spanwise location, the shock tended to stay closer to the trailing edge on the scale model as against the flight test results. This observation appears to be contrary to previous test results. For instance, References 2,3 show that under identical conditions except for Reynolds number, the shock on the scale model always appeared further upstream in relation to the full-scale aircraft wing section when the airfoil section thickness ratio was high. The phenomenon observed in the present test was somewhat perplexing since transition strips were installed on this F-5A scale model which should trigger the shock-induced flow separation in an upstream location on the wing chord; i.e., the artificial boundary layer transition together with testing at less than flight Reynolds number should result in a relatively thicker model boundary layer, hence, leading to earlier shock-induced separation. In evaluating this problem, certain factors were noted which were believed to contribute to the scale model flow behavior: (1) the aeroelastic effect of the full-scale aircraft caused an increase in the local angle-of-attack in the outer span of the wing. It was known that in F-5A aircraft, under the conditions where the pressure data were evaluated (M = .925, h = 10,668m, Q = 14.36 KN/m^2), the wing-tip was twisted in such a manner that its local angle-of-attack was increased $1\frac{1}{2}$ to 2°; (2) the transient effect in a transonic maneuver of the aircraft where the angle-of-attack changed continuously; (3) F-5A wing has a thin airfoil section, namely NACA 65A004.8.

4.5 Typical Response Power Spectra and Dynamic Aeroelastic Effect

It was well known that under moderate to high dynamic pressures, a fairly rigid scale model such as the F-5A model will respond to the tunnel aerodynamic forces with measurable displacements. With this point in view, the F-5A scale model was instrumented to measure certain accelerations and wing root section moments as described in Table 1. The dynamic responses were dependent on the model vibration modes and the structural characteristics of the supporting system, The modal data of the fixed and the flexibly-supported models were described in subsection 2.2. Even though these dynamic characteristics were quite different from the real aircraft, the model response data may be analyzed and extended to predict full-scale aircraft responses under dynamic buffet pressures.

For Run 8, Phase I the right wing-tip acceleration (1a) data were processed into power spectra corresponding to α = 0 degree, 8 degrees, 12 degrees, 16 degrees. The spectral processing was limited to 0-200 Hz using the average of 16 records, each of 2 seconds duration. The processing bandwidth was 1/2 Hz. The power spectra obtained in this manner were presented in Figure 66. The PSD and frequency scales were the test data scales. For the power spectrum corresponding to α = 0 degree, certain peaks were identified with letters described as follows (see Figure 4):

A. Sting and Balance Bending, 6.6 Hz
B. Balance Roll, 13.6 Hz
C. Model Wing 1st Symmetrical Bending, 53.5 Hz
D. Rigid Roll Plus Wing Anti-Symmetrical Bending, 71 Hz
E. Wing Anti-Symmetrical Bending, 82.7 Hz
F. Sting and Support System Torsion, 105 Hz. The peaks appear at 120 Hz in some PSD plots may be due to the harmonics of the line noise.
G. Wing 2nd Symmetrical Bending, 171 Hz.

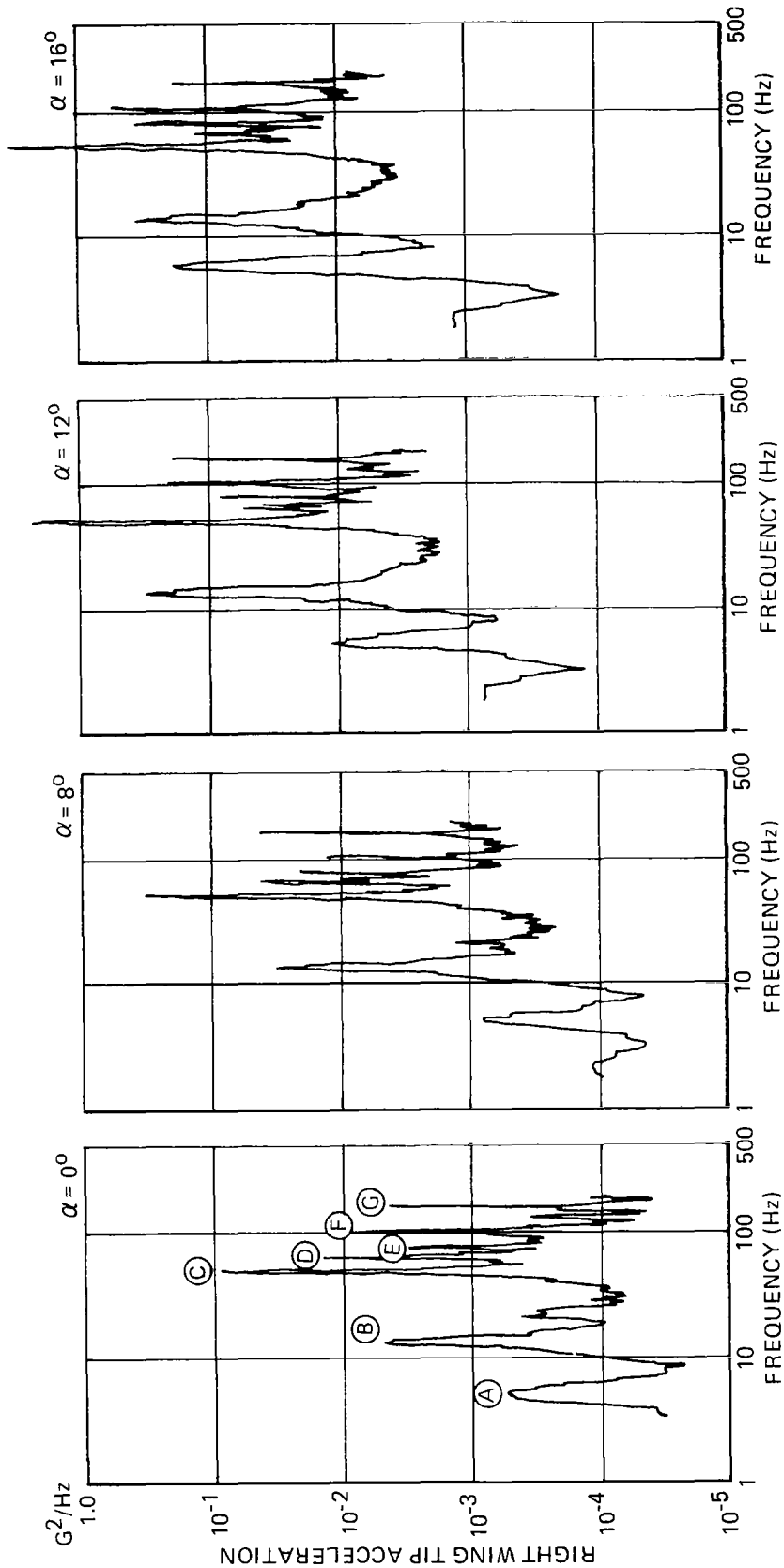

Figure 66. F-5A Scale Model Right Wing-Tip Acceleration PSD Plots, Run 8, Phase I, $\beta = 0°$, $M = .926$, $\delta_n/\delta_f = 5°/12°$, $\delta_h = 0°$. The Scales are Based on Actual Test Conditions.

In examining Figure 66, it was noted that in the very low frequency region (under 10 Hz), the increase per degree of angle-of-attack in response spectra (and rms level) was moderate for α = 0 degree to α = 8 degrees, when compared with corresponding increase for α = 8 degrees to α = 12 degrees. In reviewing the static and dynamic pressure data (Figure 10), α = 8 degrees may be considered as the approximate condition where buffet onset took place. The model responded with increasing rate of intensity after buffet onset. It was also noted that except for the mode corresponding to model support system bending, the change in wing-tip responses from α = 12 degrees to α = 16 degrees was very moderate. This was consistent with the dynamic buffet pressure data, where the spectral density level reached a plateau corresponding to large angles-of-attack well after buffet onset (See Figures 47, 48).

In Figure 67,68, the acceleration PSD's at the left wing-tip (2a) and the CG (3a) were processed and plotted. The test conditions were identical to those of Figure 66. The peaks of the PSD's at α = 0 degree were identified with the same letters as in Figure 66. A comparison of Figures 66,67, showed that the left and right wing-tip responded to both symmetrical and antisymmetrical modes with fairly even intensity for all angles-of-attack. The only exception was for peaks (A), (B) at α = 16 degrees. The difference in the tip responses for the latter case seemed to indicate some asymmetrical model motion, possibly due to the asymmetrical mass inertia distribution (cut-outs, channels, etc.) in the wing structures. The CG PSD plots (Figure 68) showed the ever increasing PSD intensity with α corresponding to the support system bending (A). As was expected, the peaks corresponding to the model antisymmetrical modes (D), (E) were relatively low at the CG.

The roll moment data acquired by the 6-component balance were processed into PSD's and presented in Figure 69. Peak identifications for the PSD of α = 0 degree were the same as the previous figures (Figures 66 - 68), with the exception that the peak at (C) (60 Hz) seemed to indicate a line noise. The 120 Hz peak at (F) also contributed to line noise harmonics.

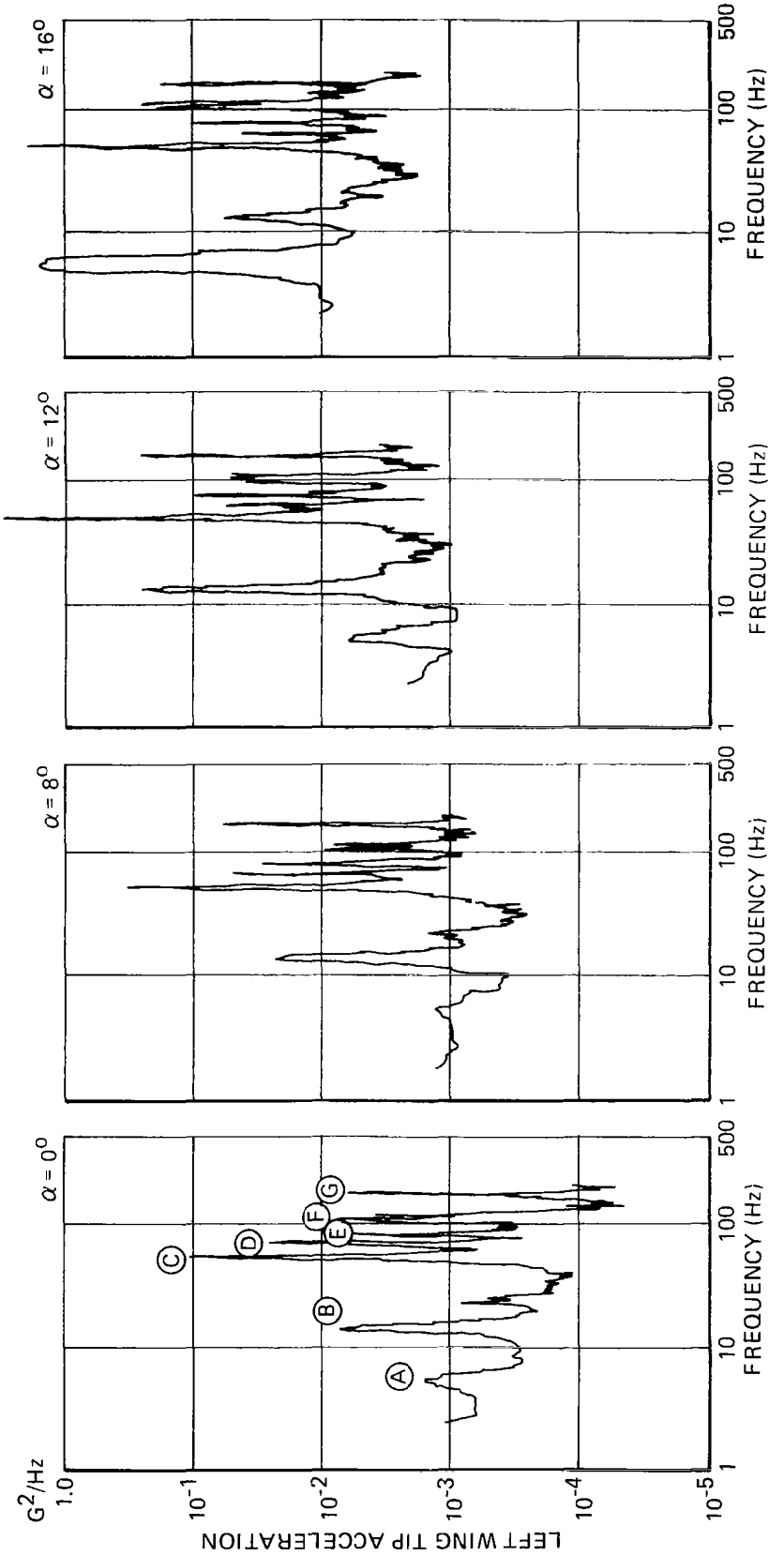

Figure 67. F-5A Scale Model Left Wing-Tip Acceleration PSD Plots, Run 8, Phase I, $\beta = 0°$, $M = .926$, $\delta_n/\delta_f = 5°/12°$, $\delta_h = 0°$.

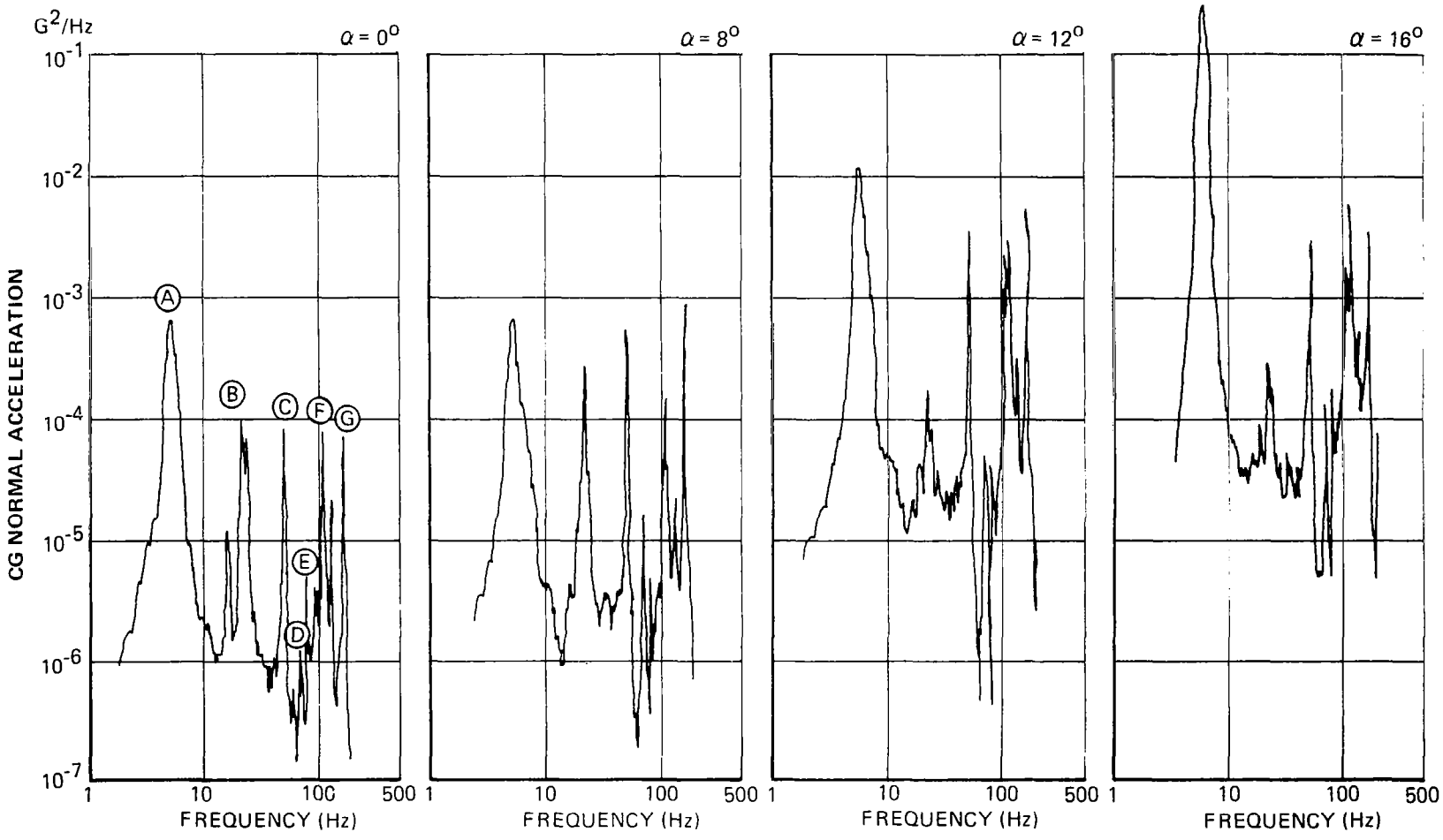

Figure 68. F-5A Scale Model CG Acceleration PSD Plots, Run 8, Phase I, $\beta = 0°$, M = .926, $\delta_n/\delta_f = 5°/12°$, $\delta_h = 0°$.

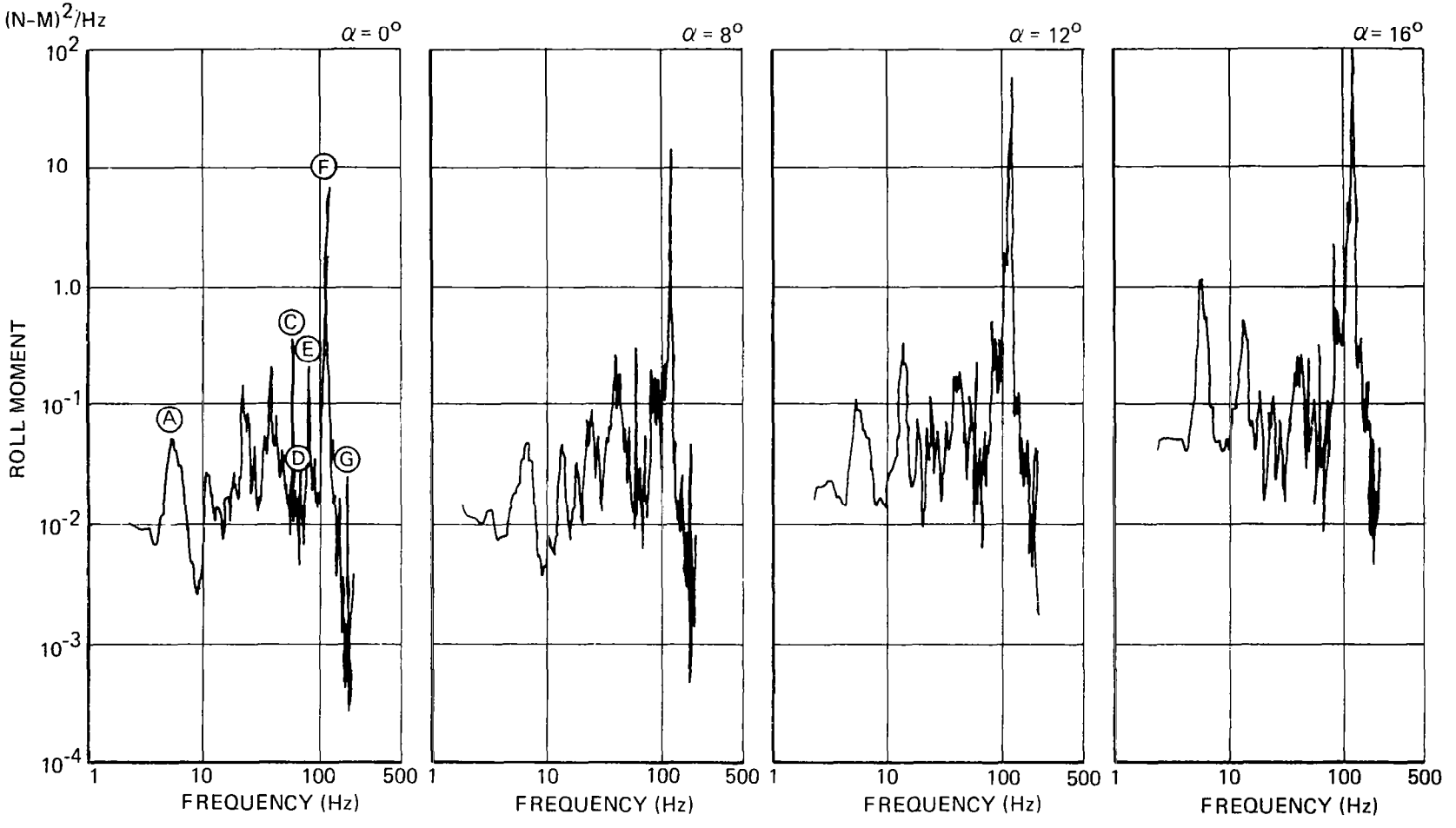

Figure 69. F-5A Scale Model Roll Moment PSD Plots, Run 8, Phase I, $\beta = 0°$, $M = .926$, $\delta_n/\delta_f = 5°/12°$, $\delta_h = 0°$.

For the F-5A scale model, semi-conductor type strain gages(Kulite ULP-120-160) were installed near the semi-span root sections. Since the wing structure was made of solid steel with cut-outs and harness channels, etc., it was not possible to install gages which yielded sectional bending and torsion moment data directly. Through a pretest calibration procedure using various loading conditions, calibration formulas were developed to give approximately sectional bending and torsional moments based on gage outputs. Applying these formulas, the bending and torsional moments were acquired for Run 8. The corresponding PSD plots for four angles-of-attack (α = 0°, 8° 10°, 12°, 16°) were presented in Figures 70, 71. Identical peak mode designations (as in Figure 66) were applied on these figures for α = 0 degree. Referring to Figure 70, the bending moment PSD level behavior as a function of α was somewhat similar to the wing-tip acceleration PSD level variations (Figure 66,67). The torsional moment plots (Figure 71) featured lower PSD levels as compared to the bending moments. This was to be expected since the F-5A wing featured a moderate sweep back. Again the trend of PSD level increases with α was consistent with the dynamic pressure and acceleration PSD data presented previously.

In order to demonstrate the impact of the rigid body and flexible mode motions to the unsteady pressure forces, the model right wing-tip acceleration PSD for Run 43, Phase I, at α = 8 degrees is presented in Figure 72. Referring to the figure, the spectral peaks noted as (A) through (G) were identified previously. The seven peak frequencies were identified by arrowheads on the corresponding pressure PSD plots of Figures 61-63. An examination of the figures indicated that only corresponding to mode (A), the low frequency sting and balance bending mode, there appeared prominent pressure peak. The other modes (B) through (G) were not prominently represented in the corresponding pressure PSD plots. In general, it might be concluded that only very low frequency modes (10 Hz or less) had a prominent effect on the separated flow dynamic pressures.

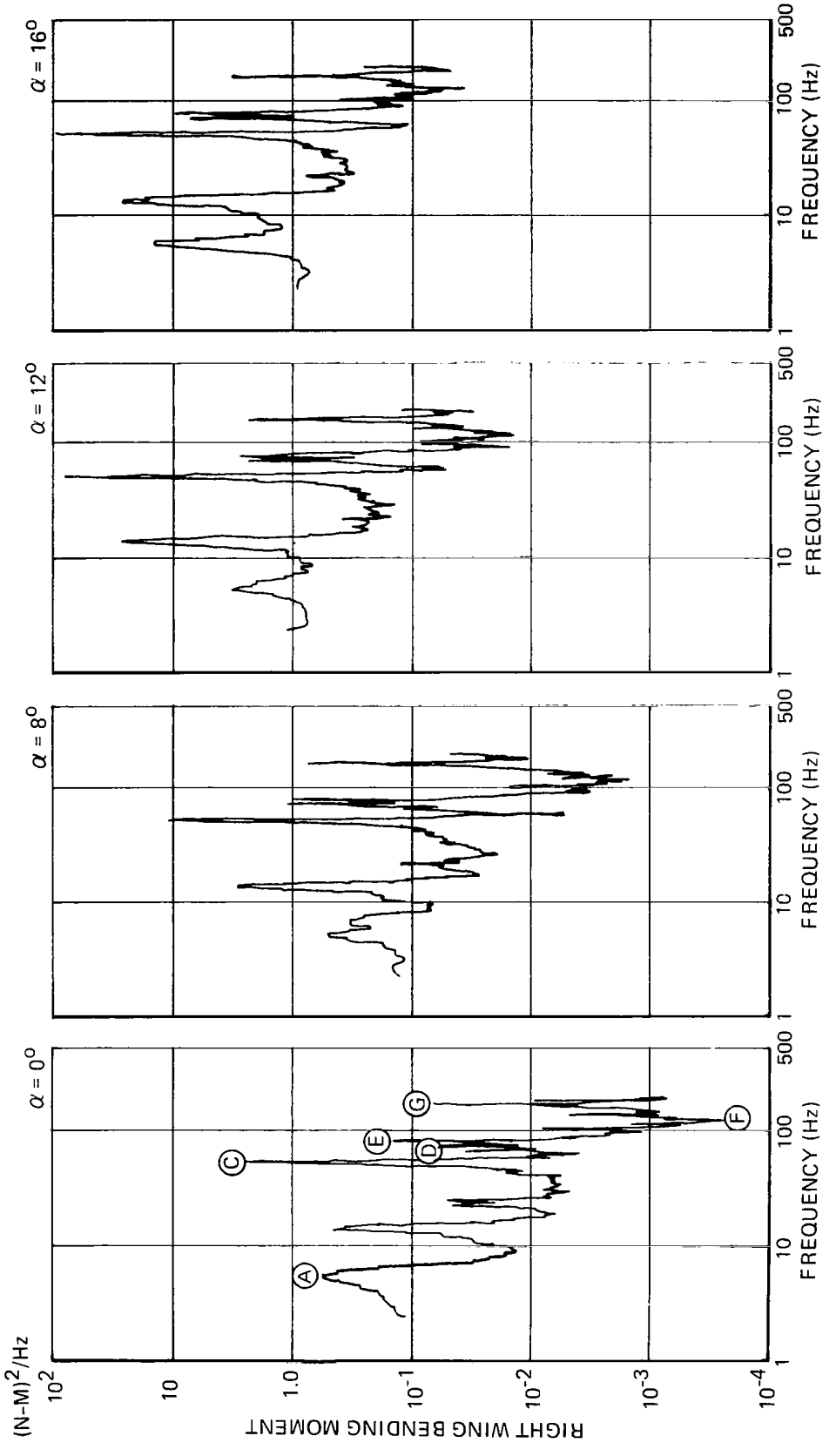

Figure 70. F-5A Scale Model, Right Wing Root Section Bending Moment PSD Plots, Run 8, Phase I, $\beta = 0°$, M = .926. $\delta_n/\delta_f = 5°/12°$, $\delta_h = 0°$.

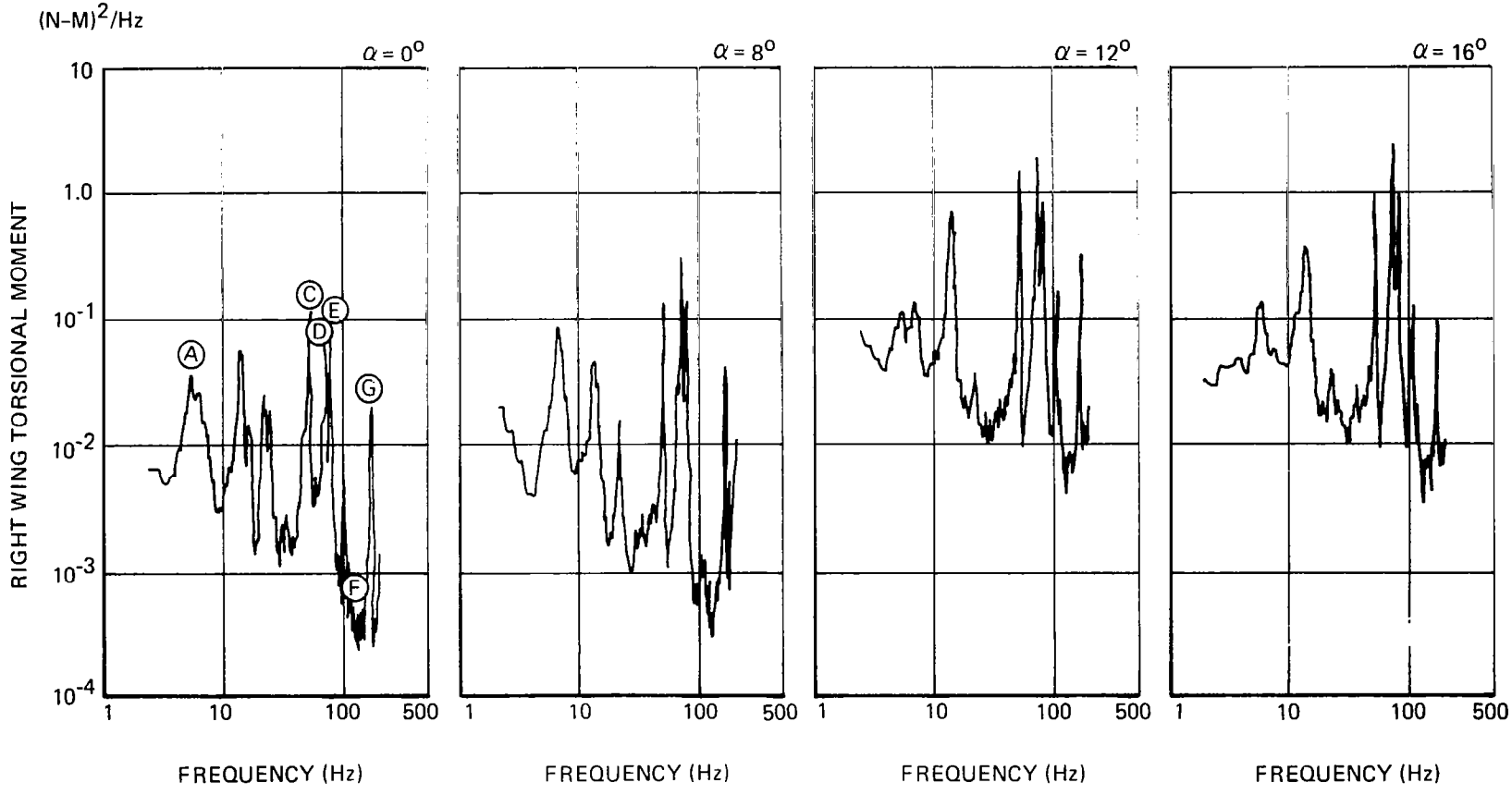

Figure 71. F-5A Scale Model, Right Wing Root Section Torsional Moment PSD Plots, Run 8, Phase I, $\beta = 0°$, M = .926, $\delta_n/\delta_f = 5°/12°$, $\delta_h = 0°$.

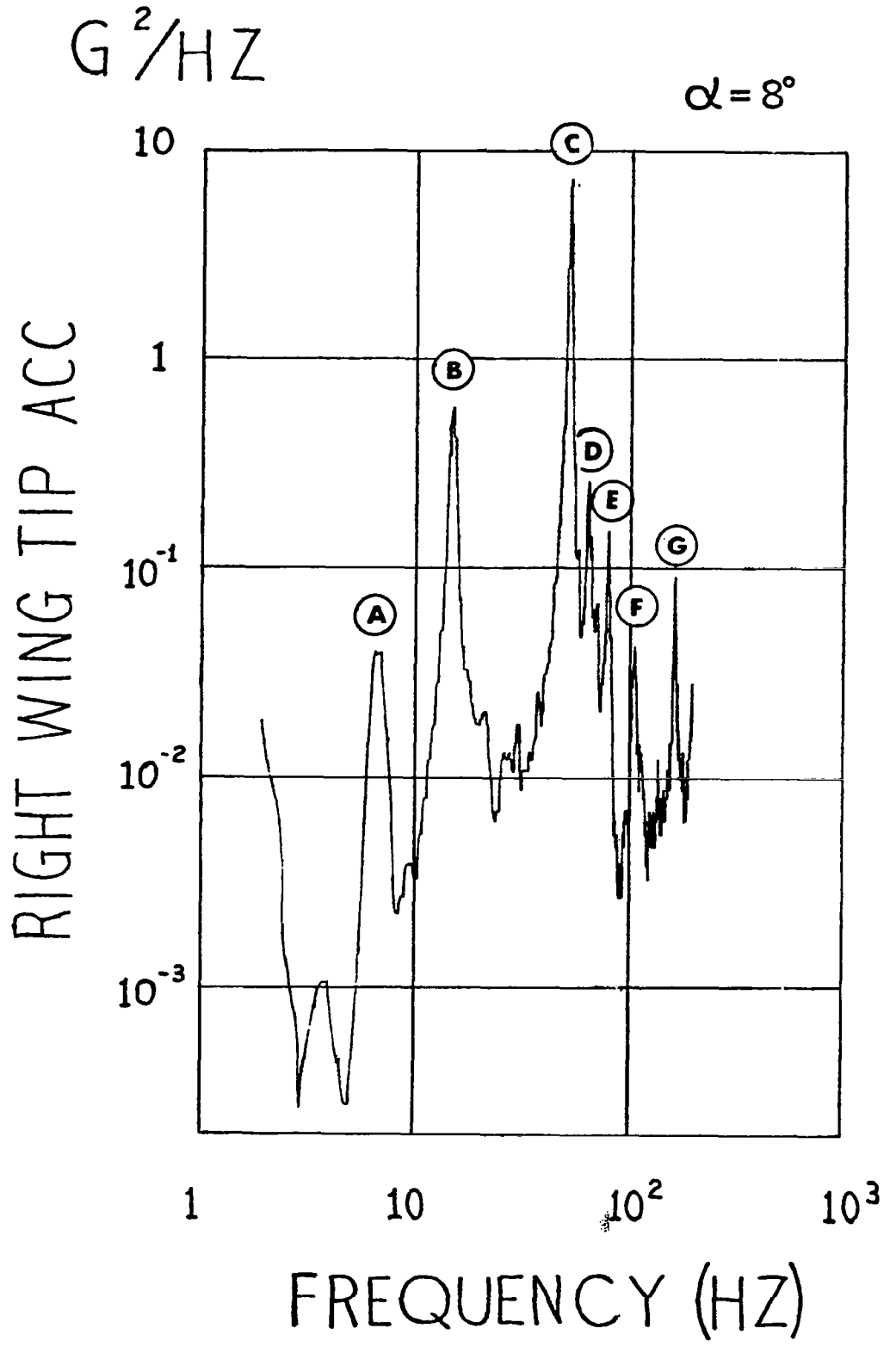

Figure 72. PSD of Right Wing-Tip Acceleration of F-5A Scale Model, Run 43, Phase I, $\alpha = 8°$, $\beta = 0°$, $M = .75$, $\delta_n/\delta_f = 0°/0°$ $\delta_h = 0°$

4.6 Low Frequency Range Pressure and Response PSD Data Corresponding to Maximum Wing-Rock Motion

As described previously in subsection 3.6, during Phase II test, the model oscillated in roll as the angle-of-attack setting approached a critical value. In order to define the correlation between the roll oscillations and the dynamic buffet pressures or the model accelerations, PSD plots of fluctuating pressures and responses were generated to cover the low frequency range (0.5 Hz to approximately 100 Hz) for two typical cases when the maximum wing-rock type motion occurred. For Run 26, $\alpha = \alpha^* = 10°$, the model oscillated steadily and continuously throughout the recording period (Figure 35). For Run 5, $\alpha = \alpha^* = 10°$, the motion was highly nonstationary. The oscillations started in a random manner, reached a maximum amplitude and then died out (Figures 36). Corresponding Phase I data (Run 51 and Run 8) were also processed for comparison purposes. The results are presented below.

Run 26 of Phase II test was conducted in test model Configuration 11, $\delta_n/\delta_f = 0°/0°$, $\delta_h = -10°$, $\delta_a = 0°/0°$, $\beta = 8°$, Sidewinder missiles at wingtips, M = .925, and $\alpha^* = 10°$. The corresponding Phase I test with a regular sting mount was Run 51. Typical pressure and response data of both runs were processed into power spectra at $\alpha = 10°$ where the steady, high-amplitude roll oscillations occurred during Phase II test. The spectral processing was limited to 0.5 - 100 Hz using the average of 8 records, each of 4 seconds duration. The acceleration spectral data at the right wingtip and the CG are presented in Figure 73. The plots on the left hand side are for Run 51, Phase I. The right hand side plots are for Run 26, Phase II. Referring to the response data, the major peaks were identified as below:

	PHASE I	PHASE II
A	Balance-Sting Bending	Sting Bending
B	Balance Roll	Roll Device Oscillation
C	First Wing Symmetrical Bending	First Wing Symmetrical Bending

The PSD plots for right wing-tip acceleration indicated a difference of 37 dB in the first response peak (under 10 Hz) between the two runs, reflecting the large-amplitude roll oscillations in Phase II.

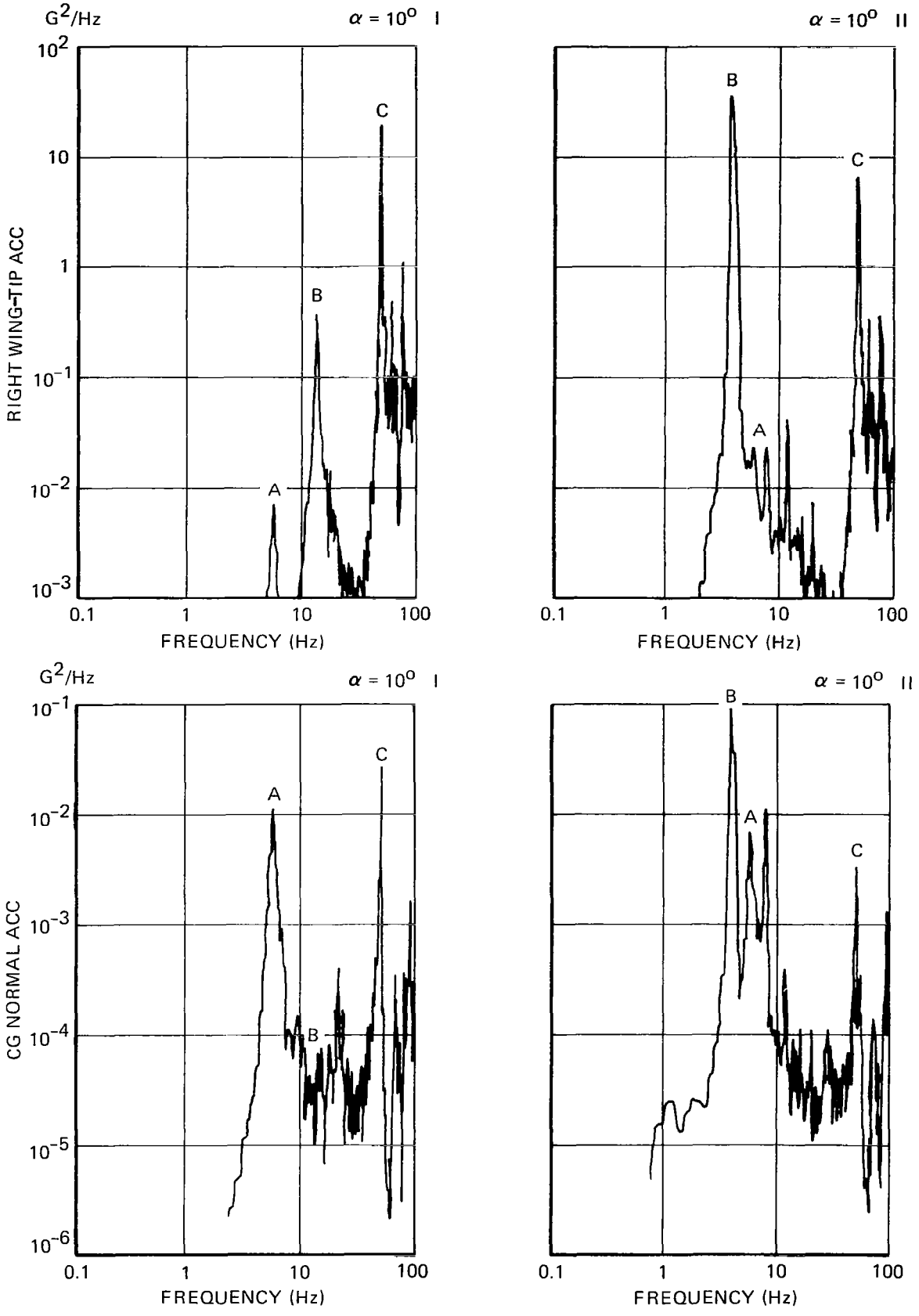

Figure 73. PSD of Right Wing-Tip Acceleration and CG Acceleration of the F-5A Scale Model, Run 51, Phase I (left) vs. Run 26, Phase II, $\alpha = 10°$, $\beta = 8°$, $M = 0.925$, $\delta_n/\delta_f = 0°/0°$, $\delta_h = -10°$.

In examining the pressure data, the dynamic pressure coefficient plots for Run 51, Phase I and Run 26, Phase II at $\alpha = 0°$ and $\alpha = 10°$ are shown in Figure 74. It was observed that the dynamic pressure levels in the inboard portion of the right wing upper surface for Phase II data at $\alpha = 10°$ were much higher in comparison with the Phase I data. This seemed to be a common trend for the windward side of the wing semi-span of the model with a sideslip when α approached the critical angle-of-attack. The pressure PSD plots for transducer Nos. 3, 10, 11, 17, 22, 24 are presented in Figures 75 to 77 respectively. The locations of the transducers are given below:

Transducer Number	Surface	% Semi-Span	% Chord
3	RH Wing Upper	85	40
10	RH Wing Upper	61	21
11	RH Wing Upper	61	60
17	RH Wing Upper	33	42
22	RH Tail Upper	47	40
24	RH Tail Lower	47	40

For Run 51, Phase I, the pressure peak corresponding to the Balance-Sting bending mode (as identified by letter A in the left hand side plots of Figures 75 to 77) may be clearly observed, while the pressure peaks corresponding to the other modal response frequencies above 10 Hz, if observable, were obscure. On the other hand, the pressure PSD's for Run 26, Phase II, featured a prominent peak corresponding to the natural roll frequency (as identified by letter B in the right hand side plots of Figures 75-77), with a number of unidentified lesser pressure peaks below 50 Hz. Corresponding to the first wing bending mode (51.6 Hz), no prominent pressure peak was in evidence. It was noteworthy that the pressure peak level at 4 Hz was extremely high for most of the transducers. No corresponding flight test results have yielded such a pressure level during wing rock in transonic flight. A key reason for the lack of a corresponding high pressure peak for aircraft wing rock might be due to the lack of sustained low frequency oscillation data covering a long time span. The pressure spectral data at frequencies above 100 Hz, not presented here, showed much less differences in both amplitude and

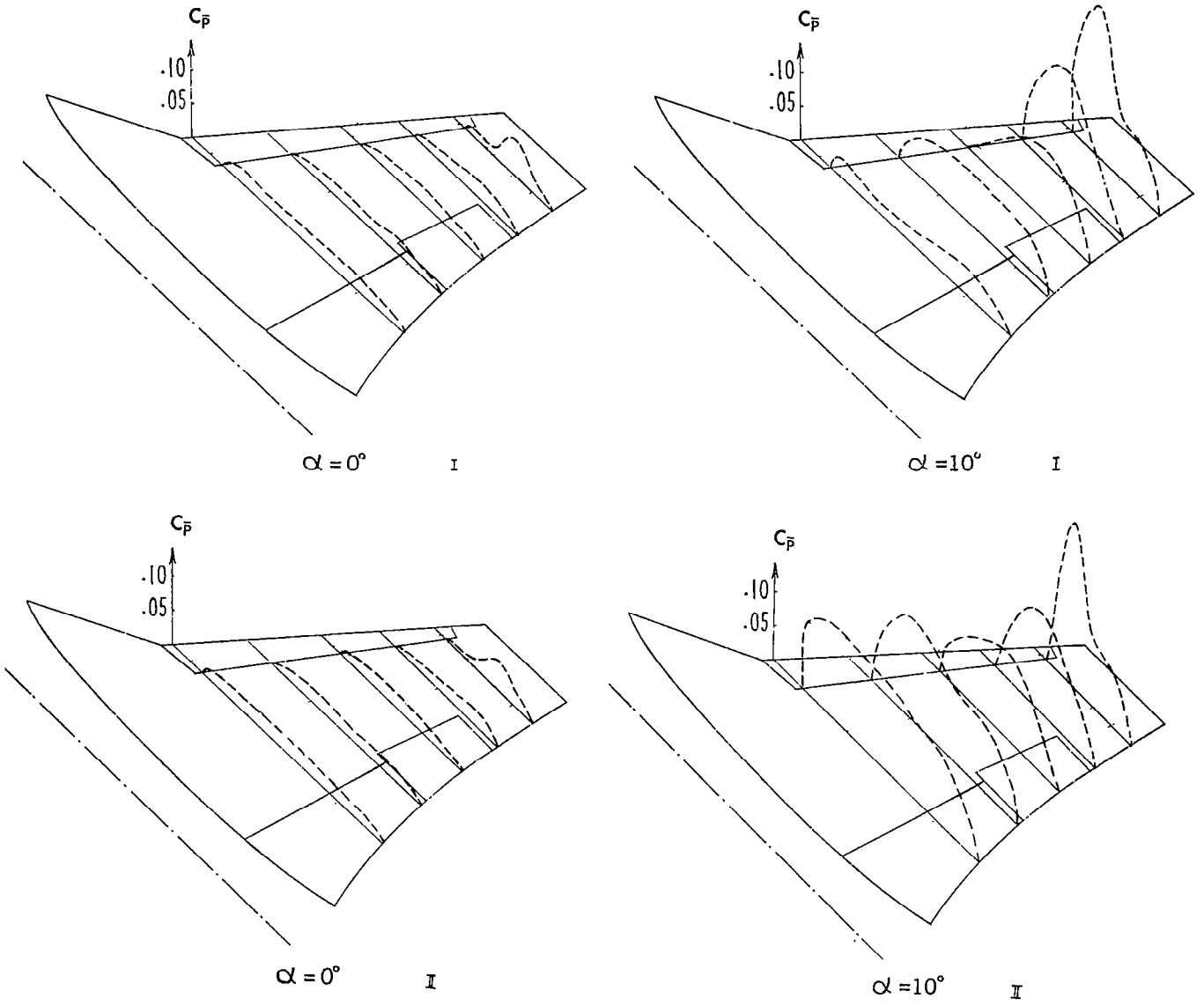

Figure 74. Comparison of Dynamic Pressure Coefficient Distributions for the Fixed Model, Run 51, Phase I (top) and the Oscillating Model, Run 26, Phase II, $\beta = 8°$, $M = 0.925$, $\delta_n/\delta_f = 0°/0°$, $\delta_h = -10°$.

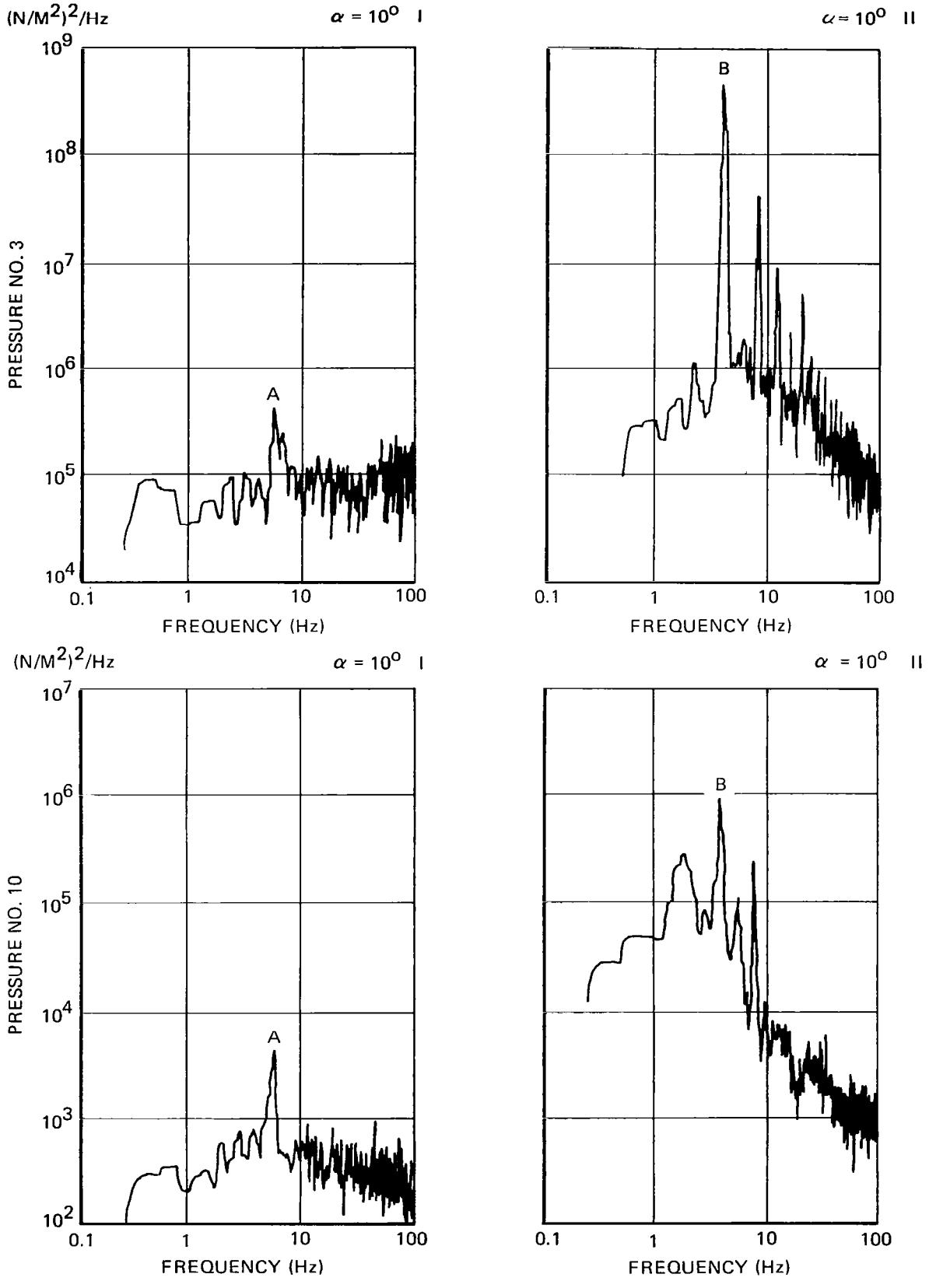

Figure 75. Comparison of Wing Pressure PSD Data for the Fixed Model, Run 51, Phase I (left) and the Oscillating Model, Run 26, Phase II, $\alpha = 10°$, $\beta = 8°$, $M = 0.925$, $\delta_n/\delta_f = 0°/0°$, $\delta_h = -10°$.

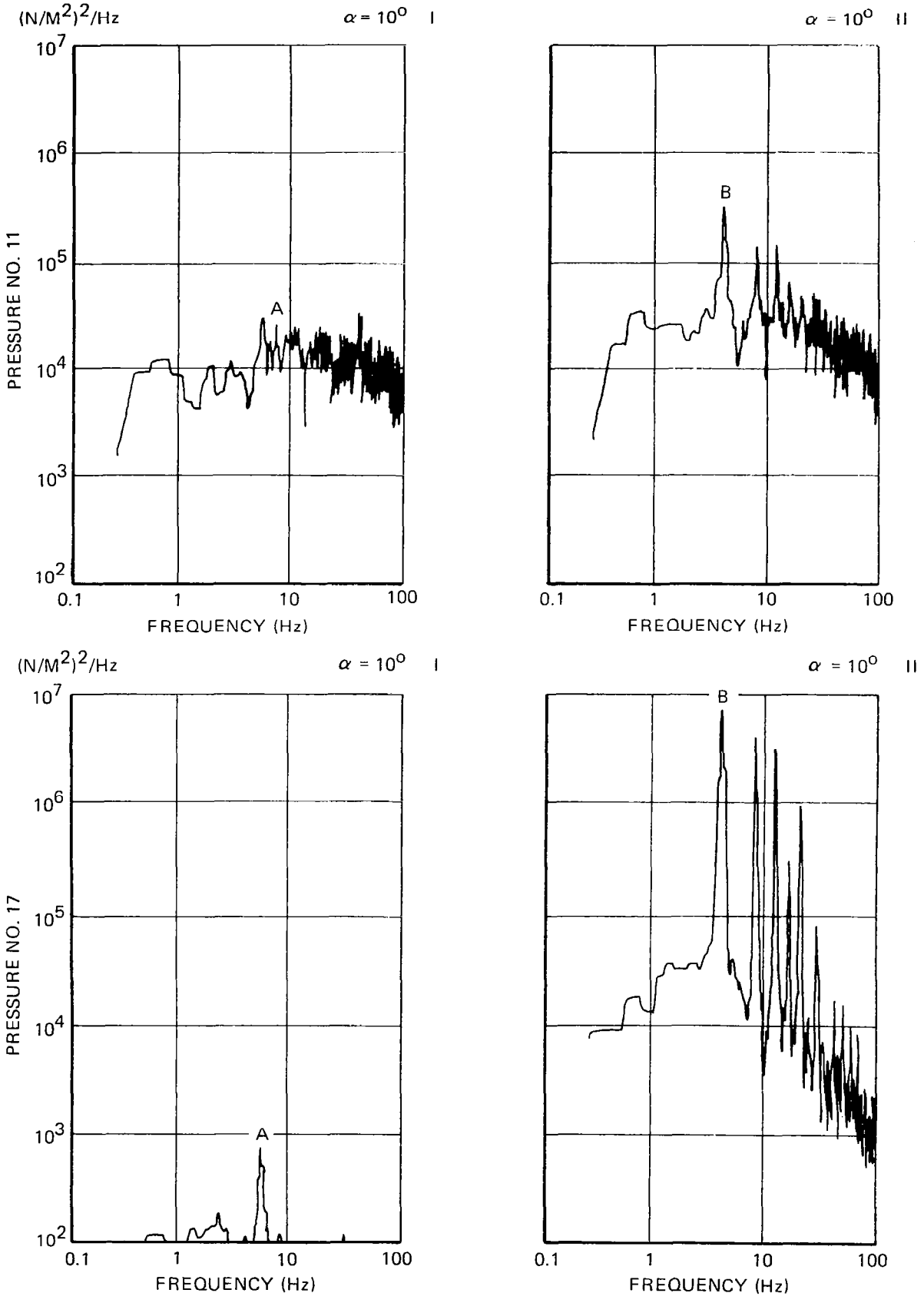

Figure 76. Comparison of Wing Pressure PSD Data for the Fixed Model, Run 51, Phase I (left) and the Oscillating Model, Run 26, Phase II, $\alpha = 10°$, $\beta = 8°$, $M = 0.925$, $\delta_n/\delta_f = 0°/0°$, $\delta_h = -10°$

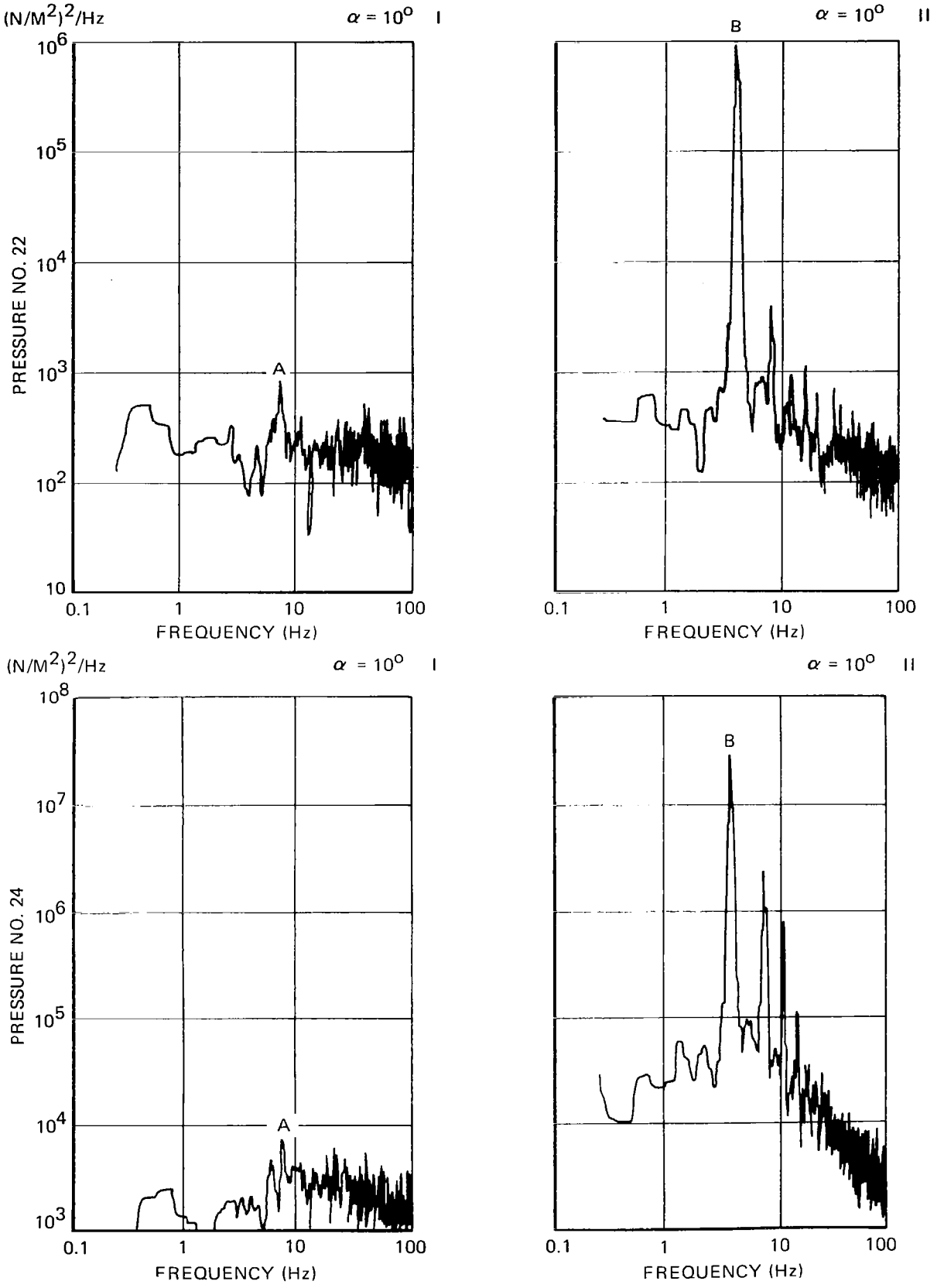

Figure 77. Comparison of Horizontal Tail Surface Pressure PSD Data for the Fixed Model, Run 51, Phase I (left) and the Oscillating Model, Run 26, Phase II, $\alpha = 10°$, $\beta = 8°$, $M = 0.925$, $\delta_n/\delta_f = 0°/0°$, $\delta_h = -10°$

the spectral make-up for the two runs except for the transducers located on the inboard portion of the wing semi-span. The data presented above demonstrated the frequency-dependency, as well as the dependency on the deflection modes, of the dynamic pressures as excited by the flexible responding structures.

For Run 5, Phase II test, the random appearance of the roll oscillations and the subsequent reduction in oscillation amplitude made the recorded pressure and response data highly nonstationary. In contrast, in order to maintain a high degree of frequency resolution as required in the low frequency range, and to keep the standard error to an acceptable level, substantial duration of stationary real time data are needed. It is well known that the normalized standard error ϵ for a highly resolved PSD estimate $\hat{G}_x(f)$ from a sample record $x(t)$ with a true PSD function $G_x(f)$ is

$$\epsilon = \frac{\text{s.d.}\left[\hat{G}_x(f)\right]}{G_x(f)} \approx (B_e T)^{-1/2}$$

where B_e = the equivalent bandwidth of the filter

T = the sample record length

By examining the real time data of the roll oscillations as shown in Figure 36, it was noted that the high amplitude oscillations lasted only 2-4 seconds. The equivalent bandwidth of the filter (analog) used in the spectral processing was 0.375 Hz. In order to maintain reasonable statistical accuracy, Run 5, Phase I data were processed using three different sample record lengths (8 sec, 16 sec, and 32 sec) to cover the time span where roll oscillations were at high amplitudes. In Figure 78, selected spectral data of the model response (Right Wing-Tip Acceleration) and the unsteady aerodynamic pressure (Tranducer No. 3) are presented for comparison purpose. Plots (a) of Figure 78 are for Run 8, Phase I. Plots (b), (c), (d) are for Run 5, Phase II. The sample record lengths used and the corresponding normalized standard errors are described below:

(a)	T = 32 sec	ϵ = .2886
(b)	T = 32 sec	ϵ = .2886
(c)	T = 16 sec	ϵ = .4082
(d)	T = 8 sec	ϵ = .5774

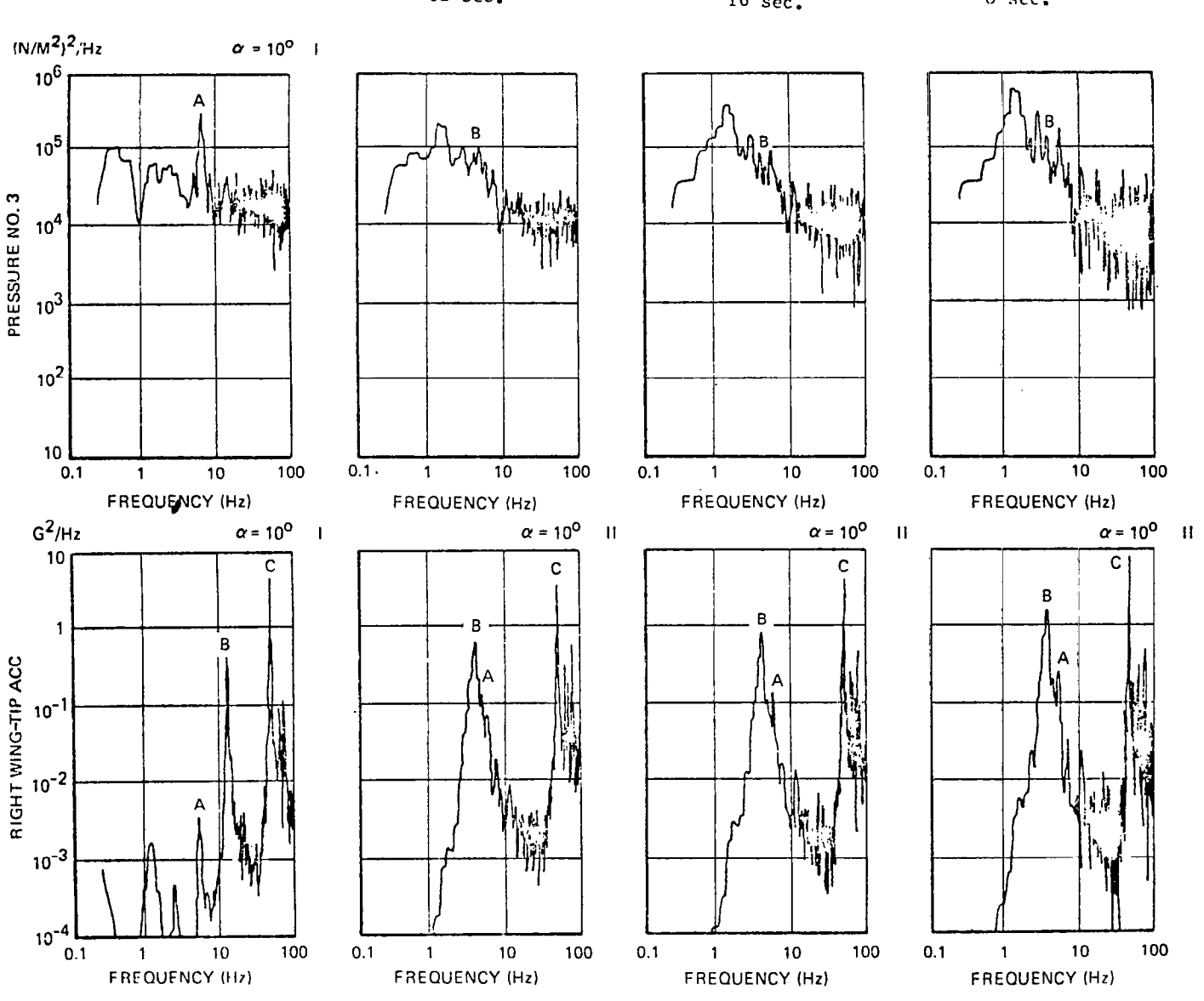

Figure 78. PSDs of Pressure No. 3 and Right Wing-Tip Acceleration Based on Run 8, Phase I (left) and Run 5, Phase II Data, $\alpha = 10°$, $\beta = 0°$, $M = 0.925$, $\delta_n/\delta_f = 5°/12°$, $\delta_h = 0°$.

The major peaks of the response data were again identified by letters A, B, and C as in the previous case. For the pressure spectral data, only the peaks corresponding to the Sting-Balance Bending mode (A) for Phase I and the Natural Roll Frequency (B) for Phase II are identified. In examining the Phase II plots, it was observed that the shorter the duration of the sample record length, the higher the peaks values. This was to be expected. For the same reason, no prominent peak corresponding to the Natural Roll Frequency was observed on the pressure PSD plots.

Response data and pressure data at key locations recorded during Run 5 and Run 26 of Phase II test and Run 8 of Phase I test at $\alpha = 10°$ were digitized to determine the input-output phase relationship as well as the picture of the makeup of the rigid body modes (roll, yaw, pitch) and the mode coupling. The recorded data were digitized with a sampling rate of 521 samples/second, and a low-pass analog filter with a cutoff frequency of 220 Hz was used during the digitizing process. The data being digitized are listed below.

Run 5, Phase II, $\alpha = 10°$	--	Roll, yaw, right and left wing-tip accelerations (1a, 2a), transducer Nos. 1, 3, 4, 12
Run 8, Phase I, $\alpha = 10°$	--	Right and left wing-tip accelerations (1a, 2a), transducer Nos. 1, 3, 4, 12
Run 26, Phase II, $\alpha = 10°$	--	Roll, yaw, pitch, right and left wing-tip accelerations (1a, 2a), transducer No. 4

The Fourier transforms of the above-listed data were generated by a Spectral Analysis computer program using the Fast Fourier Transform method. Four records, each of 2 seconds duration, were used for averaging purposes. (The segment used in Run 5, Phase II data is indicated by letter B in Figure 36a.) The Fourier transform data corresponding to two specific frequencies were of interest, i.e., the natural frequencies corresponding to the roll device oscillation for Phase II test (4.07 Hz) and the first wing symmetrical bending mode (51.88 Hz). The results on the relative phase relationship (in degrees) are presented below:

	Run 5, Phase II, α =10°, M = 0.925 δ_n/δ_f = 5°/12°, δ_h = 0°, β = 0°		Run 8, Phase I, α =10°, M = 0.925 δ_n/δ_f = 5°/12°, δ_h = 0°, β = 0°	Run 26, Phase II, α =10°, M = 0.925 δ_n/δ_f = 0°/0°, δ_h = -10°, β = 8°	
Signal Ident.	f=4.07 Hz $\varphi-\varphi_{roll}$	f=51.88Hz $\varphi-\varphi_{1a}$	f=51.88 Hz $\varphi-\varphi_{1a}$	f=4.07 Hz $\varphi-\varphi_{roll}$	f=51.88 Hz $\varphi-\varphi_{1a}$
Roll	0°	-	-	0°	-
Pitch	-	-	-	161.8°	-
Yaw	2.0°	-	-	-2.0°	-
1a	-3.2°	0°	0°	-14.4°	0°
2a	177.0°	2.6°	-1.6°	10.7°	0.4°
K1	-104.9°	-30.7°	-130.6°	-	-
K3	-98.8°	-113.8°	-10.0°	-	-
K4	161.0°	-118.7°	-33.3°	170.4°	34.5°
K12	177.9°	-156.9°	-38.6°	-	-
Modal Force	-	-109.7°	-37.6°	-	34.5°

The last row gives the phase angles between the modal responses (1a) and the modal forces contributed by the pressures measured at the transducers listed above, corresponding to the first wing symmetrical bending mode. Based on the data obtained, it was clear that the yaw angle and pitch angle oscillations had the same major frequency with a slight phase shift from the roll oscillations.

4.7 Wake Flow Effect and Horizontal Tail Buffet

Even prior to flow separation on the aircraft wing, the wake flow and its effect on the tail surfaces and the overall responses of the aircraft were very complicated. Wing surface flow separation (shock or otherwise induced) further complicated the picture. In addition, the tail surfaces might also encounter shock-induced flow separation, depending on the aircraft angle-of-attack and the tail surface setting.

In order to examine the wake flow effect on the horizontal tail due to flow separation, the dynamic pressure data of Run 19, Phase I were processed. Run 19 was conducted in test model configuration 3. The configuration featured wing-tip-mounted Sidewinder missiles. The leading edge and trailing edge flap angles were 5°/12°. The aileron and horizontal tail surface settings were 0 degree and -10 degrees, respectively. The nominal sideslip angle was 0 degree. The run was conducted at M = 0.925.

Run 19 covered the following angle-of-attack settings; 0°, 4°, 6°, 8°, 10°, 12°, and 14°. Among these, the dynamic pressure data of transducer Nos. 14, 17, 22, 23, 24, and 25, corresponding to α = 0°, 8°, 10°, and 14° were digitized in order to perform spatial correlation for each pair of transducers using a spectral analysis computer program. Transducer No. 14 was located at 47 percent semi-span and 80 percent chordwise location on the trailing edge flap upper surface of the right wing. Transducer No. 22 was located on the upper surface of the horizontal tail at the same semi-span location downstream of No. 14 and at 40 percent chordwise location. Transducer 24 was located on the lower surface, directly under transducer 22. Transducer Nos. 17, 23, and 25 were located at 33 percent wing semi-span, with No. 17 at 42 percent chordwis location of the right wing top surface. Transducers 23 and 25 were at 40 percent chord of the horizontal tail with No. 23 on the upper surface and No. 25 on the lower surface. The severity of the wake flow and its effect on tail buffet may be estimated through the following:

1. Whether or not flow separation takes place in that part of the wing span directly upstream of the tail surface.
2. High PSD level of the dynamic pressures on the tail.
3. Good correlation existed between dynamic pressures measured on the wing surface near the trailing edge and on the tail surface downstream.

The dynamic pressure data measured at the above-mentioned transducers were digitized with a rate of 10,400 samples/second and the corresponding folding frequency was 5200 Hz. A low pass analog filter with a cutoff frequency of 4500 Hz was used during the digitizing process. Spatial correlation between transducer pairs were performed in the form of cross-correlation, cross-power spectra, and coherency function. In order to show the general trend of the coherency function, a time span of 0.2 second was chosen. The maximum time lag used in cross-correlation computation was one fourth of the time span.

Prior to presenting the spatial correlation data of the transducer pairs, the static pressure coefficient (C_p) and the rms dynamic pressure coefficient ($C_{\tilde{p}}$) distributions on the right wing upper surface were examined to trace the shock/boundary layer interaction and the separated flow regions. The results are presented in Figure 79. It can be seen that transducer No. 14 was in the separated flow region for $\alpha > 8°$, while the local flow at transducer No. 17 became separated at approximately $\alpha = 12°$

Spatial correlation calculations were performed for all possible pair combinations of pressures at the six transducer locations. High level correlations existed between (24, 25) for $\alpha = 0°$; (14,22) and (24,25) for $\alpha = 10°$; (22, 23) and (24, 25) for $\alpha = 14°$. Typical spatial correlation plots for transducer pair (24, 25) at $\alpha = 0°$, (14, 22) at $\alpha = 10°$, and (22, 23) at $\alpha = 14°$ are presented in Figures 80-82, respectively. On plot (b) of those figures, the cross-power spectrum and the coherency function are presented. The unit or the modulus is $(N/m^2)^2/Hz$, the phase angle unit is degree. On plot (a), the auto-correlation functions and the normalized cross-covariance function (the cross-correlation coefficient) are given. The unit of the auto-correlation functions (the top two plots) is $(N/m^2)^2$. In addition to spatial correlation, cross-power spectra, etc., the power spectral density functions of the six pressure transducers were also processed based on the digitized pressure data corresponding to various angle-of-attack settings. For each power spectrum, data were processed using three continuous frequency ranges with different bandwidths. The amounts of real time data used for the three frequency ranges are described in the following table.

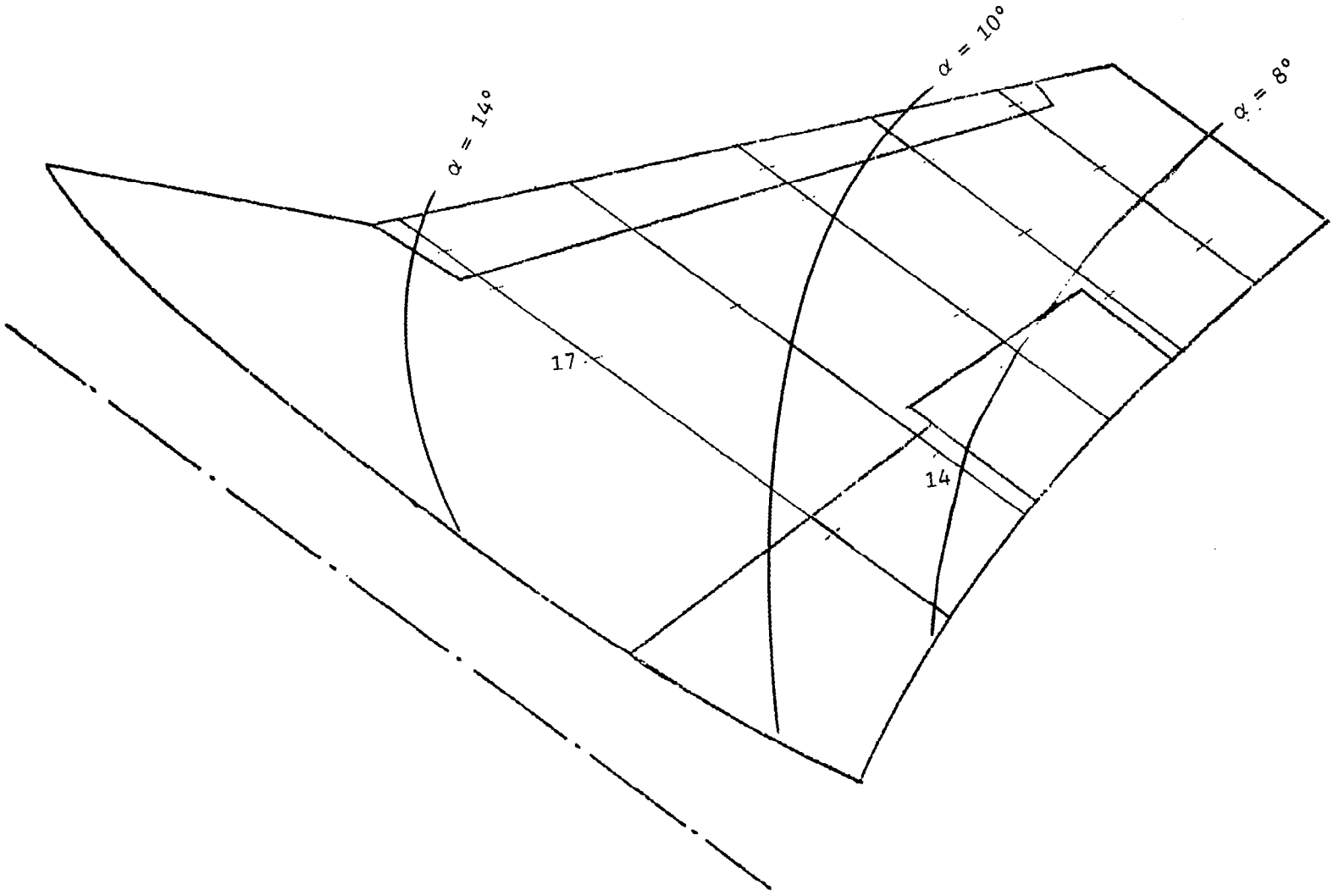

Surface Separation Boundary Mapping for
= -10°

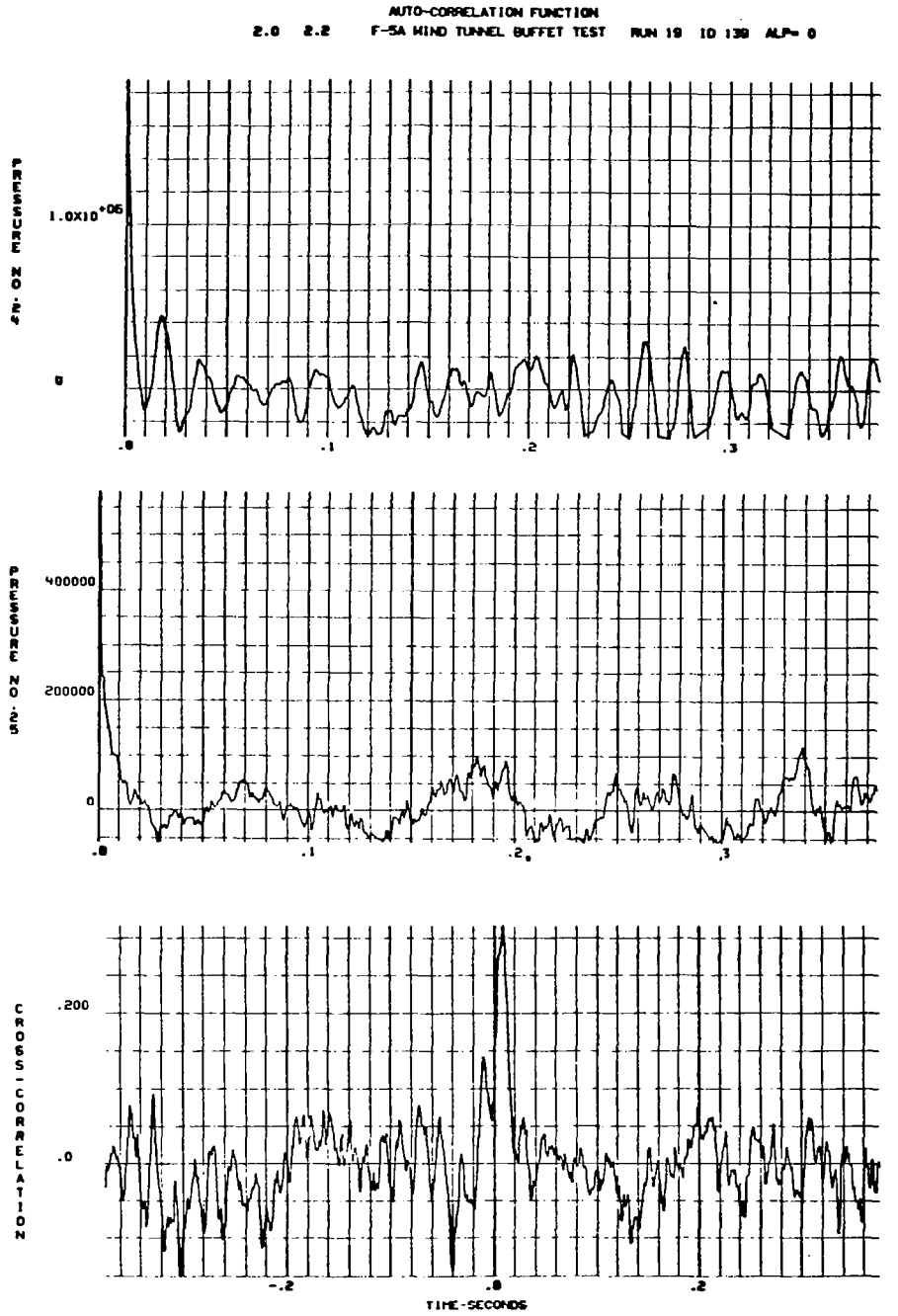

(a) The Auto and Cross-Correlation Functions

Figure 80. Spatial Correlation for Transducer Pair (24, 25) of Run 19, Phase I, α = 0°, β = 0°, M = 0.925, δ_n/δ_f = 5°/12°, δ_h = -10° (Continued)

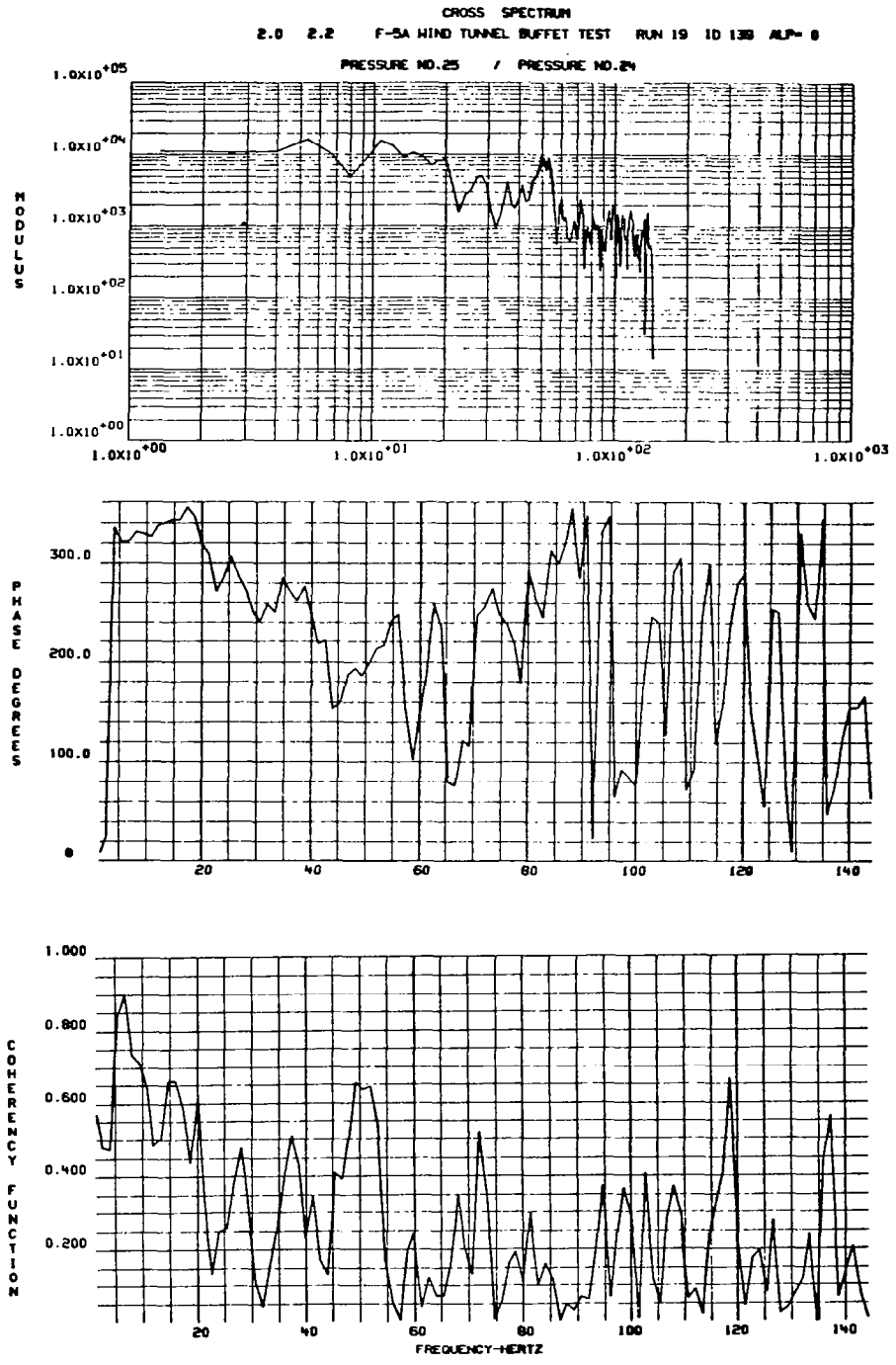

(b) The Cross-Power Spectrum and the Coherency Function

Figure 80. Spatial Correlation for Transducer Pair (24, 25) of Run 19, Phase I, $\alpha = 0°$, $\beta = 0°$, M = 0.925, $\delta_n/\delta_f = 5°/12°$, $\delta_h = -10°$ (Concluded)

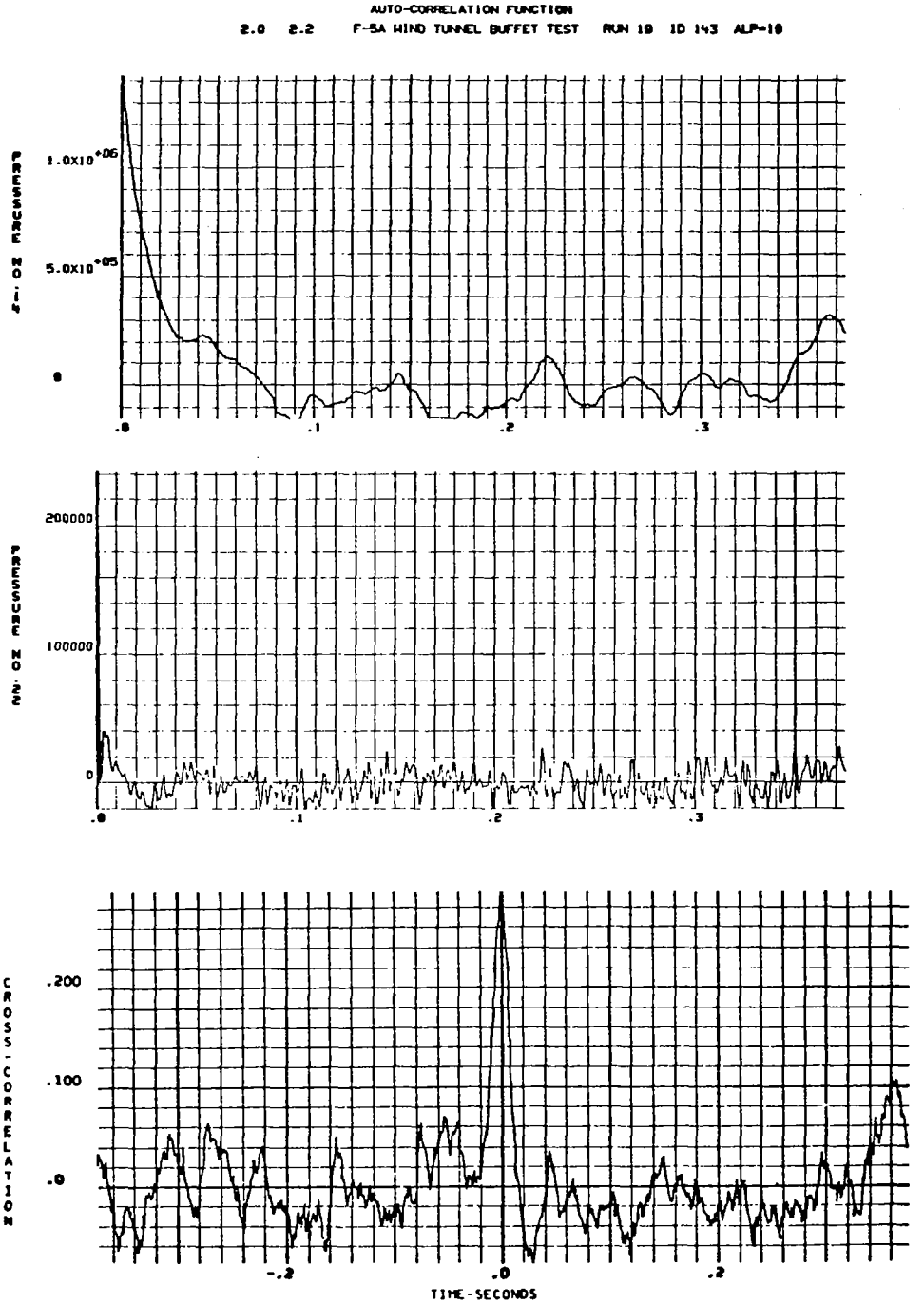

(a) The Auto and Cross - Correlation Functions

Figure 81. Spatial Correlation for Transducer Pair (14, 22) of Run 19, Phase I, α = 10°, β = 0°, M = 0.925, δ_n/δ_f = 5°/12°, δ_h = -10° (Continued)

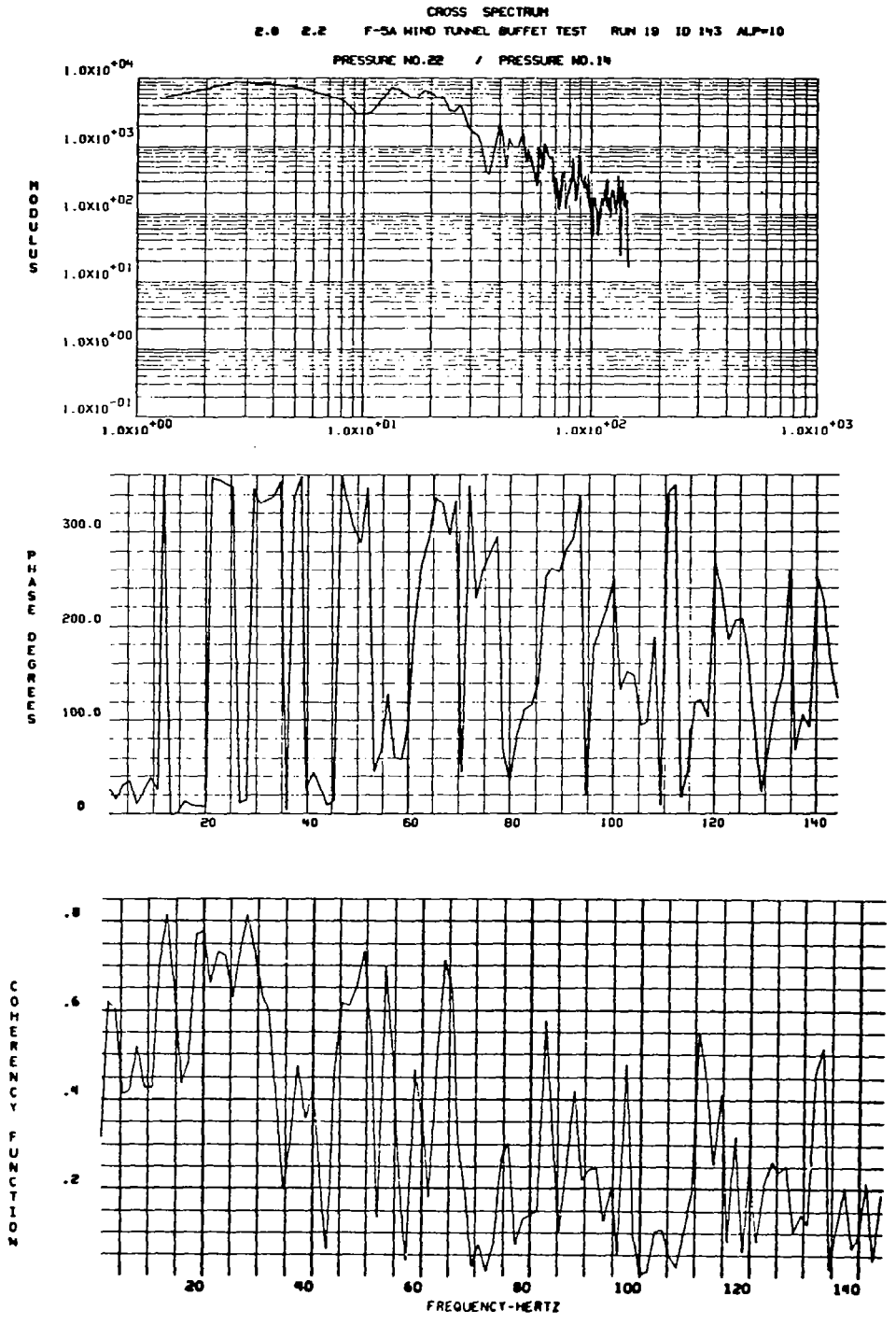

(b) The Cross-Power Spectrum and the Coherency Function

Figure 81. Spatial Correlation for Transducer Pair (14, 22) of Run 19, Phase I, α = 10°, β = 0°, M = 0.925, δ_n/δ_f = 5°/12°, δ_h = -10° (Concluded)

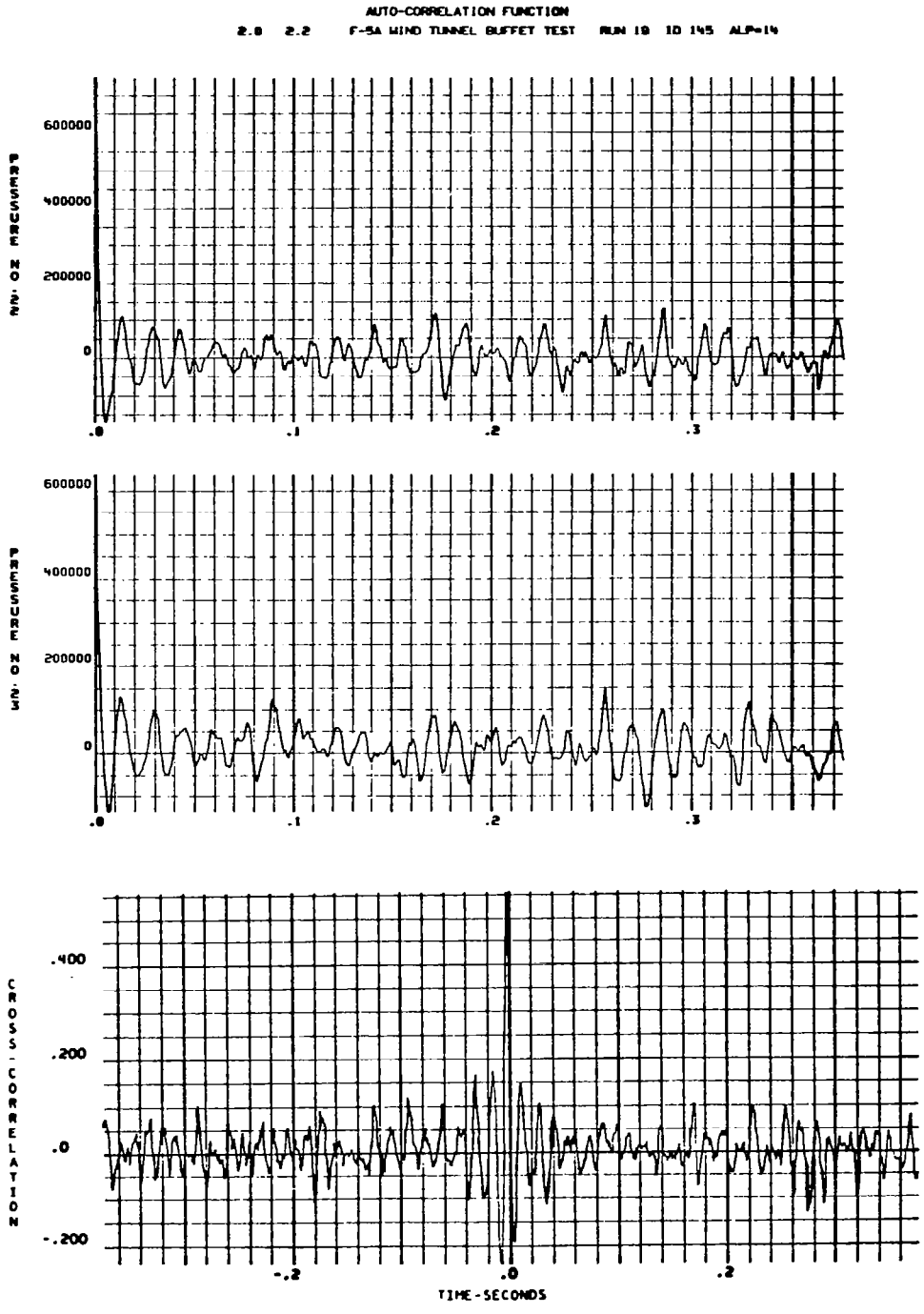

(a) The Auto and Cross-Correlation Functions

Figure 82. Spatial Correlation for Transducer Pair (22, 23) of Run 19, Phase I, α = 14°, β = 0°, M = 0.925, δ_n/δ_f = 5°/12°, δ_h = -10° (Continued)

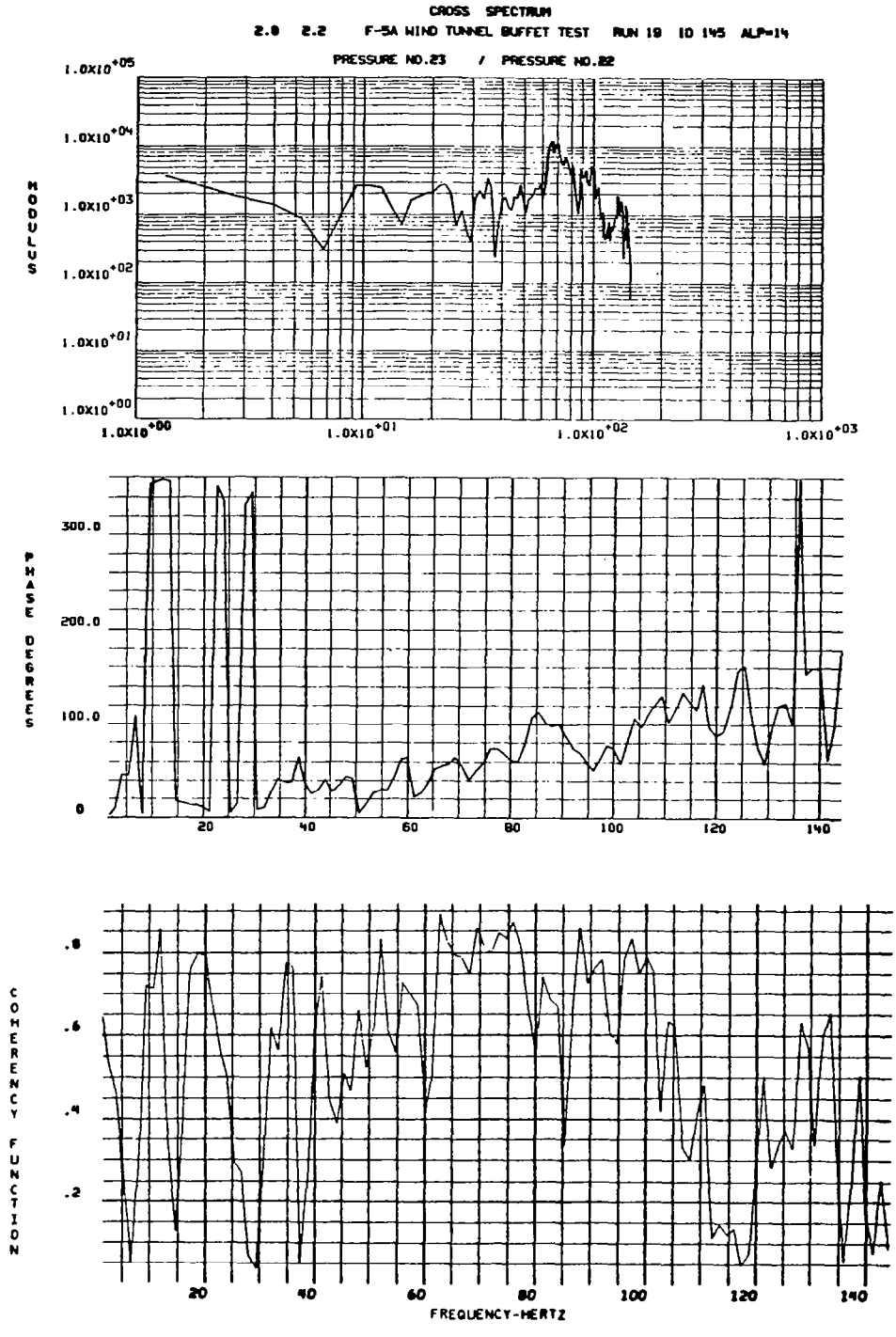

(b) The Cross-Power Spectrum and the Coherency Function

Figure 82. Spatial Correlation for Transducer Pair (22, 23) of Run 19, Phase I, α = 14°, β = 0°, M = 0.925, δ_n/δ_f = 5°/12°, δ_h = -10° (Concluded)

FREQ. RANGE (Hz)	RECORD PROCESSED (sec)	NUMBER OF RECORDS USED	TOTAL PROCESSED DATA TIME (sec)
2-100	2.0	15	30
100-800	0.2	16	3.2
800-4500	0.1	16	1.6

Note that the frequency ranges stated above were the test frequency scales. The power spectral density plots for all transducers (Nos. 14, 17, 22-25) corresponding to α = 0°, 8°, 10°, 14° are presented in Figures 83 through 86, respectively. All scales used in Figures 80 through 86 were modified to conform to the equivalent flight test condition of the F-5A.

Referred to Figure 83, the high PSD levels of transducer Nos. 24, 25 at α = 0° indicated possible shock-induced flow separation on the tail lower surface due to the negative tail deflection, δ_h = -10°. Good spatial correlation (Figure 58) with ρ_o = 0.3156 at τ' = .00955 sec (ρ_o = maximum correlation coefficient, τ' = time delay) between the two transducers was observed. However, the different auto-correlation function shapes indicated zero or minimum convection between transducer pair (24,25).

As angle-of-attack increased to 8 degrees (Figure 84), moderate higher PSD levels on the upper tail surface (as well as on the upper wing surface) indicated the wake flow effect. On the other hand, the slightly lower PSD levels of transducer Nos. 24, 25 (lower tail surface) implied that the severity of tail buffet was reduced by increasing the angle-of-attack.

At α = 10°, the tail section chord was parallel to the mean flow direction. At this time, the dynamic pressures on the tail were caused essentially by the wake flow, and the rms coefficients for all locations on the tail surface were in the order of 0.1. Compared to α = 8° case, the PSD levels showed moderate increase for all transducers. This increase was more pronounced for the frequency range up to 100 Hz. The approximately 15 dB increase in the PSD level of transducer No. 14 (Figure 85) signaled the local flow separation (also see Figure 79). Good spatial correlation existed between transducer pair (14, 22) as shown in Figure 81 indicating strong wake flow condition. The maximum value of the major peak of the correlation coefficient was 0.296 at τ' = 0. No clear convection mechanism was observed. Poor correlation existed between transducer Nos. 14 and 24. However, good correlation with ρ_o = 0.497 at τ' = 0.0015 sec. existed between transducer Nos. 24 and 25.

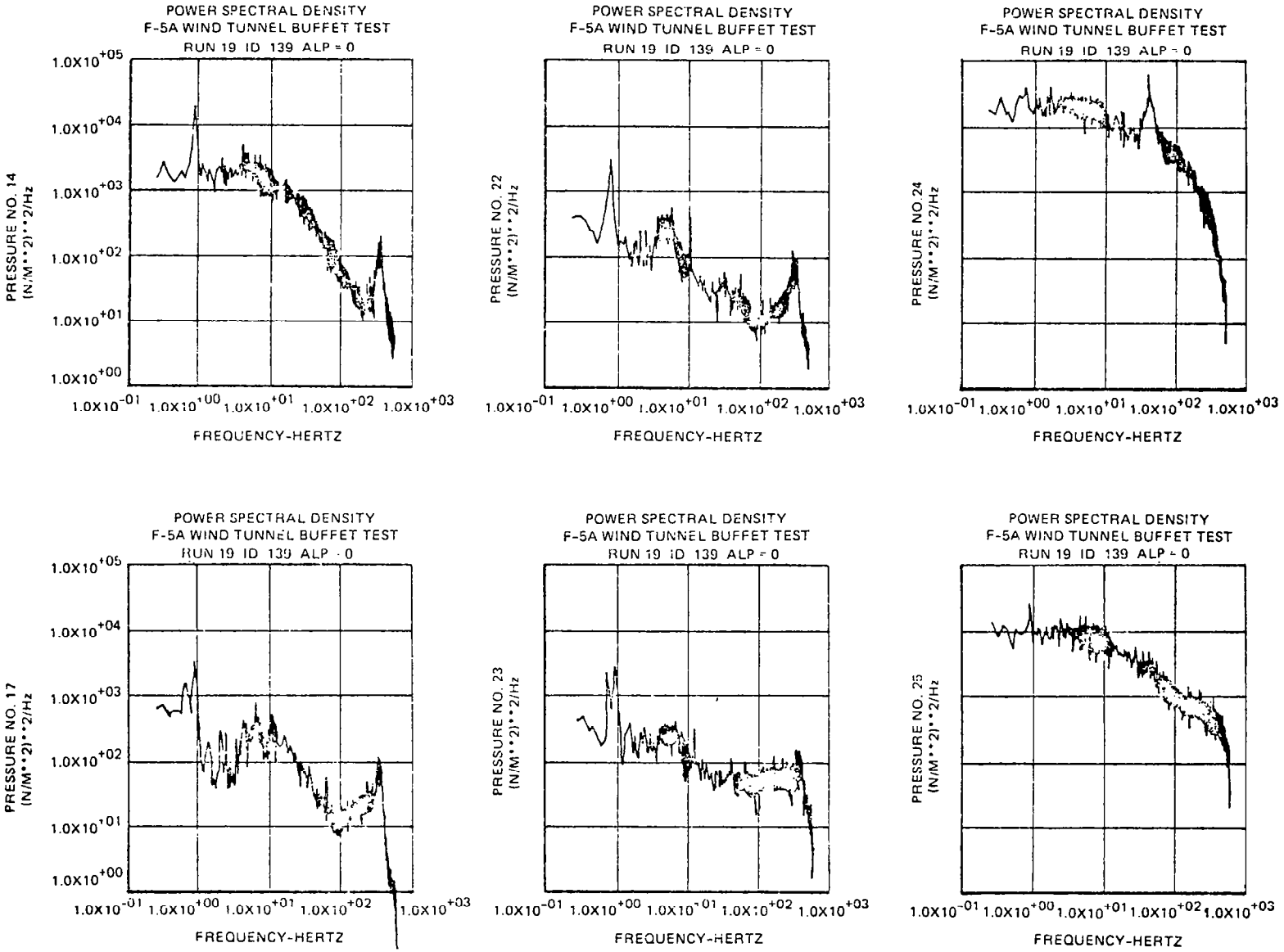

Figure 83. Pressure PSD Plots of Transducer Nos. 14, 17, 22-25 for Run 19, Phase I, $\beta = 0°$, $\alpha = 0°$, M = 0.925, $\delta_n/\delta_f = 5°/12°$, $\delta_h = -10°$.

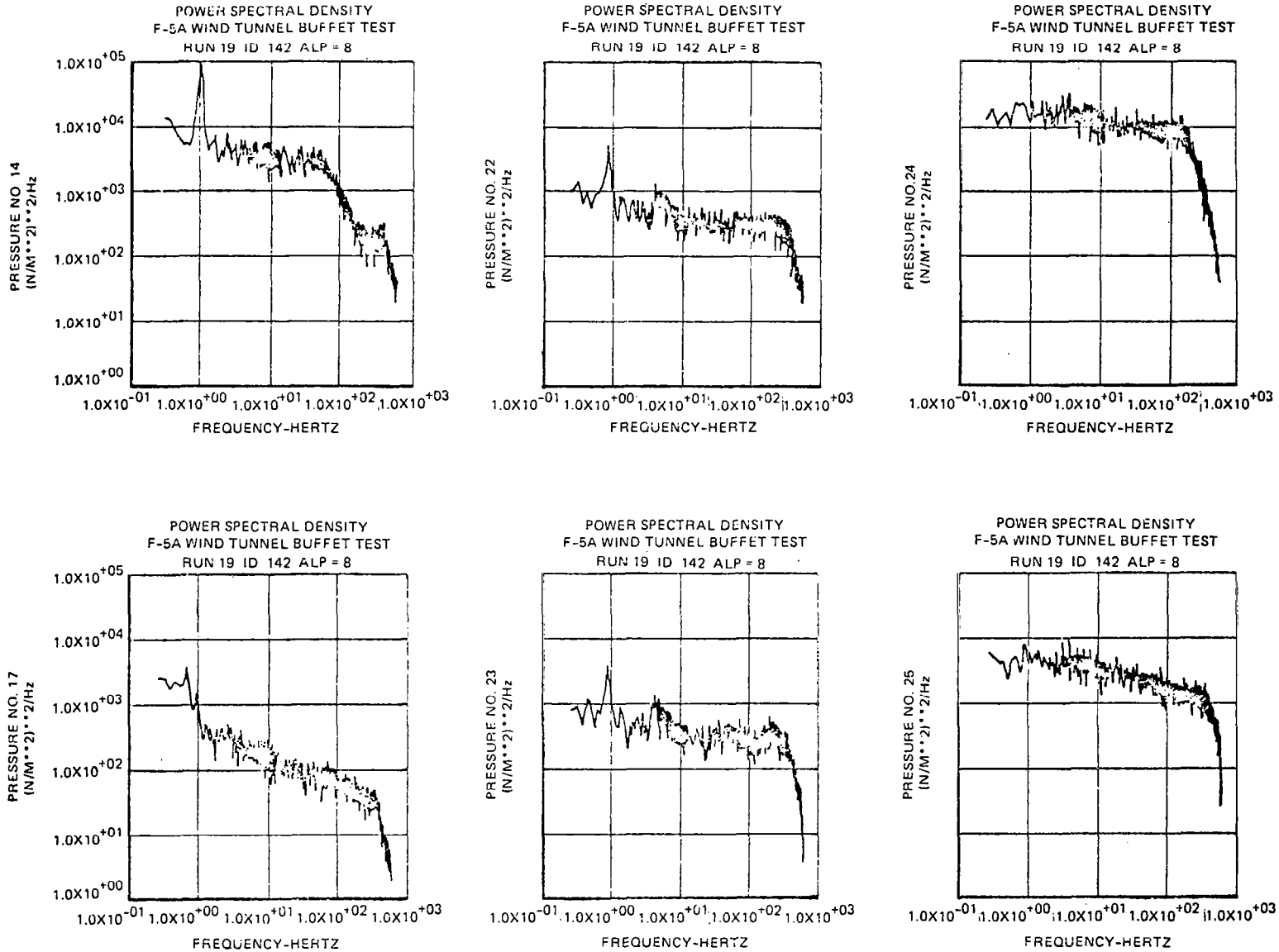

Figure 84. Pressure PSD Plots of Transducer Nos. 14, 17, 22-25 for Run 19, Phase I, $\alpha = 8°$, $\beta = 0°$, M = 0.925, $\delta_n/\delta_f = 5°/12°$, $\delta_h = -10°$

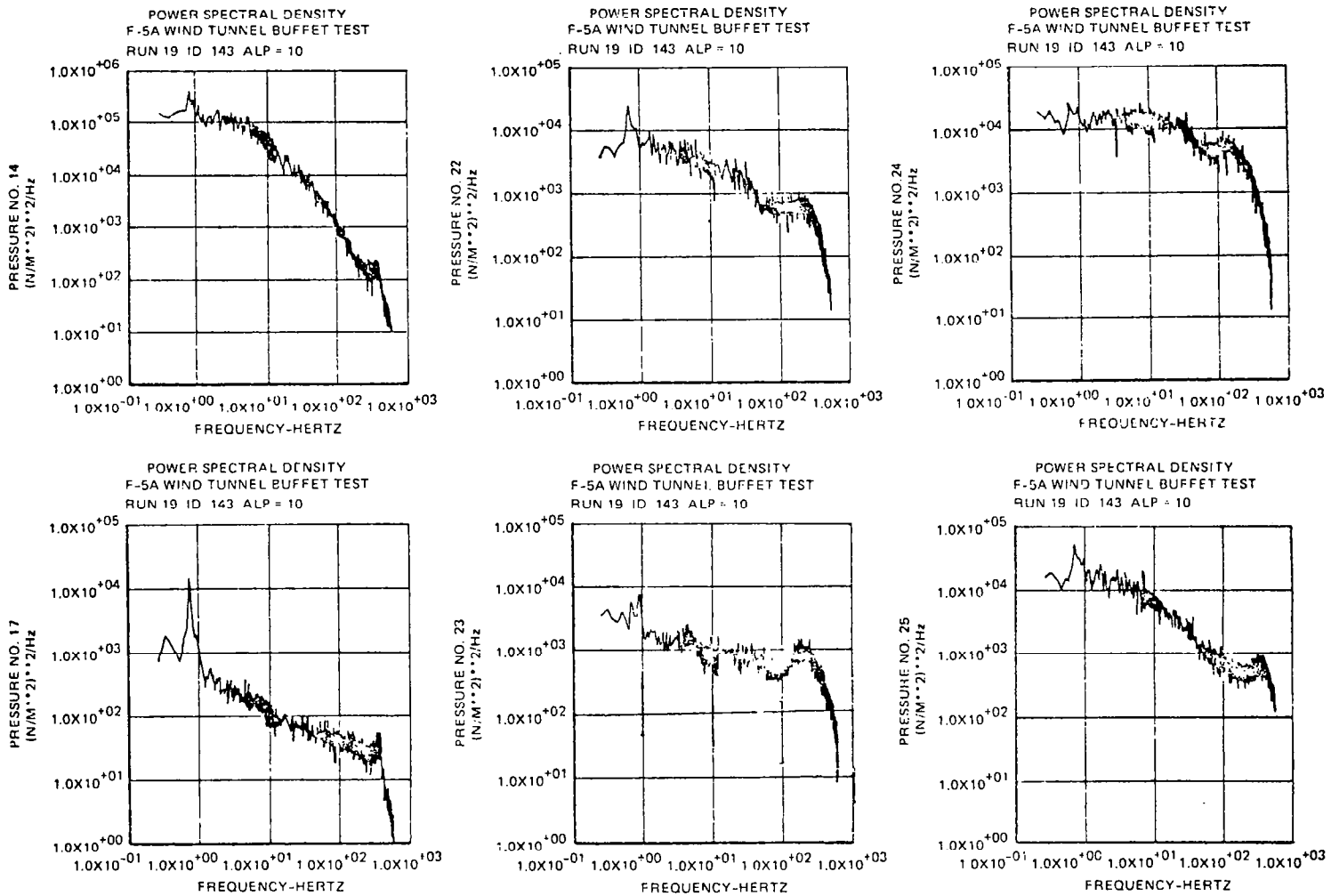

Figure 85. Pressure PSD Plots of Transducer Nos. 14, 17, 22-25 for Run 19, Phase I, $\alpha = 10°$, $\beta = 0°$, $M = 0.925$, $\delta_n/\delta_f = 5°/12°$, $\delta_h = -10°$.

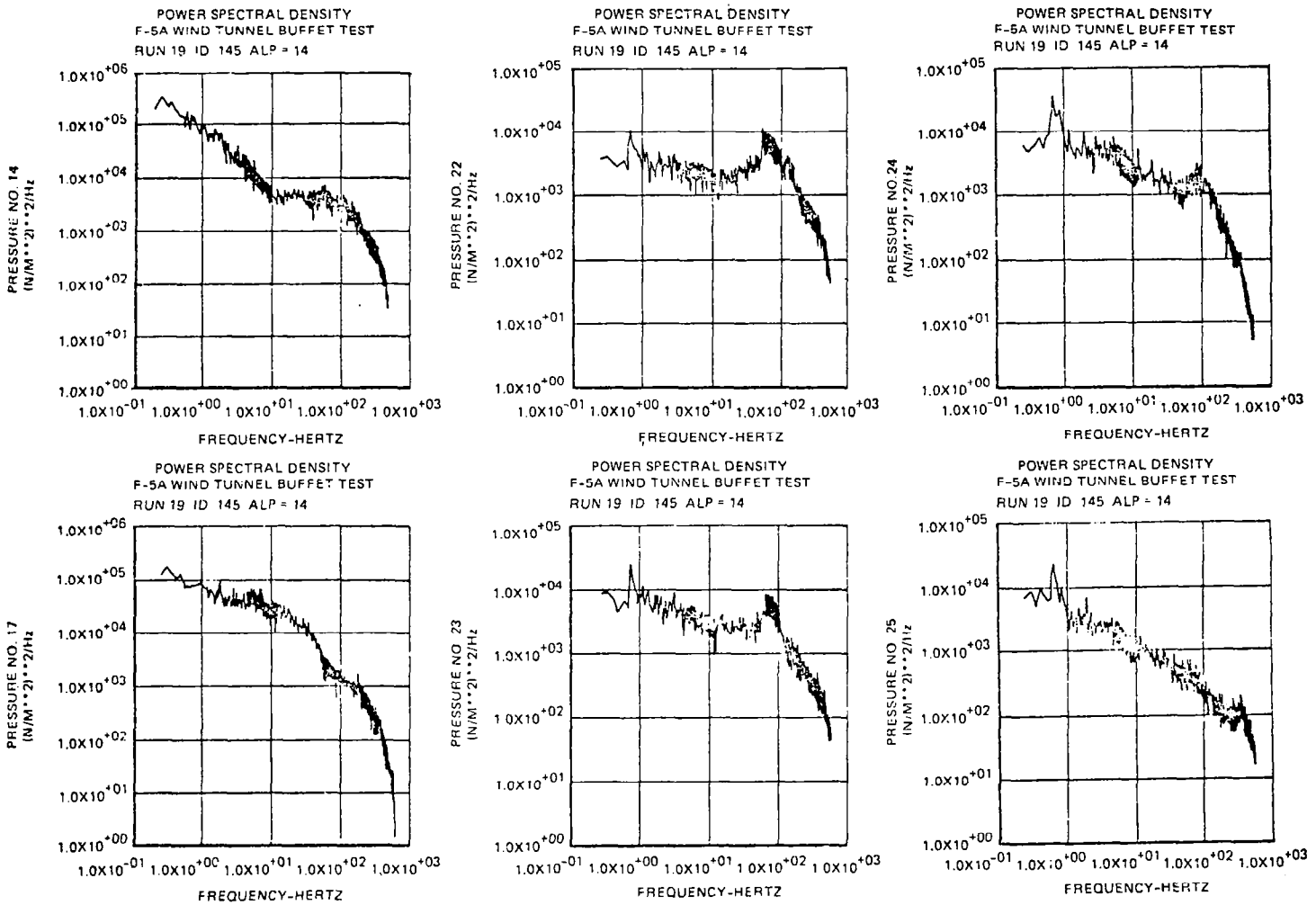

Figure 86. Pressure PSD Plots of Transducer Nos. 14, 17, 22-25 for Run 19, Phase I, $\alpha = 14°$, $\beta = 0°$, M = 0.925, $\delta_n/\delta_f = 5°/12°$, $\delta_h = -10°$

Beyond α = 10°, the rms pressures on the lower surface of the tail decreased, while those on the upper surface increased. At α = 14°, both transducer Nos. 14 and 17 were under the separated flow. Spatial correlation between transducer pair (14,22) was weak, while transducer pair (22, 23) were wel correlated with ρ_o = 0.5526 at τ'= 0.0023 sec (Figure 82). Both transducers had similar PSD functions (Figure 86). The lag time suggested a convection speed of 236m/sec in the outboard direction, (see Reference 1, p. 109). Transducer pair (24,25) were also well correlated with ρ_o = 0.4197 at τ' = -0.0015 sec, but substantial difference in PSD pattern was observed.

Additional processing of the wake flow and tail surface pressure data was performed with special attention directed toward the establishment of an overall picture of the wake flow pattern, as well as the effect of the tail surface setting under otherwise identical flow conditions. In Figures 87 through 90, the dynamic pressure coefficients measured at transducer Nos. 14, 18, 22-25 of four cases of Phase I data corresponding to variable tail surface settings are plotted vs. angle-of-attack. Transducer Nos. 14 and 18 were located on the trailing edge flap, upper surface of the right wing at 47 percent and 33 percent semi-span locations, respectively. Transducer Nos. 22 and 23 were located on the upper surface of the horizontal tail and transducer Nos. 24 and 25 on the lower surface. Transducer Nos. 22, 24 were located downstream of No. 14 while transducer Nos. 23,25 were located downstream of No. 18. The test configurations and the run conditions of Figures 87 through 90 are described below:

FIGURE NO.	TEST PHASE RUN NO.	CONFIGURATION NO.	δ_n/δ_f	δ_h	M
87	I-8	2	5°/12°	0°	0.925
	I-19	3	5°/12°	-10°	0.925
88	I-39	9	0°/0°	0°	0.925
	I-49	11	0°/0°	-10°	0.925
89	I-13	2	5°/12°	0°	0.750
	I-22	3	5°/12°	-10°	0.750
90	I-43	9	0°/0°	0°	0.750
	I-52	11	0°/0°	-10°	0.750

Referring to Figures 87 through 90, the development of the wake flow pattern, the effect of the tail surface settings, and the horizontal tail buffet phenomenon could be detected by the trend of the dynamic pressure coefficients

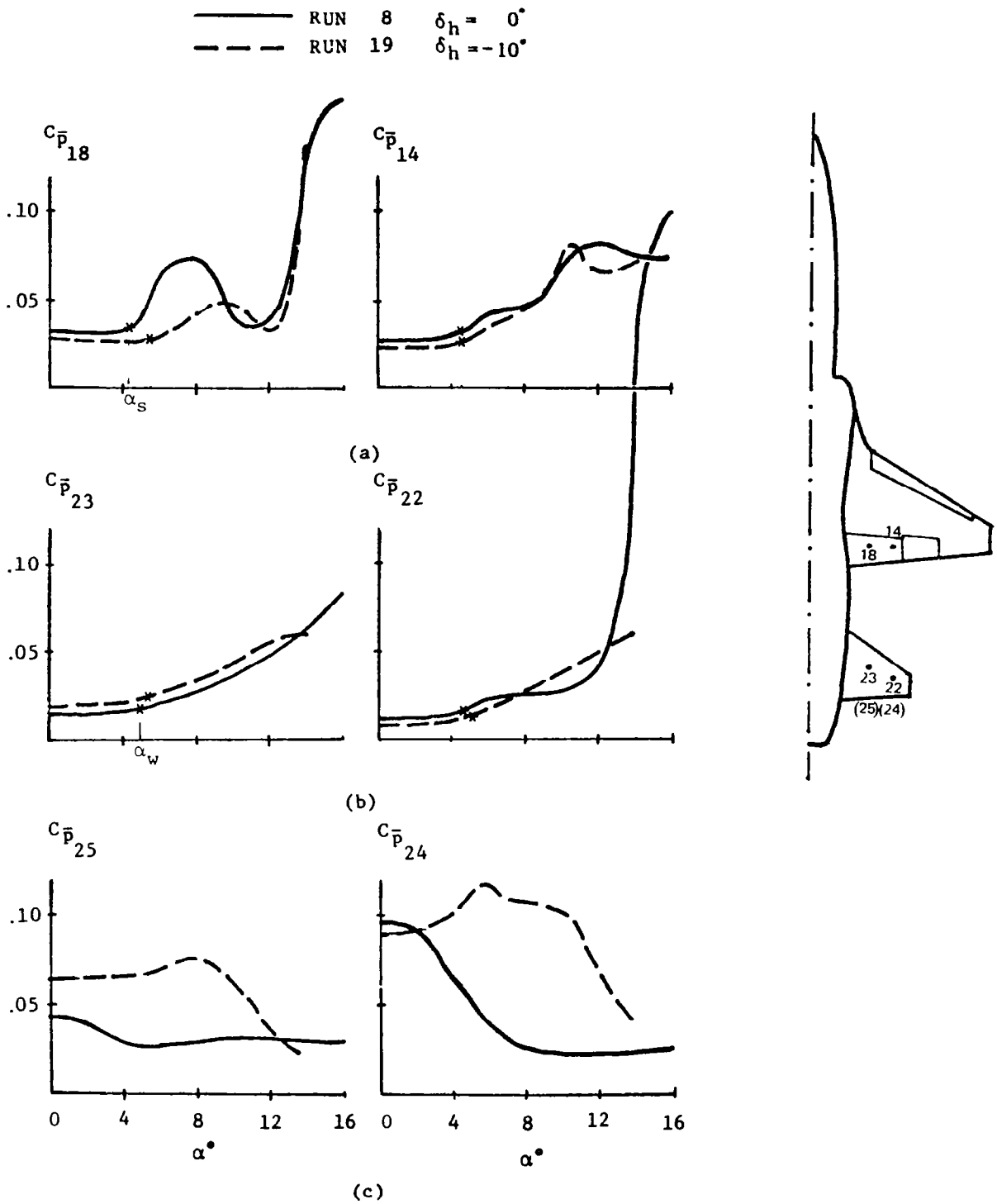

Figure 87. Dynamic Pressure Coefficient Comparison Due to Tail Deflection Effect - Run 8 vs. Run 19, Phase I, δ_n/δ_f = 5°/12°, M = 0.925

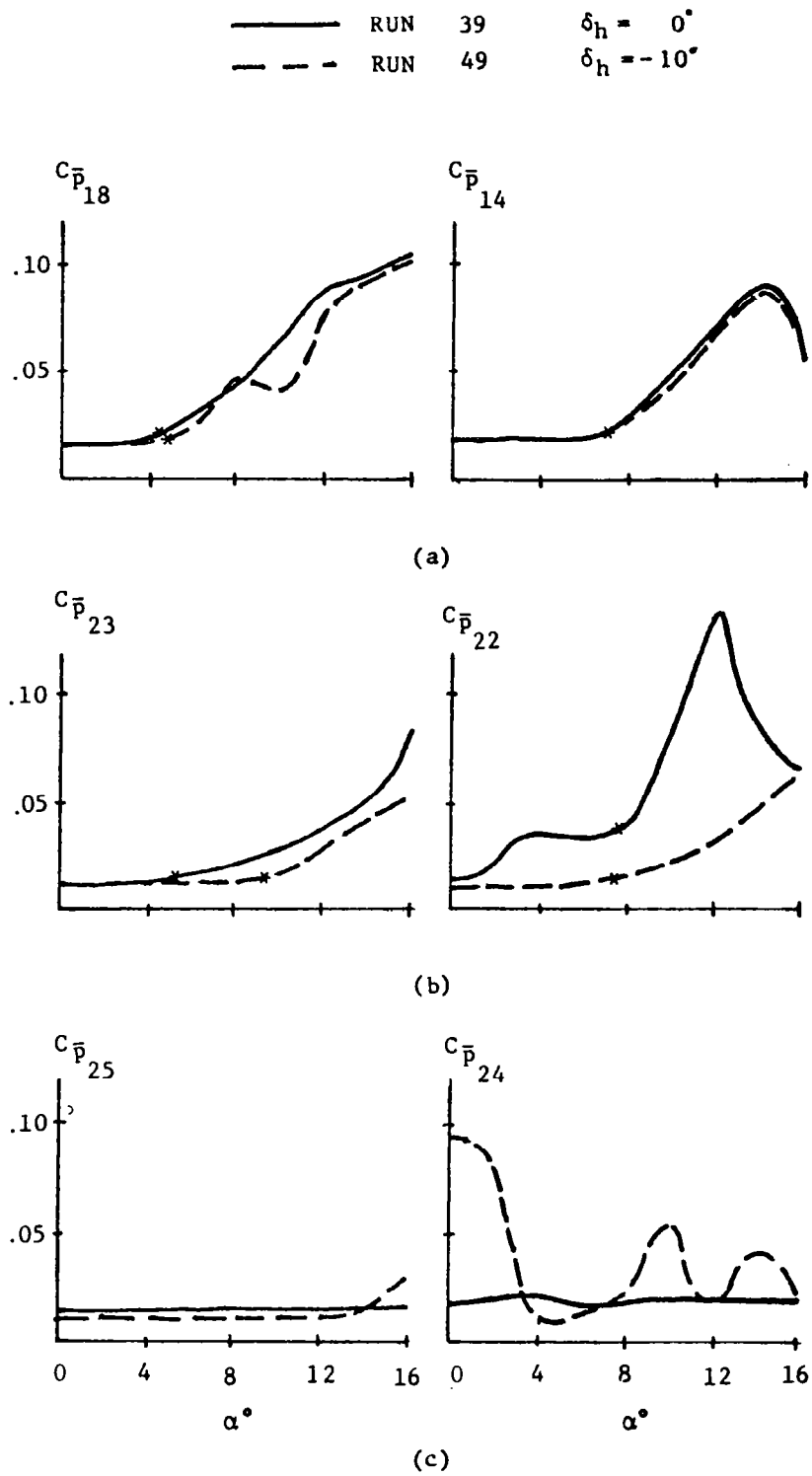

Figure 88. Dynamic Pressure Coefficient Comparison Due to Tail Deflection Effect - Run 39 vs. Run 49, Phase I, $\delta_n/\delta_f = 0°/0°$, M = 0.925

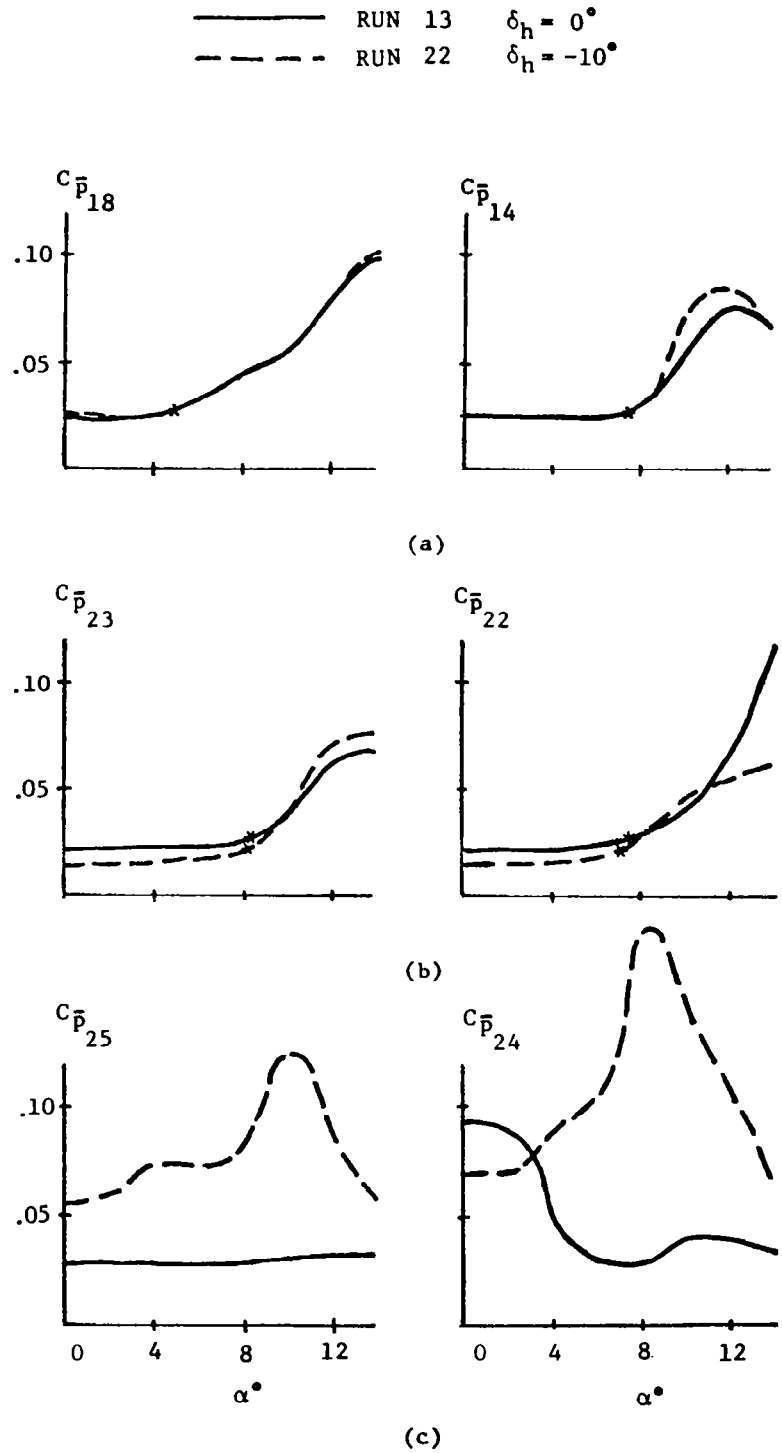

Figure 89. Dynamic Pressure Coefficient Comparison Due to Tail Deflection Effect - Run 13 vs. Run 22, Phase I, δ_n/δ_f = 5°/12°, M = 0.75.

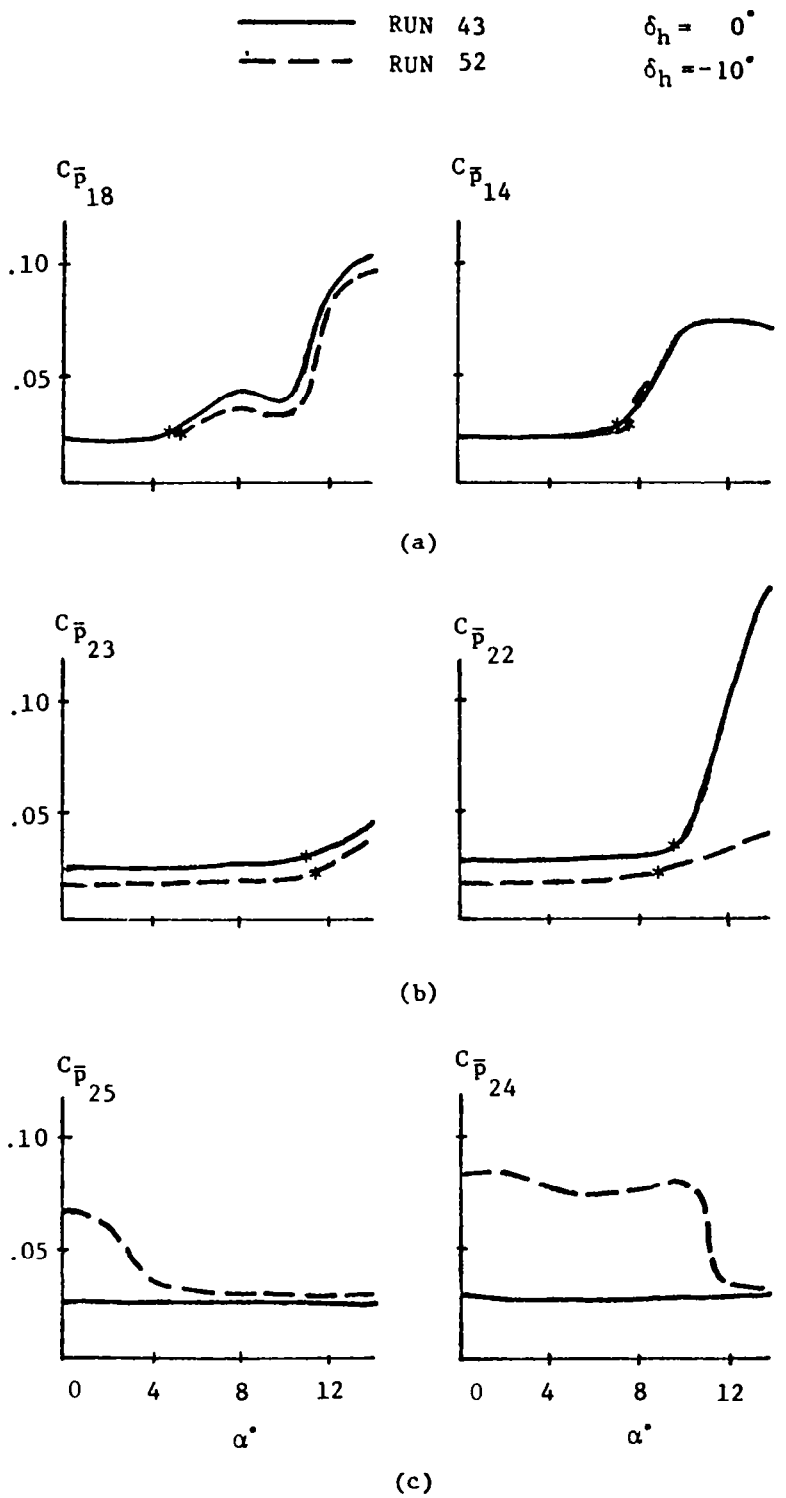

Figure 90. Dynamic Pressure Coefficient Comparison Due to Tail Deflection Effect - Run 43 vs. Run 52, Phase I, $\delta_n/\delta_f = 0°/0°$, M = 0.75.

as a function of angle-of-attack. In plots (a) of these figures (transducer Nos. 14 and 18), asterisks are used to indicate the angle-of-attack setting α_s, above which the $C_{\bar{p}}$ values increased in such a manner as to indicate local flow separation. It may be seen that

$\alpha_s \simeq 5°$ for transducer No. 18 (33% semi-span)

$\alpha_s \simeq 7°$ for transducer No. 14 (47% semi-span)

Furthermore, the solid lines denote the $\delta_h = 0^o$ cases and the dotted lines denote the $\delta_h = -10^o$ cases. In plots (b) (transducer Nos. 22, and 23, tail upper surface), asterisks are used to indicate the initial angles-of-attack α_w ($\geq \alpha_s$) beyond which the horizontal tail surface flow pattern was influenced by the wake flow during wing buffet, where the rms dynamic pressures increased substantially. Wake flow effect on the horizontal tail upper surface could be traced for both $\delta_h = 0°$ and $-10°$ cases. For the configurations with 0 degree horizontal tail surface setting, the very high rms dynamic pressures of transducer No. 22 at high angles-of-attack indicated the horizontal tail top surface buffet. The extremely high $C_{\bar{p}}$ value (0.298) of Run 8 at $\alpha = 16°$ (Figure 82b) was one of the highest rms dynamic pressures recorded in the test program.

The flow patterns developed on the horizontal tail lower surface as shown in plots (c) of Figures 87 through 90 were quite different from those on the upper surface. For the configurations with zero degree of horizontal tail setting, high rms dynamic pressures were observed at low angles-of-attack ($\alpha < 4°$) when the leading edge and trailing edge flaps of the model were deflected (solid lines in Figures 87c and 89c). It can be visualized that the high dynamic pressures on the tail lower surface were caused by the wake flow due to the deflected trailing edge flap. Otherwise, no wake flow effect due to wing buffet (except for transducer No. 24 of Run 13 in Figure 89c) was observed.

For the configurations with -10 degrees horizontal tail setting (δ_h), the high $C_{\bar{p}}$ values of transducer Nos. 24 and 25 at lower angle-of-attack settings (dotted lines in plots c of Figures 87 through 90) indicated shock-induced flow separation on the tail lower surface due to the negative tail deflection. As the angle-of-attack increased, the combined effects of tail buffet and wake flow due to wing buffet made the rms dynamic pressure levels of transducer Nos. 24 and 25 even higher for the configurations with deflected leading

edge and trailing edge flaps (Figures 87c and 89c). However, $C_{\bar{p}}$ values dropped when the angle-of-attack setting exceeded 10 degrees where the negative horizontal tail setting cancelled the angle-of-attack setting. For the configurations with retracted leading edge and trailing edge flaps (Figures 84c and 86c), the effect of wake flow due to wing buffet to the tail lower surface was minimum. The reduction in $C_{\bar{p}}$ for transducer Nos. 24, 25 at very high α (>12°) and $\delta_h = -10°$ also may be contributed to the wing downwash effect which tended to steer the wake flow downward and away from the horizontal tail.

4.8 Correlation Study of Pressure Data Under Sideslip Conditions

In order to further examine the sideslip angle effect on the buffet pressure distributions, the dynamic pressure data of Run 11 and Run 12, Phase II, were processed. Both runs featured the same model configuration except for the nominal sideslip angle which was +8 degrees for Run 11 and -8 degrees for Run 12. The configuration featured wing-tip-mounted Sidewinder missiles. The leading edge and trailing edge flap angles were 5°/12°. The aileron and horizontal tail surface settings were 0° and -10°, respectively. The Mach number was 0.925.

The majority of the pressure transducers were located on the right-hand side of the wing and the horizontal tail. Taking advantage of the model symmetry along the vertical plane, a comprehensive pressure distribution may be synthesized by making use of the pressure data of two sideslip angles ($\pm 8°$). For instance, for Run 11, $\beta = 8°$, the leeward (left-hand) side pressure data were substituted by the leeward (right-hand) side pressure data of Run 12, $\beta = -8°$.

The rms pressure coefficient ($C_{\bar{p}}$) data for the two runs mentioned above were processed. The initial development of the flow separation for Run 11 was similar to those for Run 6, Phase II (Figure 34) which featured the same model configuration except that $\delta_h = 0°$. However, up to $\alpha = 4°$ no flow separation was detected on the right wing upper surface. At $\alpha = 6°$ shock-induced separation appeared at 61% and 47% semi-span, 60% chordwise positions (transducer Nos. 11 and 13). At $\alpha = 8°$ the separated flow region was extended outboard toward the tip. At $\alpha = 10°$, a major expansion of the separation bubble

took place. Except for the extended leading edge flap and the wing root area, most of the top surface of the right wing was in the separated flow region (Figure 91). As α reached 12°, the right wing upper surface became completely separated. On the other hand, the high rms dynamic pressures on the horizontal tail lower surface at lower angle-of-attack settings (0-8°) indicated the shock-induced flow separation due to the negative tail deflection $\delta_h = -10°$.

For Run 12, $\beta = -8°$ case, the flow patterns developed on the right wing upper surface (equivalent to the left wing upper surface for Run 11, $\beta = 8°$) were quite different from those corresponding to Run 11. At $\alpha = 4°$ local flow separated at 33% semi-span, 82% chordwise position (transducer No. 18) and also at 85% semi-span, 45% chordwide location and its downstream region (transducer Nos. 3, 4, 5). At $\alpha = 6°$ approximately 70% of the wing upper surfaces were in the separated flow region. At $\alpha = 8°$ the flow was separated except for an area on the extended leading edge flap. For $\alpha = 10°$, the flow on the entire wing upper surface became separated (Figure 91). The rms dynamic pressures on the horizontal tail lower surface at low angle-of-attack settings also indicated shock-induced flow separation. However, the $C_{\bar{p}}$ values on the leeward side of the horizontal tail was 30% lower than that for the windward side at $\alpha = 0°$. In observing the development of the flow patterns on both the windward and leeward sides of the aircraft under sideslip, the following conclusions may be drawn:

On the windward side, flow separation originated at the center portion of the wing semi-span, then extended outboard toward the tip, and then extended inboard toward the root section. On the leeward side, flow separation originated near the tip and extended toward the center.

The flow on the leeward side wing upper surface became separated with lower angle-of-attack settings as compared to the windward side. In general, it took approximately an additional 2° to develop an equivalent separated flow pattern on the windward side of the wing upper surface in comparison with that on the leeward side. Both the wing leading edge sweep-back and the fuselage wake effect are considered to be the leading contributing factors to the difference in flow separation development on both sides of the wing with sideslip.

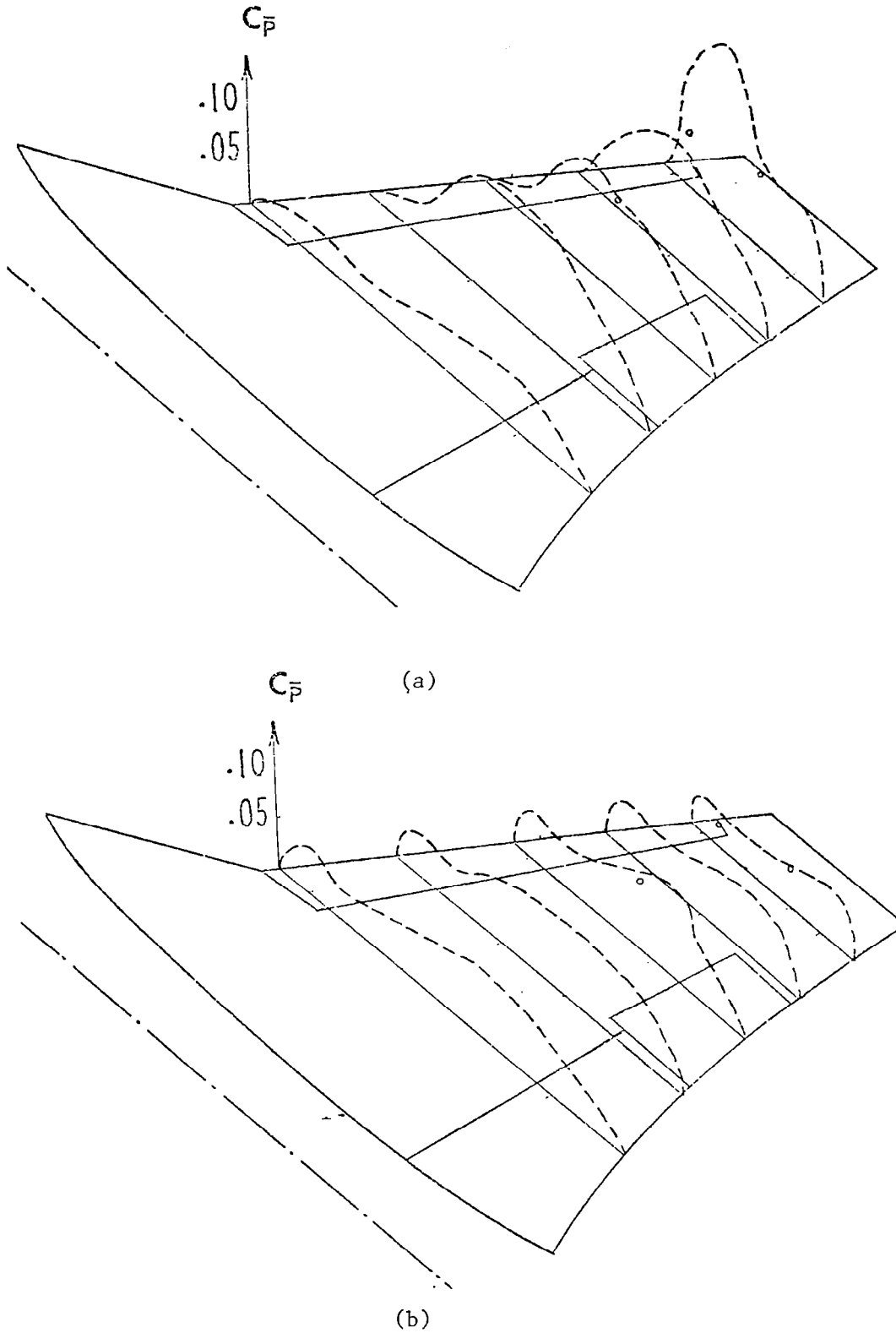

Figure 91. Dynamic Pressure Coefficient Distributionsof the F-5A Scale Model - Configuration 3 , Phase II, (a) Run 11, $\alpha = 10^{o}$, $\beta = 8^{o}$, (b) Run 12, $\alpha = 10^{o}$, $\beta = -8^{o}$, M = 0.925, $\delta_n/\delta_f = 5°/12°$, $\delta_h = -10°$

On the test model, three pressure transducers (Nos. 26 to 28) were installed on the left wing top surface at location symmetrical to transducers No. 2, 4, 11 on the right wing top surface. In case the model featured perfect aerodynamic symmetry about its vertical plane, then the pressure data of transducer Nos. 26-28 under a sideslip condition should be identical to those of transducer Nos. 2, 4, 11 respectively when the sideslip angle was changed from positive to negative, or vice versa. To check the validity of this assumption, the $C_{\bar{p}}$ coefficients based on transducer Nos. 26 to 28 for $\beta = 8°$ case were overplotted on the right wing $C_{\bar{p}}$ data for $\beta = -8°$ case in small circles, Figure 91(a). Similarly, the $C_{\bar{p}}$ coefficients based on transducer Nos. 26-28 for $\beta = -8°$ case, were overplotted on the $C_{\bar{p}}$ data of the right wing for $\beta = 8°$ case, Figure 91(b). Allowing for minor irregularities in model configuration and variations in test conditions, the closeness of the left and right wing rms pressure data for equal and opposite sideslip angle ($\pm 8°$) as indicated in Figure 86, seemed to justify the assumption of model symmetry and thus the feasibility of transferring the right wing pressure data to the left wing with the sign of the sideslip angle reversed.

In order to study the pressure spatial correlations under the sideslip condition, the measured dynamic pressure data corresponding to $\alpha = 10°$ were digitized. The pressure data digitized and processed were transducer Nos. 1, 3, 4, 12, 14, 17, 22, 24, 27. Their locations are given below.

Transducer No.	Surface	% Semi-Span	% Chord
1	RH Wing Upper	85	10
3	RH Wing Upper	85	40
4	RH Wing Upper	85	60
12	RH Wing Upper	47	44
14	RH Wing Upper	47	80
17	RH Wing Upper	33	42
22	RH Tail Upper	47	40
24	RH Tail Lower	47	40
27	LH Wing Upper	85	60

Transducer Nos. 22, 24 were located downstream of No. 14, and No. 24 was directly under No. 22. Transducer No. 27 was located on left wing with the same relative position as No. 4 on right wing. The pressure data were digitized with a rate of 15,625 samples/sec and the corresponding folding frequency was 7,812 Hz. A low pass analog filter with a cutoff frequency of 7000 Hz was used during the digitizing process. Applying the digitized data, spatial correlation

between transducer pairs were performed using a spectral analysis computer program. A time span of 0.131 second was used. The maxium time lag used in the cross-correlation computation was one-fourth the time span. The corresponding frequency increment was 15 Hz (approximately 2 Hz increment on the equivalent aircraft scale).

The cross-correlation coefficient and the coherency function plots generated by the computer program showed poor correlation between all transducer pairs except (1, 3) and (22, 24) for both $\beta = 8°$ and $\beta = -8°$ cases. Typical plots are presented in Figures 92-98. The frequency scale was modified to conform to the equivalent flight test condition of the F-5A. In order to show the general trend of the coherency function in a linear frequency scale, the frequency range shown in Figures 92-98 was limited up to 157 Hz on the equivalent aircraft scale (approximately 1,200 Hz on the wind tunnel test frequency scale). The definition of cross-correlation coefficient and coherency function may be found in Reference 1.

Figure 92 showed the coherency function and the cross-correlation coefficient distribution for transducer pair (1, 3) for $\beta = 8°$ case. Under this test condition, the flow at transducer No. 1 was unseparated while No. 3 was approximately under the shock interaction line. The figure showed moderate correlation between the pair for frequency up to 55 Hz. The maximum cross-correlation coefficient ρ_o was 0.36. For $\beta = -8°$ case, Figure 93, both transducers were in the separated flow region. Pressures were rather well correlated with $\rho_o = 0.7$ and convection from No. 1 to No. 3 could be detected. The spatial correlation between transducer pairs (4, 27) and (22,24) are presented in Figures 94 - 97. Figures 94,95 yielded the information about the degree of correlation between pressures on right and left wing upper surfaces. No significant correlation was detected. Figures 96, 97, showed that the degree of correlation of the pressures on upper and lower surfaces of right horizontal tail (transducer Nos. 22, 24) was almost as strong as that of two adjacent wing pressure stations for both $\beta = 8°$ and $\beta = -8°$ cases. The cross-correlation function plots had a high peak at $t = 0$ and low level values throughout the remaining time scale. The negative peak value was confirmed by the phase difference of 180° for the two stations as shown in Figure 98. Furthermore, the PSD shapes for transducer Nos. 22, 24 were similar. All the observations gave clues as to the wake flow makeup near the tail surface as the tail section chord was parallel to the mean flow direction. The average phase

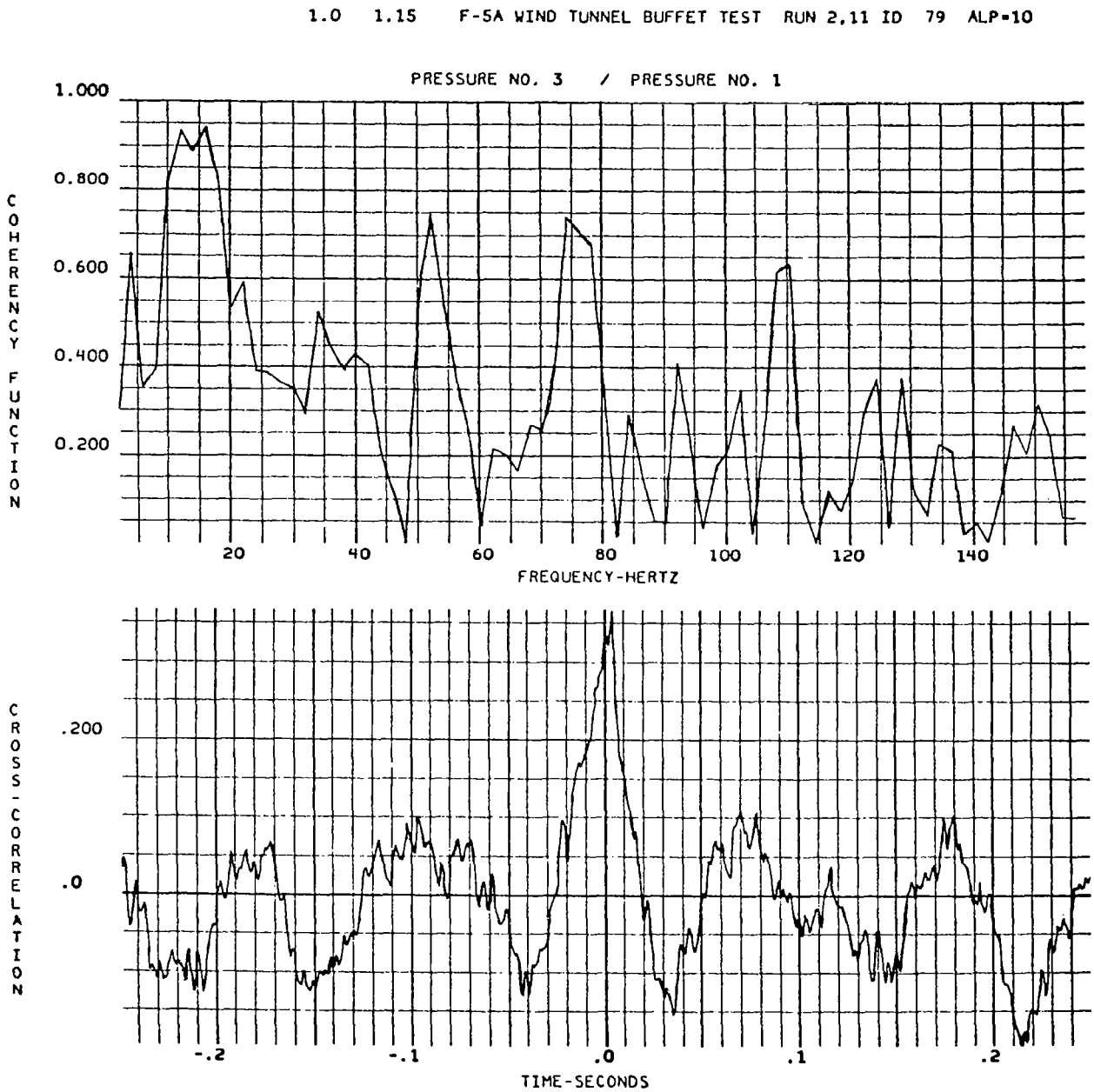

Figure 92. Spatial Correlation Plots for Transducer Pair (1, 3) of Run 11, Phase II, $\alpha = 10^{\circ}$, $\beta = 8^{\circ}$, M = 0.925, $\delta_n/\delta_f = 5°/12°$, $\delta_h = -10°$

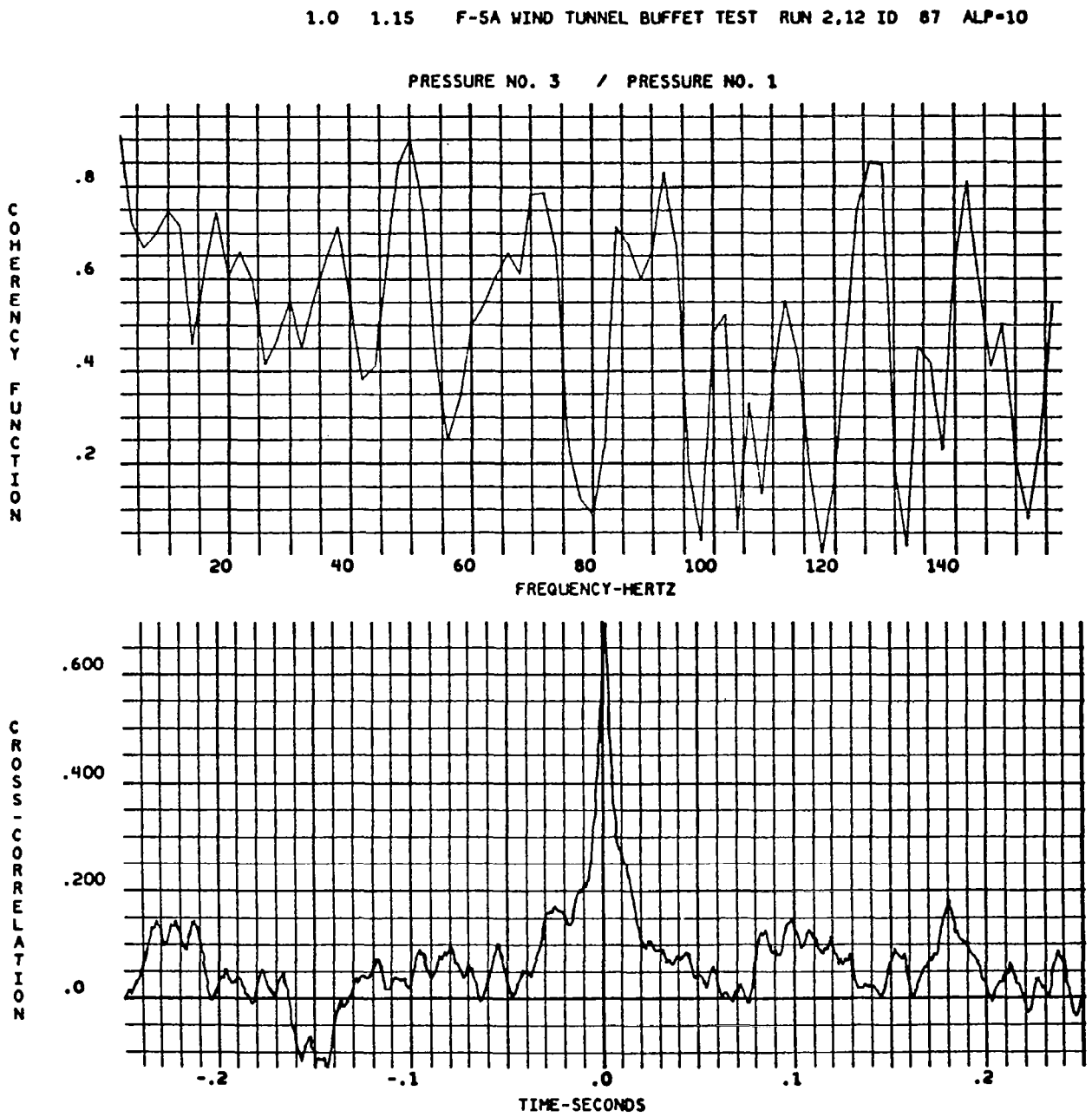

Figure 93. Spatial Correlation Plots for Transducer Pair (1, 3) of Run 12, Phase II, $\alpha = 10^{o}$, $\beta = -8^{o}$, M = 0.925, $\delta_n/\delta_f = 5°/12°$, $\delta_h = -10°$

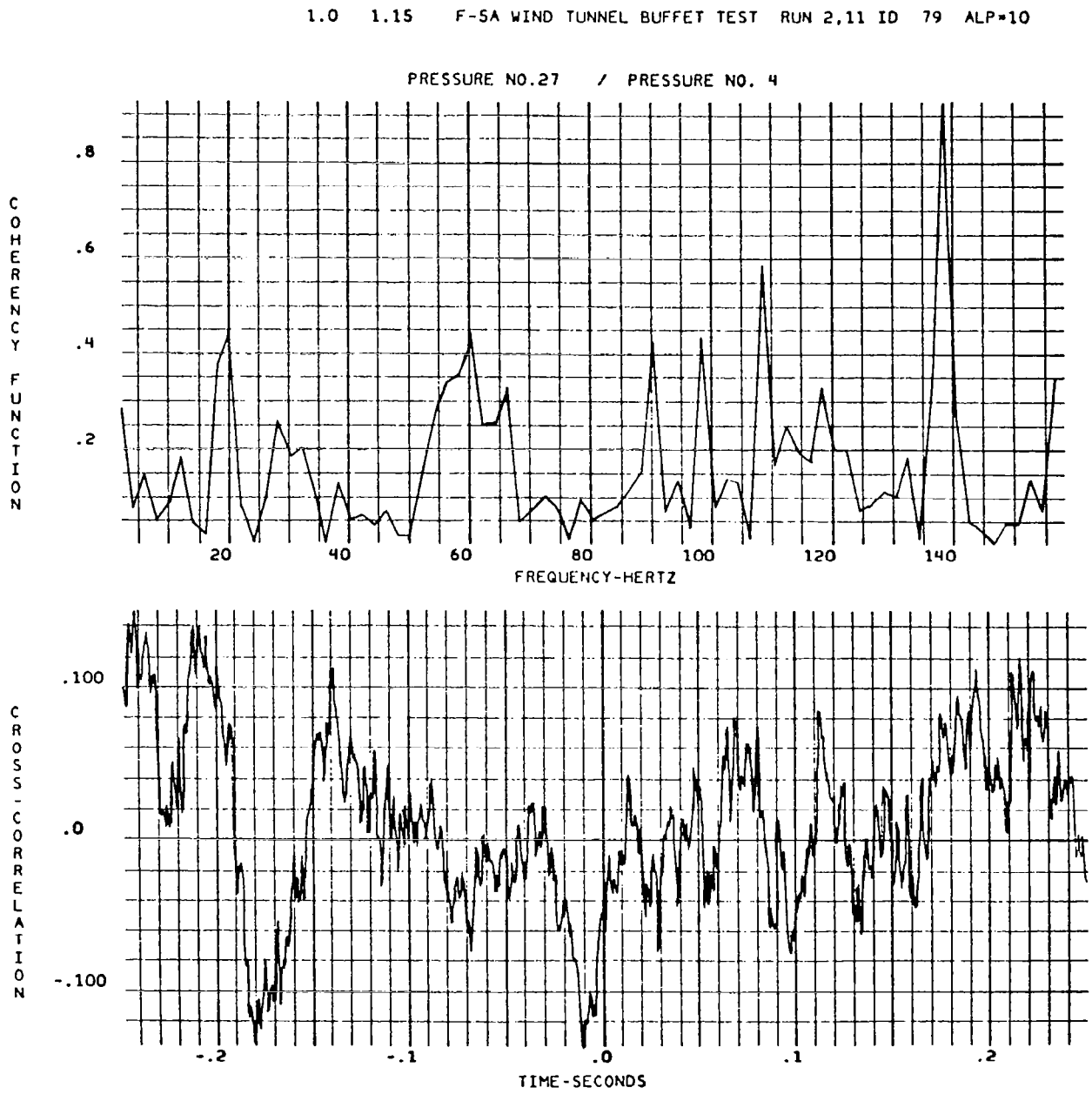

Figure 94. Spatial Correlation Plots for Transducer Pair (4, 27) of Run 11, Phase II, $\alpha = 10^{o}$, $\beta = 8^{o}$, M = 0.925, $\delta_n/\delta_f = 5°/12°$, $\delta_h = -10°$

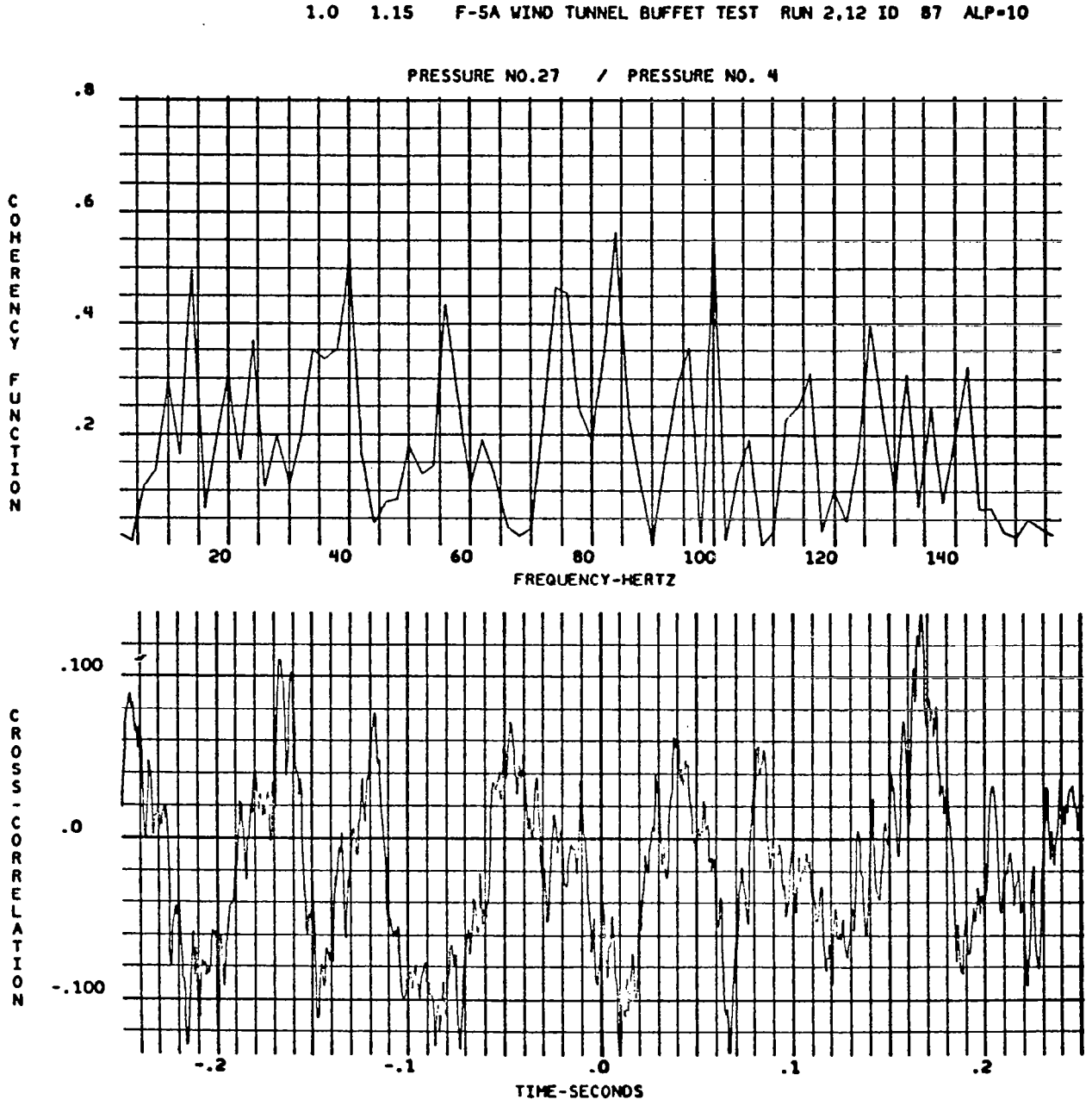

Figure 95. Spatial Correlation Plots for Transducer Pair (4, 27) of Run 12, Phase II, $\alpha = 10^{o}$, $\beta = -8^{o}$, M = 0.925, $\delta_n/\delta_f = 5°/12°$, $\delta_h = -10°$

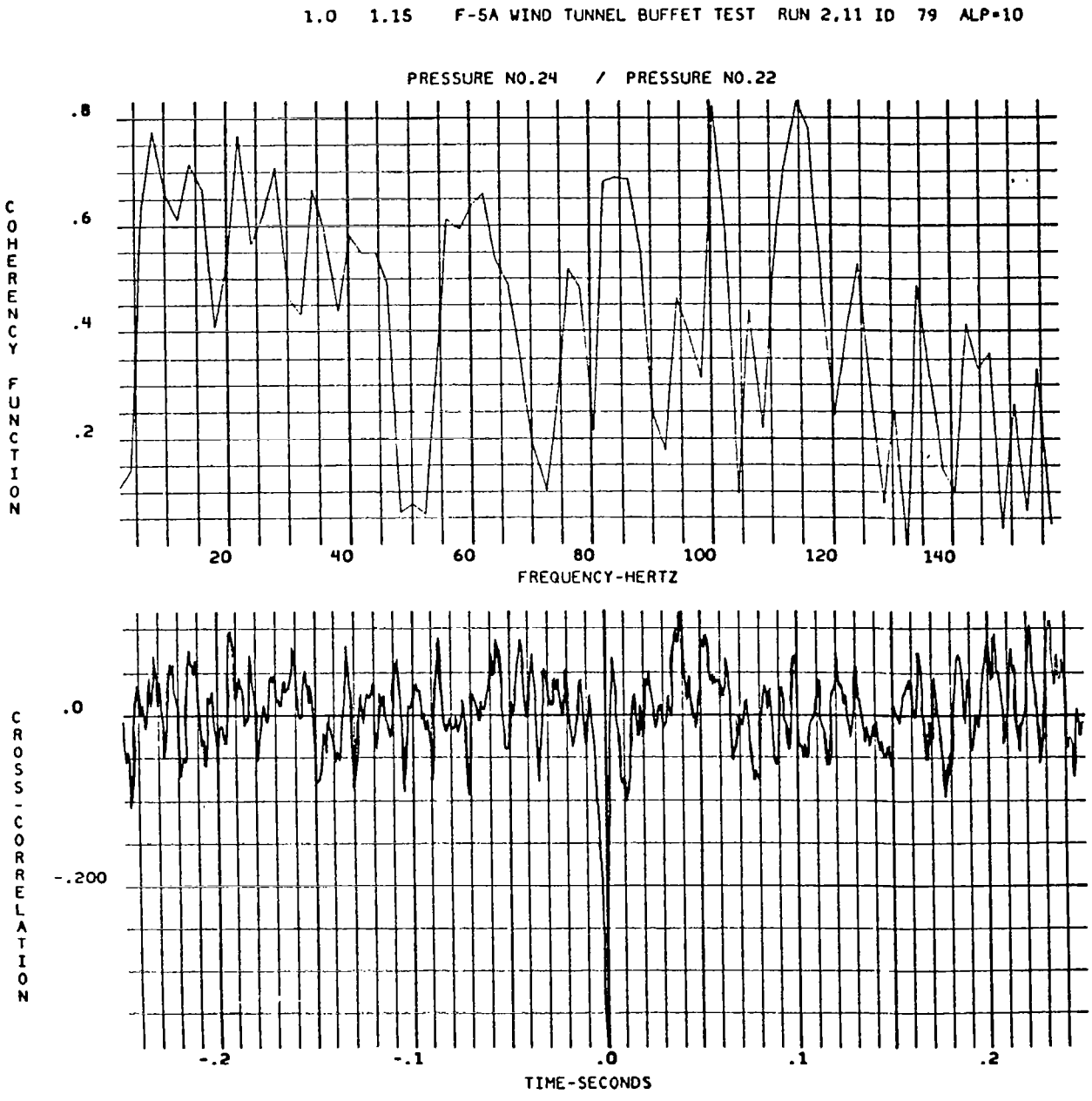

Figure 96. Spatial Correlation Plots for Transducer Pair (22, 24) of Run 11, Phase II, $\alpha = 10^{\circ}$, $\beta = 8^{\circ}$, M = 0.925, $\delta_n/\delta_f = 5°/12°$, $\delta_h = -10°$

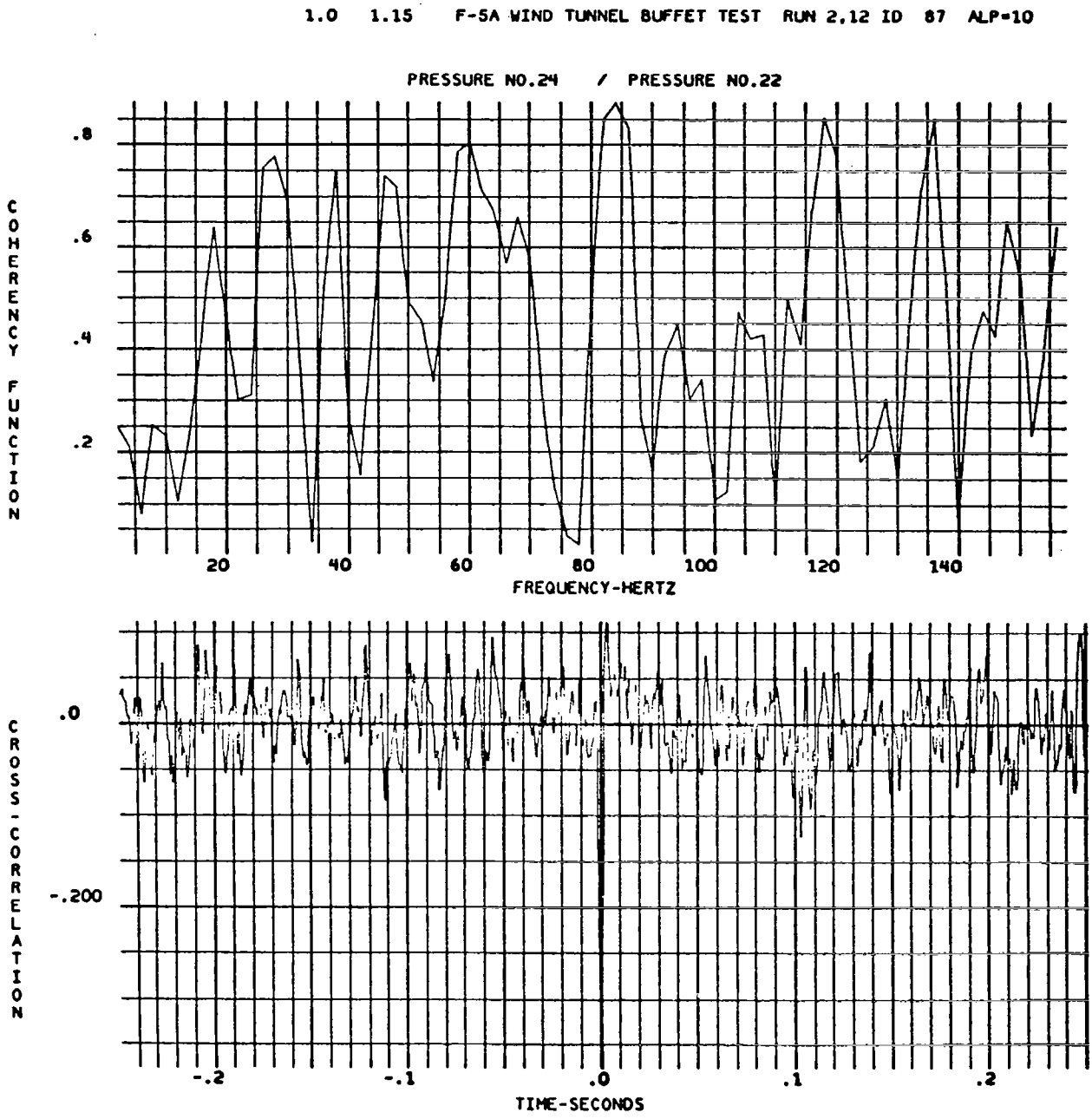

Figure 97. Spatial Correlation Plots for Transducer Pair (22, 24) of Run 12 Phase II, $\alpha = 10^{o}$, $\beta = -8^{o}$, M = 0.925, $\delta_n/\delta_f = 5°/12°$, $\delta_h = -10°$

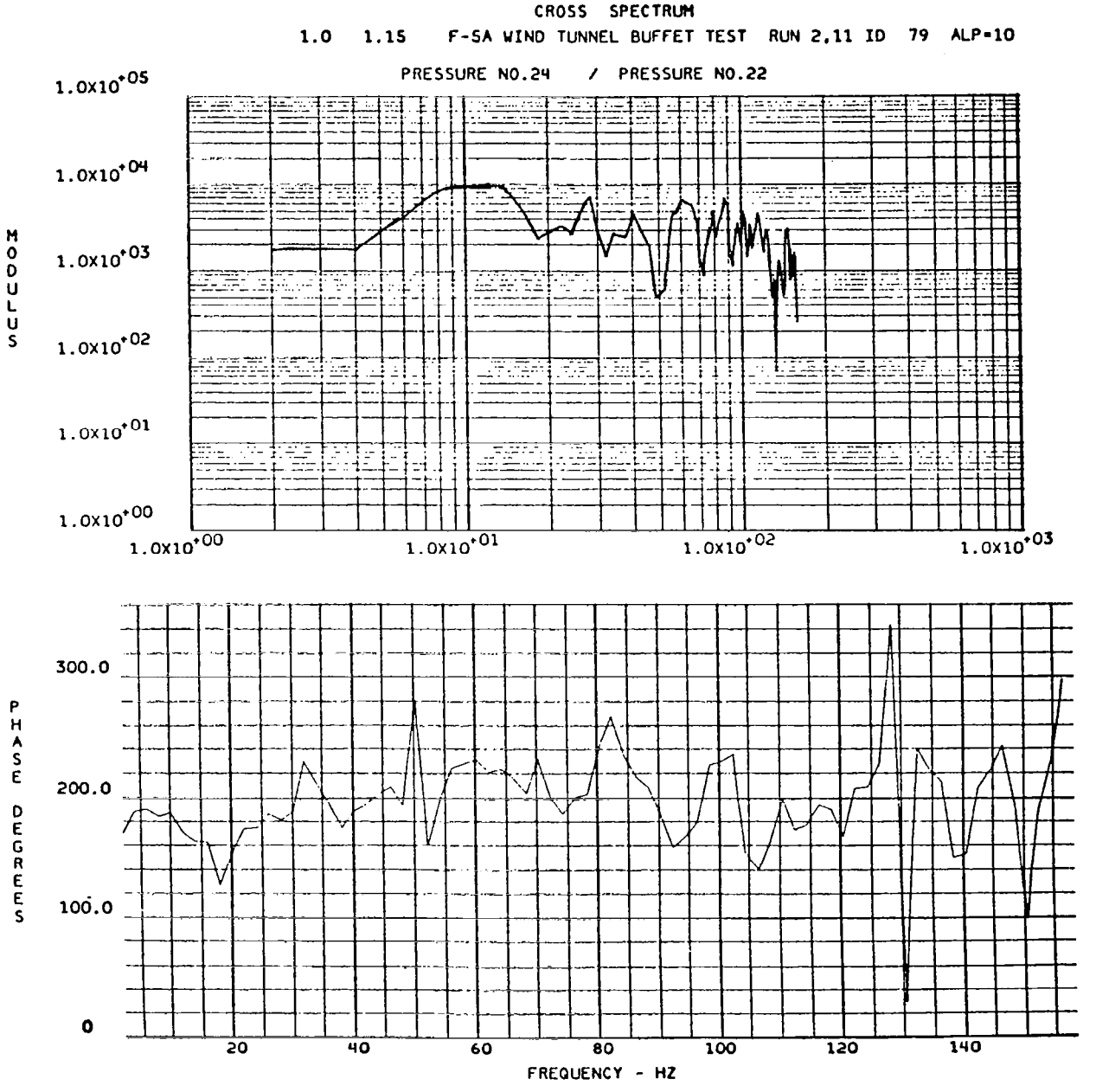

Figure 98. Modulus and Phase Angles of Pressure Cross-Spectrum for Transducer Pair (22, 24) of Run 11, Phase II, $\alpha = 10^{\circ}$, $\beta = 8^{\circ}$, $M = 0.925$, $\delta_n/\delta_f = 5°/12°$, $\delta_h = -10°$

angle difference of 180° seemed to be generated by the induced pressure due to random tail motion.

4.9 Non-dimensional Power Spectra of the Dynamic Pressures

In phase II, Runs 10 and 14 were performed under almost identical conditions Specifically, the test conditions are as follows:

Model Configuration 3, $\delta_n/\delta_f = 5°/12°$

$\delta_a = 0°/0°$, $\delta_h = -10°$

$\beta = 0°$

$M = 0.929$

$R_N = 7.447 \times 10^6$/m (2.27×10^6/ft)

$P_o = 29.90$ KN/m^2 (624.5 psf)

$P_T = 52.19$ KN/m^2 (1090 psf)

$Q = 18.05$ KN/m^2 (377.0 psf)

For $\alpha = 8°$, a number of dynamic pressure data were converted into power spectra. The spectra were plotted in a non-dimensional form so as to compare with non-dimensional power spectra data collected by Dennis G. Mabey (Reference 4) according to the convention orginated by T. B. Owen (Reference 7). In both references, the data were plotted as:

$\sqrt{nF(n)}$ vs $n = fL/V$

where f = frequency, Hz

L = a characteristic length (the bubble length in Reference 4)

V = the freestream velocity

$F(n)$ = contribution to $< P^2 > /q^2$ in frequency band Δf

P = the fluctuating pressure

$Q = q$ = the freestream dynamic pressure

In Figures 99 to 101, the non-dimensional pressure spectra for transducer Nos. 18, 22, 23 are plotted for F-5A model corresponding to $\alpha = 8°$, Run 14, Phase II described previously. The coordinators are:

$\Phi f/Q^2$ vs $k = \omega b/U$

where Φ = the power spectral density

ω = circular frequency = $2\pi f$

b = a characteristic length (the mean aerodynamic chord)

$U = V$ = the freestream velocity

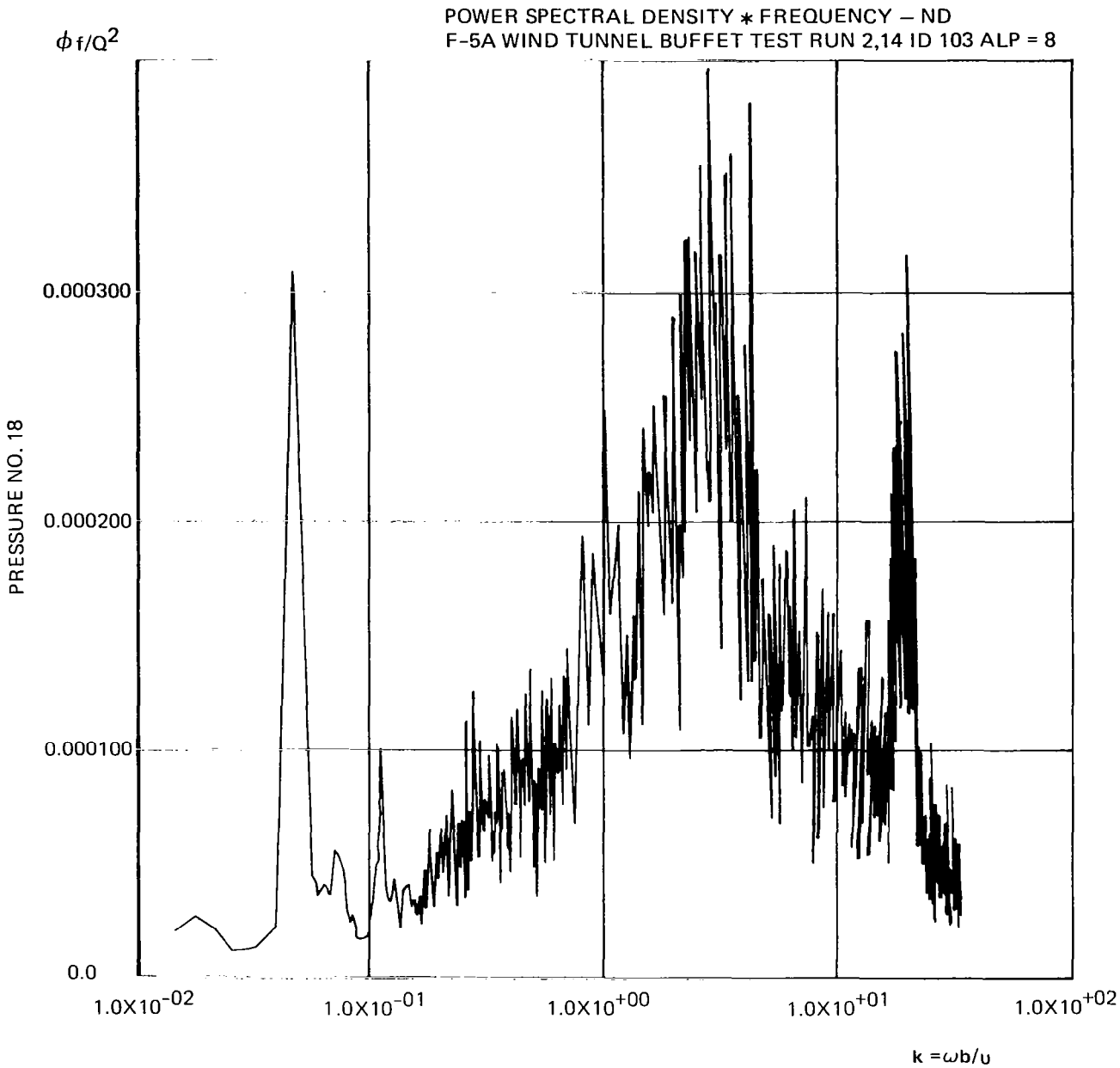

Figure 99. Non-Dimensional Pressure PSD of Transducer No. 18 Recorded at $\alpha = 8°$, Run 14, Phase II, $\beta = 0°$, M = 0.929, $\delta_n/\delta_f = 5°/12°$, $\delta_h = -10°$

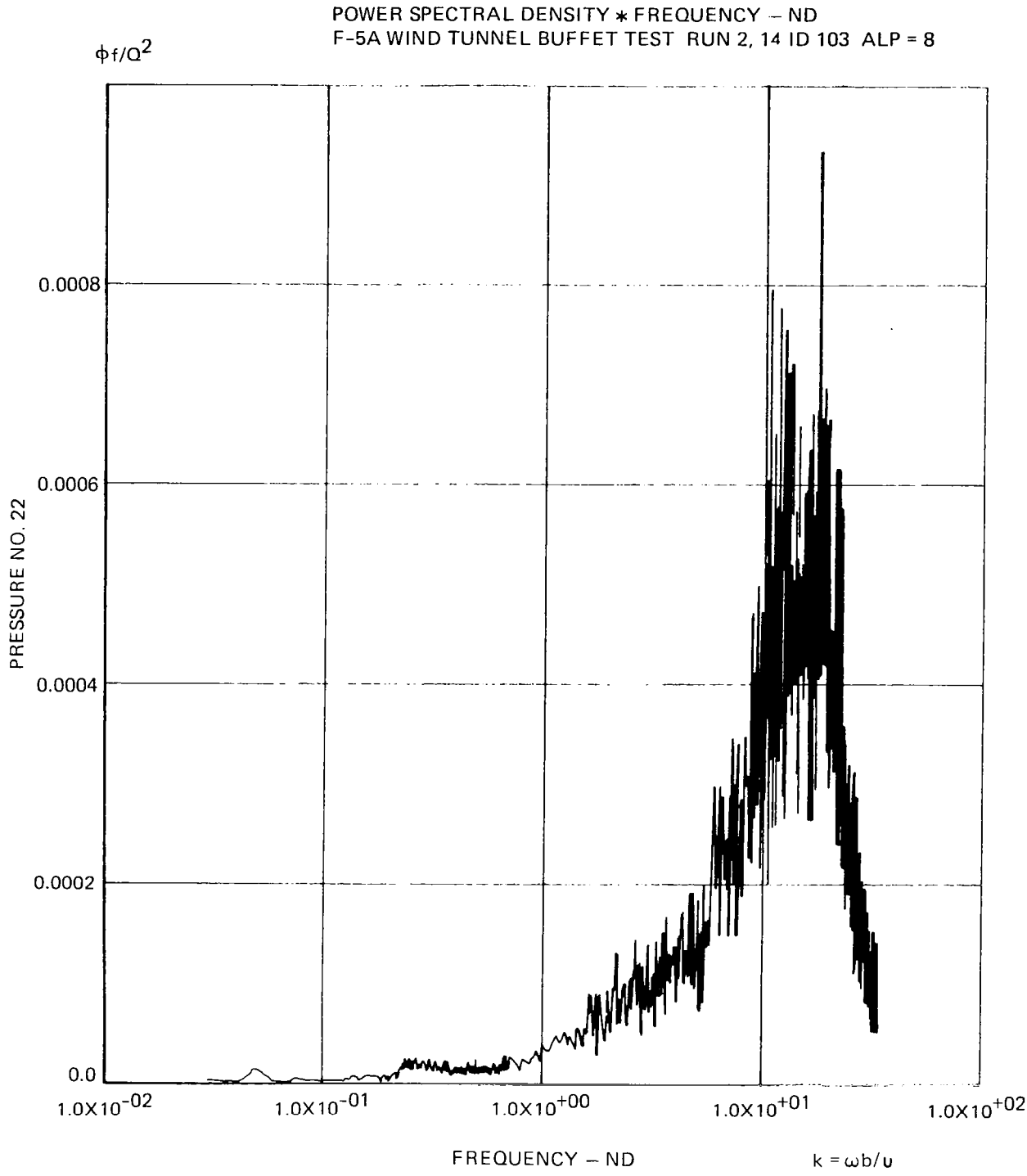

Figure 100. Non-Dimensional Pressure PSD of Transducer No. 22 Recorded at $\alpha = 8°$, Run 14, Phase II, $\beta = 0°$, M = 0.929, $\delta_n/\delta_f = 5°/12°$, $\delta_h = -1C$

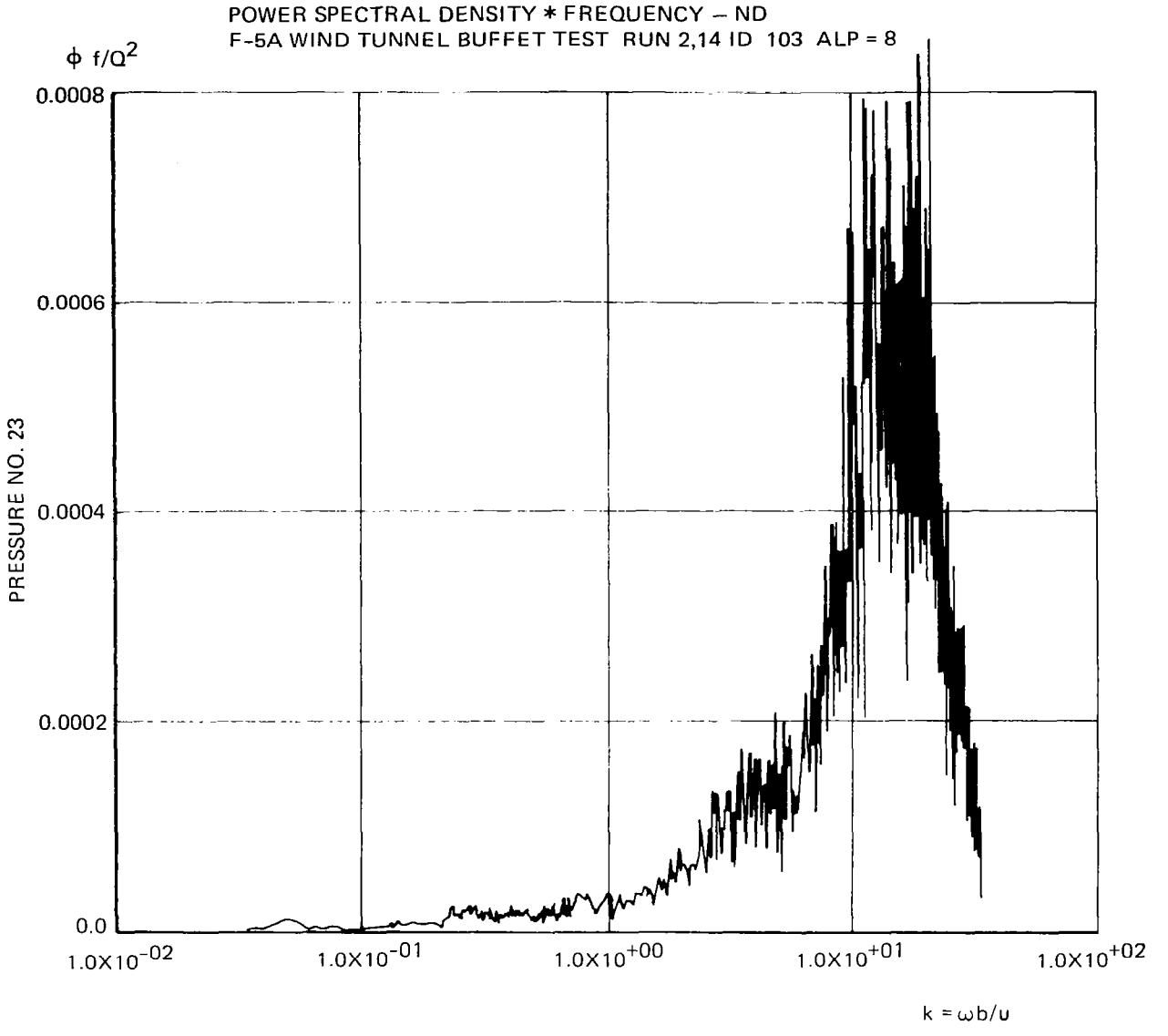

Figure 101 Non-Dimensional Pressure PSD of Transducer No. 23 Recorded at $\alpha = 8°$, Run 14, Phase II, $\beta = 0°$, M = 0.929, $\delta_n/\delta_f = 5°/12°$, $\delta_h = -10°$

Compared with the British convention, it is seen that:

$$\Phi f/Q^2 = nF(n)$$

$$k = 2\pi(b/L)n$$

so that the spectral plots of Figures 99 to 101 can be compared readily with the British data shown in Reference 4. In the above, the ratio (b/L) is the ratio between the aircraft mean aerodynamic chord and the separation bubble length. Except for the PSD peak at k = .05 for transducer No. 18 corresponding to the first symmetrical wing bending mode, the general patterns of the non-dimensional PSD's of the F-5A data are qualitatively comparable to those compiled in Reference 4.

Section 5

ANALYTICAL PROGRAM - SCALE MODEL STABILITY PREDICTION ALLOWING FOR AEROELASTIC EFFECT

The scale model used in the wind tunnel test is a structure with a flexible support. The spring constant associated with each component of the flexible support may be determined as the product of the square of the measured natural frequency (in rad/sec) and the total mass or mass moment-of-inertia of the scale model associated with that degree of freedom. For flexibly-supported structures, the equations of motion in the frequency domain ay be written as:

$$\begin{bmatrix} K_{11} & K_{12} \\ K_{21} & K_{22} + K_S \end{bmatrix} \begin{Bmatrix} h_1 \\ h_2 \end{Bmatrix} + i\omega \begin{bmatrix} C_{11} & C_{12} \\ C_{21} & C_{22} \end{bmatrix} \begin{Bmatrix} h_1 \\ h_2 \end{Bmatrix} - \omega^2 \begin{bmatrix} M_1 & 0 \\ 0 & 0 \end{bmatrix} \begin{Bmatrix} h_1 \\ h_2 \end{Bmatrix} = \begin{Bmatrix} f_1 \\ f_2 \end{Bmatrix} \qquad (8)$$

where K, C, M are the stiffness, damping, and mass matrices of the structure; h and f represent the Fourier transforms of the deflections and external forces, respectively. In Equation (8), subscript 1 refers to the control points and subscript 2 refers to the reference point where the flexible support is attached. K_S is a diagonal matrix whose elements represent the spring constants associated with various degrees of freedom of the flexible support. It is noted that an infinite spring constant implies a rigid constraint, while a zero spring constant implies a free flight condition. The values of K_S in Equation (8) are assumed to be finite, and that:

$$K_{si} = M_{si}\, \omega^2_{si} \qquad (9)$$

In Equation (9), M_{si} is the total mass or mass moment-of-inertia of the structure in the direction of the i-th degree of freedom, and ω_{si} is the measured nautral frequency in rad/sec. To simplify the calculation procedure, the mass of the structure is assumed to be concentrated at the control points.

The governing equation for an undamped natural vibration of flexibly-supported structure is simple:

$$\begin{bmatrix} K_{11} & K_{12} \\ K_{21} & K_{22} + K_S \end{bmatrix} \begin{Bmatrix} x_1 \\ x_2 \end{Bmatrix} = \omega_F^2 \begin{bmatrix} M_1 & 0 \\ 0 & 0 \end{bmatrix} \begin{Bmatrix} x_1 \\ x_2 \end{Bmatrix} \qquad (10)$$

where x is the mode shape and ω_F is the resonance frequency. Equation (10) may be simplified by introducing a control point rigid transformation matrix T whose columns are composed of rigid body modes associated with the unit movement of each degree of freedom of the flexible support, respectively. The matrix T satisfies the following relationship:

$$\begin{bmatrix} K_{11} & K_{12} \\ K_{21} & K_{22} \end{bmatrix} \begin{bmatrix} T \\ I \end{bmatrix} = [0] \tag{11}$$

$$\begin{aligned} K_{12} &= -K_{11}\, T \\ K_{22} &= T^T K_{11}\, T \end{aligned} \tag{12}$$

Since, for $K_S = 0$, the structure is free to move as a rigid body in the flexibly-supported directions, substituting Equations (9) and (12) into Equation (10) gives:

$$\{x_2\} = \left[T^T K_{11} T + M_S \omega_S^2\right]^{-1} \left[T^T K_{11}\right] \{x_1\} \tag{13}$$

and the eigen equation is then:

$$\left[K_{11} - K_{11}\, T \left[T^T K_{11}\, T + M_S \omega_S^2\right]^{-1} T^T K_{11}\right] \{x_1\} = \omega_F^2 \left[M_1\right] \{x_1\} \tag{14}$$

Let X be a modal matrix whose columns are composed of modal shapes x. The orthogonality conditions between modes lead to the following diagonal matrix expressions for modal masses and modal stiffnesses:

$$\begin{aligned} \left[M_F\right] &= \left[X_1^T M_1 X_1\right] \\ \left[K_F\right] &= \left[X_1^T \; X_2^T\right] \begin{bmatrix} K_{11} & K_{12} \\ K_{21} & K_{22} + K_S \end{bmatrix} \begin{bmatrix} X_1 \\ X_2 \end{bmatrix} = \left[M_F\right] \left[\omega_F^2\right] \end{aligned} \tag{15}$$

With the available modal data, the structure deflections may be represented as:

$$\begin{Bmatrix} h_1 \\ h_2 \end{Bmatrix} = \begin{bmatrix} X_1 \\ X_2 \end{bmatrix} \{\alpha\} \tag{16}$$

where α is the modal amplitude matrix. Premultiplying Equation (1) by $\left[X_1^T \; X_2^T\right]$ and using Equations (15) and (16) yields the modal equation of motion in the following form:

$$\left[Z_F\right]\{\alpha\} = \left[M_F\left(\omega_F{}^2 + ig_F\omega\omega_F - \omega^2\right)\right]\{\alpha\} = \left[X_1{}^T \; X_2{}^T\right]\begin{Bmatrix} f_1 \\ f_2 \end{Bmatrix} = \{F\} \qquad (17)$$

provided that the damping matrix $[C]$ satisfies the following conditions:

$$\left[C_F\right] = \left[X_1{}^T \; X_2{}^T\right]\begin{bmatrix} C_{11} & C_{12} \\ C_{21} & C_{22} \end{bmatrix}\begin{bmatrix} X_1 \\ X_2 \end{bmatrix} = \left[\omega_F{}^{-1}\right]\left[g_F\right]\left[K_F\right] \qquad (18)$$

where g_F is the modal damping coefficient matrix.

The instability characteristics along the roll axis of the flexibly-supported model may be determined by the use of the dynamic equations applied in stability and control studies. The lateral stability equations of a rigid aircraft in terms of the stability derivatives derived with respect to a body axes system with the origin at the center of gravity and x-z plane the plane of symmetry, may be written as follows:

$$I_{xx}\dot{p} - I_{xz}\dot{r} = \frac{qSb}{U}\left(C_{\ell\beta}\, U\, \beta + \frac{b}{2} C_{\ell r} r + \frac{b}{2} C_{\ell p}\, p\right) \qquad (19)$$

$$mU\left(\dot{\beta} + \cos\alpha_o\, r - \sin\alpha_o\, p\right) = \frac{qS}{U}\left(C_{y\beta}\, U\, \beta + \frac{b}{2} C_{yr}\, r + \frac{b}{2} C_{yp}\, p\right) \qquad (20)$$

$$I_{zz}\dot{r} - I_{xz}\dot{p} = \frac{qSb}{U}\left(C_{n\beta}\, U\, \beta + \frac{b}{2} C_{nr}\, r + \frac{b}{2} C_{np}\, p\right) \qquad (21)$$

where p, β, r are the roll rate, the side-slip angle, and the yaw rate, respectively, m is the mass, I_{xx}, I_{zz} are the moments of inertia about the roll and yaw axes, respectively; I_{xz} is the product of inertia. U is the flight speed; α_o is the initial angle-of-attack; b is the span of the aircraft and S is the wing area, ρ is the air density and q is the dynamic pressure. The other expressions in Equations(19-21)are the non-dimensional aerodynamic derivatives that are the functions of aircraft configuration, the altitude, the angle-of-attack, the Mach number, and the Reynolds number. For a given flight condition, the solution of the eigen-equations(19-21)yields the aircraft modal data, including the Dutch roll oscillation which is of special interest in aircraft buffet studies. In applying the dynamic Equations(19-21)to the flexibly-supported

scale model, proper spring and damping terms representing the supporting system reactions as well as a number of fundamental wing bending-torsion modes were added. The dynamic equations in the matrix form are described below.

$$\left[\begin{bmatrix} K_r & 0 \\ 0 & K_f \end{bmatrix} + \lambda \begin{bmatrix} C_r - A_{rr} & -A_{rf} \\ -A_{fr} & C_f - A_{ff} \end{bmatrix} + \lambda^2 \begin{bmatrix} M_r & 0 \\ 0 & M_f \end{bmatrix}\right] \begin{Bmatrix} \alpha_r \\ \alpha_f \end{Bmatrix} = 0 \quad (22)$$

where α are the modal amplitudes. In Equation(22), subscript r refers to the supporting system modes and subscript f refers to the structural flexible modes. The expressions of the modal spring, damping and mass terms $(K, C, M)_{r,f}$ are given in Equations (15)and (18). $A_{(\ )}$ represents the generalized aerodynamic matrices. The eigen-value λ is in general a complex number

$$\lambda = i\omega\,(1 + i\zeta) \quad (23)$$

where ω is the angular frequency and ζ the damping ratio. The criterion

$$\zeta > 0$$

indicates that the motion is stable.

Let

$$\{\alpha_r\}^T = \underline{\text{roll angle, side deflection, yaw angle}} \quad (24)$$

then the matrix A_{rr} in Equation (22) may be approximated in terms of the nondimensional aerodynamic derivatives by means of Equations (19 to 21)

$$[A_{rr}] = \frac{qSb}{2U} \begin{bmatrix} b\,C_{\ell p} & 2\,C_{\ell\beta} & b\,C_{\ell r} \\ C_{yp} + \frac{2mU^2}{qSb} \sin\alpha_o & \frac{2}{b}\,C_{y\beta} & C_{yr} - \frac{2mU^2}{qSb} \cos\alpha_o \\ b\,C_{rp} & 2\,C_{n\beta} & b\,C_{nr} \end{bmatrix} \quad (25)$$

In predicting the instability characteristic of the flexibly-supported model, the scale model modal data were generated under the following conditions:

1. The weight and the mass moment of inertia about roll axis of the model match their measured values.
2. The natural frequencies, corresponding to the spring support modes and the first wing bending (- torsion) mode match their measured values.

The F-5A basic aerodynamic stability and control data (Reference 12) were used to determine the aerodynamic derivatives, which are functions of altitude, Mach number and angle-of-attack, under various test conditions.

Using the above formulation, the analytical computation of the instability characteristics of the flexibly-supported scale model for α = 0°, 4°, 8°, 12° was performed for the following configurations:

Mach Number	0.925	0.75
Free stream speed	299 m/sec	249 m/sec
Free stream dynamic pressure	18.37 KN/m^2	15.9 KN/m^2
Equivalent altitude	10,668 m	7,772 m

Three supporting system modes and two structural flexible modes were used in the analysis. The damping coefficient corresponding to the roll motion was 0.024, the lowest damping level used during the tests.

The calculated instability characteristics along the roll axis of the model are presented in Figure 102. Since the natural frequencies generated by the eigen-value problem were so close to their undamped values, only the damping ratio ζ (Equation 23) is plotted vs. angle-of-attack.

Referring to Figure 102, the damping for the wing rock type oscillations of the scale model decreases rather rapidly with increasing angle-of-attack beyond 8 degrees. It can be visualized that, for each configuration, there was a critical angle-of-attack α^* at which the model started to oscillate in a random manner. For the scale model tested, wing rock appeared at approximately α^* = 8° to 12° for M = 0.925, depending on the test configurations. For M = 0.75, the values of α^* are higher in comparison with those corresponding to M = 0.925 cases. This trend is consistent with the analytical predic-

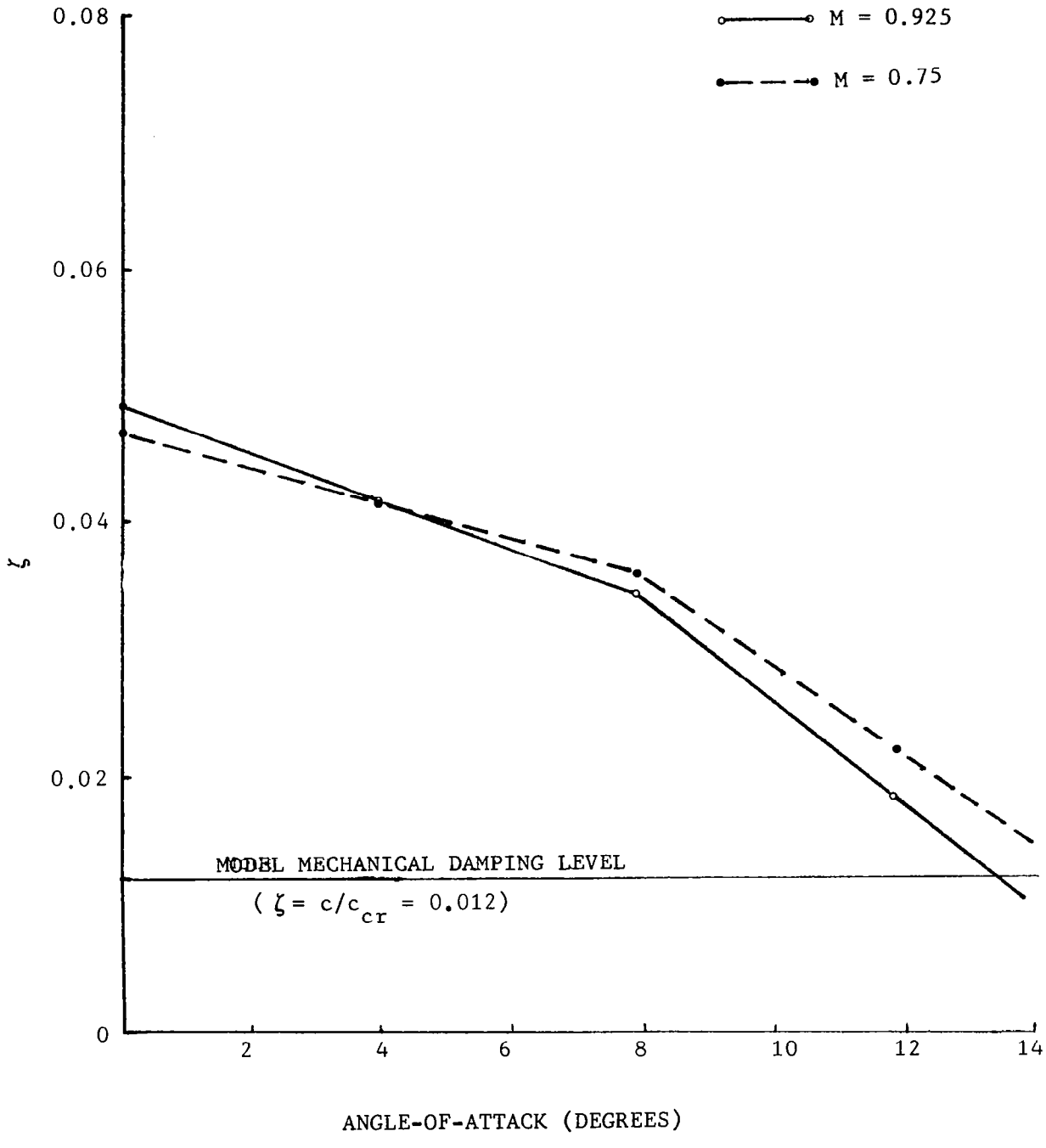

Figure 102. Prediction on the Instability Characteristics Along the Roll Axis of the Flexibly-Supported Scale Model, M = 0.75 and M = 0.925.

tion as shown in Figure 102. In a free flight condition, near zero or no mechanical damping exists. For this case, the zero damping level will be moved to the $\zeta = 0.012$ line. As a result, the $\zeta - \alpha$ curve of Figure 102 indicates the aircraft becomes unstable at $\alpha \simeq 14°$ for M = 0.925.

A similar approach could be applied to predict the aircraft instability characteristics in free flight conditions by dropping the K_r, C_r terms in Equation (22). However, it must be remembered that the results of the wind tunnel test can only be applied to free flight stability considerations in a qualitative manner. This is because the yaw and sideslip responses, which are important in Dutch roll, for free flight were not adequately modelled in the wind tunnel test. In the following, the results of predicted Dutch roll motion of F-5A are presented.

	M = 0.925, h = 10,668 m		M = 0,75, h = 7,772 m	
	f (Hz)	ζ	f (Hz)	ζ
$\alpha = 0°$	0.412	0.1009	0.34	0.1087
$\alpha = 4°$	0.456	0.1161	0.372	0.131
$\alpha = 8°$	0.536	0.1339	0.44	0.1476
$\alpha = 12°$	0.619	0.0805	0.493	0.1115

Based on the above data, the following conclusions are drawn:

1. The highest aerodynamic damping occurs at $\alpha \simeq 8°$. Beyond this point, damping decreases rather rapidly indicating wing rock instability at higher α angles.

2. In free flight condition, the predicted wing rock occurs at lower angle-of-attack when M = 0.925 as compared to the M = 0.75 case. This conclusion is in line with the test results and the analytical prediction for the scale model.

Section 6

CONCLUSIONS

In the report, the wind-tunnel test program, the processed data, and the correlation results between the wind tunnel data and the buffet flight data are presented. Also included are the results obtained based on the parametric studies of the wind-tunnel data (by varying either the model configuration or the test condition). In the following, the key conclusions and observations are presented.

1. The separation region was developed over the upper wing surface with increasing angle-of-attack. The development of the separated flow over a "substantial" part of the outer wing occurred within a relatively narrow angle-of-attack range ($\Delta \alpha \sim 2°$). For tests conducted at a fixed angle-of-attack in this range, the dynamic pressures were found to be highly non-stationary, particularly in the shock/boundary layer interaction region.

2. In general, the development and expansion of the flow separation region on the model wing surface were similar to the results acquired during a previous buffet flight test program of the F-5A aircraft. At M = 0.925, the shock boundry was initiated near the trailing edge of the wing-tip region and gradually expanded toward the inboard and upstream region with increasing angle-of-attack. For M = 0.75 the flow separation was leading edge induced.

3. In comparison with the zero sideslip angle case, the effect of positive sideslip angle (for the windward side of the wing semi-span) tended to move the shock and shock-induced flow separation downstream and to create a favorable flow condition in its wing-tip region which retarded the local flow separation. On the leeward side of the wing semi-span (negative sideslip angle condition), flow separation seemed to originate at the wing-tip region. Furthermore, the flow on the leeward side wing upper surface became separated with lower angle-of-attack settings (approximately 2°) as compared to the windward side.

4. As compared to the cases with tip-mounted missiles, the lack of tip-mounted missiles and their trailing vortex flow seemed to aggravate the situation and make the shock location and the resulting flow pattern less stable. However, the tip-mounted missiles had an adverse effect in promoting the flow separation at a certain critical α angle. This effect was greatly diminished after the critical angle-of-attack was surpassed.

5. The deflection of the horizontal tail (to -10°) tended to delay or alternate the shock-induced flow separation in that part of the wing direction upstream of the tail. Correspondingly, for a moderate angle-of-attack, the shock strength and the level of dynamic pressure behind the shock tended to be stronger in the outer half span of the wing as compared to the zero horizontal tail surface setting case. The effect of the tail surface setting became less prominent as the angle-of-attack was further increased.

6. At moderate angle-of-attack, the deflected leading edge flap tended to push the flow separation boundary further downstream as compared to the case of the retracted flap. The extended trailing edge flap tended to keep the shock-induced flow separation region further upstream in the inboard region at a moderate angle-of-attack. This can be attributed to the increase camber in the inboard portion of the wing semi-span for the extended flap cases.

7. For angles-of-attack under the critical angle α^* (the angle-of-attack at which the flexibly-supported model started to oscillate along the roll axis), the trends of the shock development and the expansion of the flow separation region were the same for the fixed and flexibly-supported models. However, substantial deviation in local pressures did exist. At the critical angle-of-attack α^*, the flexibly-supported model motion tended to make the dynamic pressure distribution more even, spacewise, as compared to the fixed model. For $\alpha > \alpha^*$, the difference in the dynamic pressures of the models tended to diminish as the angle-of-attack was further increased.

8. When maximum wing-rock motion occurred, the dynamic pressure peak levels corresponding to the natural roll frequency were extremely high for most of the transducers of the flexibly-supported model, in comparison with the corresponding pressure data for the regularly-supported model.

9. For the configurations with 0 degree horizontal tail surface setting, the very high dynamic pressures on the horizontal tail upper surface at high angles-of-attack indicated the horizontal tail upper surface buffet. On the lower surface, high dynamic pressures caused by the wake flow due to the deflected trailing edge flap were observed at low angles-of-attack.

10. For the configurations with -10 degrees horizontal tail setting, the high dynamic pressures on the horizontal tail lower surface at lower angles-of-attack indicated shock-induced flow separation due to the negative tail deflection. As the angle-of-attack increased, the combined effects of tail buffet and wake flow due to wing buffet made the dynamic pressure levels on the horizontal tail lower surface even higher for the configurations with deflected leading edge and trailing edge flaps. However, dynamic pressure levels dropped when the angle-of-attack setting exceeded 10 degrees where the negative horizontal tail setting cancelled the angle-of-attack setting. The effect of wake flow due to wing buffet on the dynamic pressures on the tail lower surface was minimum. For the configurations with retracted leading edge and trailing edge flaps, the reduction in the dynamic pressure levels on the horizontal tail lower surface at very high angles-of-attack also may be contributed to the wing downwash effect which tended to steer the wake flow downward and away from the horizontal tail.

11. The trend of development and expansion of the flow separation region were similar for the wind-tunnel model test and the corresponding flight test. In general, measured in angle-of-attack, it took the scale model approximately an additional 2° to 4° to develop a similar separation flow pattern on the top wing surfaces. The Reynolds number effect was less significant. For M = 0.925 case, at a given spanwise location, the shock tended to stay closer to the

trailing edge on the scale model as against the flight test results. Certain factors were noted which were believed to contribute to the scale model flow behavior: (1) the aeroelastic effect of the full-scale aircraft caused an increase in the local angle-of-attack in the outer span of the wing; (2) the transient effect in a transonic maneuver of the aircraft where the angle-of-attack changed continuously; (3) F-5A wing has a thin airfoil section, namely NACA 65A004.8; (4) transition strips were installed on this F-5A scale model which should trigger the shock induced flow separation in an upstream location on the wing chord.

12. For given test condition, the instability characteristics along the roll axis of the flexibly-supported model was predicted vs. angle-of-attack using the dynamic equations employed in stability and control studies. A similar approach may be applied to predict the aircraft instability characteristics in a free flight. With additional refinements in the analytical formulation, the approach can be extended to include the steady state sideslip angle as a parameter in the wing rock stability prediction.

13. The flexibly-supported model is important in simulating the wing rock oscillations in a transonic maneuver. Based on the pressure and response data acquired when the model was near stationary and when it was excited by flow to oscillate in roll, the following conclusions may be drawn.

A. Wing rock was generated by a limit cycle mechanism due to the fluctuating pressure changes on the wing top surface, especially near the wing tip region. In the cases observed, the major reason for the pressure changes was the motion induced $\Delta\alpha$ which alternately caused leading edge stall and recovery. The amount of energy input to the limit cycle, to be consumed by aerodynamic and/or mechanical damping, may be evaluated quantitatively.

B. Based on kinematics, the roll oscillations acted together with α_o, β to cause substantial $\Delta\alpha$ changes which contributed to the limit cycle. Wing rock amplitude was thus dependent on the steady state sideslip angle β.

C. With a sideslip angle β, the upper wing surface on the windward side contributed the majority of the fluctuating pressures which caused wing rock.

D. With $\Delta\alpha$, the local fluctuating pressure coefficient followed the ramp curve during leading edge stall and the consequent loss of lift. Dynamic overshoot was observed in both the lift loss and recovery phases.

E. Based on the observations of the wind tunnel test data, a preliminary mathematical model of aircraft wing rock was developed which illustrated the motion-coupled limit cycle mechanism. Since the limit cycle defining the energy input to the aircraft was dependent on a number of flight condition parameters, no uniqueness condition can be established at this time to define and predict wing rock. Nevertheless, it is known that wing rock was directly related to the lift loss (ramp) of the C_p vs. α curve covering the fluctuating-pressure-active region of the wing. Additional acquisition and processing of controlled test data as those described above may further refine and quantify the preliminary mathematical model of aircraft wing rock described in this report.

14. In actual transonic maneuver flight tests of F-5A aircraft, two distinct points were identified as the buffet onset and wing rock with increasing α. The corresponding model tests at fixed α conditions did not reflect the buffet onset point because of the substantial mechanical damping of the model. The critical α^* angle, at which the model became unstable and oscillated in roll, was in most cases within $\pm 2^\circ$ of the wing rock α recorded in actual flight tests.

REFERENCES

1. Hwang, C., and Pi, W. S., "Investigation of Northrop F-5A Wing Buffet Intensity in Transonic Flight," NASA CR-2484, November 1974.

2. Loving, D. L., "Wind Tunnel-Flight Correlation of Shock-Induced Separated Flow," NASA-TN-D3480, 1966.

3. "The Interaction Between Local Effects at the Shock and Rear Separation - A Source of Significant Scale Effects in Wind Tunnel Tests on Airfoils and Wings," Transonic Aerodynamics, AGARD Proceeding, CP - 35, September 1968.

4. Mabey, D.G., "Analysis and Correlation of Data on Pressure Fluctuations in Separated Flow," J. Aircraft, Volume 9, Number 9, September 1972

5. Dods, J. B., Jr. and Hanly, R. D., "Evaluation of Transonic and Supersonic Wind Tunnel Back-Ground Noise and Effects of Surface Pressure Fluctuation Measurements," AIAA Paper 72-1004, September, 1972

6. Titiriga, A. Jr., "F-5A Transonic Buffet Flight Test," AFFDL-TR-69-110, October 1969.

7. Owen, T. B., "Techniques of Pressure Fluctuation Measurements Employed in the RAE Low Speed Wind Tunnels," AGARD Report 172, 1958, also Aeronautical Research Council Report 10780.

8. Ericksson, L. E. and Reding, J. P., "Dynamic Stall Analysis in Light of Recent Numerical and Experimental Results," Journal of Aircraft, Vol. 13, No. 4. April 1976.

9. Liiva, J., "Unsteady Aerodynamics and Stall Effects on Helicopter Rotor Blades Airfoil Sections," Journal of Aircraft, Vol. 6, No. 1, Jan. 1969.

10. Halfman, R. L., Johnson, H. C., Haley, S. M., "Evaluation of High-Angle-of-Attack Aerodynamic Derivative Data and Stall Prediction Techniques," NACA TN-2533, November, 1951.

11. Phillippe, J. J., "Dynamic Stall: An Example of Strong Interaction Between Viscous and Inviscid Flows," AGARD Fluid Dynamics Panel Symposium on Unsteady Aerodynamics, Ottawa, Canada, September, 1977.

12. "Basic Aerodynamic Stability and Control Data, F-5," Northrup Corp., Aircraft Division, NOR67-42, March 1967.

1. Report No.	2. Government Accession No.	3. Recipient's Catalog No.
NASA CR-3061		

4. Title and Subtitle	5. Report Date
"Investigation of Steady and Fluctuating Pressures Associated with the Transonic Buffeting and Wing Rock of a One-Seventh Scale Model of the F-5A Aircraft"	November 1978
	6. Performing Organization Code
7. Author(s)	8. Performing Organization Report No.
Chintsun Hwang and W. S. Pi	
	10. Work Unit No.
9. Performing Organization Name and Address	
Northrop Corporation, Aircraft Division Hawthorne, California	11. Contract or Grant No. NAS2-8734
	13. Type of Report and Period Covered
12. Sponsoring Agency Name and Address	Contractor Report
National Aeronautics and Space Administration Washington, D. C. 20546	14. Sponsoring Agency Code

15. Supplementary Notes

16. Abstract

The report describes a wind tunnel test of a 1/7 scale F-5A model and the evaluation of pressure, force, and dynamic response measurements during buffet and wing rock. Effects of Mach number, angle of attack, sideslip angle, and control surface settings were investigated. The mean and fluctuating static pressure data are presented and correlated with some corresponding flight test data of a F-5A aircraft. Details of the instrumentation and the specially designed support system which allowed the model to oscillate in roll to simulate wing rock are also described. A limit cycle mechanism causing wing rock was identified from this study, and this mechanism is presented.

17. Key Words (Suggested by Author(s))	18. Distribution Statement
Buffeting, Wing Rock, Stability and Control, Aerodynamic Loads, Separated Flow	Unclassified Star Category 02

19. Security Classif. (of this report)	20. Security Classif. (of this page)	21. No. of Pages	22. Price*
Unclassified	Unclassified	213	$9.25

*For sale by the National Technical Information Service, Springfield, Virginia 22161

NASA-Langley, 1978